

**EXPLORING INDIVIDUAL SUPRAMOLECULAR
INTERACTIONS AND STIMULI-RESPONSIVE POLYMERS BY
AFM-BASED FORCE SPECTROSCOPY**

PROEFSCHRIFT

ter verkrijging van
de graad van doctor aan de Universiteit Twente,
op gezag van de rector magnificus,
Prof. Dr. H. W. M. Zijm,
volgens besluit van het College voor Promoties
in het openbaar te verdedigen
op donderdag 10 februari 2005 om 13.15 uur

door

Shan Zou

Geboren op 06 augustus 1975
te Changchun, China

Dit proefschrift is goedgekeurd door:

de Promotor: Prof. Dr. G. J. Vancso

Assistent-promotor: Dr. H. Schönherr

This work has been supported by the MESA⁺ Institute for Nanotechnology (MESA⁺ Strategic Research Orientation Nanolink) of the University of Twente.

Exploring individual supramolecular interactions and stimuli-responsive polymers by
AFM-based force spectroscopy

Shan ZOU © 2005

Ph.D. Thesis

University of Twente,

Enschede, the Netherlands

ISBN 90-365-2132-7

Printed by PrintPartners Ipskamp, Enschede, the Netherlands, 2005

Contents

Chapter 1	Molecular Forces in Supramolecular and Macromolecular Chemistry	1
1.1	Measuring Forces and Mechanical Properties of Macromolecules	1
1.2	Thesis Work	2
Chapter 2	Nanostructures, Molecular Interactions and Single Molecule Force Spectroscopy	5
2.1	Nano-Objects and Nanoarchitectures	5
2.2	Molecular Interactions and Physics	15
2.3	AFM-Based Single Molecule Force Spectroscopy	21
2.4	Closing Remarks	34
Chapter 3	Probing Individual Supramolecular Host-Guest Interactions by Single Molecule Force Spectroscopy	41
3.1	Introduction	41
3.2	Evaluation of the Thermodynamics of Complexation in Solution and on Surfaces	44
3.3	Specific Interactions of β -CD – Guest Adsorbate Complexes by SMFS	45
3.4	Model of the Unbinding Forces and Comparison to Experimental Data	49
3.5	Probing Host-Guest Complex Rupture Forces for Multivalent Interactions by SMFS	50
3.6	Conclusions	53
3.7	Experimental	54
3.8	Appendix	55
Chapter 4	Tunable Surface Molecular Recognition of 2-Ureido-Pyrimidinone Moieties via Quadruple Hydrogen Bonds	63
4.1	Introduction	63
4.2	Molecular Recognition of UPys on Gold Surfaces	64
4.3	Complex Stability	67
4.4	Conclusions	70
4.5	Experimental	70
4.6	Appendix	73
Chapter 5	Rupture Forces of Single Quadruple Hydrogen Bonding Dimers: From Thermodynamic Equilibrium to Non-Equilibrium	75
5.1	Introduction	75
5.2	Rupture Forces of Individual Quadruple Hydrogen Bonding Arrays	76

5.3	Correlation between Rupture Forces and Loading Rates	79
5.4	Crossover from Thermodynamic Quasi-Equilibrium to Non-Equilibrium	82
5.5	Conclusions	83
5.6	Experimental	84
5.7	Appendix	87
Chapter 6	Stretching and Rupturing Individual Supramolecular Macromolecules by Force Spectroscopy	89
6.1	Introduction	89
6.2	Stretching and Rupturing of Individual Supramolecular Polymers	91
6.3	Discussion	94
6.4	Conclusions	96
6.5	Experimental	97
6.6	Appendix	98
Chapter 7	Grafting of Single, Stimuli-Responsive Poly(ferrocenylsilane) Polymer Chains to Gold Surfaces	101
7.1	Introduction	101
7.2	Control of PFS Surface Coverage	104
7.3	Isolation of PFS Macromolecules	109
7.4	AFM-Based Single Molecule Force Spectroscopy	112
7.5	Discussion	113
7.6	Conclusions	119
7.7	Experimental	119
Chapter 8	Force Spectroscopy of Individual Stimuli-Responsive Poly(ferrocenylsilane) Macromolecules: Towards a Redox-Driven Molecular Motor	125
8.1	Introduction	125
8.2	Single Chain Elasticity Measurements on Neutral PFS Macromolecules	130
8.3	Single Chain Elasticity Measurements on Oxidized PFS Macromolecules	133
8.4	Changing the Elasticity of PFS between the Neutral and Oxidized States	137
8.5	Chemically and Electrochemically Induced Mechanical Work	137
8.6	Efficiency of Converting Electrochemical Energy to Mechanical Work	139
8.7	Conclusions	140
8.8	Experimental	140
	Summary	143
	Samenvatting	147
	Acknowledgement	151
	Publications	153
	Curriculum vitae	154

Chapter 1

Molecular Forces in Supramolecular and Macromolecular Chemistry

1.1 Measuring Forces and Mechanical Properties of Macromolecules

The importance of forces responsible for specific interactions between (bio)macromolecules has been recognized for a long time.^{1,2} However, only in the past decade have scientists developed instrumentation and methodologies to directly measure mechanical properties of single macromolecules, as well as interaction forces between individual molecules under physiological conditions. Such specific interactions resulting from multiple weak, non-covalent bonds formed between defined portions of interacting molecular partners regulate the complex diversity of life. For instance, hydrogen bonding has been shown to be a feature of all known double helical structures of nucleic acids and the basis for genetic coding in all living organisms.³ Similarly, it is H-bonds and other supramolecular interactions that stabilize the secondary structures (i.e. α -helix and β -pleated sheet) of proteins.

The advent of probe microscopes, in particular atomic force microscopy (AFM),⁴ has opened new horizons of molecular force measurements in material and life sciences.⁵⁻¹¹ Other techniques have also been employed to directly probe weak molecular forces, including the surface forces apparatus, magnetic beads, biomembrane force probes, the flow chamber apparatus, optical tweezers and force clamps.¹²⁻¹⁶ The great advancement of AFM-based single molecule force spectroscopy (SMFS), which can be used to measure inter- and intramolecular interaction forces from ca. 10 piconewtons to several nanonewtons and distances from the Ångström to the micrometer length scales, has enabled one to determine interaction forces at the level of single molecules and/or their complexes, as well as to evaluate mechanical properties of biological and synthetic macromolecules.^{11,17,18}

With the rapidly expanding knowledge about atomic and molecular forces and their relation to structures and functions, a multitude of essential processes, such as molecular recognition and protein folding–unfolding, have become accessible for research with unparalleled resolution and sensitivity.^{1,19} In these biochemical processes, weak interactions

govern intermolecular recognition and biochemical processes that occur (due to strengths of weak interactions) within the range of thermal fluctuations at body temperature.³ The understanding of mechanical and conformational properties of biomacromolecules may provide insights into the molecular basis of the elasticity of cell-wall constituents, protein folding and protein-protein assemblies.

In living organisms molecular forces also play a crucial role for specific “molecular machines”, such as ATP synthases rotary motors and kinesin / myosin “cargo trains”, which fulfill biological functions.²⁰⁻²² Such “molecular machines” are usually “fuelled” by energy gained in molecular redox processes. Stimuli-responsive polymers, such as redox active organometallic macromolecules, can be considered as model systems for molecular motors. Molecular motors convert e.g. chemical and/or optical energy into mechanical work and motion. Force spectroscopy, (due to e.g. its sensitivity) is, in principle, a suitable approach to address the origin of function of such molecular motors at the single molecule level.²³⁻²⁶ The availability of force, distance and velocity as direct experimentally controllable parameters in single molecule experiments provides a basis for new theories describing the role of mechanical force in molecular motors.^{27,28}

1.2 Thesis Work

This Thesis describes molecular force measurements and their interpretation in supramolecular host-guest and H-bonding systems, as well as the direct detection of individual supramolecular polymer chains and investigations of mechanical properties of stimuli-responsive macromolecules as a model system to realize electrochemically powered molecular motors by AFM-based force spectroscopy.

In Chapter 2, some fundamental aspects of nanotechnology are discussed from the perspective of molecular scale structures, as well as architectures, molecular interactions and characterization approaches using AFM-based single molecule force spectroscopy.

Chapter 3 describes systematic studies of individual supramolecular host-guest interactions in aqueous medium between α -cyclodextrin (α -CD) receptor cavities in self-assembled monolayers (SAMs) and various apolar guest molecules attached to AFM tips by force spectroscopy.²⁹ Due to fast unbinding-rebinding kinetics on the experimental time scale, host-guest unbinding was probed under conditions of quasi-thermodynamic equilibrium. The unbinding forces of single host-guest complexes were found to correlate with the corresponding values of equilibrium complexation constants. Molecular rupture forces were successfully

described as a function of complexation constants with an equilibrium model based on the potential energy landscape of tip-surface interaction.

We developed a molecular platform for the controlled immobilization and growth of supramolecular architectures on various substrates, as described in Chapter 4. This platform is based on the self-complementary molecular recognition of 2-ureido-4[1H]-pyrimidinone (UPy) moieties via quadruple hydrogen bonding.³⁰ Depending on the choice of solvent and temperature, reversible supramolecular recognition between surface-immobilized adsorbates and external guests occurred, as shown by X-ray photoelectron spectroscopy (XPS), differential pulse voltammetry (DPV), AFM and surface plasmon resonance (SPR) methods. The tunable complex stability on surfaces renders these systems highly suitable for the construction of directionally defined surface-immobilized supramolecular architectures.

The relationship between unbinding forces of single quadruple H-bonding arrays and loading rates is presented in Chapter 5. The value of unbinding forces of individual supramolecular complexes can be directly determined by force spectroscopy in both thermodynamic quasi-equilibrium and non-equilibrium states. Equilibrium and non-equilibrium conditions could be achieved by controlling the temperature.

Direct probing of reversible supramolecular polymer chains is the main theme of Chapter 6. In poly(ethylene glycol) (PEG)-based UPy supramolecular polymer materials, the individual reversible linking sites along a supramolecular polymer chain, i.e. the complexes based on self-complementary recognition of UPys, act as independent bonds in series. The stretching of individual supramolecular polymer chains, as described in this Chapter, opens the pathway to elucidate properties of these dynamic, reversibly aggregated polymers as functions of various external parameters at the single molecule level.

In Chapter 7, the unique combination of both visualization and force sensing capabilities of AFM was utilized to locate, to physically contact and finally to stretch, individual stimuli-responsive macromolecules.³¹ Redox-responsive poly(ferrocenylsilane) (PFS) molecules were attached individually to gold surfaces, whereby the surface coverage of PFS macromolecules could be conveniently controlled. AFM, contact angle, as well as cyclic and differential pulse voltammetry measurements were carried out to characterize the morphology, wettability, and surface coverage of the grafted layers in order to optimize conditions for obtaining molecularly isolated PFS molecules. The isolated PFS macromolecules were subjected to in situ AFM-based force spectroscopy measurements. The single chain elasticity behavior of PFS in isopropanol was successfully fitted with the modified freely-jointed chain (m-FJC) model.

The investigation of external stimuli-responsive PFS polymers, as a model system to realize an electrochemically powered molecular motor, is discussed in Chapter 8. The changes of the parameters describing single chain elasticity in neutral and in oxidized PFS chains were determined by force spectroscopy. The single chain elasticity can be reversibly controlled in situ by adjusting the applied potential in electrochemical SMFS experiments. For a defined operating cycle of a PFS-based molecular motor, the efficiency was estimated as 5%. In principle, PFS-based single molecule motors can be optimized by reducing the input energy to reach an efficiency of 10%.

References:

- (1) Stryer, L. *Biochemistry*; 4th Ed.; W. H. Freeman and Company: New York, 1995.
- (2) Lehn, J. M. *Angewandte Chemie-International Edition* **1988**, *27*, 89-112.
- (3) Jeffrey, G. A.; Saenger, W. *Hydrogen Bonding in Biological Structures*; Spinger-Verlag: Berlin, 1991.
- (4) Binnig, G.; Quate, C. F.; Gerber, C. *Physical Review Letters* **1986**, *56*, 930-933.
- (5) Florin, E. L.; Moy, V. T.; Gaub, H. E. *Science* **1994**, *264*, 415-417.
- (6) Lee, G. U.; Chrisey, L. A.; Colton, R. J. *Science* **1994**, *266*, 771-773.
- (7) Janshoff, A.; Neitzert, M.; Oberdorfer, Y.; Fuchs, H. *Angewandte Chemie-International Edition* **2000**, *39*, 3213-3237.
- (8) Zlatanova, J.; Lindsay, S. M.; Leuba, S. H. *Progress in Biophysics & Molecular Biology* **2000**, *74*, 37-61.
- (9) Schönherr, H.; Beulen, M. W. J.; Bügler, J.; Huskens, J.; van Veggel, F. C. J. M.; Reinhoudt, D. N.; Vancso, G. J. *Journal of the American Chemical Society* **2000**, *122*, 4963-4967.
- (10) Zapotoczny, S.; Auletta, T.; de Jong, M. R.; Schönherr, H.; Huskens, J.; van Veggel, F. C. J. M.; Reinhoudt, D. N.; Vancso, G. J. *Langmuir* **2002**, *18*, 6988-6994.
- (11) Zhang, W.; Zhang, X. *Progress in Polymer Science* **2003**, *28*, 1271-1295.
- (12) Israelachvili, J. N. *Intermolecular and Surface Forces*; 2nd Ed.; Academic Press, London, 1991.
- (13) Smith, S. B.; Finzi, L.; Bustamante, C. *Science* **1992**, *258*, 1122-1126.
- (14) Evans, E.; Ritchie, K.; Merkel, R. *Biophysical Journal* **1995**, *68*, 2580-2587.
- (15) Ashkin, A.; Schutze, K.; Dziedzic, J. M.; Euteneuer, U.; Schliwa, M. *Nature* **1990**, *348*, 346-348.
- (16) Fernandez, J. M.; Li, H. B. *Science* **2004**, *303*, 1674-1678.
- (17) Clausen-Schaumann, H.; Seitz, M.; Krautbauer, R.; Gaub, H. E. *Current Opinion in Chemical Biology* **2000**, *4*, 524-530.
- (18) Dufrene, Y. F. *Nature Reviews Microbiology* **2004**, *2*, 451-460.
- (19) Buckingham, A. D.; Legon, A. C.; Roberts, S. M. *Principles of Molecular Recognition*; Blackie: London, 1993.
- (20) Crandall, B. C. *Nanotechnology : Molecular Speculations on Global Abundance*; MIT Press: Cambridge, 1996.
- (21) Sauvage, J.-P. E. *Molecular Machines and Motors*; Springer: Berlin, 2001.
- (22) Wilson, M.; Kannangara, K.; Smith, G.; Simmons, M.; Raguse, B. *Nanotechnology*; Chapman & Hall/CRC Press: Boca Raton, Florida, 2002.
- (23) Simmons, R. *Current Biology* **1996**, *6*, 392-394.
- (24) Schliwa, M. *Nature* **1999**, *397*, 204-205.
- (25) Junge, W. *Proceedings of the National Academy of Sciences of the United States of America* **1999**, *96*, 4735-4737.
- (26) Banting, G.; Higgins, S. J. *Molecular Motors*; London: Portland Press, 2000.
- (27) Fisher, M. E.; Kolomeisky, A. B. *Proceedings of the National Academy of Sciences of the United States of America* **1999**, *96*, 6597-6602.
- (28) Keller, D.; Bustamante, C. *Biophysical Journal* **2000**, *78*, 541-556.
- (29) Auletta, T.; de Jong, M. R.; Mulder, A.; van Veggel, F. C. J. M.; Huskens, J.; Reinhoudt, D. N.; Zou, S.; Zapotoczny, S.; Schönherr, H.; Vancso, G. J.; Kuipers, L. *Journal of the American Chemical Society* **2004**, *126*, 1577-1584.
- (30) Zou, S.; Zhang, Z. H.; Förch, R.; Knoll, W.; Schönherr, H.; Vancso, G. J. *Langmuir* **2003**, *19*, 8618-8621.
- (31) Zou, S.; Ma, Y.; Hempenius, M. A.; Schönherr, H.; Vancso, G. J. *Langmuir* **2004**, *20*, 6278-6287.

Chapter 2

Nanostructures, Molecular Interactions and Single Molecule Force Spectroscopy

The evolution of nanotechnology is discussed from the perspective of molecular scale structures, as well as architectures, molecular interactions and characterization, using atomic force microscopy (AFM)-based single molecule force spectroscopy. This Chapter begins with an introduction to the bottom-up paradigm of nanoscience and nanotechnology. The key concepts of this paradigm are explored through visualizing, addressing and manipulating well-defined molecular nanostructures. Fundamental characterization of molecular interactions combined with visualization and molecular manipulation, enable us to expand the basic understanding of these systems. This basis allows us to make rational predictions and to control the design of the corresponding nanoscale building blocks and platforms. The enhanced understanding of the elastic behavior of single polymer chains, binding potentials of supramolecular interactions, protein folding pathways, molecular motors, and DNA mechanics, has opened new perspectives in material and life sciences.

2.1 Nano-Objects and Nanoarchitectures

Nanotechnology encompasses the production and application of physical, chemical and biological systems at scales ranging from individual atoms or molecules to submicron dimensions, as well as the integration of the resulting nanostructures into larger systems.¹⁻³ It is widely considered as the ultimate manufacturing technology that allows thorough, inexpensive control of the structure of matter on the atomic level. One-to-one control of a nanoscale object by another nano-object or a micro- (or macro-) object is essential. Nanotechnology is likely to have a profound impact on economy and society in the twenty-first century, comparable to that of semiconductor technology, information technology, cellular and molecular biology.

Nanotechnology is not synonymous with chemistry, since it is specific and concerned with observing atoms and molecules, and manipulating them through visualization at the nanoscale. However, it may eventually encompass all of chemistry and a large part of physics and molecular biology.

The discovery of novel materials, processes, and phenomena at the nanoscale, as well as the new experimental and theoretical techniques provide opportunities for the development of innovative nanosystems. Nanostructured materials (although here it is not a one-to-one control of the nano-objects) are expected to possess various unique structures, properties and applications.⁴ Research in nanotechnology promises breakthroughs in areas, such as materials and

manufacturing, nanoelectronics, medicine and healthcare, energy, and information technology. It is widely believed that nanotechnology will initiate the next industrial revolution.^{5,6}

In this section, bottom-up controlled molecular structures and architectures from biological systems to synthetic supramolecular chemistry are summarized.

2.1.1 Bottom-Up Strategy of Nanotechnology

The fabrication of conventional devices relies on the assembly of macroscopic building blocks with specific configurations. The shapes of these components are carved out of larger materials by exploiting physical methods. This *Top-down* approach is very powerful and can effectively deliver microscaled objects. However, this strategy becomes increasingly challenging as the dimensions of the target structures approach the nanoscale. Nature efficiently builds nanostructures by relying on (bio)chemical approaches. Small molecular building blocks are assembled with a high degree of structural control in nanoscaled materials with defined shapes, properties and functions. In contrast to the top-down physical methods, tiny components are connected to produce larger objects in these *Bottom-up* chemical approaches.^{1,7,8} By mimicking nature's *Bottom-up* strategy, indeed, it is now possible to assemble any kind of device or functional system, ranging from functional materials to ultra-sensitive medical sensors and nanocomputers.⁹⁻¹⁶ In Sections 2.1.2 – 3 the creation of nanostructures, including single molecules as objects, as well as supramolecular architectures, will be discussed.

2.1.2 Biomolecular Objects: Nucleic Acids and Amino Acids

Nanoscience and nanotechnology are rather new words, but not entirely new fields. Nature has many objects and processes that function on the nanoscale.^{15,17} The understanding of these functions can guide us in imitating and producing nanodevices and nanomaterials. In the form of deoxyribonucleic acid (better known as DNA), the macromolecular nucleic acids are of prime importance because they are identically replicated and inherited from one generation to the next. The information about every feature of each molecule contained in a living being is encoded in the nucleotide sequence of its DNA, which is translated into the amino acid sequences of proteins.¹⁷

The monomer units of DNA are nucleotides, and the polymer is known as a "polynucleotide". Each nucleotide consists of a 5-carbon sugar (deoxyribose), a nitrogen-containing base attached to the sugar, and a phosphate group. There are four different types of nucleotides found in DNA (adenine, thymine, guanine and cytosine, which are more commonly represented by the letters A, T, G, C: Figure 2.1A), differing only in the nitrogenous base. The characteristics of the subunits are such that adenine will bind to thymine, and guanine will bind

to cytosine (Figure 2.1B). Therefore, if the two polynucleotide strands are made with the appropriate complementary sequence, the two strands will bind together. Here, H-bonding interactions play a crucial role, determining biomolecular geometry and biological processes (e.g. DNA replication).¹⁸ The structure that most people are familiar with is the famous double helix. Biology uses DNA to store information. In fact, the whole blueprint of the structure of each cell in the human body is stored in the DNA — the information that tells certain cells to become liver, muscle or nerve cells, where and how to grow bonds, which proteins (see below) to manufacture and much else. The double strands wrap around a common axis to form a right-handed double helix with a diameter of ca. 2 nm.¹⁹⁻²³ In DNA, approximately ten base pairs define each helical turn corresponding to a helical pitch of ca. 3 nm. Considering that these molecules can incorporate up to about 10^{11} base pairs, end-to-end lengths of only few nanometers to meters can be reached.

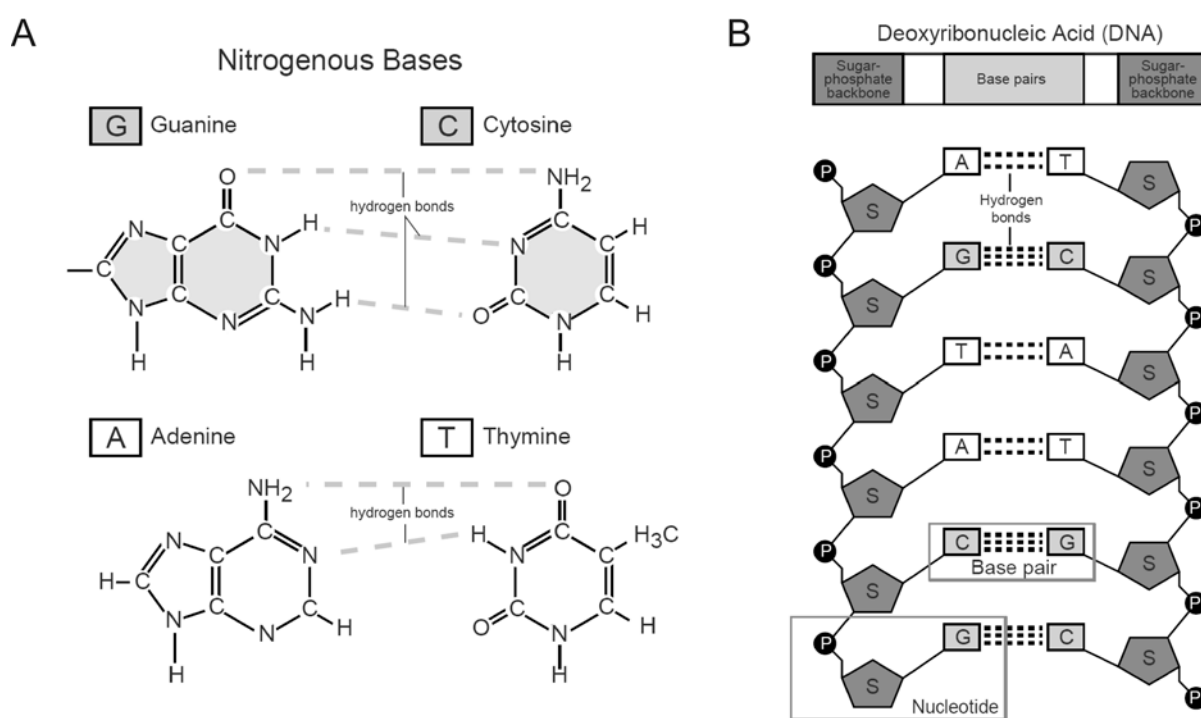


Figure 2.1. (A) The chemical structure of the four bases in DNA. (B) Polynucleotide strands incorporate alternating phosphate and sugar residues joined by covalent bonds. Each sugar carries one of four heterocyclic bases (adapted from the Internet <http://www.accessexcellence.org/RC/VL/GG/basePair2.html>).

Nature's *Bottom-up* approach for fabricating nanostructures is not limited to nucleic acids. Proteins are also built by joining simple molecular objects, the amino acids, responsible for the higher level structure and biological function of a protein.¹⁷ More precisely, nature relies on 20 amino acids to assemble linear polymers, so-called polypeptides. The secondary, tertiary and quaternary structures of a protein are mainly stabilized by non-covalent interactions, i.e. H-bonds, hydrophobic interactions, and van der Waals forces.^{17,18} Considering that proteins can

incorporate more than one polypeptide chain (note: for a single strand with 100 repeat amino acid units, a total of 20^{100} unique combinations of polypeptide sequences are possible) with over 4000 amino acid residues each, it is obvious that an enormous number of different biomolecules can be formed relying on the same fabrication strategy with really small quantity of building blocks (objects).² The amazing thing, however, is that out of all the possible structures the macromolecules (polypeptides) could adapt during formation (folding) process, one specific, stable, three-dimensional structure of each protein exists that exhibits the required biological activity.

Using four DNA bases, and 20 amino acids, it is possible to build vast quantities of different nanomaterials, nanostructures and scaffolds, and even some functioning nanomachines. For instance, beads-on-a-string structures of DNA-streptavidin complexes on substrate surfaces were detected using atomic force microscopy (AFM) (Figure 2.2).²⁴⁻²⁷ Depending on the size of the DNA and the number of streptavidin molecules included, supramolecular complexes with dimensions of 100 to 200 nm were formed, as shown in Figure 2.2B.

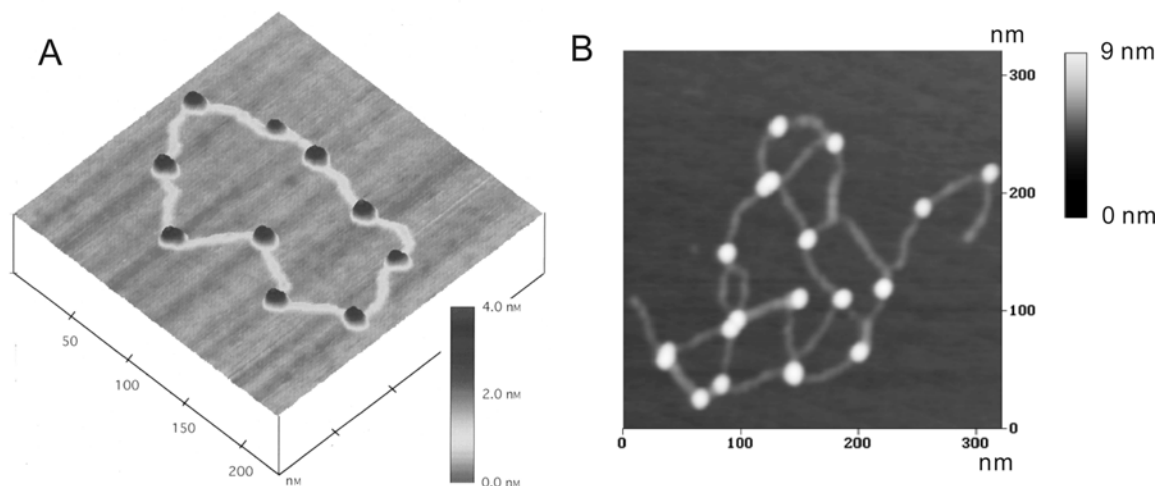


Figure 2.2. AFM images of DNA-streptavidin complexes (A) simple ring structure; (B) connected ring structure (adapted from ref [24,27]).

2.1.3 Carbon-Based Nano-Objects

Nano-objects of carbon are of particular interest in nanotechnology, including Buckminsterfullerenes and carbon nanotubes (Figure 2.3).²⁸⁻³⁴ The regular spherical fullerenes (e.g., C_{60}) exhibit the ability of carbon to form zero dimensional quantum dots of subnanometer dimensions, and one-dimensional quantum wires in the form of carbon nanotubes that cover a range of dimensions from several micrometers (length) down to a few nanometers (diameter). Atoms in C_{60} molecules are held together by strong covalent bonds, and interact weakly with neighbouring C_{60} molecules. C_{60} fullerenes can be considered as individual nanoscale building blocks of subnanometer size (diameter 0.7 nm), which can be manipulated using scanning

tunneling microscopy (STM) probe tips.³⁵ Moreover, it has been proposed that a C_{60} can be “rolled” along the surface of a suitable ionic substrate by a rotating external electric field, utilizing the large size and polarizability of C_{60} , which allows one to build nanostructures by one-to-one control of the individual constituents.³⁶ Fullerenes are not only interesting as individual nano-objects, but also as material for structures in the medium range of the nanoscale. Thus, regular structures on this length scale can be realized by a self-organization process during the thermal activation of fullerene crystals. Single crystals exhibit a photo-induced surface reconstruction that leads to periodic structures with dimensions of 30 – 40 nm.³⁷

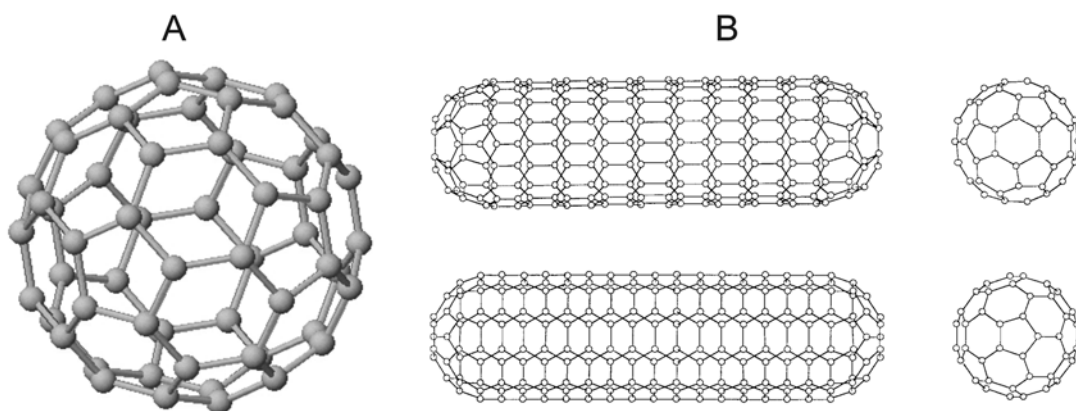


Figure 2.3. Drawings of (A) C_{60} : Buckminsterfullerene and (B) two nanotubes which are capped by one half of a C_{60} molecule (adapted from ref [33]).

The synthesis of single-wall nanotubes (SWNT) was reported by Smalley *et al.*³⁸ in high yields using lasers as energy source. This technique yielded SWNT with uniform diameters of about 1.38 nm each,³⁸ as calculated from X-ray diffraction studies. Multi-wall nanotubes (MWNT) can reach diameters in excess of 100 nm with hierarchies of several levels of helical structures. Besides continuous walls, spiral cross-sections were also observed.³² The unique combination of the physical structure (high aspect ratio and nanometer-scale radius of curvature of the tip), mechanical properties such as stiffness and strength, chemical stability, and electrical properties make carbon nanotubes also useful for field-emitting devices and electrical devices, particularly in cases where nanotubes serve as molecular wires.³⁹⁻⁴¹ Other applications include the use of SWNT and MWNT as ultrasharp tips for scanning force microscopy, electromechanical actuators, sensing devices for chemical or biological molecules, and reinforcement agents, when used in nanocomposites.⁴²⁻⁴⁵

2.1.4 Synthetic Dendrimers

One of the strategies for the fabrication of objects with three-dimensionally defined geometries and a covalently bound molecular structure is based on dendrimer synthesis (Figure 2.4A).^{46,47} As a result of branches, relatively large molecules can be formed, such as the

polyamidoamine (PAMAM) dendrimers, shown in Figure 2.4B.⁴⁸⁻⁵³ Their distinctive structural attribute is the fractal geometry and their unique physical property is the high monodispersity. In the presence of dendrimers, novel metal nanoparticles have been produced in aqueous solutions or organic solvents.⁵⁴⁻⁶¹ A dendrimer can function as a capping material or allow encapsulation of nanoparticles inside its volume, depending on the size of the dendrimer and on the interactions between metal ions and functional groups of the dendrimer.

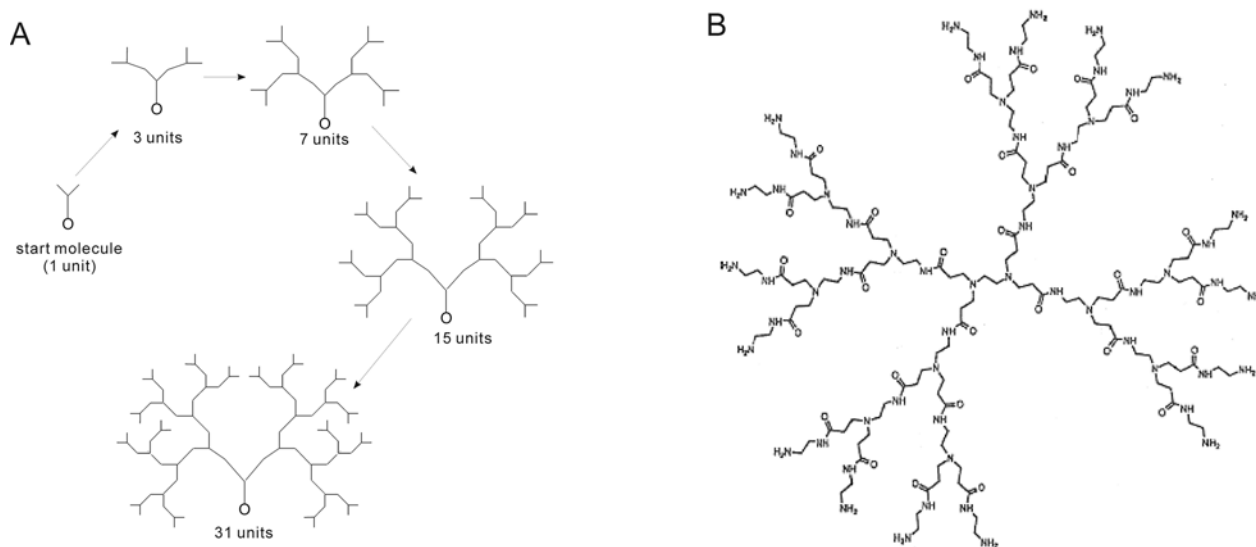


Figure 2.4. (A) Scheme of stepwise synthesis of dendritic molecules. (B) Generation 2 PAMAM dendrimer.

2.1.5 Macrocycles

Due to the π -electron-donating structure and the binding ability with electron acceptors, macrocycle polyethers e.g. crown ethers (Figure 2.5A), have become active units in the development of synthetic molecular shuttles and rotors.^{13,62,63}

Cyclodextrins, a class of supramolecular host molecules, are cyclic oligosaccharides that consist of six (α -cyclodextrin), seven (β -cyclodextrin, Figure 2.5B), or eight (γ -cyclodextrin) glucose moieties. The most striking feature of cyclodextrins is their central cavity, shaped by the carbon atoms of the glucose units, rendering it relatively apolar. This cavity enables the inclusion of a variety of organic molecules in aqueous solution.^{64,65}

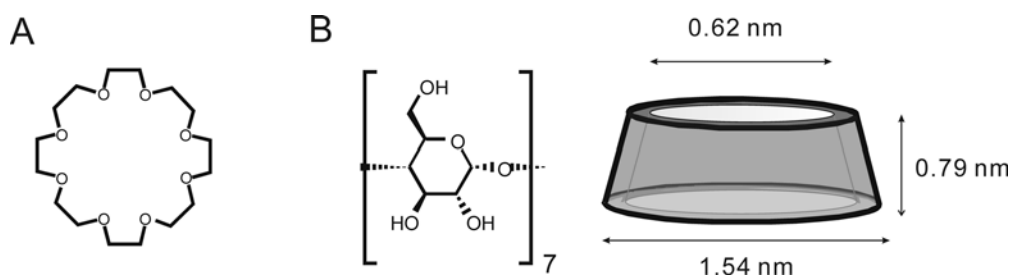


Figure 2.5. The structures of (A) crown ether and β -cyclodextrin (B).

The driving force for the inclusion of “guest” molecules into the cavity has been extensively studied.^{15,64,66-68} Complexation by cyclodextrins is governed by several factors, the most important of which are van der Waals and hydrophobic interactions, and conformational changes or strain release of the cyclodextrin molecule upon complexation.⁶⁷

2.1.6 Nanoarchitectures with Controlled Structure and Designed Properties and Functions

Molecular self-assembly is the spontaneous organization of molecules into stable, structurally well-defined aggregates.^{69,70} The basic principles of molecular self-assembly – using multiple weak, reversible interactions, e.g. hydrogen bonds, ionic bonds and van der Waals interactions (cf. section 2.2) to assemble individual molecular subunits into stable aggregates that represent a thermodynamic minimum of these interactions⁷¹ – are vitally important in biology,^{72,73} and have stimulated the development of new strategies and applications in nanotechnology and supramolecular technology.

Self-assembly is a route to structures having a high degree of perfection. Due to the fabrication of structures in thermodynamic minima (i.e. defects are rejected), it is possible to use molecular self-assembly to fabricate molecularly defined and determined nanostructures.¹

The basic principle of molecular self-assembly for the formation of non-biological systems has many precedents, including hydrogen-bonded aggregates⁷⁴⁻⁷⁶ (see Figure 2.6 and 2.9), templated crystals,^{77,78} colloids,⁷⁹ micelles,⁸⁰ liquid crystals,⁸¹ and artificial peptide tubules.⁸²⁻⁸⁴ The self-assembly of a complex molecular box with 36 hydrogen bonds, consisting of two stacked cyclic rosettes, as demonstrated by Reinhoudt *et al.*,⁸⁵⁻⁸⁹ is shown in Figure 2.6.

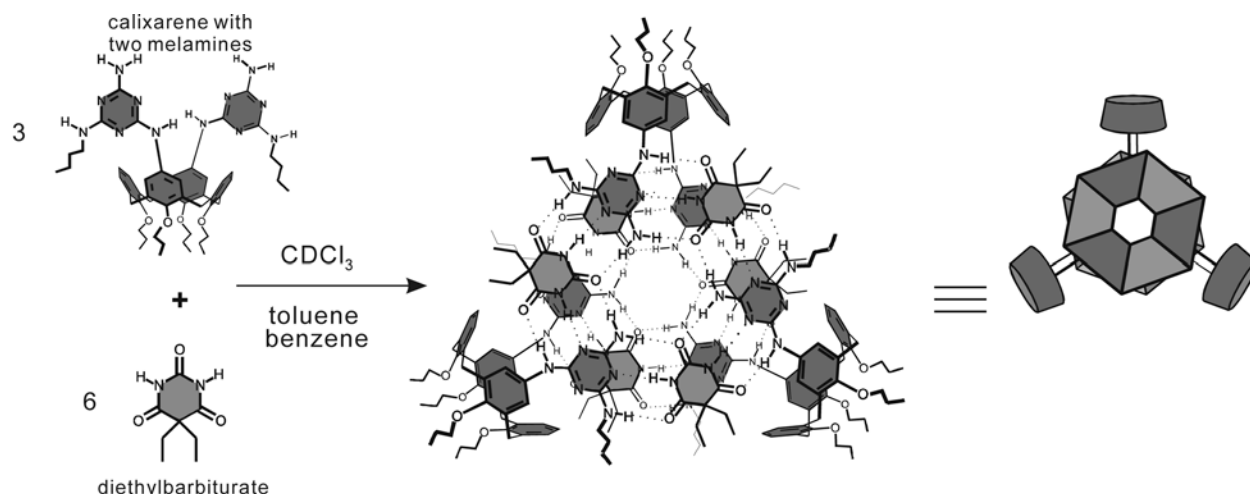


Figure 2.6. Hydrogen bonded rosette structures of calixarene molecules in solution (adapted from ref [85,86]).

The cyclic rosettes are formed by 3 bis-melamine functionalized calixarene molecules and 6 diethylbarbiturate molecules. The two stacked rosettes are linked by calixarene molecules.

Again, the corresponding supramolecular interactions are essential for the construction of nanostructures and also assist in molecular recognition. The examples mentioned above are usually formed in solution. The development of molecule-based devices requires identification of methods to transfer and anchor the functional structures to solid states.

Two main approaches for the deposition of organized molecular arrays on supports have emerged. In the first approach, amphiphilic molecular building blocks are compressed into monolayers at air/water interfaces. The resulting films can be transferred on supporting solids using the Langmuir-Blodgett (LB) technique. Alternatively, certain molecules can be designed to self-assemble on the surfaces of suitable solids from liquid or vapor phases and form self-assembled monolayers.

Langmuir-Blodgett Films

Films of amphiphilic molecules can be deposited on a variety of solid supports using the LB technique (Figure 2.7). This method can be extended to electroactive compounds as well, incorporating hydrophilic and hydrophobic groups.⁹⁰

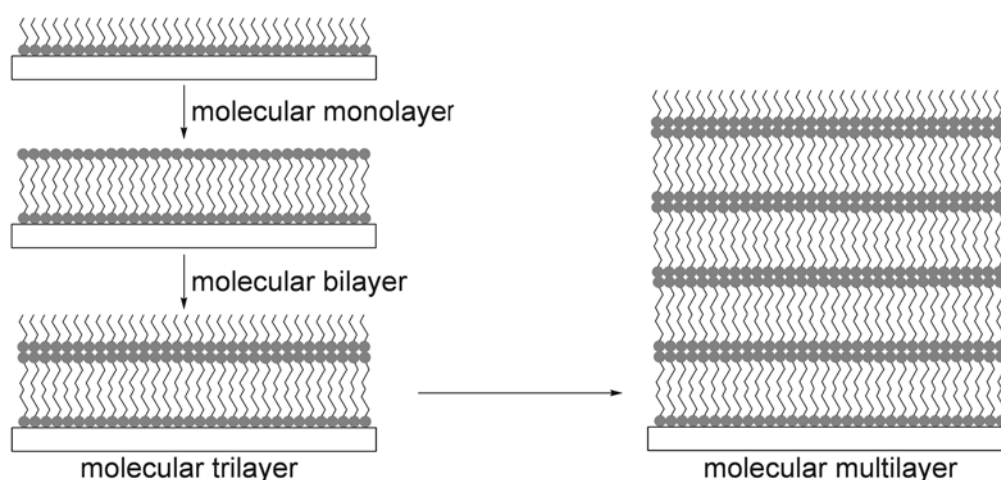


Figure 2.7. Langmuir-Blodgett films on solid substrates. A single passage of the substrate through the air/water interface generates a monolayer (left top); repeated passages result in multilayer formation with alternating orientations.

The ability to transfer electroactive monolayers from air/water interfaces to electrode surfaces can be exploited to fabricate molecule-based electronic devices. In particular, arrays of interconnected electrode/monolayer/electrode tunneling junctions can be assembled combining the LB technique with electron beam evaporation.⁶²

A major problem of LB films is the existence of a significant number of defects, which necessitates fabrication in clean room environments. An alternative strategy for molecular device fabrication relies on self-assembly on solid surfaces using e.g. thiols on gold.

Self-Assembled Monolayers

Self-assembled monolayers (SAMs), Figure 2.8, have been widely studied and well developed among the self-assembled systems.⁹⁰⁻⁹⁴ SAMs were preceded historically by LB monolayers, which are not sufficiently robust for applications, as mentioned before.⁹⁰ Typical examples are alkanethiolates on gold⁹⁵ and alkylsiloxanes on hydroxyl-terminated silicon.⁹⁶ The formation of a compact monolayer occurs spontaneously. This is different from LB films on liquid surfaces, which require compression for the generation of a monolayer. Organic thiols, sulfides and disulfides, phosphonic acid, phosphines and isocyanates exhibit the ability to generate SAMs. Suitable substrates are noble metals with easily polarizable shells that form poorly dissolvable sulfides, such as Au, Ag, or Pt, or other metals and semiconductors, such as Cu, Pd, GaAs, and InP.⁹⁷ Detailed descriptions of characterization approaches for SAMs have been described in many books and reviews.^{1,90,92,98} Shortly, the combination of several techniques, e.g. contact angle measurements, infrared spectroscopy, X-ray photoelectron spectroscopy, surface plasmon resonance measurements, and scanning probe microscopy, often yield complementary information that can characterize the SAMs.

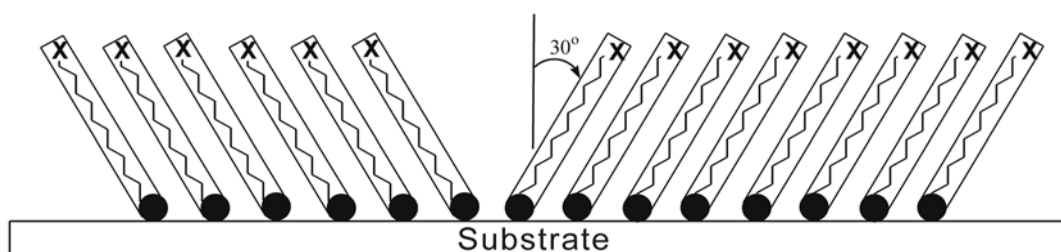


Figure 2.8. Representation of a highly ordered self-assembled monolayer.

Thiol-based SAMs are often used as molecular platforms for surface and AFM tip functionalization, as we show later. The ability of thiols to self-assemble on the surface of gold can be exploited to fabricate nanocomposite materials integrating organic and inorganic components.⁹⁹⁻¹⁰¹ Detailed studies on SAMs of different supramolecular host-guest systems, H-bonding systems, and end-functionalized polymers are presented in Chapters 3 to 7.

Properties and Functions by Design: Supramolecular Polymers

Linear supramolecular polymer chains can be assembled via self-complementary method utilizing weak interactions.¹⁰² Hydrogen bonding units based on 2-ureido-4[1H]-pyrimidinones (UPys) with donor-donor-acceptor-acceptor (DDAA) arrays, which dimerize in solution, constitute a very well known example. These complexes show an association constant of 6×10^7 M⁻¹ at room temperature in chloroform. Bifunctional compounds (Figure 2.9), possessing two of these UPys, can form very stable and long polymer chains via quadruple H-bonds in solutions,

which were discovered and described by Meijer, Sijbesma and co-workers.¹⁰³⁻¹⁰⁶ Although supramolecular polymers based on bifunctional UPy derivatives in many ways behave like conventional polymers, the strong temperature and solvent dependence of their mechanical properties really sets them apart from conventional polymers.¹⁰⁶ At room temperature, the supramolecular polymers show viscoelastic behavior in bulk and solution, whereas at elevated temperatures liquid-like properties are observed.^{105,107} These changes are due to the effects of temperature and solvent on the reversible polymer chain. Because of the temperature or solvent dependence of the association constant value of UPy, the average degree of polymerization of the chains is drastically reduced at elevated temperatures or in DMSO (which competes for H-bonds with other UPy units).

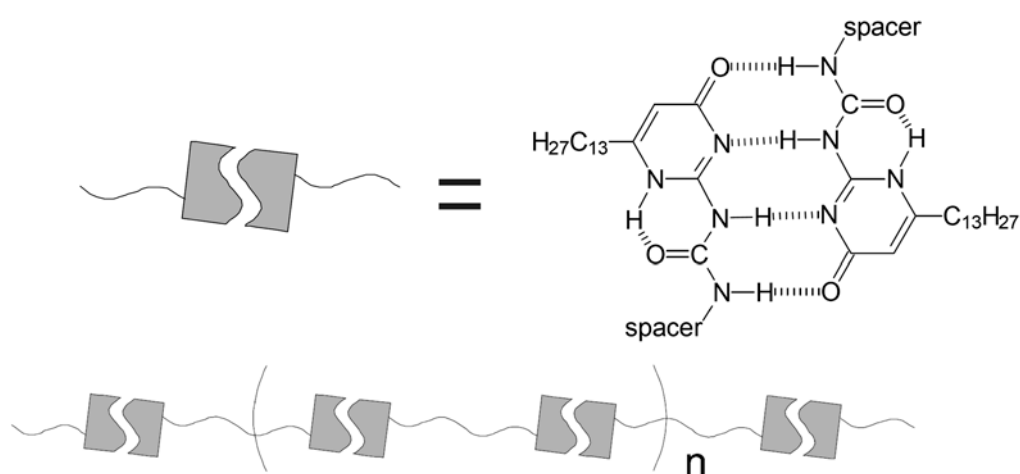


Figure 2.9. Polymeric assembly of a bifunctional ureidopyrimidinone derivative.

Bifunctional (or multifunctional) molecules, which interact via directional and supramolecular forces, can form self-assembled polymeric systems. Such systems have been reported by Whitesides *et al.*¹⁰⁸ and Reinhoudt *et al.*,¹⁰⁹ consisting of “tapes” and sheets formed from e.g. cyanuric acid or barbituric acid and melamine.

The quadruple hydrogen-bonded UPy unit has been further employed in the chain extension of telechelic polysiloxanes, poly(ethylene/butylenes), polyethers, polyesters and polycarbonates.¹⁰⁷ In these compounds, the material properties were shown to improve dramatically upon functionalization, and materials were obtained that combine many of the mechanical properties of conventional macromolecules.^{106,107}

The study of pyrimidinone-based supramolecular architectures at surfaces and interfaces will be discussed in Chapters 4 to 6. These structures were used in our research to construct surface-immobilized supramolecular architectures, as well as to mimic the supramolecular interactions mediated via H-bonds in nature.

2.2 Molecular Interactions and Physics

2.2.1 Interactions

In addition to the elementary composition, the interactions between the atoms determine the properties of the material. Hence, the understanding of the interactions in a structure is essential for the understanding of structure-property-function relationships.

With the decrease of size and system dimensions towards the nanoscale, the behavior and characteristics of isolated molecules gain increasing importance. Eventually, individual molecules (which exhibit thermal and structural fluctuations) will determine the behavior of nano-systems. In general, interactions between atoms, groups of atoms, ions and molecules can vary widely with respect to their character and their strength. To differentiate, these interactions are divided into classes known as bond types.

In contrast to classical synthetic chemistry, where strong covalent bonds are important, the medium and weak non-covalent interactions are of particular importance in nanotechnology. The importance of weak bonds increases with the increasing size of the aggregates constructed, which is comparable to what happens in nature. Thus, the following sections will introduce the key classes of chemical bonds and discuss their importance to nanotechnology.

2.2.1.1 Van der Waals Interactions

When atoms approach each other, the electrons of one atom deform the distribution of the electrons of the other atom. This deformation disturbs the charge distribution in such a way that the sum of the energies of the electron clouds of the two approaching atoms is lower than the sum of the energies of initially isolated atoms. This difference in energy determines the strength of the bond. Dispersion forces, which act between all atoms and molecules, make up the most important contribution to the van der Waals interactions. Israelachvili has given a detailed summary of van der Waals interactions between different types of atoms and molecules with or without medium effects.¹¹⁰

For different pairs of bodies (molecules or particles) of different geometries consisting of a large number of atoms, the van der Waals pair potential, $w(r) = -C / r^n$ (C is the coefficient of the pair potential, and r is the distance between two molecules or particles), will be different. For example,¹¹⁰ in the “sphere-flat surface” model the additive van der Waals interaction free energy between the two bodies is written as:

$$W \approx -4 \frac{AR}{6D} \quad 2.1$$

where A is the Hamaker constant which is defined as $A \propto \phi^2 C \psi_1 \psi_2$; ψ_1 and ψ_2 are the number of atoms per unit volume in the sphere (radius of R) and surface. The force is then obtained by differentiating the energy with respect to the distance D : $F \propto \frac{AR}{6D^2}$.

Van der Waals interactions play an important role in all phenomena involving intermolecular forces. While belonging to weak bonds, they are always present.¹¹⁰ They are also essential for living cells, especially in the creation of the three-dimensional structure of proteins. In cells, van der Waals interactions are a prerequisite for the composition of lipid bilayer membranes and the inclusion of membrane proteins in these layers. In analogy to these structures in nature, van der Waals interactions are important in supramolecular chemistry for the arrangement of complex molecular aggregates based on smaller units.

2.2.1.2 Hydrogen Bonding

For a liquid with a low molar mass, water has unexpectedly high melting and boiling points. These properties of water indicate the existence of intermolecular interactions that are stronger than that expected for ordinary liquids involving only dispersion forces.^{111,112} To understand, which bond is responsible for this interaction, a simple way is to look at the distances between various atomic centers. The intramolecular O–H distance is about 0.10 nm, as expected for the covalent bond,¹¹⁰ but the intermolecular O···H distance is only 0.176 nm, much less than the 0.26 nm expected from the sum of the two van der Waals radii. Thus, the intermolecular O···H bond is implicated to possess some covalent character. Such bonds are known as *hydrogen bonds*.^{113,114}

Hydrogen bonds are not unique to water; they exist between electronegative atoms, e.g. N, O, F and Cl, and H atoms covalently bound to electronegative atoms. Originally, it was believed that the hydrogen bond was quasi-covalent, but it is now accepted that the hydrogen bond is predominantly an electrostatic interaction. The hydrogen bond between two groups, XH and Y, is usually denoted by X–H···Y. The strengths of most hydrogen bonds lie between 10 and 40 kJ mol⁻¹, which makes them stronger than a typical van der Waals interaction (~1 kJ mol⁻¹) but still much weaker than covalent or ionic bonds (~500 kJ mol⁻¹).¹¹⁰

The directional characteristic and specificity of hydrogen bonds provide the ability to form weak three-dimensional “structure”, which appears very important for instance in proteins, linking different segments together inside the molecules, and in nucleic acids where they are responsible for the stability of the DNA helix (c.f. section 2.1.2). The dominance of H-bonding forces in secondary structures of biomacromolecules, such as polypeptides and polynucleotide;

in micelles and in biological membranes, often determines the subtle details of molecular and macromolecular structures.¹⁷

In Chapter 5 and 6, force measurements on quadruple hydrogen bonding supramolecular system will be investigated in detail.

2.2.1.3 Other Interactions

Covalent Bonds and Metallic Bonds^{110,115}

The creation of strong chemical bonds by exchange of binding electrons can take place without asymmetric distribution of the electron density.

The metallic bond is of special interest in micro and nanotechnology due to the broad application of metals and semiconductors as electrical or electronic materials. Additionally, metallic bonds facilitate the adhesion and both electrical and thermal conductivity at interfaces between different metals and inside alloys.^{7,115} Graphically demonstrating Louis de Broglie's theory that all elementary particles behave as both waves and particles, researchers at IBM used the STM technique to create and image a circular "quantum corral" of 48 iron atoms on the surface of a copper crystal.¹¹⁶ The corral, 14 nm in diameter, induced the copper electrons to dramatically display their wavelike nature by exciting the otherwise planar array of copper electrons into a standing wave pattern. "When electrons are confined to length-scales approaching the de Broglie wavelength, their behavior is dominated by quantum mechanical effects."¹¹⁶ Briefly, the corralled atoms share their electrons to create a standing wave of quantum-mechanical densities that the STM can perceive.

In contrast to the typically extended electron states in solids in the case of the metallic bond, in some cases the covalent bond can lead to molecules consisting of only two atoms, e.g., oxygen or nitrogen found in air. Covalent bonds can also affect just several or a high number of atoms. So the results can be linear, disk-shaped, globular molecules or solids extended in three dimensions.^{110,115} The creation of molecular nanostructures relies on the degrees of freedom of individual bonds on one hand, and the rigidity of certain parts of the molecules on the other hand. Hence double bonds, bridged structures, and multiple ring systems of covalent units are important motifs for the molecular architecture in molecular nanotechnology.

Ionic Interactions^{110,117}

If there are large differences in the electronegativities of atoms, a transfer of one or more electrons from the less to the more electronegative interacting partner is observed. The resulting bond is not determined by the binding electrons, but by the interactions of the ions (charged

atoms) created by the electron transfer. The Coulomb force of two ions with charges Q_1 and Q_2 is comparable to a covalent bond:

$$F \approx 4 \frac{dW(r)}{dr} \approx \frac{Q_1 Q_2}{4\pi\epsilon_0\epsilon_r r^2} \approx \frac{z_1 z_2 e^2}{4\pi\epsilon_0\epsilon_r r^2} \quad 2.2$$

Here z_1 and z_2 are the ionic valencies, ϵ_0 is the dielectric permittivity of free space (8.854×10^{-12} C² J⁻¹ m⁻¹) and ϵ_r is the dielectric constant of the medium.

Pure electrostatic interactions between ionized atoms, as in the case of salts, are of less interest in nanotechnology. In contrast, molecular ions and also polyions are of particular interest in polymer science, as well as in microbiology.³ Macromolecules often exhibit a multitude of similar functional groups. If these groups are readily ionized, this effect results in polyionic macromolecules. Stable multilayers and complex molecular aggregates can be obtained by polyions interacting with small ions of opposite charge or with polyionic partners.¹¹⁸ Surface charges, electrostatic repulsions and electrostatic attractions are essential for the manipulation of macromolecules, supramolecular aggregates, micelles and nanoparticles in the liquid phase.¹¹⁸

Dipole-Dipole Interactions^{110,117}

Owing to the differences in electronegativity, molecules consisting of different atoms normally exhibit an inhomogeneous electron distribution. Such molecules, with one or more dipole moments, attract each other.¹¹⁷ The dipole moments and their orientation determine the strength of the dipole-dipole interaction. When two point dipoles are lying in line at a distance r apart and are oriented relative to each other, the maximum attraction occurs and the energy is given as:¹¹⁰

$$W \approx \frac{4 \pi \sigma_1 \sigma_2}{4\pi\epsilon_0\epsilon_r r^3} \quad 2.3$$

where σ is electric dipole moment (C m).

The dipole-dipole interaction is not as strong as the ionic interaction, and usually is not able to produce any long-range alignment of polar molecules in the liquid state.¹¹⁰

Coordinative Bonds^{119,120}

Coordination interactions are created by the provision of an electron pair from one of the ligands and the existence of double unoccupied orbitals at the other binding partner.¹¹⁹ The stability of such coordinative bonds lies between the strengths of the weaker dipole-dipole interactions and of covalent bonds. Thus it is well suited for the realization of adjustable binding strengths and lifetimes of molecules. This is of great importance for the construction of

supramolecular architectures. Nature also uses this principle of finely tunable binding strengths of complex bonds, e.g., in the Co- or Fe-complexes of the heme groups of enzymes.¹⁷

Beside anions and small molecules, ring-shaped molecules, extended molecules and macromolecules can also act as ligands.^{120,121} Because the central particle and the ligands are often ions, coordinative bound architectures, in addition to exhibiting complex and covalent bonds, also display ionic and dipole-dipole interactions, representing a complex structure.

Polyvalent Bonds^{115,122}

Polyvalent or multivalent interactions are the simultaneous association of multiple ligands on one entity (a molecule or a surface) to multiple receptors on another entity.¹²² Multivalent interactions are omnipresent in biology (e.g. in infectious diseases, in processes involving antibodies, metastasis, platelet activation, inflammation, and in many conditions in which cells interact with surfaces).^{17,122} Multiple simultaneous interactions have unique collective properties that are qualitatively different from the properties of their monovalent (individual) constituents.^{122,123} The mobility of molecular groups determines the size of cooperative effective sections in large molecules, which are able to bind externally in a polyvalent manner. This is well known from the melting behavior of double-stranded DNA. The thermally induced separation of the two strands connected by hydrogen bonds requires rupturing the bridges. Over a length of about 40 bases, the melting temperature does not increase further, pointing to an independent movement of strand sections above a critical length.^{2,122}

Confirming, understanding, and quantifying the importance of multivalency in biological interactions, and moving this fundamental knowledge towards applications in the design of drugs and materials will be important in the preparation of dynamic or self-repairing materials for application in medicine, materials science and nanotechnology.¹²²

2.2.2 Potential Energy and Force^{110,117,124}

Modern understanding of intermolecular forces began in physics of gases in the 19th century. A satisfactory understanding of intermolecular interactions, however, has been developed in the 1930's using quantum mechanics. Intermolecular interactions are usually expressed in potential energies, as opposed to forces, as it is energies (enthalpy, free energy) which are traditionally measured e.g. in thermochemistry (by calorimetry). For example, in the grand-canonical ensemble, the relationship between the amount of work that can be done by a chemical reaction is referred to as the change in Gibbs free energy, ΔG . The change in Gibbs free energy depends on the difference between the enthalpy (ΔH) that can be obtained from

the system and the energy that is consumed in driving the reaction against any forces, which makes it non-spontaneous. Thus,

$$\Delta G = \Delta H - T\Delta S \quad 2.4$$

where T is the temperature and ΔS relates to the change in the spontaneity factor, the entropy S . The macroscopic (thermodynamic, ensemble) and the microscopic (atomic, molecular) modes are connected via the Boltzmann equation:

$$S = k \ln \Omega \quad 2.5$$

where k is the Boltzmann constant and Ω is related to the probability density distribution of the various microstates (on the atomic/molecular level), corresponding to the given macroscopic (thermodynamic) state.

Furthermore, thermodynamics and statistical physics deal with various ensembles (of atoms and molecules) and use ensemble averaged values, and molar quantities to describe interaction energies and thermodynamic potentials. The choice of the problem variables and fluctuating (constant) parameters define the type of ensemble and herewith the thermodynamic potentials.

In nanotechnology we deal with a finite (rather small) number of atoms, molecules and their discrete “building blocks”. Thus, in place of molar averages, it is more convenient to use forces between the individual “building units”. It has been the measurements and control of these forces at the level of individual atoms and molecules that has actually enabled nanoscale fabrication and thus initiated (among a few other enabling approaches) the advent of nanotechnology.

Intermolecular (interatomic) potential energy $V(r)$ as a function of the separation distance, r , and the interaction force, $F(r)$ are related via simple expressions: $V(r) = \int_{\infty}^r F(r) dr$ and $F(r) = -\frac{dV(r)}{dr}$.

The full force law $F(D)$ between two surfaces of physical bodies that consist of a large number of atoms, i.e. the force F as a function of surface separation D , can be measured in a number of ways. The simplest is to move the base of a spring by a known amount. The most direct way is to suspend one of them from a spring and measure the adhesion or “pull-off” force needed to separate the two bodies from its deflection. If k_s is the stiffness of the force-measuring spring and D the distance the two surfaces jump apart when they separate, then the adhesion force F_s is given by

$$F_s = F_{\max} = k_s D \quad 2.6$$

2.3 AFM-Based Single Molecule Force Spectroscopy

The combination of high force selectivity with high spatial resolution of AFM allows one to perform mechanical experiments with single molecules. The intermolecular interactions in both biological macromolecules and synthetic polymer systems can be directly probed by using AFM-based single molecule force spectroscopy (SMFS).^{125,126} This new experimental platform has extended the understanding of molecular mechanisms of biological processes in life science and of material properties in polymer physics. In this section, following a brief summary of the principles of the AFM technique and the SFMS experiment, including the calibration of the force sensing cantilever, the focus is on the detection of single chain elasticity of macromolecules, unbinding of individual receptor-ligand pairs, unfolding pathways of proteins, and DNA mechanics, as well as studies of molecular motors, by SMFS.

2.3.1 AFM Technique and SMFS Experiment

With the development of precise instrumentation, many elegant force sensing techniques differing in the range of force and measurement timescale, have become available. Clausen-Schaumann *et al.*¹²⁷ summarized and compared the most important experimental tools for single molecule studies, which are magnetic beads,¹²⁸ optical tweezers,¹²⁹ glass microneedles,¹³⁰ the biomembrane force probe (BFP),¹³¹ force clamp,^{132,133} and AFM¹³⁴ (cf. Table 1 in reference [127]). With the accessible force window, the whole range from entropic forces at several femtonewtons to the rupture of covalent bonds at a few nanonewtons can be investigated. Also, by combining the methods, a dynamic range from $\sim 10 \mu\text{s}$ to more than 1 s can be achieved.

2.3.1.1 AFM Technique

AFM has been used and developed first as an imaging tool (microscope, nanoscope). The principle of AFM is to scan across the sample surface by a very sharp tip attached to a flexible cantilever. The force between the tip and the sample is continuously measured by monitoring the deflection of the cantilever (typical spring constant of $0.01 - 1 \text{ N m}^{-1}$). The scheme of a typical set-up is shown in Figure 2.10A. A piezoelectric transducer is used in order to position the sample accurately. AFM cantilevers and tips are often made of silicon or silicon nitride. The radius of the apex of the tip lies between few 10's to 100 nm (Figure 2.10B and C). The cantilever deflection is most frequently monitored by an optical beam deflection technique utilizing a laser beam, which is reflected off the end of the cantilever and collected by a four-segment photo detector (position-sensitive detector).

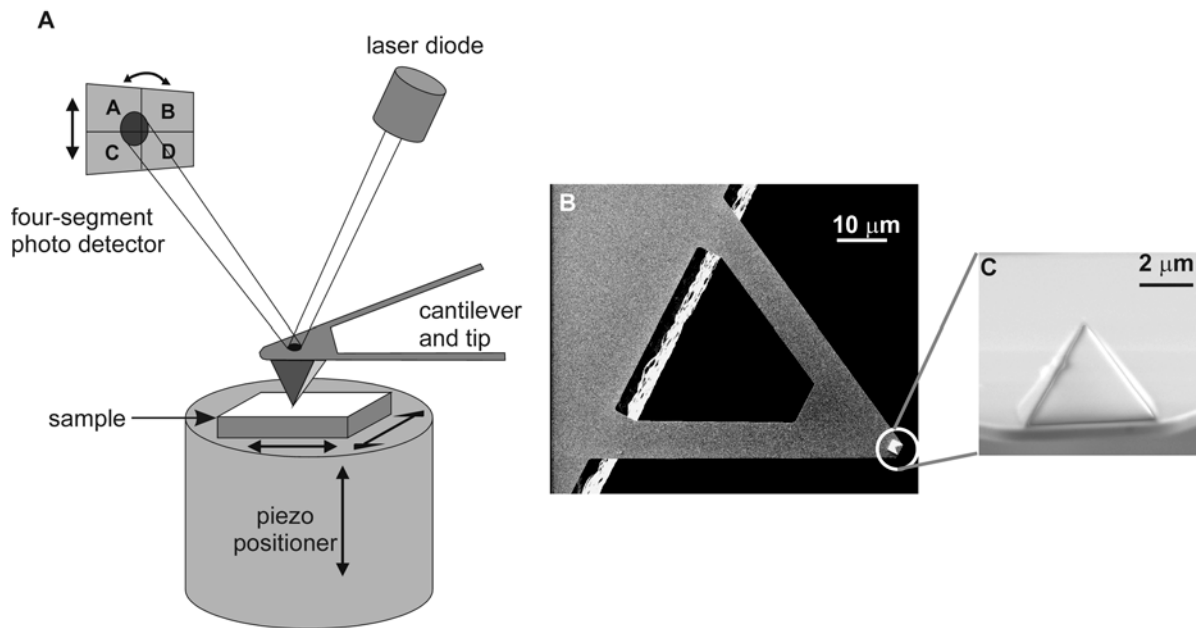


Figure 2.10. (A) Schematic diagram of contact mode AFM. (B) Scanning electron microscopy (SEM) images of a V-shaped silicon nitride cantilever (top view) and (C) tip (side view).

2.3.1.2 Force-Displacement Measurements

Interactions, such as the van der Waals interactions, dipolar interaction, hydrogen bonding and electrostatic forces described in Section 2.2, can be probed by typical AFM force-displacement measurements. In Figure 2.11, the movement of the sample and corresponding cantilever deflection are schematically depicted and the corresponding force-displacement plot is shown.

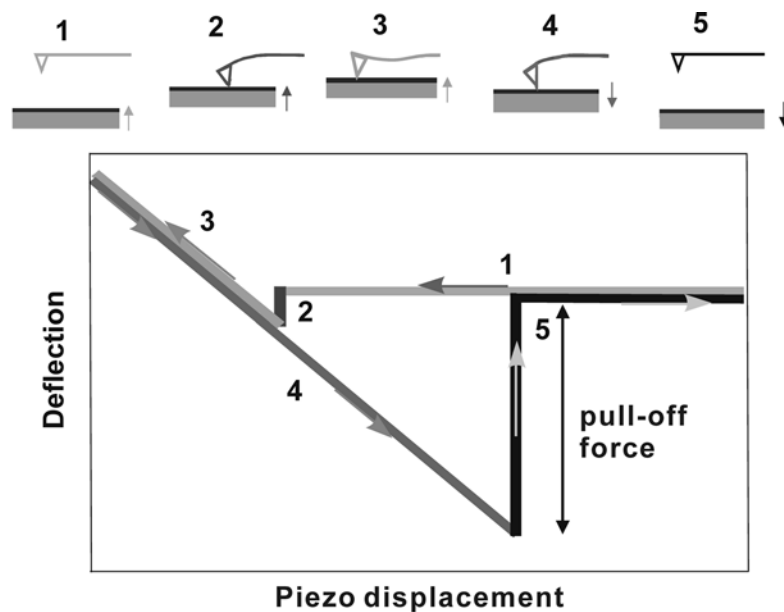


Figure 2.11. Scheme of the force-displacement measurement by an AFM tip on a surface. From point 1 the tip begins to approach the sample surface; at point 2 the tip jumps into contact with the surface; from 2 to 3 a repulsive force dominates the interaction between the tip and the surface; upon separation adhesive forces are noticed until point 4; finally at point 5 the tip will jump out of contact. A typical deflection-displacement curve with the five characteristic steps of the cycle is shown in the bottom graph.

The measured cantilever deflection z can be converted to the corresponding force F , by applying Hooke's law, if the spring constant k of the lever is known:

$$F = k \cdot z. \quad 2.7$$

The adhesion force between AFM tip and sample is characterized by the pull-off force. A quantitative determination of forces requires a thorough calibration of the cantilever spring constant.

2.3.1.3 Spring Constants

An important property of any probe used for the force-displacement method is the spring constant of the probe. There are three basic types of techniques for determining the spring constant: vibrational,¹³⁵⁻¹⁴² static loading^{139,143-147} and theoretical¹⁴⁸⁻¹⁵⁰ techniques. Hodges¹⁵¹ has reviewed all these methods in detail. Here, we briefly summarize the thermal oscillation method, which we used in our measurements (see also Chapters 3, 5 to 7).

Thermal motion of the molecules in air at temperature T , causes the cantilever to oscillate with an amplitude x_0 , so that:

$$\frac{1}{2} m \omega_0^2 \langle x_0^2 \rangle = \frac{1}{2} k_B T \quad 2.8$$

with the effective mass of the cantilever m , the resonant frequency ω_0 , and Boltzmann's constant k_B , the bracket denotes the ensemble averaging. Since $\omega_0^2 = k/m$, the spring constant of the cantilever k is obtained as:

$$k = \frac{k_B T}{\langle x_0^2 \rangle} \quad 2.9$$

where $\langle x_0^2 \rangle$ denotes the mean square cantilever displacement, which can be directly measured from the power spectrum of the cantilever. This result obtained by Hutter and Bechhoefer¹⁴⁰ ignores damping effects. The error quoted in their own measurement of the spring constant was 5%. In the thermal excitation technique the cantilever is positioned far away from the sample (where the tip is not affected by long-range forces) so that the motion experienced is purely due to thermal fluctuations.

2.3.1.4 AFM-Based SMFS

Among all force spectroscopy techniques, AFM-based SMFS has proven to be a versatile platform for the investigation of single molecules, though its sensitivity is not the highest.^{127,152} The principle of SMFS experiments using AFM has been thoroughly described in reviews¹⁵²⁻¹⁵⁴ and other papers.^{127,155-160} In brief, macromolecular chains functionalized with a guest moiety are adsorbed onto a solid substrate by physical or chemical adsorption and form an ultrathin film.

The tip, derivatized with a receptor moiety, is then brought into contact with the sample film (which is mounted onto a piezo tube) by the movement of the piezo. During this process, the cantilever stays free if there are no long-range interactions, as shown in Figure 2.12 (1). While the tip is in contact with the sample, force is applied to the sample and molecules can adsorb onto the tip by intermolecular forces (specific interactions shown in Figure 2.12 (2)). As a result of the applied force, the cantilever bends against the substrate and a repulsive signal is recorded. Upon separation of the tip and the sample, Figure 2.12 (3), the macromolecule that links the tip and the substrate starts to be stretched (Figure 2.12 (4)), resulting in bending of the cantilever towards the substrate. When the linker is stretched further, the weakest point along the structure will break, or a segment of the macromolecule detaches from the substrate or the tip. The cantilever then rapidly goes back to its relaxed state, causing a sudden drop on the force trace. This maximum force value is attributed to the rupture force of the unit that is unbound gets separated (e. g. ligand - receptor complex, host-guest complex and other supramolecular complexes). The “stretching” region (from 3 to 4 in Figure 2.12) describes the elasticity of the macromolecular spacer.

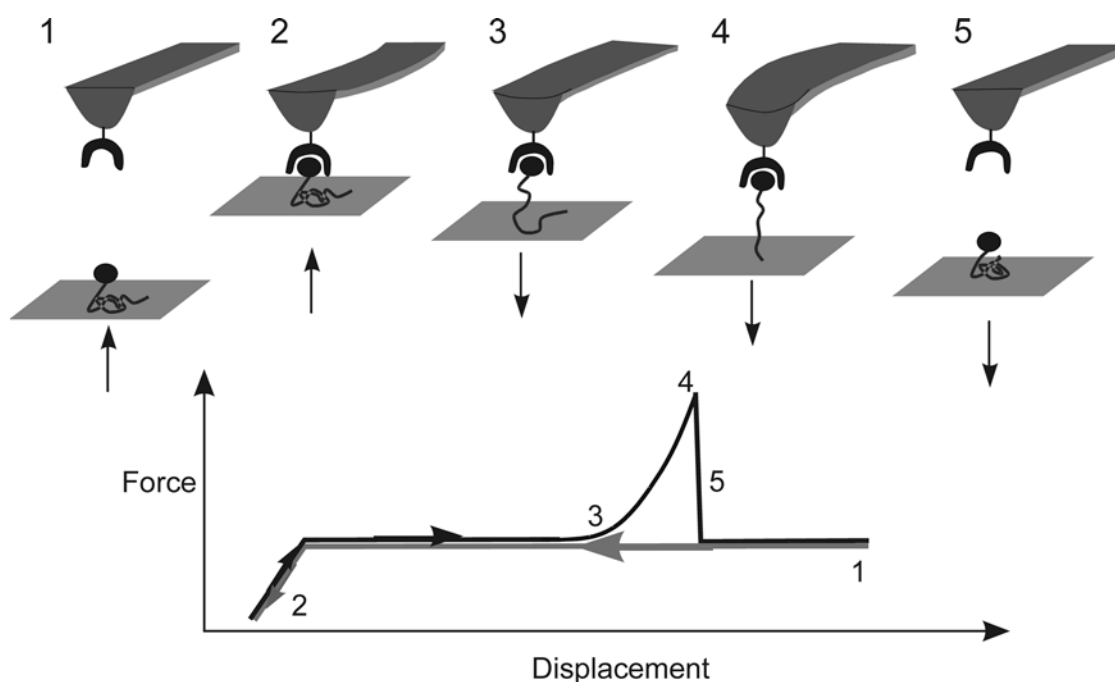


Figure 2.12. Schematic illustration of the single molecule force-displacement measurement on surface attached single polymer chains. Here the vertical scale is mirrored with respect to scale in Figure 2.11.

2.3.2 Single Molecule Studies

2.3.2.1 Stretching of Single Polymer Chains

Understanding the elastic behavior, or deformation, of an individual macromolecular chain is an essential issue in (bio)polymer science, which deepens the understanding of the relationship

between primary chemical composition and the macroscopic properties of polymeric materials.¹⁶¹ Mechanical experiments with individual flexible synthetic polymers and natural macromolecules under solution conditions have become possible with precise measurements of intramolecular forces by SMFS.¹⁵²⁻¹⁵⁴

Freely-Jointed Chain Model and Worm-Like Chain Model

In SMFS experiments, the stretching of an individual polymer chain is recorded by the force-extension (or deflection-separation) curve consisting of the elastic response of the polymer chain followed by a sudden drop in the force (or deflection) upon the detachment of the chain from the AFM tip or substrate (Figure 2.11 and 2.12). For small deflection (low forces) first the macromolecular chains become oriented (without essential bond angle deformation and stretching of covalent bonds). In this regime the restoring force has an entropic nature. In the high-force range, upon further stretching, the elastic characteristics of a polymer chain become dominating, i.e. the restoring force is governed by the distortion of the bond angles and covalent bonds. The quantitative analysis of the experimental elastic force-displacement profiles is based on the entropic contribution at low stretching forces. Based on thermodynamic considerations, the two most prominent models, i.e. the *freely-jointed chain* (FJC) model and the *worm-like chain* (WLC) model (Figure 2.13) are the most often used to describe the measured force-extension profiles of individual polymer chains.

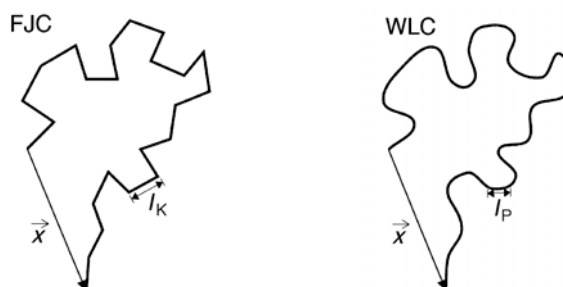


Figure 2.13. Schematic representation of the freely-jointed chain (FJC) and the worm-like chain (WLC) models (adapted from ref [154]).

In the FJC model, a polymer is described as a chain of N rigid Kuhn segments with equal length I_k (Kuhn length). Under higher forces the sections of the chain are no longer oriented in a random fashion and the molecule is predominately aligned along the direction of the external force. The extension x can be expressed as a function of the pulling force F :

$$x(F) = L \left[\coth\left(\frac{FI_k}{k_B T}\right) - \frac{k_B T}{FI_k} \right] = LL \left[\frac{\coth\left(\frac{FI_k}{k_B T}\right)}{\frac{FI_k}{k_B T}} \right] \quad 2.10$$

Here, L is the Langevin function and the contour length is defined as $L = N \cdot I_k$. For flexible polymer chains, the FJC model describes the stretching behavior of the individual chain reasonably well.^{125,157,162} However, the FJC model solely considers entropic effects and fails to

describe the stretching of molecules for $x \sim L$. In order to optimize the FJC model, the deformation of bonds and bond angles must be taken into account. An exact description would require the knowledge of intramolecular potentials and the molecular structures, which in some cases are provided by computer simulations. Generally, a generic approach based on the introduction of the segment elasticity K_{segment} (which can be directly determined by force spectroscopy) is chosen, to produce a modified FJC model (m-FJC):^{163,164}

$$x(F) \mid \left[\coth\left(\frac{FI_k}{k_B T}\right) - 4 \frac{k_B T}{FI_k} \right] \left[L_{\text{contour}} - 2 \frac{n}{K_{\text{segment}}} F \right] \quad 2.11$$

This additional enthalpic term in equation 2.11 gives rise to a linear increase in the force for large extensions ($x \sim L$). The m-FJC model has been successfully utilized to describe a variety of different synthetic polymers, as well as polysaccharides.^{155,159,160,165-169}

The WLC model, which treats the conformation of a polymer chain as a continuous entity, describes a polymer chain as a homogenous string of constant bending elasticity. Although entropic and enthalpic contributions are combined in this approach, the extension is limited by the contour length of the polymer. The following approximation gives an expression for the force-distance relationship:

$$F(x) \mid \frac{(k_B T)^2}{b} \left\{ \frac{1}{4} \left(1 + \frac{x}{L}\right)^2 - 2 \frac{x}{L} + \frac{1}{4} \right\} \mid \frac{k_B T}{I_p} \left\{ \frac{1}{4} \left(1 + \frac{x}{L}\right)^2 - 2 \frac{x}{L} + \frac{1}{4} \right\} \quad 2.12$$

where I_p is the persistence length and b denotes the bending modulus of the polymer. The WLC model has been successfully applied to describe the elastic behavior of DNA,¹²⁸ muscle^{170,171} and adhesion proteins.^{172,173} For small extensions, the difference between the WLC and the FJC model is negligible, since the equilibrium conformation of both model chains is Gaussian-like. At low forces, the persistence and Kuhn lengths are related by: $I_k = 2I_p$.

A Criterion for Single Chain Detection

During SMFS experiments, several criteria are used as standards to ensure single chain rather than multi-chain stretching. First, if only one single force signal appears in the force profiles, it suggests that single chain stretching is obtained. Second, from the above models, one thing in common can be found that $F(x)$ is a function of x/L . The elasticity of a linear polymer scales with its contour length, while the intrinsic properties, i.e. I_k , and K_{segment} are independent of the polymer length. Thus, polymers with the same composition, but different length, can be described by a common force-extension curve $F(x/L)$. If the fitting parameters are identical to within experimental error, then it is likely that single molecule stretching is obtained. Finally, the comparison of normalized force traces obtained during different measurements can produce

strong evidence for single molecule detection. The force curves are normalized by their extension lengths at the same force value.¹⁵⁹ For a given force-extension curve, the length value can be measured for a selected force value, e.g. 300 pN; then, the extension value of the force curve is divided by this length. Finally, the processed force curves are plotted together (Figure 2.14B).¹⁷⁴ If single molecules are stretched, the normalized force curves superimpose very well due to the intrinsic scaling of elasticity with contour length.

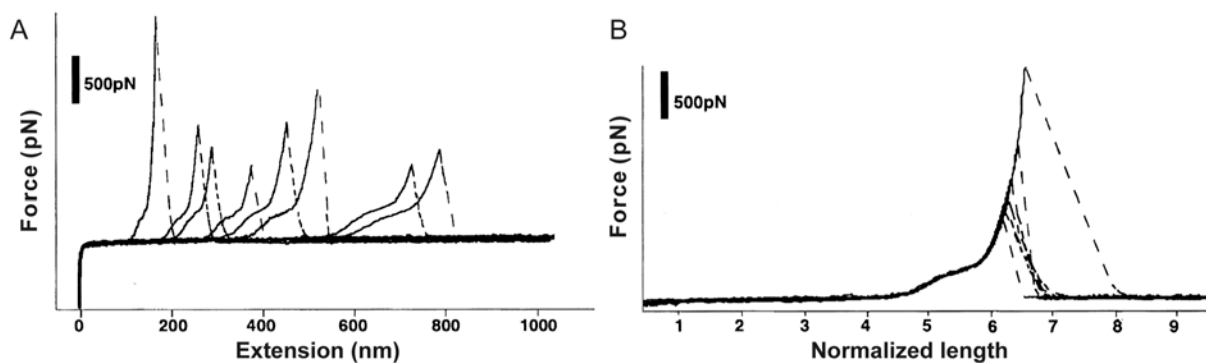


Figure 2.14. (A). Force-extension curves of carboxymethylated amylose in PBS buffer. (B). Superposition of normalized curves showed that single molecules of one class are indeed observed (adapted from ref [174]).

In addition, the small tip radius of 20-50 nm allows only a few molecules to interact with the tip. Even if more than one strand links to the tip in parallel, it is very unlikely that two of them have exactly the same length, so they will cause differently rising slopes in a single force curve, each of which reflects the elasticity of a single strand.

2.3.2.2 Molecular Interactions

Rupture Forces of Molecular Bonds

Specific interactions underlying molecular recognition may lead to non-covalent bonds between biological macromolecules, which are composed of a few tens of weakly interacting pairs of units such as van der Waals interaction, hydrogen bonds, polar and electrostatic bonds, as introduced in the previous section.^{16,161} For probing the strength of these interactions, e.g. receptor – ligand binding bonds, Evans *et al.* developed both a theoretical basis which constitutes the foundation for experimental dynamic force spectroscopy.^{131,175-177} In the model, the strength of weak non-covalent bonds was studied in aqueous condition using Kramers' theory¹⁷⁸ for reaction kinetics in liquids under the influence of an externally applied force. The predicted dependence of the unbinding force on the loading rate applied to the receptor-ligand bond reveals details of the molecular dynamics and energy landscapes of the recognition process.

In this section, principles and models of receptor-ligand binding complex systems established by Evans *et al.* are summarized.

(a) Single Bond^{179,180}

The binding energy E_B , given by the free energy difference between the bound and the free states, is the common parameter to describe the strength of a bond. E_B determines the ratio of bound complexes, $[AB]$, to the product of free reactants, $[A][B]$, at equilibrium in solution. At thermodynamic equilibrium, the number of complexes that form per unit of time, $k_{on}[A][B]$, equals the number of complexes that dissociate per time unit, $k_{off}[AB]$. The kinetic rate constants, on-rate k_{on} and off-rate k_{off} , are related to the equilibrium dissociation constant K_D through $K_D = k_{off}/k_{on}$.

The average lifetime of a reversible ligand-receptor bond, $t_{off}(0)$, is given by $t_{off}(0) = 1/k_{off}$. Therefore, ligands will dissociate from receptors without any force applied to the bond at time larger than $t_{off}(0)$. When a force is applied on a bound complex, a deformation of the interaction energy landscape occurs corresponding to the addition of the potential related to the external force. This results in a lowering of the activation energy barrier, as shown in Figure 2.15A. Thus the input of thermal energy by forces acting in this time regime reduces the bond lifetime. The lifetime $t_{off}(f)$ of a bond loaded with a constant force f is given as:

$$t_{off}(f) = t_D \exp\left(\frac{E_b - fx}{k_B T}\right) \quad 2.13$$

Here, x is interpreted as the distance of the energy barrier E_b from the energy minimum along the direction of the applied force; t_D is the diffusive relaxation time of bound complex. Compared to the lifetime at zero force, $t_{off}(0)$, for a single sharp energy barrier,

$$t_{off}(f) = t_{off}(0) \exp\left(\frac{-fx}{k_B T}\right) \quad 2.14$$

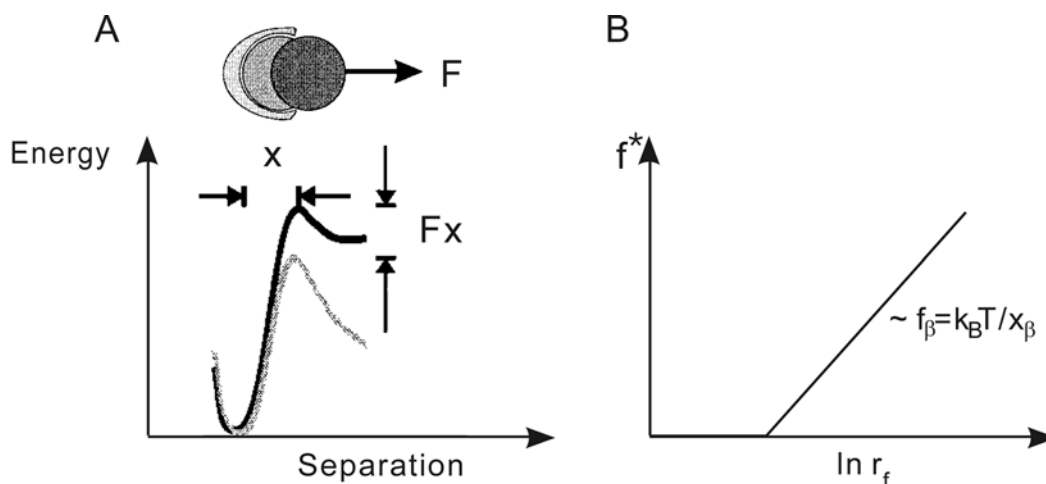


Figure 2.15. (A) Dissociation over a single sharp energy barrier. The barrier is decreased by the applied constant force F , a characteristic length scale x is interpreted as the distance of the energy barrier from the energy minimum along the projection of the force. (B) Dynamic strength spectra for unbinding over the conceptual energy barrier in (A). The most likely detachment force f^* vs. $\ln(\text{loading rate})$, i.e. $\ln r_f$, can be plotted as a straight line with a slope $f_\beta = k_B T/x_\beta$ set by the projected location of the barrier x along the direction force (reproduced from ref [179,180]).

In far from equilibrium situations, the two binding partners are further separated after dissociation has occurred. Therefore, rebinding and back-reactions are negligible. During force determination in AFM measurements (or other techniques like BFP), an effective force increase or loading rate r_f can be deduced from $r_f = df/dt$. Using $t_{\text{off}}(f) = k_{\text{off}}^{-1}(f)$ relates the kinetic off-rate at a given force f , $k_{\text{off}}(f)$ to the off-rate at zero force, $k_{\text{off}}(0)$:

$$k_{\text{off}}(f) \approx k_{\text{off}}(0) \exp(x f / k_B T) \quad 2.15$$

As a function of loading rate r_f , the most probable force for rupture f^* in the case of a single sharp energy barrier can be written as (Figure 2.15B):

$$f^* \approx f \ln(r_f / r_f^0) \quad 2.16$$

which introduces the thermal force $f = k_B T / x$, and a thermal scale for loading rate $r_f^0 \approx f / t_{\text{off}}(0)$. The unbinding force (f^*) scales linearly with the logarithm of the loading rate. For a single barrier, this would give rise to a simple, linear dependence of the force versus log loading rate, as shown in Figure 2.15B.

In cases where more barriers are involved along the escape pathway, the curve will follow a sequence of linear regimes, each of which marks a particular barrier. Hence, transition from one regime to the other is associated with a sudden change of slope determined by the characteristic barrier length scale.^{177,179,181}

The molecular bond strengths investigated by SMFS range from the sequence specific base-pairing forces of DNA as 9 pN for adenine-thymine and 20 pN for guanine-cytosine¹⁸² to the rupture of single covalent bonds at ~ 2 nN.¹⁸³ Specific non-covalent molecular bonds are of particular interest in the intermediate strength range as found in biomolecular complexes. In fact, the first AFM single-molecule unbinding experiment was carried out on a specific receptor-ligand system: i.e. streptavidin-biotin pairs, primarily focusing on the bond strengths measured as ca. 250 pN at a loading rate of 10^5 pN/s. It was later found with biomembrane force probe (BFP), with which the force loading rate applied to the pairs was varied over six orders of magnitude, that bond dissociation for this system under AFM conditions is a non-equilibrium dynamic process. Since then, several rate-dependent AFM experiments have also confirmed the logarithmic dependence of the apparent bond strength on the force loading rates, as predicted by equation 2.15.¹⁸⁴⁻¹⁸⁷

Including biotin-avidin/streptavidin, prominent binding partners, such as antibody-antigen,¹⁸⁸⁻¹⁹² as well as complementary DNA bases/strands^{125,127,180,184,193} have been investigated focusing on non-covalent interaction forces by SMFS. The sequence specific base-

paring rupture force values of 9 pN for adenine-thymine and 20 pN for guanine-cytosine base pairs¹⁸⁴ are consistent with earlier data obtained from the unzipping of lambda phage DNA with glass microneedles.¹⁹⁴ The accessibility of the full force range in SMFS including the force-induced melting of DNA^{127,195} has also opened new perspectives to study interactions of DNA with cancer drugs,¹⁹⁶ as well as with intercalating dyes.¹⁹⁷ The investigation of DNA/RNA mechanics using force spectroscopy has been reviewed by Gaub *et al.*¹²⁷ and Williams *et al.*^{198,199} in detail. Finally we note that more complex biological systems involving living cell adhesion have contributed to the understanding of adhesion-controlled cellular functions.^{166,200-205}

Inspired by biological systems, reversible and artificial complexes with specific non-covalent interactions exhibit great importance in material science.¹²⁰ First studies on coordination complexes include the biologically relevant histidin-tag/Ni(II) nitrilotriacetate complexes,^{185,186} and various metal-terpyridine complexes.²⁰⁶ These reversible and specific bindings between certain ligand-metal pairs may introduce the selectivity for the formation of ordered assemblies, which is highly interesting for the design of nanoarchitectures from individual molecules.

(b) Crossover from Near-Equilibrium to Far-From-Equilibrium Unbinding and Effect of Soft Polymer Linkages on Strengths¹⁸¹

As described in Figure 2.15A, the energy landscape of the bond is tilted, when an external force is applied, which increases the opportunity of the bond rebinding after a rupture. In AFM experiments, a transient capture well occurs, (which enables the rebinding) when pulling on the bond, due to the presence of the linkage (the spacer + cantilever), as illustrated in Figure 2.16A.

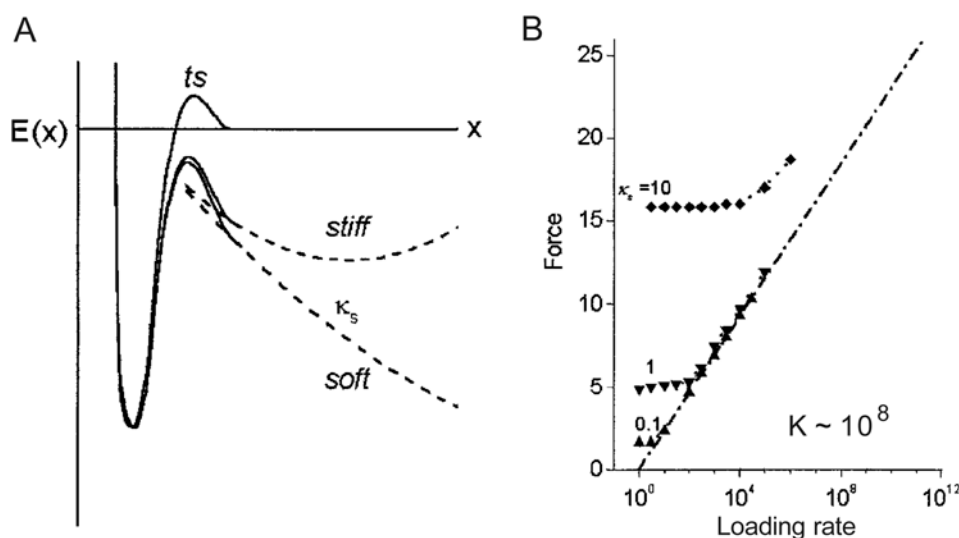


Figure 2.16. (A) Conceptual energy landscapes for a simple bond pulled by a soft and a stiff spring, respectively. (B) Dynamic spectra of most frequent rupture force produced at low loading rates by rebinding as a function of probe linkage stiffness. Equilibrium constant $K_{eq} = t_{off}/t_{on}$ (reproduced from ref [181,207]).

Only if the linkage is very soft, or the applied force becomes large enough to drop the energy level of the capture well below the bound state, the energy landscape approaches the far-from-equilibrium condition. Thus the crossover from near-equilibrium to far-from-equilibrium situations can be defined as the forward rate of barrier pathway overcomes the backward rate, i.e. $k_{\text{on}} \gg k_{\text{off}}$. Here, the ratio of rebinding-to-unbinding rates will diminish as it is proportional to $\exp(-f^2/2 \kappa_s)$,* and the crossover force is found from the ratio:¹⁸¹

$$k_{\text{on}}/k_{\text{off}} \sim \exp\left(-\frac{f^2}{2\kappa_s}\right) \frac{t_{\text{off}}}{t_{\text{on}}} \frac{K_{\text{eq}}}{\Psi_s} \frac{v}{v_s} \frac{L_p}{cb} \quad 2.17$$

In order to achieve complete unbinding (far-from-equilibrium), the force must rise above $f_{\text{c}} \sim \sqrt{2\kappa_s k_B T \ln K_{\text{eq}}}$, and the equilibrium constant K_{eq} equals to $t_{\text{off}}/t_{\text{on}}$. Together with equation 2.16, the loading rate r_f can be written as:

$$r_f \sim \frac{v}{t_{\text{off}}} \exp\left(-\frac{f_{\text{c}}^2}{2\kappa_s}\right) \frac{v}{v_s} \frac{L_p}{cb} \quad 2.18$$

The influence of linkage stiffness κ_s on both crossover force f_{c} and rupture loading rate r_f is shown in Figure 2.16B. The experimental results showed that the stiffer the linkage, the larger loading rate is needed to achieve unbinding.

The polymer linkers, used in single molecule experiments, help holding back the rebinding events. At low speed (i.e. in near-equilibrium situations), however, the bond strength can be altered by polymer linkages. Under far-from-equilibrium, the most likely rupture force can be written as:

$$f^* \sim f_{\text{c}} \left(\frac{v_s}{v} \right)^{1/2} \frac{L_p}{cb} \frac{1}{\ln\left(\frac{v_s}{v}\right)} \quad 2.19$$

where v is a characteristic velocity, $v \sim (L_p/t_{\text{off}})(x/cb)^{1/2}$; L_p is the contour length and b is the persistence length; for a freely-jointed polymer $\alpha = 1$ and $c = 1$; for a worm-like polymer, $\alpha = 2$ and $c = 4$. Equation 2.19 shows that, far-from-equilibrium, the bond strength approaches the expected proportionality to logarithm of the detachment rate at high loading speeds ($v_s \gg v$).

(c) Multiple Bonds^{181,207}

Force spectra for multiple bonds can provide useful insights into the nature of hidden interactions in a molecular assembly. However, the effect of cooperativity in multiple bond detachment is complicated and thus difficult to be measured. Here, we only consider the case of bonds in series (Figure 2.17), i.e. the force is equally applied to each bond. In any states, such a

* The dimensionless linkage stiffness $\kappa_s = \kappa_s x^2/k_B T$, and force $f = f/x$.

system behaves like a “macro-single bond” with a barrier given by the sum of the individual barrier energies.²⁰⁸

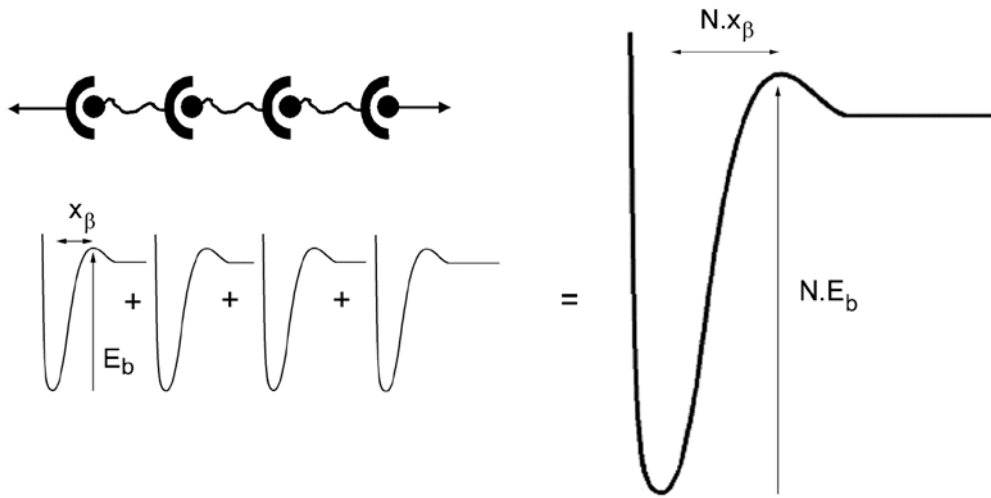


Figure 2.17. A system of identical attachments that fail cooperatively when loaded in series can be considered as a single bond with a barrier scale N -times that of the single bond (adapted from ref [181]).

For a simple ideal bond, the lifetime is set by the exponential magnitude of the energy barrier with a diffusive relaxation time (equation 2.13). With N -identical bonds, cooperative unbinding leads to a large increase in the time scale for dissociation:

$$t_{\text{off}}/N \approx N t_{\text{off}} \exp \left(\frac{N - 10E_b}{k_B T} \right) \quad 2.20$$

For identical bonds in series, each bond contributes an increase in length along the direction of force i.e. $x = N x$, and the thermal force scale is lowered N fold, i.e. f/N . Hence, for N bonds in series, far-from-equilibrium, the force can be approximated as:

$$f^* = f/N \left[\ln/r_f \left(2 \ln/N \right) \left(\frac{N - 10E_b}{k_B T} \right) \right] \quad 2.21$$

Here, each bond experiences the same force and any rupture event leads to the rupture of the attachment. Thus in far-from-equilibrium situations, the rate of rupture events is N times faster than the rate of one bond, which weakens the attachment slightly compared to that of a single bond at a given loading rate:

$$f^* = f \left[\ln/r_f \left(4 \ln/N \right) \right] \quad 2.22$$

Here, r_f is the dimensionless loading rate.

Protein Folding and Unfolding²⁰⁹⁻²¹³

Mechanical unfolding experiments on the modular protein titin,^{170,209,210} which consists of repeating globular domains, have demonstrated the use of SMFS not only for the determination

of mechanical properties of individual proteins, but also for the study of protein-folding mechanisms (Figure 2.18).²¹¹⁻²¹³

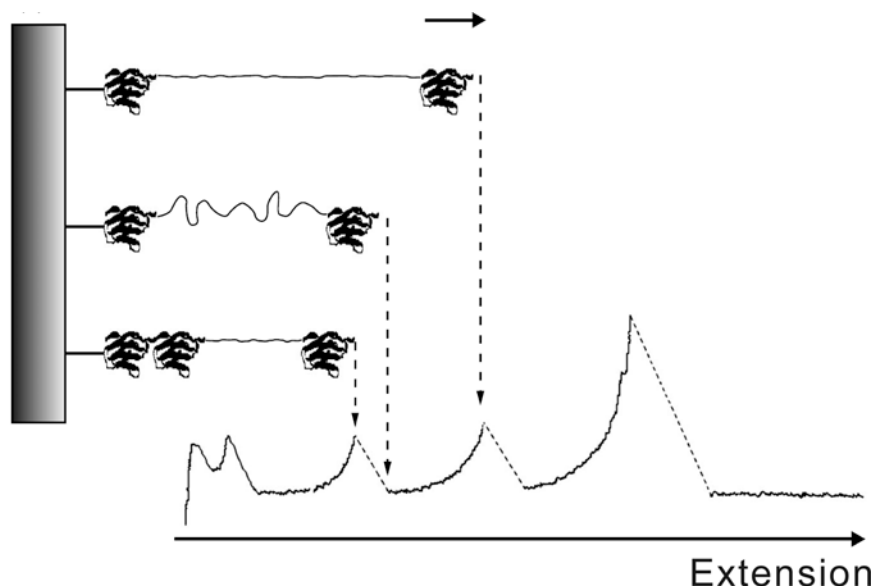


Figure 2.18. Typical force-distance profile recorded upon stretching a modular protein/polypeptide. The measured saw-tooth pattern results from a coexistence of folded and unfolded domains: each domain individually unfolds until the whole protein has been denatured. Each “peak” of the curve indicates one unfolding event. The distance between two peaks reflects the contour length of the previously unfolded domain, which adds to the overall length of the unfolded polypeptide chain (adapted from ref [170]).

Numerous recombinant proteins, containing tandems of one or a few types of Ig domains from titin, were produced by genetic engineering in order to mimic native titin in a simplified version. By using SMFS, Li *et al.*^{171,214} have shown that the Ig domains from the proximal part of titin could be unfolded by stretching forces in the 150 to 200 pN range with all Ig domains demonstrating similar mechanical strength. In contrast, the Ig domains from the distal part of titin required stronger stretching forces (200 – 350 pN) and showed a strong hierarchy in their mechanical strength.

The unfolding of protein globules provides an interesting conceptual approach for material scientists. It has been suggested that the dissipation of mechanical stress into the rupture of globular intra- and intermolecular polypeptide aggregates could be the origin for the unique fracture resistance of biominerals.²¹⁵

Molecular Motors

Molecular motors convert chemical energy into mechanical work and motion, which makes them a natural platform for the use of force spectroscopy to address the origin of their function at the single-molecule level. For example, in recent years, the stepwise motion of single kinesin molecules along microtubule tracks, and the discrete rotations of single F_1 subunits of the F_0F_1 -

ATP synthase were detected.^{216,217} Based on mechanochemical studies, under controlled external loads, distances and velocities in single-molecule experiments,²¹⁸ new theories on the generation of mechanical work by molecular motors have evolved.^{219,220}

SMFS has also proven to be a powerful tool in the investigation of “molecular motors”, whose working principle is based on the energy conversion cycle of stimuli-responsive polymers. Hugel *et al.*²²¹ have investigated by SMFS, in combination with optical excitation in total internal reflection, synthetic bi-stable photosensitive azobenzenes in a polymer chain. The schematic illustration of the transition of the two energy states and its corresponding force curves obtained from the SMFS measurements are shown in Figure 2.19.

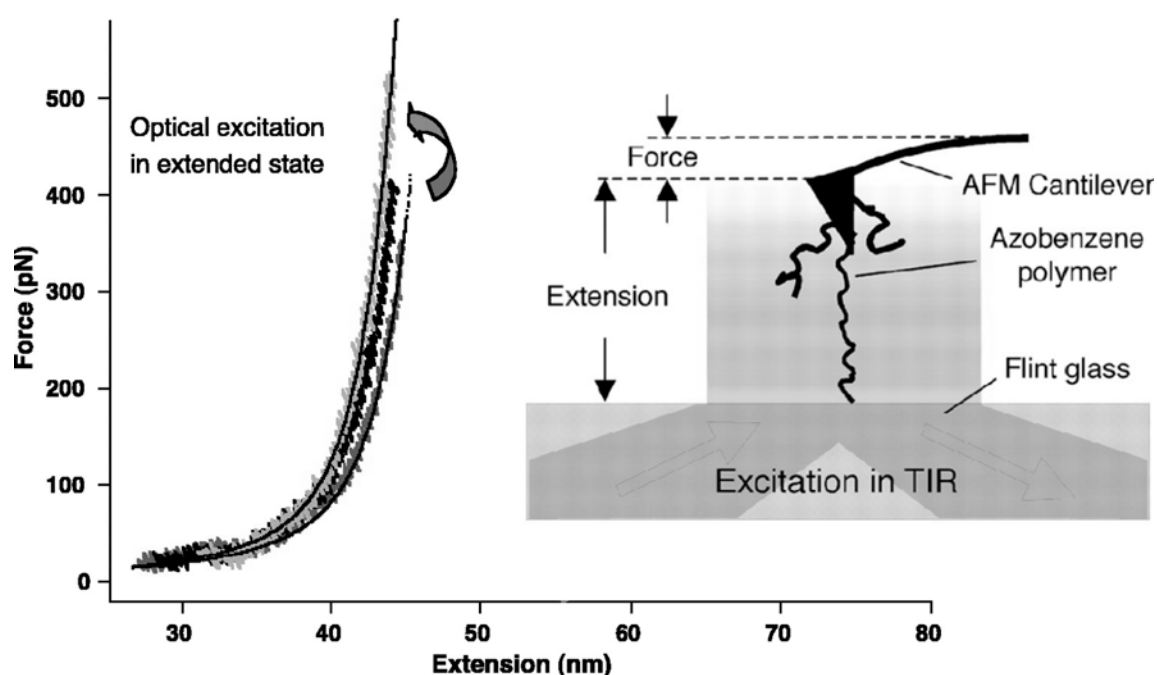


Figure 2.19. SMFS force measurements of azobenzene polymer chains at different conformational states (extended states and relaxed states) (reproduced from ref [221]).

These macromolecules are able to optically lengthen and contract by switching the azo groups between their trans and cis isomeric states. The polymer was found to contract against external forces along the backbone, thus delivering mechanical work upon irradiation. In addition, this polymer can work in a repetitive mode, which is the first demonstration of optomechanical energy conversion in a single molecule device. The creation of “smart” surfaces using stimuli-responsive polymers has also been demonstrated by Chilkoti *et al.*^{222,223} These authors studied distance-dependent colorimetric properties of gold nanoparticles and the thermal response of an elastin-like polypeptide (ELP) biopolymer. The phase transition of the ELP at the surface was thoroughly investigated to reversibly address an ELP fusion protein to a surface.

2.4 Closing Remarks

With the emergence of the prefix *nano* in science and technology, many established fields were revisited and integrated to achieve new scientific objectives and technological applications. In this chapter, a brief account has been given on bottom-up controlled molecular nanostructures from biological systems to synthetic supramolecular chemistry. The understanding of physical interactions on the nanoscale and the development of force spectroscopy allow structural and functional investigations on the single molecule level. A clear trend towards the investigation of dynamic processes and the interaction of single molecules with each other, as well as with their environment, can be observed. Together with new theoretical concepts of polymers and biomolecules under mechanical tension, force measurements will generate new insight into molecular interactions and their relation to structures and functions.

References:

- (1) Timp, G. E. *Nanotechnology*; Springer: New York, 1999.
- (2) Wilson, M.; Kannangara, K.; Smith, G.; Simmons, M.; Raguse, B. *Nanotechnology*; Chapman & Hall/CRC Press: Boca Raton, Florida, 2002.
- (3) Gross, M. *Travels to the Nanoworld: Miniature Machinery in Nature and Technology*; Plenum Trade: New York, 1999.
- (4) Amato, I. *Nanotechnology*, www.ostp.gov/nstc/html/iwgn/iwgn.public.brochure/welcome.htm, 2000.
- (5) Drexler, K. E. *Nanosystems: Molecular Machinery, Manufacturing and Computation*; John Wiley&Sons: New York, 1992.
- (6) Fujita, H. *Micromachines as Tools for Nanotechnology*; Springer: Berlin, 2003.
- (7) Rosoff, M. *Nano-Surface Chemistry*; Marcel Dekker: New York, 2002.
- (8) Lieber, C. M. *MRS Bulletin* **2003**, 28, 486-491.
- (9) Hall, J. S. *Nanotechnology* **1994**, 5, 157-167.
- (10) Zhong, Z. H.; Wang, D. L.; Cui, Y.; Bockrath, M. W.; Lieber, C. M. *Science* **2003**, 302, 1377-1379.
- (11) Sauvage, J.-P. E. *Molecular Machines and Motors*; Springer: Berlin, 2001.
- (12) Balzani, V.; Credi, A.; Raymo, F. M.; Stoddart, J. F. *Angewandte Chemie-International Edition* **2000**, 39, 3349-3391.
- (13) Ballardini, R.; Balzani, V.; Credi, A.; Gandolfi, M. T.; Venturi, M. *Accounts of Chemical Research* **2001**, 34, 445-455.
- (14) Liz-Marzan, L. M.; Kamat, P. V. *Nanoscale Materials*; Kluwer Academic Publishers: Boston, 2003.
- (15) Lehn, J. M. *Supramolecular Chemistry: Concepts and Perspectives*; VCH, Weinheim, 1995.
- (16) Goodsell, D. S. *Bionanotechnology: Lessons from Nature*; Wiley-Liss, Inc., Hoboken: New Jersey, 2004.
- (17) Stryer, L. *Biochemistry*; 4th Ed.; New York: Freeman, 1995.
- (18) Jeffery, G. A.; Saenger, W. *Hydrogen Bonding in Biological Structures*; Springer-Verlag: Berlin, 1991.
- (19) Keller, D.; Bustamante, C.; Keller, R. W. *Proceedings of the National Academy of Sciences of the United States of America* **1989**, 86, 5356-5360.
- (20) Hansma, H. G.; Vesenka, J.; Siegerist, C.; Kelderman, G.; Morrett, H.; Sinsheimer, R. L.; Elings, V.; Bustamante, C.; Hansma, P. K. *Science* **1992**, 256, 1180-1184.
- (21) Vesenka, J.; Guthold, M.; Tang, C. L.; Keller, D.; Delaine, E.; Bustamante, C. *Ultramicroscopy* **1992**, 42, 1243-1249.
- (22) Samori, B.; Siligardi, G.; Quagliariello, C.; Weisenhorn, A. L.; Vesenka, J.; Bustamante, C. *Proceedings of the National Academy of Sciences of the United States of America* **1993**, 90, 3598-3601.
- (23) Hansma, H. G.; Revenko, I.; Kim, K.; Laney, D. E. *Nucleic Acids Research* **1996**, 24, 713-720.
- (24) Niemeyer, C. M.; Adler, M.; Pignataro, B.; Lenhart, S.; Gao, S.; Chi, L. F.; Fuchs, H.; Blohm, D. *Nucleic Acids Research* **1999**, 27, 4553-4561.
- (25) Niemeyer, C. M.; Adler, M.; Lenhart, S.; Gao, S.; Fuchs, H.; Chi, L. F. *ChemBiochem* **2001**, 2, 260-264.
- (26) Niemeyer, C. M.; Adler, M.; Gao, S.; Chi, L. F. *Bioconjugate Chemistry* **2001**, 12, 364-371.
- (27) Niemeyer, C. M. *Current Opinion in Chemical Biology* **2000**, 4, 609-618.
- (28) Kroto, H. W.; Heath, J. R.; O'Brien, S. C.; Curl, R. F.; Smalley, R. E. *Nature* **1985**, 318, 162-163.

- (29) Fuller, R. *The Artifacts of R. Buckminster Fuller: A Comprehensive Collection of His Designs and Drawings*; Garland Publishing: New York, 1984.
- (30) Rohlfing, E. A.; Cox, D. M.; Kaldor, A. *Journal of Chemical Physics* **1984**, *81*, 3322-3330.
- (31) Bacon, R. *Journal of Applied Physics* **1960**, *31*, 283-290.
- (32) Iijima, S. *Nature* **1991**, *354*, 56-58.
- (33) Bethune, D. S.; Kiang, C. H.; Devries, M. S.; Gorman, G.; Savoy, R.; Vazquez, J.; Beyers, R. *Nature* **1993**, *363*, 605-607.
- (34) Harris, P. J. F. *Carbon Nanotubes and Related Structures*; Cambridge University Press, 1999.
- (35) Stroschio, J. A.; Eigler, D. M. *Science* **1991**, *254*, 1319-1326.
- (36) Viitanen, J. *Journal of Vacuum Science & Technology B* **1993**, *11*, 115-116.
- (37) Jiang, L.; Kim, Y.; Iyoda, T.; Li, J.; Kitazawa, K.; Fujishima, A.; Hashimoto, K. *Advanced Materials* **1999**, *11*, 649-653.
- (38) Iijima, S.; Ichihashi, T. *Nature* **1993**, *363*, 603-605.
- (39) Bachtold, A.; Hadley, P.; Nakanishi, T.; Dekker, C. *Science* **2001**, *294*, 1317-1320.
- (40) Vajtai, R.; Wei, B. Q.; Zhang, Z. J.; Jung, Y.; Ramanath, G.; Ajayan, P. M. *Smart Materials & Structures* **2002**, *11*, 691-698.
- (41) Jarillo-Herrero, P.; Sapmaz, S.; Dekker, C.; Kouwenhoven, L. P.; van der Zant, H. S. J. *Nature* **2004**, *429*, 389-392.
- (42) Dai, H. J.; Hafner, J. H.; Rinzler, A. G.; Colbert, D. T.; Smalley, R. E. *Nature* **1996**, *384*, 147-150.
- (43) Baughman, R. H.; Cui, C. X.; Zakhidov, A. A.; Iqbal, Z.; Barisci, J. N.; Spinks, G. M.; Wallace, G. G.; Mazzoldi, A.; De Rossi, D.; Rinzler, A. G.; Jaschinski, O.; Roth, S.; Kertesz, M. *Science* **1999**, *284*, 1340-1344.
- (44) Kong, J.; Franklin, N. R.; Zhou, C. W.; Chapline, M. G.; Peng, S.; Cho, K. J.; Dai, H. J. *Science* **2000**, *287*, 622-625.
- (45) Dillon, A. C.; Jones, K. M.; Bekkedahl, T. A.; Kiang, C. H.; Bethune, D. S.; Heben, M. J. *Nature* **1997**, *386*, 377-379.
- (46) Buhleier, E.; Wehner, W.; Vogtle, F. *Synthesis* **1978**, 155-158.
- (47) Dykes, G. M. *Journal of Chemical Technology and Biotechnology* **2001**, *76*, 903-918.
- (48) Zeng, F. W.; Zimmerman, S. C. *Chemical Reviews* **1997**, *97*, 1681-1712.
- (49) Narayanan, V. V.; Newkome, G. R. *Topics in Current Chemistry*, **1998**, *197*, 19-77.
- (50) Matthews, O. A.; Shipway, A. N.; Stoddart, J. F. *Progress in Polymer Science* **1998**, *23*, 1-56.
- (51) Chow, H. F.; Wang, Z. Y.; Lau, Y. F. *Tetrahedron* **1998**, *54*, 13813-13824.
- (52) Vogtle, F.; Gestermann, S.; Hesse, R.; Schwierz, H.; Windisch, B. *Progress in Polymer Science* **2000**, *25*, 987-1041.
- (53) Smith, D. K.; Diederich, F. *Topics in Current Chemistry* **2000**; *210*, 183-227.
- (54) Esumi, K.; Kameo, A.; Suzuki, A.; Torigoe, K. *Colloids and Surfaces A: Physicochemical and Engineering Aspects* **2001**, *189*, 155-161.
- (55) Esumi, K.; Suzuki, A.; Aihara, N.; Usui, K.; Torigoe, K. *Langmuir* **1998**, *14*, 3157-3159.
- (56) Garcia, M. E.; Baker, L. A.; Crooks, R. M. *Analytical Chemistry* **1999**, *71*, 256-258.
- (57) Zhao, M. Q.; Crooks, R. M. *Advanced Materials* **1999**, *11*, 217-220.
- (58) Zhao, M. Q.; Crooks, R. M. *Chemistry of Materials* **1999**, *11*, 3379-3385.
- (59) Chechik, V.; Zhao, M. Q.; Crooks, R. M. *Journal of the American Chemical Society* **1999**, *121*, 4910-4911.
- (60) Zhao, M. Q.; Crooks, R. M. *Angewandte Chemie-International Edition* **1999**, *38*, 364-366.
- (61) Rossell, O.; Seco, M.; Caminade, A. M.; Majoral, J. P. *Gold Bulletin* **2001**, *34*, 88-94.
- (62) Pease, A. R.; Jeppesen, J. O.; Stoddart, J. F.; Luo, Y.; Collier, C. P.; Heath, J. R. *Accounts of Chemical Research* **2001**, *34*, 433-444.
- (63) Collin, J. P.; Dietrich-Buchecker, C.; Gavina, P.; Jimenez-Molero, M. C.; Sauvage, J. P. *Accounts of Chemical Research* **2001**, *34*, 477-487.
- (64) Bender, M. L.; Komiyama, M. *Cyclodextrin Chemistry*; Berlin: Springer, 1978.
- (65) Szejtli, J. *Cyclodextrin Technology*; Kluwer, Dordrecht, 1988.
- (66) Behr, J.-P. *The Lock and Key Principle: The State of the Art*; Wiley: Chichester, 1994.
- (67) Wenz, G. *Angewandte Chemie-International Edition* **1994**, *33*, 803-822.
- (68) Rekharsky, M. V.; Inoue, Y. *Chemical Reviews* **1998**, *98*, 1875-1917.
- (69) Whitesides, G. M.; Mathias, J. P.; Seto, C. T. *Science* **1991**, *254*, 1312-1319.
- (70) Lindsey, J. S. *New Journal of Chemistry* **1991**, *15*, 153-180.
- (71) McGrath, K. P.; Kaplan, D. L. *Mater. Res. Soc. Symp. Proc.* **1994**, *330*, 61-68.
- (72) Kossovsky, N.; Millett, D.; Gelman, A.; Sponsler, E.; Hnatyszyn, H. J. *Bio-Technology* **1993**, *11*, 1534-1536.
- (73) McGrath, K. P.; Kaplan, D. L. *Macromolecular Symposia* **1994**, *77*, 183-189.
- (74) Sherrington, D. C.; Taskinen, K. A. *Chemical Society Reviews* **2001**, *30*, 83-93.
- (75) Mathias, J. P.; Seto, C. T.; Simanek, E. E.; Whitesides, G. M. *Journal of the American Chemical Society* **1994**, *116*, 1725-1736.

- (76) Mathias, J. P.; Simanek, E. E.; Zerkowski, J. A.; Seto, C. T.; Whitesides, G. M. *Journal of the American Chemical Society* **1994**, *116*, 4316-4325.
- (77) Archibald, D. D.; Mann, S. *Nature* **1993**, *364*, 430-433.
- (78) Heywood, B. R.; Mann, S. *Chemistry of Materials* **1994**, *6*, 311-318.
- (79) Leff, D. V.; Ohara, P. C.; Heath, J. R.; Gelbart, W. M. *Journal of Physical Chemistry* **1995**, *99*, 7036-7041.
- (80) Menger, F. M. *Angewandte Chemie-International Edition* **1991**, *30*, 1086-1099.
- (81) De Gennes, P. G. *The Physics of Liquid Crystals*; 2nd ed.; Oxford University Press: New York, 1993.
- (82) De Santis, P.; Morosetti, S.; R., R. *Macromolecules* **1974**, *7*, 52-58.
- (83) Ghadiri, M. R.; Granja, J. R.; Milligan, R. A.; McRee, D. E.; Khazanovich, N. *Nature* **1993**, *366*, 324-327.
- (84) Ghadiri, M. R.; Granja, J. R.; Buehler, L. K. *Nature* **1994**, *369*, 301-304.
- (85) Vreekamp, R. H.; vanDuynhoven, J. P. M.; Hubert, M.; Verboom, W.; Reinhoudt, D. N. *Angewandte Chemie-International Edition* **1996**, *35*, 1215-1218.
- (86) Timmerman, P.; Vreekamp, R. H.; Hulst, R.; Verboom, W.; Reinhoudt, D. N.; Rissanen, K.; Udachin, K. A.; Ripmeester, J. *Chemistry-A European Journal* **1997**, *3*, 1823-1832.
- (87) Jolliffe, K. A.; Timmerman, P.; Reinhoudt, D. N. *Angewandte Chemie-International Edition* **1999**, *38*, 933-937.
- (88) Prins, L. J.; Timmerman, P.; Reinhoudt, D. N. *Pure and Applied Chemistry* **1998**, *70*, 1459-1468.
- (89) Kerckhoffs, J.; van Leeuwen, F. W. R.; Spek, A. L.; Kooijman, H.; Crego-Calama, M.; Reinhoudt, D. N. *Angewandte Chemie-International Edition* **2003**, *42*, 5717-5722.
- (90) Ulman, A. *An Introduction to Ultrathin Organic Films: From Langmuir-Blodgett to Self-Assembly*; Academic Press: New York, 1991.
- (91) Wasserman, S. R.; Whitesides, G. M.; Tidswell, I. M.; Ocko, B. M.; Pershan, P. S.; Axe, J. D. *Journal of the American Chemical Society* **1989**, *111*, 5852-5861.
- (92) Dubois, L. H.; Nuzzo, R. G. *Annual Review of Physical Chemistry* **1992**, *43*, 437-463.
- (93) Whitesides, G. M.; Grzybowski, B. *Science* **2002**, *295*, 2418-2421.
- (94) Spinke, J.; Liley, M.; Schmitt, F. J.; Guder, H. J.; Angermaier, L.; Knoll, W. *Journal of Chemical Physics* **1993**, *99*, 7012-7019.
- (95) Nuzzo, R. G. Allara, D. L. *Journal of the American Chemical Society* **1983**, *105*, 4481-4483.
- (96) Sagiv, J. *Journal of the American Chemical Society* **1980**, *102*, 92-98.
- (97) Xia, Y. N.; Whitesides, G. M. *Angewandte Chemie-International Edition* **1998**, *37*, 551-575.
- (98) Whitesides, G. M.; Laibinis, P. E. *Langmuir* **1990**, *6*, 87-96.
- (99) Gittins, D. I.; Bethell, D.; Nichols, R. J.; Schiffrin, D. J. *Advanced Materials* **1999**, *11*, 737-740.
- (100) Gittins, D. I.; Bethell, D.; Nichols, R. J.; Schiffrin, D. J. *Journal of Materials Chemistry* **2000**, *10*, 79-83.
- (101) Gittins, D. I.; Susha, A. S.; Schoeler, B.; Caruso, F. *Advanced Materials* **2002**, *14*, 508-512.
- (102) Lehn, J. M. *Angewandte Chemie-International Edition* **1988**, *27*, 89-112.
- (103) Lange, R. F. M.; Beijer, F. H.; Sijbesma, R. P.; Hooft, R. W. W.; Kooijman, H.; Spek, A. L.; Kroon, J.; Meijer, E. W. *Angewandte Chemie-International Edition* **1997**, *36*, 969-971.
- (104) Beijer, F. H.; Kooijman, H.; Spek, A. L.; Sijbesma, R. P.; Meijer, E. W. *Angewandte Chemie-International Edition* **1998**, *37*, 75-78.
- (105) Folmer, B. J. B.; Sijbesma, R. P.; Versteegen, R. M.; van der Rijt, J. A. J.; Meijer, E. W. *Advanced Materials* **2000**, *12*, 874-878.
- (106) Brunsveld, L.; Folmer, B. J. B.; Meijer, E. W.; Sijbesma, R. P. *Chemical Reviews* **2001**, *101*, 4071-4097.
- (107) ten Cate, A. T.; Sijbesma, R. P. *Macromolecular Rapid Communications* **2002**, *23*, 1094-1112.
- (108) Whitesides, G. M.; Simanek, E. E.; Mathias, J. P.; Seto, C. T.; Chin, D. N.; Mammen, M.; Gordon, D. M. *Accounts of Chemical Research* **1995**, *28*, 37-44.
- (109) Bielejewski, A. G.; Marjo, C. E.; Prins, L. J.; Timmerman, P.; de Jong, F.; Reinhoudt, D. N. *Journal of the American Chemical Society* **2001**, *123*, 7518-7533.
- (110) Israelachvili, J. N. *Intermolecular and Surface Forces*; 2nd Ed.; Academic Press, London, 1991.
- (111) Vinogradov, S. N.; Linnell, R. H. *Hydrogen Bonding*; Van Nostrand Reinhold: New York, 1971.
- (112) Jeffery, G. A. *An Introduction to Hydrogen Bonding*; Oxford University Press: New York, 1997.
- (113) Joesten, M. D.; Schaad, L. J. *Hydrogen Bonding*; Dekker: New York, 1974.
- (114) Schuster, P.; Zundel, G.; Sandorfy, C. *The Hydrogen Bond*; North-Holland: Amsterdam, 1976.
- (115) Crandall, B. C. *Nanotechnology : Molecular Speculations on Global Abundance*; MIT Press: Cambridge, 1996.
- (116) Crommie, M. F.; Lutz, C. P.; Eigler, D. M. *Science* **1993**, *262*, 218-220.
- (117) Scheiner, S. *Molecular Interactions : From van der Waals to Strongly Bound Complexes* Chichester: John Wiley & Sons, 1997.
- (118) Decher, G. *Science* **1997**, *277*, 1232-1237.
- (119) Dunitz, J. D. *Coordinative Interactions*; Springer: Berlin, 1973.
- (120) Wilkinson, G. Gillard, R. D; MacClevarty, J. A. *Comprehensive Coordination Chemistry: The Synthesis, Reactions, Properties & Applications of Coordination Compounds*; Oxford: Pergamon Press, 1987.
- (121) Hatzor, A.; Moav, T.; Cohen, H.; Matlis, S.; Libman, J.; Vaskevich, A.; Shanzer, A.; Rubinstein, I. *Journal of the American Chemical Society* **1998**, *120*, 13469-13477.

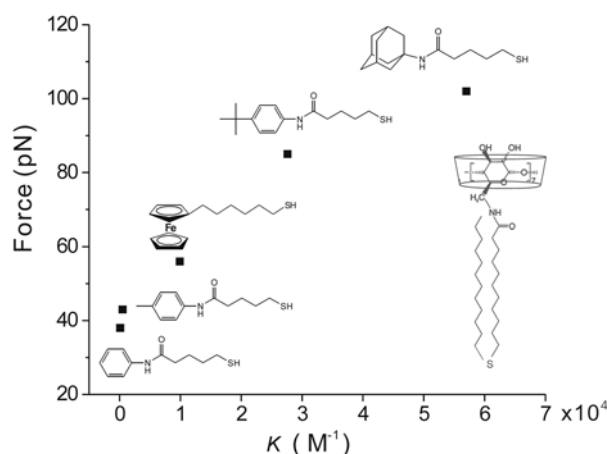
- (122) Mammen, M.; Choi, S. K.; Whitesides, G. M. *Angewandte Chemie-International Edition* **1998**, *37*, 2755-2794.
- (123) Siegel, R. W. *MRS Bulletin* **1990**, *15*, 60-67.
- (124) Kittel, C. *Thermal Physics*; John Wiley & Sons: New York, 1969.
- (125) Lee, G. U.; Chrisey, L. A.; Colton, R. J. *Science* **1994**, *266*, 771-773.
- (126) Florin, E. L.; Moy, V. T.; Gaub, H. E. *Science* **1994**, *264*, 415-417.
- (127) Clausen-Schaumann, H.; Seitz, M.; Krautbauer, R.; Gaub, H. E. *Current Opinion in Chemical Biology* **2000**, *4*, 524-530.
- (128) Smith, S. B.; Finzi, L.; Bustamante, C. *Science* **1992**, *258*, 1122-1126.
- (129) Ashkin, A.; Schutze, K.; Dziedzic, J. M.; Euteneuer, U.; Schliwa, M. *Nature* **1990**, *348*, 346-348.
- (130) Kishino, A.; Yanagida, T. *Nature* **1988**, *334*, 74-76.
- (131) Evans, E.; Ritchie, K.; Merkel, R. *Biophysical Journal* **1995**, *68*, 2580-2587.
- (132) Schlierf, M.; Li, H. B.; Fernandez, J. M. *Proceedings of the National Academy of Sciences of the United States of America* **2004**, *101*, 7299-7304.
- (133) Fernandez, J. M.; Li, H. B. *Science* **2004**, *303*, 1674-1678.
- (134) Binning, G.; Quate, C. F.; Gerber, C. *Physical Review Letters* **1986**, *56*, 930-933.
- (135) Sader, J. E.; Larson, I.; Mulvaney, P.; White, L. R. *Review of Scientific Instruments* **1995**, *66*, 3789-3798.
- (136) Sader, J. E. *Review of Scientific Instruments* **1995**, *66*, 4583-4587.
- (137) Sader, J. E. *Journal of Applied Physics* **1998**, *84*, 64-76.
- (138) Sader, J. E.; Chon, J. W. M.; Mulvaney, P. *Review of Scientific Instruments* **1999**, *70*, 3967-3969.
- (139) Cleveland, J. P.; Manne, S.; Bocek, D.; Hansma, P. K. *Review of Scientific Instruments* **1993**, *64*, 403-405.
- (140) Hutter, J. L.; Bechhoefer, J. *Review of Scientific Instruments* **1993**, *64*, 1868-1873.
- (141) Walters, D. A.; Cleveland, J. P.; Thomson, N. H.; Hansma, P. K.; Wendman, M. A.; Gurley, G.; Elings, V. *Review of Scientific Instruments* **1996**, *67*, 3583-3590.
- (142) Maeda, N.; Senden, T. J. *Langmuir* **2000**, *16*, 9282-9286.
- (143) Butt, H. J.; Jaschke, M. *Nanotechnology* **1995**, *6*, 1-7.
- (144) Senden, T. J.; Ducker, W. A. *Langmuir* **1994**, *10*, 1003-1004.
- (145) Gibson, C. T.; Watson, G. S.; Myhra, S. *Nanotechnology* **1996**, *7*, 259-262.
- (146) Comella, B. T.; Scanlon, M. R. *Journal of Materials Science* **2000**, *35*, 567-572.
- (147) Holbery, J. D.; Eden, V. L.; Sarikaya, M.; Fisher, R. M. *Review of Scientific Instruments* **2000**, *71*, 3769-3776.
- (148) Neumeister, J. M.; Ducker, W. A. *Review of Scientific Instruments* **1994**, *65*, 2527-2531.
- (149) Hazel, J. L.; Tsukruk, V. V. *Thin Solid Films* **1999**, *339*, 249-257.
- (150) Hazel, J. L.; Tsukruk, V. V. *Journal of Tribology-Transactions of the ASME* **1998**, *120*, 814-819.
- (151) Hodges, C. S. *Advances in Colloid and Interface Science* **2002**, *99*, 13-75.
- (152) Zhang, W.; Zhang, X. *Progress in Polymer Science* **2003**, *28*, 1271-1295.
- (153) Hugel, T.; Seitz, M. *Macromolecular Rapid Communications* **2001**, *22*, 989-1016.
- (154) Janshoff, A.; Neitzert, M.; Oberdorfer, Y.; Fuchs, H. *Angewandte Chemie-International Edition* **2000**, *39*, 3213-3237.
- (155) Marszalek, P. E.; Oberhauser, A. F.; Pang, Y. P.; Fernandez, J. M. *Nature* **1998**, *396*, 661-664.
- (156) Ludwig, M.; Rief, M.; Schmidt, L.; Li, H.; Oesterhelt, F.; Gautel, M.; Gaub, H. E. *Applied Physics A-Materials Science & Processing* **1999**, *68*, 173-176.
- (157) Ortiz, C.; Hadziioannou, G. *Macromolecules* **1999**, *32*, 780-787.
- (158) Bemis, J. E.; Akhremitchev, B. B.; Walker, G. C. *Langmuir* **1999**, *15*, 2799-2805.
- (159) Zou, S.; Zhang, W. K.; Zhang, X.; Jiang, B. Z. *Langmuir* **2001**, *17*, 4799-4808.
- (160) Wang, C.; Shi, W. Q.; Zhang, W. K.; Zhang, X.; Katsumoto, Y.; Ozaki, Y. *Nano Letters* **2002**, *2*, 1169-1172.
- (161) Fleer, G. J.; Cohen Stuart, M. A.; Scheutjens, J. M. H. M.; Cosgrove, T. *Polymers at Interfaces*; London: Chapman & Hall, 1993.
- (162) Senden, T. J.; di Meglio, J. M.; Auroy, P. *European Physical Journal B* **1998**, *3*, 211-216.
- (163) Smith, S. B.; Cui, Y. J.; Bustamante, C. *Science* **1996**, *271*, 795-799.
- (164) Rief, M.; Oesterhelt, F.; Heymann, B.; Gaub, H. E. *Science* **1997**, *275*, 1295-1297.
- (165) Kikuchi, H.; Yokoyama, N.; Kajiyama, T. *Chemistry Letters* **1997**, 1107-1108.
- (166) Fritz, J.; Katopodis, A. G.; Kolbinger, F.; Anselmetti, D. *Proceedings of the National Academy of Sciences of the United States of America* **1998**, *95*, 12283-12288.
- (167) Li, H. B.; Zhang, W. K.; Zhang, X.; Shen, J. C.; Liu, B. B.; Gao, C. X.; Zou, G. T. *Macromolecular Rapid Communications* **1998**, *19*, 609-611.
- (168) Li, H. B.; Rief, M.; Oesterhelt, F.; Gaub, H. E.; Zhang, X.; Shen, J. C. *Chemical Physics Letters* **1999**, *305*, 197-201.
- (169) Zhang, W. K.; Xu, Q. B.; Zou, S.; Li, H. B.; Xu, W. Q.; Zhang, X.; Shao, Z. Z.; Kudera, M.; Gaub, H. E. *Langmuir* **2000**, *16*, 4305-4308.
- (170) Rief, M.; Gautel, M.; Oesterhelt, F.; Fernandez, J. M.; Gaub, H. E. *Science* **1997**, *276*, 1109-1112.

- (171) Li, H. B.; Linke, W. A.; Oberhauser, A. F.; Carrion-Vazquez, M.; Kerkvliet, J. G.; Lu, H.; Marszalek, P. E.; Fernandez, J. M. *Nature* **2002**, *418*, 998-1002.
- (172) Fritz, J.; Anselmetti, D.; Jarchow, J.; FernandezBusquets, X. *Journal of Structural Biology* **1997**, *119*, 165-171.
- (173) Jarchow, J.; Fritz, J.; Anselmetti, D.; Calabro, A.; Hascall, V. C.; Gerosa, D.; Burger, M. M.; Fernandez-Busquets, X. *Journal of Structural Biology* **2000**, *132*, 95-105.
- (174) Li, H.; Rief, M.; Oesterhelt, F.; Gaub, H. E. *Applied Physics A-Materials Science & Processing* **1999**, *68*, 407-410.
- (175) Evans, E.; Ritchie, K. *Biophysical Journal* **1997**, *72*, 1541-1555.
- (176) Evans, E.; Ritchie, K. *Biophysical Journal* **1999**, *76*, 2439-2447.
- (177) Merkel, R.; Nassoy, P.; Leung, A.; Ritchie, K.; Evans, E. *Nature* **1999**, *397*, 50-53.
- (178) Kramers, H. A. *Physica* **1940**, *7*, 284-304.
- (179) Evans, E. *Faraday Discussions* **1998**, *111*, 1-16.
- (180) Strunz, T.; Oroszlan, K.; Schafer, R.; Guntherodt, H. J. *Proceedings of the National Academy of Sciences of the United States of America* **1999**, *96*, 11277-11282.
- (181) Evans, E. *Annual Review of Biophysics and Biomolecular Structure* **2001**, *30*, 105-128.
- (182) Rief, M.; Clausen-Schaumann, H.; Gaub, H. E. *Nature Structural Biology* **1999**, *6*, 346-349.
- (183) Grandbois, M.; Beyer, M.; Rief, M.; Clausen-Schaumann, H.; Gaub, H. E. *Science* **1999**, *283*, 1727-1730.
- (184) Rief, M.; Pascual, J.; Saraste, M.; Gaub, H. E. *Journal of Molecular Biology* **1999**, *286*, 553-561.
- (185) Conti, M.; Falini, G.; Samori, B. *Angewandte Chemie-International Edition* **2000**, *39*, 215-218.
- (186) Kienberger, F. K., G.; Gruber, H. J.; Pastushenko, V. P.; Riener, C.; Trieb, M.; Knaus, H. G.; Schindler, H. G.; Hinterdorfer, P. *Single Molecules* **2000**, *1*, 59-65.
- (187) Yang, G. L.; Cecconi, C.; Baase, W. A.; Vetter, I. R.; Breyer, W. A.; Haack, J. A.; Matthews, B. W.; Dahlquist, F. W.; Bustamante, C. *Proceedings of the National Academy of Sciences of the United States of America* **2000**, *97*, 139-144.
- (188) Hinterdorfer, P.; Baumgartner, W.; Gruber, H. J.; Schilcher, K.; Schindler, H. *Proceedings of the National Academy of Sciences of the United States of America* **1996**, *93*, 3477-3481.
- (189) Dammer, U.; Hegner, M.; Anselmetti, D.; Wagner, P.; Dreier, M.; Huber, W.; Guntherodt, H. J. *Biophysical Journal* **1996**, *70*, 2437-2441.
- (190) Allen, S.; Chen, X. Y.; Davies, J.; Davies, M. C.; Dawkes, A. C.; Edwards, J. C.; Roberts, C. J.; Sefton, J.; Tendler, S. J. B.; Williams, P. M. *Biochemistry* **1997**, *36*, 7457-7463.
- (191) Willemsen, O. H.; Snel, M. M. E.; van der Werf, K. O.; de Grooth, B. G.; Greve, J.; Hinterdorfer, P.; Gruber, H. J.; Schindler, H.; van Kooyk, Y.; Figdor, C. G. *Biophysical Journal* **1998**, *75*, 2220-2228.
- (192) Ros, R.; Schwesinger, F.; Anselmetti, D.; Kubon, M.; Schafer, R.; Pluckthun, A.; Tiefenauer, L. *Proceedings of the National Academy of Sciences of the United States of America* **1998**, *95*, 7402-7405.
- (193) Boland, T.; Ratner, B. D. *Proceedings of the National Academy of Sciences of the United States of America* **1995**, *92*, 5297-5301.
- (194) EssevazRoulet, B.; Bockelmann, U.; Heslot, F. *Proceedings of the National Academy of Sciences of the United States of America* **1997**, *94*, 11935-11940.
- (195) Krautbauer, R.; Rief, M.; Gaub, H. E. *Nano Letters* **2003**, *3*, 493-496.
- (196) Krautbauer, R.; Clausen-Schaumann, H.; Gaub, H. E. *Angewandte Chemie-International Edition* **2000**, *39*, 3912-3915.
- (197) Bennink, M. L.; Scharer, O. D.; Kanaar, R.; Sakata-Sogawa, K.; Schins, J. M.; Kanger, J. S.; de Grooth, B. G.; Greve, J. *Cytometry* **1999**, *36*, 200-208.
- (198) Williams, M. C.; Rouzina, I. *Current Opinion in Structural Biology* **2002**, *12*, 330-336.
- (199) Williams, M. C.; Rouzina, I.; Bloomfield, V. A. *Accounts of Chemical Research* **2002**, *35*, 159-166.
- (200) Dammer, U.; Popescu, O.; Wagner, P.; Anselmetti, D.; Guntherodt, H. J.; Misevic, G. N. *Science* **1995**, *267*, 1173-1175.
- (201) Hemmerle, J.; Altmann, S. M.; Maaloum, M.; Horber, J. K. H.; Heinrich, L.; Voegel, J. C.; Schaaf, P. *Proceedings of the National Academy of Sciences of the United States of America* **1999**, *96*, 6705-6710.
- (202) Lehenkari, P. P.; Horton, M. A. *Biochemical and Biophysical Research Communications* **1999**, *259*, 645-650.
- (203) Grandbois, M.; Dettmann, W.; Benoit, M.; Gaub, H. E. *Journal of Histochemistry & Cytochemistry* **2000**, *48*, 719-724.
- (204) Benoit, M.; Gabriel, D.; Gerisch, G.; Gaub, H. E. *Nature Cell Biology* **2000**, *2*, 313-317.
- (205) Baumgartner, W.; Hinterdorfer, P.; Ness, W.; Raab, A.; Vestweber, D.; Schindler, H.; Drenckhahn, D. *Proceedings of the National Academy of Sciences of the United States of America* **2000**, *97*, 4005-4010.
- (206) Kudera, M.; Eschbaumer, C.; Gaub, H. E.; Schubert, U. S. *Advanced Functional Materials* **2003**, *13*, 615-620.
- (207) Evans, E.; Leung, A.; Hammer, D.; Simon, S. *Proceedings of the National Academy of Sciences of the United States of America* **2001**, *98*, 3784-3789.
- (208) Williams, P.; Evans, E. *Dynamic Force Spectroscopy: II Multiple Bonds*, 2003.
- (209) Tskhovrebova, L.; Trinick, J.; Sleep, J. A.; Simmons, R. M. *Nature* **1997**, *387*, 308-312.

- (210) Kellermayer, M. S. Z.; Smith, S. B.; Granzier, H. L.; Bustamante, C. *Science* **1997**, *276*, 1112-1116.
- (211) Tskhovrebova, L.; Han, W. H.; Trinick, J. *Biophysical Journal* **2000**, *78*, 446A-446A.
- (212) Tskhovrebova, L.; Trinick, J. *Nature Reviews Molecular Cell Biology* **2003**, *4*, 679-689.
- (213) Houmeida, A.; Thompson, B.; Tskhovrebova, L.; Knight, P. J.; Thirumurugan, K.; Stafford, W. F.; Trinick, J. *Biophysical Journal* **2004**, *86*, 212A-212A.
- (214) Li, H. B.; Fernandez, J. M. *Biophysical Journal* **2004**, *86*, 323A-323A.
- (215) Smith, B. L.; Schaffer, T. E.; Viani, M.; Thompson, J. B.; Frederick, N. A.; Kindt, J.; Belcher, A.; Stucky, G. D.; Morse, D. E.; Hansma, P. K. *Nature* **1999**, *399*, 761-763.
- (216) Junge, W. *Proceedings of the National Academy of Sciences of the United States of America* **1999**, *96*, 4735-4737.
- (217) Mehta, A. D.; Rief, M.; Spudich, J. A.; Smith, D. A.; Simmons, R. M. *Science* **1999**, *283*, 1689-1695.
- (218) Visscher, K.; Schnitzer, M. J.; Block, S. M. *Nature* **1999**, *400*, 184-189.
- (219) Keller, D.; Bustamante, C. *Biophysical Journal* **2000**, *78*, 541-556.
- (220) Fisher, M. E.; Kolomeisky, A. B. *Proceedings of the National Academy of Sciences of the United States of America* **1999**, *96*, 6597-6602.
- (221) Hugel, T.; Holland, N. B.; Cattani, A.; Moroder, L.; Seitz, M.; Gaub, H. E. *Science* **2002**, *296*, 1103-1106.
- (222) Frey, W.; Meyer, D. E.; Chilkoti, A. *Advanced Materials* **2003**, *15*, 248-251.
- (223) Frey, W.; Meyer, D. E.; Chilkoti, A. *Langmuir* **2003**, *19*, 1641-1653.

Chapter 3

Probing Individual Supramolecular Host-Guest Interactions by Single Molecule Force Spectroscopy*



Individual supramolecular host-guest interactions between α -cyclodextrin (α -CD) receptor cavities in self-assembled monolayers (SAMs) and various apolar guest molecules attached to atomic force microscopy (AFM) tips were systematically studied in aqueous medium by AFM-based force spectroscopy. Expanding on previous work that addressed the unbinding force of ferrocenyl-derivatized guest molecules and α -CD SAMs, in this work anilyl, toluidyl, tert-butylphenyl, and adamantyl guests were investigated. Due to the fast unbinding-rebinding kinetics on the experimental time scale, the host-guest unbinding was probed under conditions of quasi-thermodynamic equilibrium. For all guests the force-displacement curves measured subsequent to tip-surface contact exhibited characteristic multiple pull-off events. In experiments carried out under optimized conditions, also single pull-off events were frequently observed. The statistical analyses of the pull-off events showed several maxima in the force histograms, with characteristic rupture force quanta of 39 ± 15 , 45 ± 15 , 89 ± 15 , and 102 ± 15 pN for anilyl, toluidyl, tert-butylphenyl, and adamantyl guests, respectively. These force values, which are attributed to single host-guest complex unbinding forces, were found to be correlated with the values of equilibrium complexation constants. The experimental data agreed well with an equilibrium model based on the evaluation of the potential energy landscape of tip-surface interactions. Finally, the unbinding forces for multivalent interactions were probed using a bis-adamantyl-derivatized guest. The observed force values were consistent with theoretical considerations by Evans and coworkers.

3.1 Introduction

The design of highly efficient and selective reagents is one of the major goals of research in chemistry (catalysis) as well as in sensing technology. In this context the remarkable natural

* The work described in this Chapter was published in the following articles: Zou, S.; Zapotoczny, S.; de Jong, M. R.; Auletta, T.; Schönherr, H.; Huskens, J.; van Veggel, F. C. J. M.; Reinhoudt, D. N.; Vancso, G. J. *Polymeric Materials: Science & Engineering* **2003**, 88, 453-454; Auletta, T.; de Jong, M. R.; Mulder, A.; van Veggel, F. C. J. M.; Huskens, J.; Reinhoudt, D. N.; Zou, S.; Zapotoczny, S.; Schönherr, H.; Vancso, G. J.; Kuipers, L. *Journal of the American Chemical Society* **2004**, 126, 1577-1584.

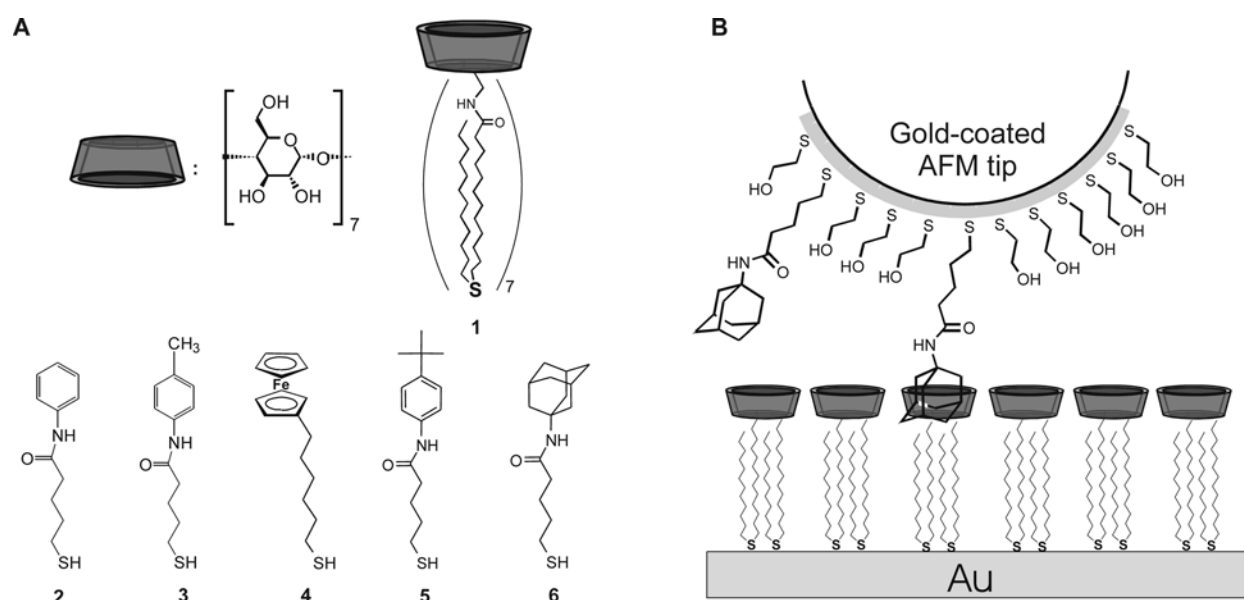
catalysts, the enzymes, have provided a major inspiration for the development of synthetic receptors based on molecular recognition.¹⁻³ The first class of substances to be used as substrate binding reagents were the cyclodextrins.⁴⁻⁶ The most important cyclodextrin, α -cyclodextrin (α -CD), is a cyclic oligosaccharide consisting of seven glucose units linked via α -1-4 glycosidic bonds. α -CD is able to form inclusion complexes with a variety of neutral and charged organic molecules in aqueous solutions.^{7,8} On the basis of numerous investigations performed using natural or substituted α -CD, biomimetic artificial sensor and molecular recognition processes have been developed.⁹⁻¹⁷

Following the advent of atomic force microscopy (AFM)¹⁸ and other sensitive force probe techniques, such as magnetic beads, optical traps, glass microneedles, biomembrane force probe and molecular force clamp approaches,¹⁹⁻²² it has become possible to directly detect molecular scale forces. These forces play an important role in many processes, including molecular recognition. Force spectroscopy provides a tool to map the energy landscape of, e.g. biologically relevant complexes, as has been demonstrated, e.g. by Merkel *et al.* on the biotin-(strept)avidin system.^{23,24} Important contributions by Evans and co-workers established the theoretical background for the interpretation of bond rupture in far from equilibrium situations, as introduced in Chapter 2. These considerations forced researchers to revise the interpretation of earlier reports on the investigation of receptor-ligand interactions (streptavidin – biotin) with fixed loading rate and spring constants of the cantilever.^{23,24}

Single molecule force spectroscopy measurements of similarly relevant bio-related systems have been reported, e. g., for the protein-A-IgG bond²⁵⁻²⁷ and single lipid anchors in membranes.²⁸ Theoretical studies that consider the effect of dynamic loading on bond rupture have been successful to describe the antibody-haptene interactions,²⁹ as well as the breaking of multiple parallel molecular bonds.³⁰ Further progress using AFM-based single molecule force spectroscopy (SMFS) has been made in the determination of unbinding forces of individual antigen-antibody complex,³¹ DNA duplexes,³² as well as the rupture forces associated with breaking covalent bonds.³³ Owing to a rapid evolution and refinement of the necessary experimental equipment that allows one to study important biomaterials in their native environments, SMFS has emerged as a widely used tool for single molecule research in the biology and biomedical-related research area.³⁴⁻³⁶

By contrast, there are much fewer reports on single molecule force spectroscopy measurements for “artificial” supramolecular systems. Previous studies in Twente have revealed the complexation behavior of ferrocenyl moieties immobilized onto an AFM tip and heptathioether α -CD self-assembled monolayers (SAMs).³⁷⁻³⁹ This supramolecular host-guest

system is characterized by fast complexation/decomplexation kinetics,[†] thus the guest moieties have the possibility to decomplex and rebind spontaneously many times during the recording of an AFM force-distance curve as long as the tip stays in close proximity to the β -CD SAM. A statistical analysis of the pull-off data for the ferrocene – β -CD system showed a periodic distribution of forces. In accordance with the long timescale of the AFM pull-off experiments (timescale $\sim 1000 \mu\text{s}$) relative to decomplexation-recomplexation dynamics, the force quantum ($55 \pm 10 \text{ pN}$) was found to be independent of the number of available guests, the loading rate, and the length of the spacer between the guest and the surface.^{38,40} The quasi-thermodynamic equilibrium conditions reported in this early work imply that there is a correlation between unbinding forces and equilibrium complexation constants for closely related guest – η -CD systems.



Scheme 3.1. (A) Chemical structure of β -CD adsorbate **1** and guest molecules **2-6** for immobilization on AFM tips. (B) Schematic drawing of single molecule force spectroscopy of **6** immobilized in a hydroxyl-terminated SAM on a gold coated AFM tip and SAM of **1** on Au(111) (five of the seven alkylsulfide substituents on the β -CD have been left away for clarity).

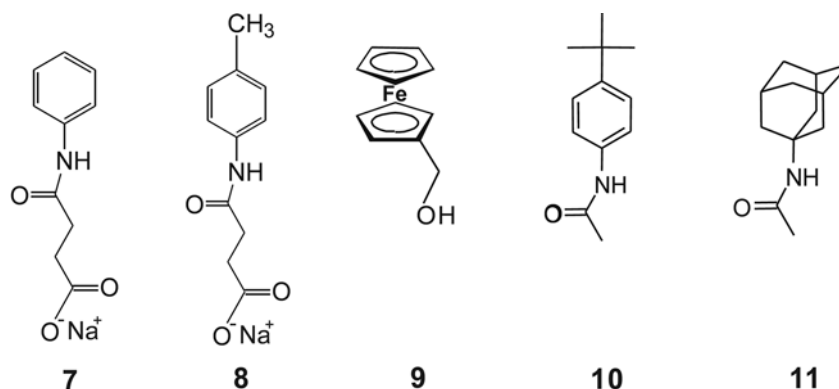
The work presented in this Chapter is an extension of the initial work and systematically addresses the relation between single host-guest complex rupture forces of β -cyclodextrin SAMs on one hand and different apolar guest molecules with different thermodynamic parameters of the complexation process, i.e. Gibbs free energy G° , on the other hand. The complexation constants for model guest compounds in solution or on β -CD SAMs were determined by

[†] The kinetics of the cyclodextrin host-guest systems is very fast. For ferrocene – β -CD complexes, the complexation constant measured for the model compound ferrocenecarboxylic acid is 2400 M^{-1} (Godinez, L. A.; Schwartz, L.; Criss, C. M.; Kaifer, A. E. *J. Phys. Chem. B* **1997**, 101, 3376-3380), while diffusion-controlled association k_{on} of ca. $10^9 \text{ M}^{-1} \text{ s}^{-1}$ can be assumed (Hammes, G. G.; Park, A. C. *J. Am. Chem. Soc.* **1968**, 90, 4151-4157). Hence an unbinding rate constant $k_{\text{off}} \sim 10^5 \text{ s}^{-1}$ is estimated and the unbinding/rebinding occurs on a timescale of $1 \mu\text{s}$ (see reference 34).

isothermal titration calorimetry (ITC) and surface plasmon resonance (SPR) measurements,⁴¹ while the single complex rupture forces were determined by SMFS. The experimental data were compared to a model based on the evaluation of the potential energy landscape of the tip-surface interactions.⁴¹

3.2 Evaluation of the Thermodynamics of Complexation in Solution and on Surfaces[‡]

In order to study the correlation of the rupture forces with the equilibrium complexation constants (and Gibbs free energy), knowledge of the corresponding parameters is required. ITC and SPR measurements were hence employed to evaluate the thermodynamics of complex formation^{41,42} in solution and on surfaces, respectively. Compounds **7-11** (Scheme 3.2) and native α -CD in solution were used as model systems for compounds **2-6** and SAMs of α -CD derivative **1** (Scheme 3.1) to investigate the host-guest (HG) complexation behavior.



Scheme 3.2. Chemical structures of model guests **7 – 11** for host-guest binding with α -cyclodextrin in solution and SAMs of **1** on Au.

The solution binding parameters for compounds **9 – 11** with native α -CD in solution, determined by ITC, were reported previously.⁴² The same approach was applied to determine the thermodynamics of the HG complexes of **7** and **8**. SPR measurements were employed to determine the complexation constants on SAMs of **1** only for compounds **9-11**. Due to the poor solubility and weak interactions for compounds **7** and **8**, SPR could not be applied.⁴¹ In this case, the data acquired in solution was used (see below). The thermodynamic parameters determined for HG complexes are summarized in Table 3.1. The experimental data for compounds **9 – 11**, obtained by means of the two independent techniques, show an excellent agreement. These results are in agreement with the phenomenon reported earlier that small guest molecules, which fit into the CD cavity, apparently do not feel the presence of the alkyl chains of **1**, leading to

[‡] This part of the work was carried out by Dr. M. R. de Jong, Dr. A. Mulder, and Dr. T. Auletta in Prof. D. N. Reinhoudt's group (SMCT) at the University of Twente.

identical binding constants in solution and at β -CD SAMs.⁴² Therefore we used these ITC data as binding parameters of compounds **7** and **8** on SAMs of **1**.

Table 3.1. Thermodynamic data for complexation of model compounds **9-11** at SAMs of **1** measured by SPR, and solution data for model compounds **7-11** with native β -CD measured by ITC.

Model guests	SPR	ITC		
	ΔG° (kcal mol ⁻¹)	ΔG° (kcal mol ⁻¹)	ΔH° (kcal mol ⁻¹)	$T\Delta S^\circ$ (kcal mol ⁻¹)
7	--- ^a	-2.3	-2.3	0
8	--- ^a	-3.0	-2.7	0.4
9	-5.4	-5.4	-6.1	-0.7
10	-6.0	-6.1	-5.2	0.9
11	-6.5	-6.6	-5.9	0.7

^a Low solubility and weak interactions with the η -CD SAMs did not allow accurate measurements of the thermodynamic parameters for this guest.

3.3 Specific Interactions of β -CD – Guest Adsorbate Complexes by SMFS

The magnitude of the single supramolecular host-guest complex rupture forces of the apolar guests, studied previously by SPR and ITC in solution (see section 3.2), on highly ordered β -CD SAMs was determined by single molecule force spectroscopy in aqueous media.

3.3.1 Rupture Forces of β -CD – Adamantane Host-Guest Complexes

Specific interactions between the β -CD host monolayers and guest **6** (Scheme 3.1) immobilized in mixed SAMs of 2-hydroxy-ethanethiol (C2OH) on AFM tips were detected in aqueous medium in force-displacement (f-d) curves, as shown in Figure 3.1. The measured cantilever deflection, corresponding to the pull-off event, was translated into force using the independently determined AFM cantilever spring constant. The f-d curves obtained using tips with 1% and higher surface coverage[§] of guest molecules showed multiple pull-off events upon retraction of the sample from the tip, as shown in Figure 3.1A. These multiple pull-off events were absent when tips without any guest or "receptor" SAMs without β -CD units were utilized. When an aqueous solution of the external guest 1-anilinonaphthalene-8-sulfonic acid (1,8-ANS, $K = 2.6 \times 10^4$ M,^{43,44} $c \sim 0.1$ mM,) was injected into the liquid cell, the number of multiple pull-off events decreased markedly.⁴⁴ This effect can be attributed to the partial blocking of the β -CD cavities due to 1,8-ANS binding to the β -CD host sites (competition of 1,8-ANS with **6**). After

[§] Mixed SAMs of C2OH and **6** in different ratios were analyzed by X-ray Photoelectron Spectroscopy (XPS). Linear correlations between the solution composition and the corresponding layers were observed, indicating that there was no preferential adsorption of one of the two adsorbates. Under such conditions (surface coverage of guest between 0.2 and 2%) surface phase segregation is unlikely.

washing away the 1,8-ANS with water, the multiple pull-offs were observed again. For the cases of guests **3** and **5**, which possess lower association constants with monolayer **1**, the number of pull-off events was reduced more drastically than reported previously.^{37,38,44} These observations are in agreement with a reversible blocking of a large portion of the available cavities in the monolayer of **1** by the external guest.

Dilution of the guest molecules in the C2OH SAMs to 0.2% led to a significant reduction in the number of pull-off events (f-d curves with pull-off events were less than 20% of the tip-sample contacts). For very sharp tips, single pull-off events were observed in more than 70% of the successful pull-off events (Figure 3.1B).

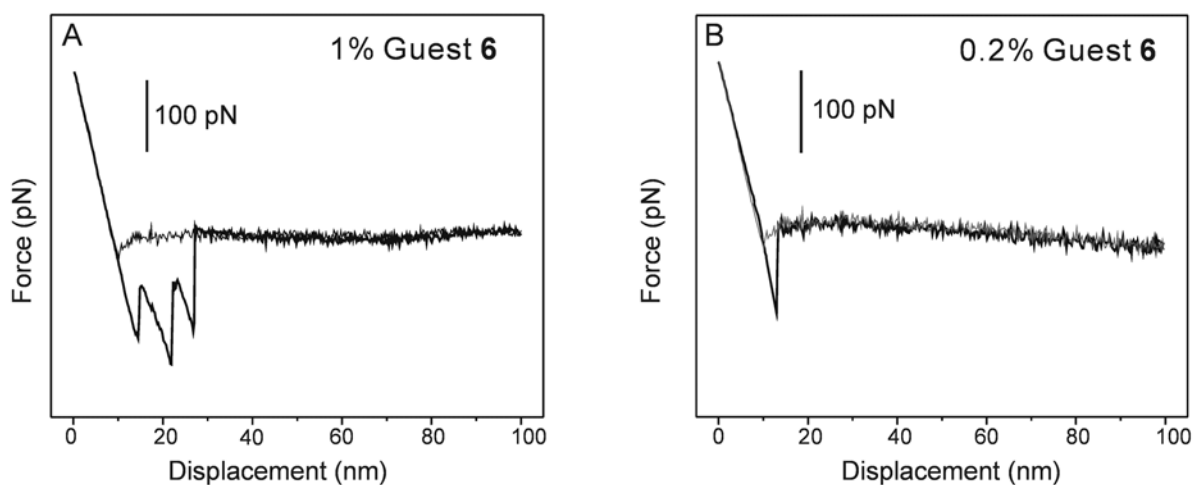


Figure 3.1. Force-displacement curves for the interaction of (A) 1% adamantane **6** and (B) 0.2% adamantane **6** and -CD SAMs **1** on Au(111) measured in MilliQ water (formal loading rate ~ 20 nN/s, temperature = 301 K).

The analyses of the rupture events observed for the interactions between -CD and **6** for two different coverages on the tip are summarized in Figure 3.2. The presence of multiple peaks in the rupture force histograms is observed for higher coverage of the guest on the tip. The local maxima occur at 100 pN and 197 pN, determined from fast Fourier transform (FFT) smoothed force histograms. The peaks are attributed to the rupture of one and two independent adamantane - -CD complexes, respectively. Based on three independent data sets, the mean value of the force quantum of 102 ± 15 pN was determined for the single adamantane - -CD complex rupture force.

The multimodal distribution of rupture forces is contrasted by the f-d data measured between AFM tips functionalized with pure C2OH SAMs and -CD SAMs, which can be described by a single broad distribution of forces centered at ~ 300 pN^{45,46} (the mean rupture force in this experiment, in which about 30 ~ 50 molecules interact, depends linearly on the tip radius).^{45,46}

For lower coverages of **6**, the distribution of the observed single pull-off events showed a single broad maximum at around 105 pN (Figure 3.2B). This value is in good agreement with the first local force maximum observed at high coverage of adamantane on the tips (Figure 3.2A) and hence is attributed to the rupture force of a single HG complex. The width of the peak, however, suggests that there is a significant contribution of a higher force component, most likely the rupture of two independent adamantane – β -CD complexes (~ 200 pN).

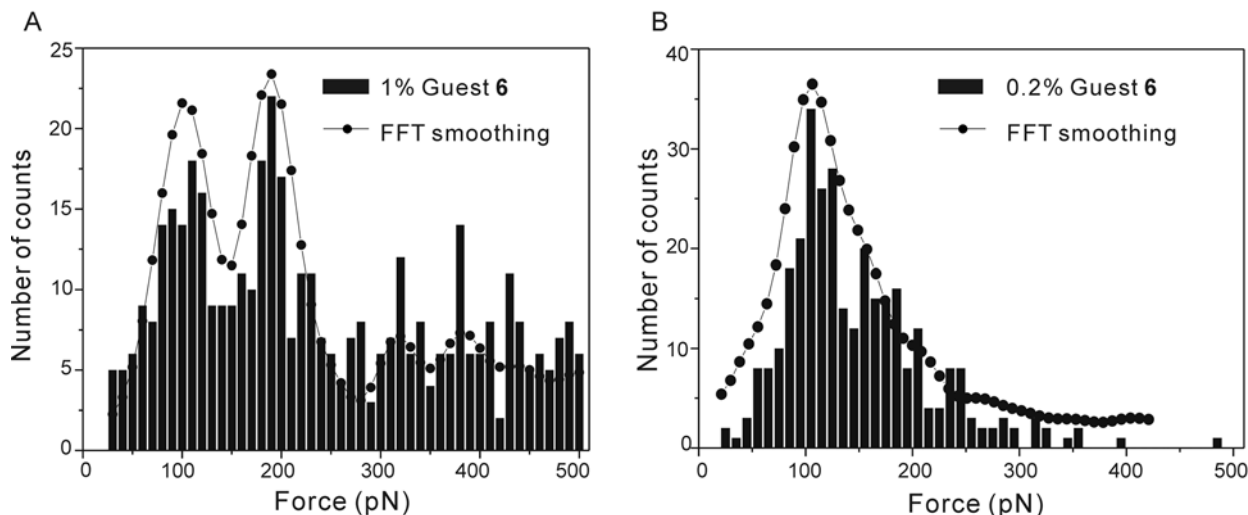


Figure 3.2. Statistical analyses of pull-off events observed for (A) multiple and (B) single pull-off events between monolayers **1** and guest **6**. The lines correspond to FFT smoothed data.

We reproducibly observed multiple pull-off events in the case of high (1%) coverage of guest molecules on AFM tips and predominantly single pull-off events in the case of low (0.2%) coverage of molecules on the tip. Thus, the number of resolved pull-off events, and hence interacting β -CD and guest moieties **6** qualitatively scales with the composition of the SAM on the functionalized AFM tips. In the case of low guest coverage on the tip, the predominant peak in the histogram is consistent with the detection of single unbinding events. These observations support the interpretation that the individually resolved pull-off events can indeed be attributed to specific host-guest complex rupture events.

In agreement with previous reports,^{37,38,47} the quantized force was unaffected by the (formal) loading rate (using linkages with the same stiffness), which was varied over several orders of magnitude in the range of $10^3 - 10^5$ pN/s, for tips covered with mixed SAMs of C2OH containing 1% of **6**. Thus, the rupture forces were probed by force spectroscopy under conditions of quasi-thermodynamic equilibrium. This interpretation implies that the rupture forces of HG complexes of different guests with different K on β -CD SAMs increase with increasing equilibrium constants.

3.3.2 Rupture Forces of η -CD – Anilyl and Toluidylthiol HG Complexes

In order to verify the above mentioned assertion that the single HG complex rupture forces scale with equilibrium complexation constants in this particular system of η -CD SAMs as host layer, SMFS measurements of the weakly binding guests **2** and **3** were carried out on SAMs of **1**. Force-displacement curves for these adsorbates (conc. 2%) also showed the characteristic multiple pull-off events (no data shown). All pull-off forces determined from individually resolved events were plotted in histograms, as shown in Figure 3.3. FFT smoothing of the force histograms for tips functionalized with **2** and **3** affords periodic distributions of forces, regardless of the bin size, with force quanta of 39 ± 15 and 45 ± 15 , respectively.

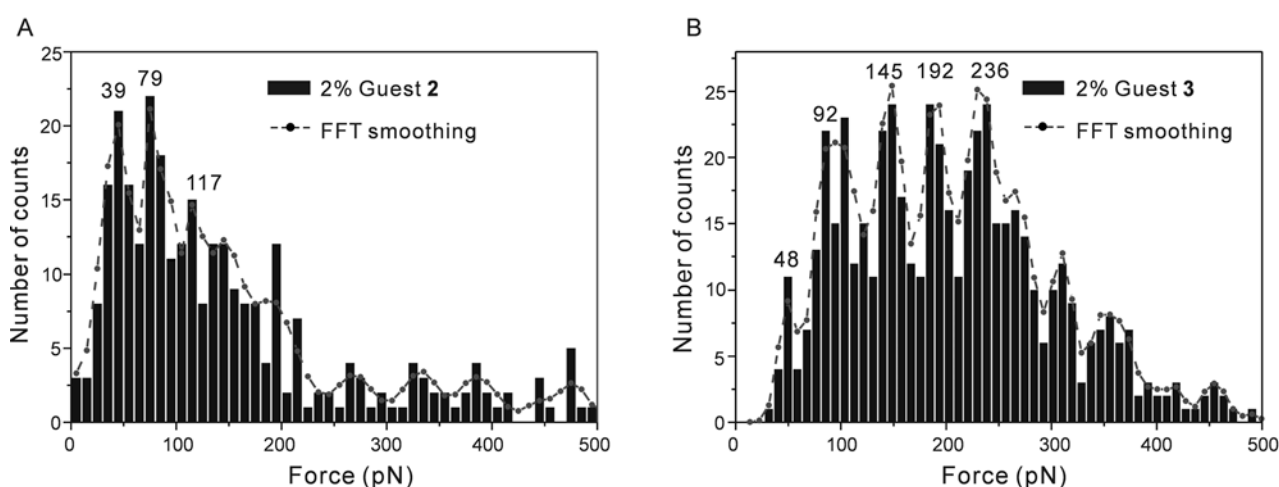


Figure 3.3. Histograms for the interaction between tips coated with (A) 2% of **2** and (B) 2% of **3** and substrates with SAMs of **1**. The curves correspond to FFT smoothed data.

Similar to the previously discussed HG pairs,^{37,38} these force quanta are attributed to the rupture force of individual supramolecular η -CD – guest complexes. The forces are significantly lower than those determined for the stronger binding guests. As shown in Table 3.2, the observed forces scale with the previously determined complexation constants for the particular binding geometry and complex type.

Table 3.2. The interaction of guests **2-6** with monolayers of **1** and with η -CD in solution.^{37,41}

Guests	$H\#M^{-1}$) monolayers 1	$H\#M^{-1}$) η -CD solution	Rupture forces (pN)
2	--- ^a	5.0×10^2	39 ± 15
3	--- ^a	1.0×10^3	45 ± 15
4	9.9×10^3	1.0×10^4	55 ± 10 ^b
5	2.6×10^4	3.0×10^4	89 ± 15 ^b
6	5.7×10^4	6.8×10^4	102 ± 15

^a Low solubility and weak interactions with the η -CD SAM did not allow accurate measurements of the thermodynamic parameters for this guest. ^bFrom ref 37 and 41.

The correlation of rupture forces and equilibrium complexation constants is also evident from Figure 3.4. Since adamantane is the strongest binding guest known for β -CD in solution, the single HG complex rupture force can be considered to be the highest (under the conditions used). The utilization of multiple parallel interactions (multivalency) is a concept to overcome this limited stability (cf. section 3.5) in the types of HG complexes studied.

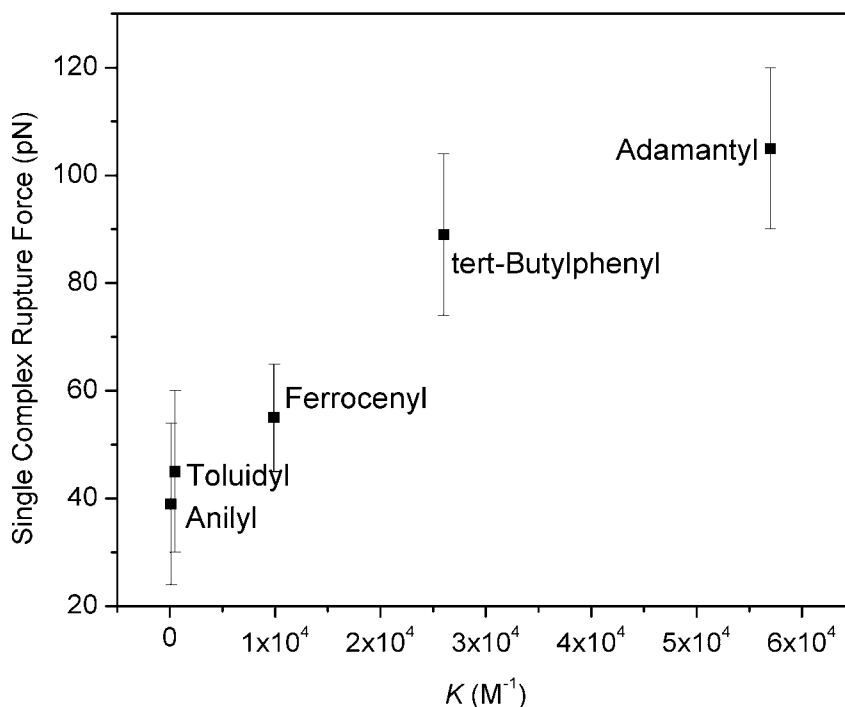


Figure 3.4. Correlation of individual unbinding forces and complexation constants K .

3.4 Model of the Unbinding Forces and Comparison to Experimental Data

In order to theoretically derive a relation between G° and the HG complex rupture force $F_{\text{pull-off}}$ for an individual host-guest pair, a model** based on a Lennard-Jones potential (LJP)^{48,49} has been developed by Huskens and Reinhoudt *et al.*^{41,44} From the model it is possible to calculate the dependence of the probability for pull-off $p_{\text{pull-off}}$, and thus of the pull-off force on the Gibbs free energy. This dependence can be compared with the experimental data obtained previously, including the data reported above in section 3.3.

The dependence of pull-off forces on G° was derived from the model as $F \propto 32.60 \Delta \sqrt{4 + G^5} 2.239$ or $F \propto 31.76 \Delta \sqrt{4 + G^5} 2.103$, for two different integration approaches, namely spherical and cylindrical integration, and is shown in Figure 3.5 (details of

** Expanding on the approach proposed by Hansma and co-workers⁴⁸ for measuring interaction potentials, Willemsen *et al.*⁴⁹ demonstrated that the total potential can be derived from the probability distribution of the tip position by monitoring the Brownian movement of an AFM tip in a potential well. The total potential consists of the sum of the harmonic cantilever potential and the tip-surface interaction potential, for details see section 3.8.

the model can be found in section 3.8). The experimentally determined values of 39 ± 15 , 45 ± 15 , 55 ± 10 , 89 ± 15 , and 102 ± 15 pN for the five host-guest complexes are shown in Figure 3.5 as well. The theoretically derived square root dependence of the pull-off force with the Gibbs free energy may be understood from the fact that a deeper potential well can be compensated by a square root change in the AFM tip position, due to the dependence of the potential energy of the cantilever on the deflection (Equation 3.4 and 3.5).

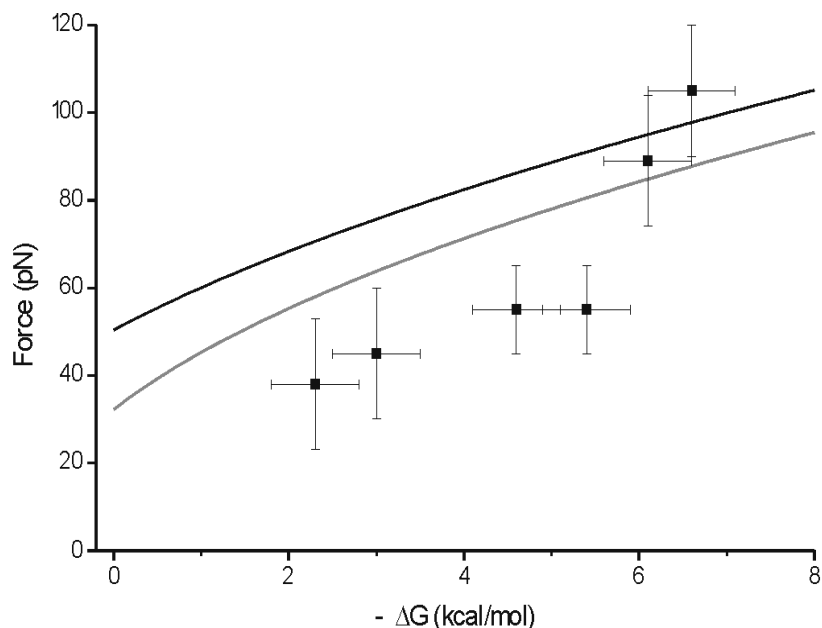


Figure 3.5. Experimental pull-off forces vs. $-\Delta G^\circ$ and calculated square root functions for spherical (equation 3.2, black line) and cylindrical integration (equation 3.3, gray line). For ferrocene two $-\Delta G^\circ$ values are reported with the same force value, due to different $-\Delta G^\circ$ measured for different model compounds.⁴¹

In Figure 3.5 it can be seen that the prediction based on the model agree well in terms of order of magnitude of the individual rupture forces, as well as the general trend of increasing rupture force with increasing $-\Delta G^\circ$. The integration volume of the cylindrical type improves the fit to the experimental data as compared to the spherical type, indicating that the assumption of a linear dissociation pathway for a guest linked to the AFM tip describes more accurately the events occurring at the molecular level. Thus, in thermodynamic quasi-equilibrium situations, the experimental data agree well with the equilibrium model that is based on the evaluation of the potential energy landscape of tip-surface interactions.

3.5 Probing Host-Guest Complex Rupture Forces for Multivalent Interactions by SMFS

In nature, the combination of multiple weak interactions between entities plays a central role in many molecular recognition processes. Although the corresponding phenomenon of

multivalency^{††} is a widely studied topic within the field of biochemistry, where numerous model systems with varying receptor topologies have been studied,⁵⁰⁻⁵⁶ the thermodynamic and kinetic characteristics associated with multivalent interactions are poorly understood. Whitesides *et al.*⁵⁷ have classified three different classes of polyvalent interactions, which are termed positively cooperative (synergistic), noncooperative (additive), or negatively cooperative (interfering), respectively.^{‡‡}

For the design and application of multivalent ligands in nanofabrication at surfaces, a fundamental understanding of multivalent interactions is crucial. Recently, the association constant (K_{divalent}) of a complex of bis-adamantly guest molecules and -CD (immobilized on surfaces as SAMs) was found to be $\sim 10^{10} \text{ M}^{-1}$, which is more than five orders of magnitude higher than the individual interaction ($\sim 5.7 \times 10^4 \text{ M}^{-1}$) and three orders of magnitude higher than the corresponding divalent interaction of guest molecules with CD in solution ($\sim 10^7 \text{ M}^{-1}$), respectively.⁵⁸⁻⁶⁰ Based on the model described above (neglecting the fact that the model is developed for *individual interactions*), we could predict a rupture force of the divalent complex of 120 ~ 130 pN. However, the magnitude of K suggests that the lifetime of a complex is of the order of 10 s.^{§§} Therefore, the unbinding is very likely *not* probed under quasi-thermodynamic equilibrium conditions. Due to the expected loading rate dependence this estimate would be an underestimate.

In order to probe the effect of multivalent interactions in bis-adamantane- -CD host-guest complexes on the single host guest complex rupture forces, the rupture forces of individual guest molecules **12** (with two adamantyl end groups, Figure 3.6) and -CD **1** immobilized in SAMs on Au(111) in aqueous medium were measured by force spectroscopy (Scheme 3.3).

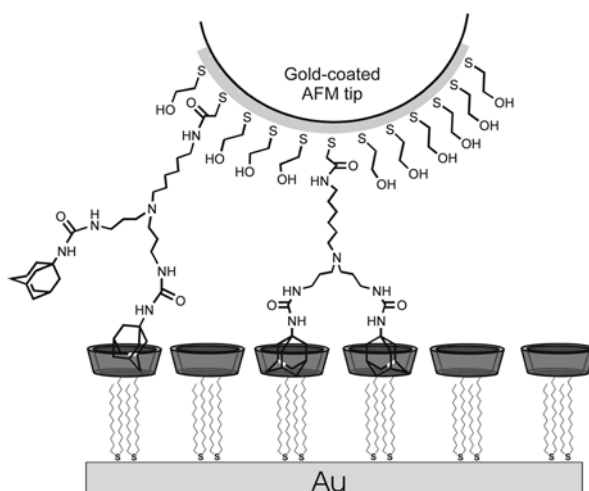
^{††} Multivalency denotes the simultaneous binding of multiple ligands on one entity (a molecule, a surface) to multiple receptors on another.⁵⁷

^{‡‡} A monovalent ligand-receptor interaction occurs with a free energy change $\div G^{\text{mono}}$. The average free energy of interaction between an Nth-order ligand moiety and the receptor moiety in a polyvalent interaction is $\div G_{\text{avg}}^{\text{poly}}$. The values of the corresponding complexation constants K are:

$$K_N^{\text{poly}} \mid \mid K_{\text{avg}}^{\text{poly}} \mid \mid K^{\text{mono}} \mid \mid \left(\div G_{\text{avg}}^{\text{poly}} \mid \mid \zeta \div G^{\text{mono}} ; N \div G_{\text{avg}}^{\text{poly}} \mid \mid \div G_N^{\text{poly}} \mid \mid \zeta N \div G^{\text{mono}} \right).$$

The definition of ζ follows the convention for the degree of cooperativity. One example of a positively cooperative polyvalent interaction ($\zeta > 1$) may be the association of pentameric cholera toxin with GM₁, an oligosaccharide portion of the GM₁ ganglioside. The binding of a bivalent antibody to ligands that are densely packed on a biological surface – such as a cell, a virus, or a solid support – is an example of negatively cooperative (or interfering; $\zeta < 1$) polyvalency.⁵⁷

^{§§} The decomplexation rate constant is estimated to be 10^{-1} s^{-1} based on the assumption of diffusion-controlled complexation (constant $\sim 10^9 \text{ (M s)}^{-1}$). Thus the binding processes occur on a time scale is 10 s.



Scheme 3.3. Schematic illustration of different unbinding behaviors of **12** immobilized on an AFM tip with SAMs of **1** on gold. In principle, the bis-adamantane derivative may interact with the -CD SAM with both adamantane units or only with a single adamantane.

The *f*-*d* curves obtained using tips with 1% guest molecules **12** showed multiple pull-off events upon retraction of the sample from the tip. The statistical analysis of the pull-forces is shown in Figure 3.6. For a coverage of 1% of **12** on the AFM tips, the distribution of rupture forces obtained from multiple pull-off events with a loading rate of ~ 20 nN/s showed a maximum around 105 pN and a second broad maximum at ~ 300 to 400 pN.

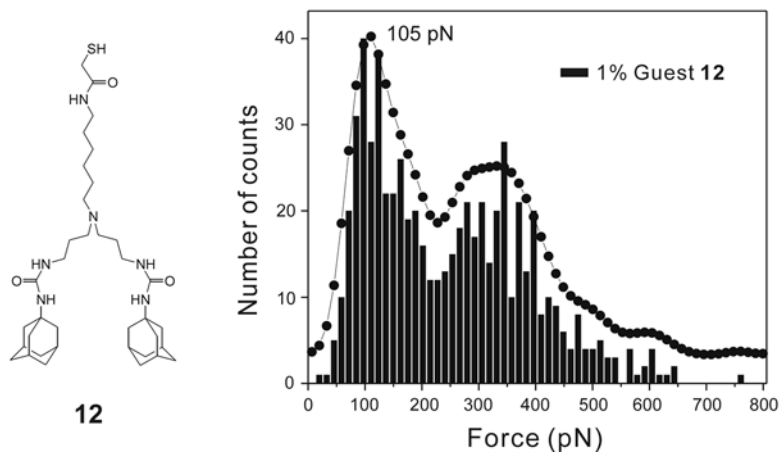


Figure 3.6. Left: Structure of bis-adamantyl guest **12**. Right: Statistical analyses of observed rupture forces of pull-off events between SAMs of **1** and 1% guest **12** on AFM tip. The curve corresponds to FFT smoothed data.

The force of 105 pN agrees well with the rupture force of single adamantanyl – -CD complexes, which is consistent with the interpretation that there may exist a fraction of singly bound (or singly unbound) adamantane units (Scheme 3.3). The peak observed is too broad in order to detect a (possibly present) peak at 120 – 130 pN as predicted above. Instead, the comparison of Figures 3.2 and 3.6 shows that the only significant difference between the data sets for monovalent (**6**) and divalent (**12**) adamantane guests is the mentioned broad peak at ~ 300 to 400 pN.

Following the theoretical considerations of Evans and coworkers,^{61,62***} the most probable rupture force for a pair of mechanically coupled guests can be calculated based on the rupture force observed for the single HG complex. For the interaction η -CD - adamantane this would lead to rupture forces of 170 pN for a pair of divalent interactions (N=2) and 330 pN for two pairs of divalent interactions (N=4).

The shoulder observed in Figure 3.6 at \sim 180 pN and the broad maximum around 300 pN are consistent with the values expected for one pair and two pairs of (divalent) η -CD - adamantane interactions, respectively, and hence may be tentatively attributed to the rupture force of one and two divalent complexes, respectively. As mentioned, such a pronounced maximum was absent in all experiments with monovalent adamantane **6** (Figure 3.2).

In principle, we expect that monovalent and divalent interactions could be differentiated in loading rate dependent measurements, as the individual interactions of **1** and a single adamantane are loading rate independent in contrast to our expectation for the divalent case. Most importantly, we observe clearly a contribution of single (monovalent) adamantane - η -CD interactions at \sim 105 pN, and hence multiples of this rupture force should also occur at \sim 220 and \sim 330 pN as these HG complexes are probed in quasi-thermodynamic equilibrium (see Figure 3.2 A). In addition, we would expect to see contributions of rupture force values of two or more individual *divalent* interactions (170 and 330 pN, see also Scheme 3.3), as well as those attributed to simultaneous unbinding of the observed individual *and* the assumed divalent complexes. Due to the absence of a clear criterion for single HG complex detection (e.g. stretching of an oligomeric spacer, see Chapter 5), these different cases cannot be differentiated at present.

3.6 Conclusions

The rupture forces of individual HG complexes between η -cyclodextrin SAMs and several surface-confined guests were determined in aqueous medium by SMFS. The analysis of the histograms revealed periodic distributions of forces, which are characteristic for each guest. The observed force quanta of 39 ± 15 , 45 ± 15 , 89 ± 15 , and 102 ± 15 pN determined for anilyl, toluidyl, tert-butylphenyl, and adamantyl guests, respectively, were attributed to the rupture of single HG complexes. These results, in combination with previous reports,^{37,38,47} and in particular the absence of loading rate dependences, indicate that the HG complex rupture forces

*** $f^* \sim N [f_{\text{single}} + 4f_{\eta} \ln(f^*/f_{\eta})]$, N is the number of parallel bonds, here N=2, f is the thermal force (for details see ref 62) here $f = 5.7$ pN, and $f_{\text{single}} = 105$ pN.

were probed under quasi-thermodynamic equilibrium. The force quanta and the thermodynamic parameters of the inclusion complexes, as determined by ITC and SPR measurements, followed the same trend. The experimental data agrees well with an equilibrium model based on the evaluation of the potential energy landscape of tip-surface interaction. Finally, the unbinding forces measured for multivalent interactions using a bis-adamantyl-derivatized guest were consistent with theoretical considerations by Evans and coworkers.

3.7 Experimental

Materials and methods. Molecules **1** ~ **12** were kindly supplied by the SMCT group of the MESA⁺ Institute for Nanotechnology. 2-hydroxy-ethanethiol (C2OH) was purchased from Aldrich and used without any further purification. Synthesis of **1** ~ **12** has been reported in ref [41,42], as well as the preparation and characterization of SAMs of **1**. All solvents used in monolayer preparation were of p.a. grade.

AFM Tip Modification. V-shaped silicon nitride cantilevers with pyramidal tips (purchased from Digital Instruments (DI), Santa Barbara, CA) were coated with ca. 2 nm Ti and ca. 75 nm Au by evaporation in high vacuum (Balzers) at SSENS b.v. (Hengelo, the Netherlands). The tips were functionalized as described previously in 1 mM ethanolic solutions containing mixtures of C2OH and a guest adsorbate **2**, **3**, or **6** (0.2, 1, and 2%), for 16h at rt.

AFM Measurements and Analysis. The AFM measurements were carried out with a NanoScope III multimode AFM (DI) utilizing a 10 σ m (E) scanner and a DI liquid cell on SAMs of **1** on atomically smooth Au(111).⁶³ The calibration of the AFM scanner in the z-direction was carried out using a set of three vertical calibration standards (TGZ 01 - 03) with step heights of 25.5, 104, and 515 nm, respectively (Silicon-MDT, Moscow, Russia). The cantilever spring constants (in the range of 0.05 - 0.10 (\pm 0.012) N/m) were calibrated using the thermal noise method.^{64,65} Force-displacement (f-d) curves were recorded in Milli-Q water at different positions on the sample surface. The loading force was kept below 500 pN. Each individually resolved pull-off event with a rupture force above the noise level of the freely vibrating cantilever (ca. 15 pN) was included in the analysis. The data were plotted in histograms, which were subsequently subjected to fast Fourier transform (FFT) filtering in order to determine the center positions of the local maxima observed. It should be mentioned that the procedure results in local maxima positions, which are independent of the bin size of the histogram.

Isothermal Titration Calorimetry.^{41,42} Titrations were performed at 25 °C using a Microcal VP-ITC titration microcalorimeter, as described in detail^{41,42}. The titrations were

analyzed using a least squares curve fitting procedure. Control experiments involved addition of η -cyclodextrin to water and addition of water to a guest solution.

Surface Plasmon Resonance.^{41,42} SPR measurements were performed in a two-channel vibrating mirror angle scan set-up based on the Kretschmann configuration, described by Lenferink *et al.*⁶⁶

3.8 Appendix

The assumptions, major steps of the calculation and relevant results of a model developed by Huskens, Reinhoudt *et al.*⁴¹ are summarized below.

3.8.1 MD Simulations⁴¹

Coordinates for the native α -CD were derived from its X-ray structure and the water molecules were removed. All calculations were done with Quanta/CHARMm 24.0 and refer to an unsubstituted ferrocene molecule. The cyclodextrin was charged with the charge template method and excess charge was smoothed over non-polar carbons and hydrogens. The ferrocene was treated as a rigid body by applying large harmonic potentials between all carbon-iron pairs. The system was heated to 300 K in 5 ps, followed by equilibration of 10 ps, after which the MD (NVE ensemble, no systematic deviation from 300 K) was performed for 100 ps. During the simulation the non-bonded list was updated every 20 time steps with a cutoff of 14 Å. The van der Waals interactions were treated with a switch function between 10 and 13 Å, whereas the shift function was applied to the electrostatic interactions (cutoff 13 Å). The time step was 1 fs, with the SHAKE algorithm placed on the hydrogens. Coordinate sets were saved regularly and used for subsequent data analysis. The interaction energy between the cyclodextrin and ferrocene were averaged over all data sets.

Figure 3.7 shows the MD simulation data (markers) obtained for a linear dissociation trajectory of ferrocene from a cyclodextrin cavity, according to the procedure described above. These data points were fitted to the LJP function in a least squares optimization routine varying ϵ , s , and z_0 . The resulting optimized fit is shown as the continuous curve in Figure 3.7. Only the well width s (7.78 Å), which correlates well to the cavity depth of cyclodextrin (8 Å), is used further on in the theoretical probability description.

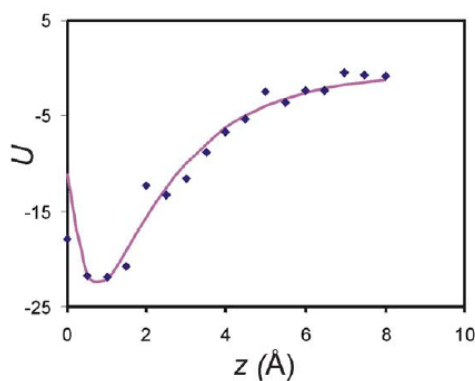


Figure 3.7. MD simulation data for the interaction energy of the dissociation of ferrocene along a linear dissociation trajectory perpendicular to the center of the cyclodextrin cavity (markers) and the fit to a LJP function (continuous line). (Adapted from ref 41.)

3.8.2 Details of the Model

The interactions of a η -CD cavity with a guest can be described by a potential energy well, the shape of which is approximated by a Lennard-Jones potential (LJP):

$$U_{LJP} = 4\kappa \left[\left(\frac{s}{2z_0} \right)^{12} - \left(\frac{s}{2z_0} \right)^6 \right] \quad 3.1$$

Here z represents the distance from the LJP minimum along the dissociation pathway, z_0 is an offset parameter with a value of $\sqrt[6]{2}s$ (assuring that the well minimum occurs at $z = 0$):

$U_{LJP}(0) = -\kappa$ and $\left. \frac{dU_{LJP}}{dz} \right|_0 = 0$, κ is the well depth, and s determines the width of the well. The

width of the well ($s = 7.78 \text{ \AA}$), which corresponds to the depth of the cyclodextrin cavity, is obtained from the MD simulation. For all other guest motifs employed in this study, we assumed the same well shape, *i.e.* s was kept constant, while κ was varied to account for changes in ΔG° .

A space integration of $U_{LJP}(z)$ allows one to correlate the depth of the well κ associated to each HG complex, to the corresponding ΔG° value, via the complexation constant K . In a first attempt, a relationship between the HG equilibrium constant K and the potential energy has been applied to simulate hydrophobic interactions and thus molecular recognition.^{67,68} This is based on the space integration of U_{LJP} with a radial dependence according to equation 3.2, where N_{av} is Avogadro's number. In our case the space integration over $z > 0$ represents a hemisphere above the η -CD cavity, while $z < 0$ represents the cavity interior (repulsive LJP interactions). This integration may not describe the 3D interaction dependence correctly since, as stated above, the pull-off trajectory of the guest out of the cavity can better be assumed to be linear. Therefore in an alternative, second integration approach, the sampled volume has been restricted to a cylinder defined by the area available for in-plane movement of the guest in the cavity ($A_{CD} = \phi r^2$ with $r =$

2Å) and the linear trajectory perpendicular to this area along which the guest is dissociated (equation 3.3).

$$K \mid 2\phi N_{av} \int_{z_{\leftarrow}}^{z_{\leftarrow}^*} z^2 e^{AU_{LJP}/RT} dz \quad 3.2$$

$$K \mid N_{av} A_{CD} \int_{z_{\leftarrow}}^{z_{\leftarrow}^*} e^{AU_{LJP}/RT} dz \quad 3.3$$

Employing $\Delta G^\circ \mid 4RT \ln K$ led to the following linear relationships: $\Delta G^\circ \mid 0.93\kappa$ 4.15 and $\Delta G^\circ \mid 0.97\kappa$ 2.79 for the spherical and the cylindrical integrations, respectively, with ΔG° and κ in kcal mol⁻¹. The ΔG° values of the HG systems studied here vary between 2.3 and 6.4 kcal mol⁻¹, as determined from ITC and SPR measurements, thus κ ranges from -6.6 – -11.4 kcal mol⁻¹ or from -5.3 – -9.5 kcal mol⁻¹, respectively.

The cantilever potential U_{tip} is described by a harmonic potential (equation 3.4)

$$U_{tip}(z) \mid \frac{1}{2}k\Delta z(z - z_I)^2 \quad 3.4$$

where $\Delta z = z - z_I$ is the cantilever deflection and z_I represents the tip position, i.e. the position of the minimum of the cantilever parabola potential, which is controlled by the piezo movement.

The total potential energy of the system can now be derived as the sum of the modified LJP, describing the HG complex, and the harmonic potential describing the cantilever potential:

$$U_{tot}(z) \mid U_{complex}(z) + 2U_{tip}(z) \quad 3.5$$

Changes in the tip position are reflected in the total potential energy curve. Initially, when the piezo has not yet been moved and no cantilever displacement occurred ($\Delta z = 0$), the position of the minima of $U_{complex}$ and U_{tip} coincide and only one minimum for U_{tot} is observed (Figure 3.8A). Retraction of the piezo (in our setup z_I was recorded in steps of 2 Å) is translated into a cantilever deflection ($\Delta z > 0$) with a shift of the parabola potential minimum z_I to the right, thus raising the minimum observed at $z = 0$ for the total potential energy curve (Figure 3.8B). Up to a certain point, only one minimum exists, called “contact”, in which the tip stays in contact with the sample while the HG complex may rapidly dissociate and reassociate. It can also be seen in Figure 3.8 that this “contact” minimum stays at the same position, i.e. at $z = 0$, owing to the larger stiffness of the complex, so that the observed deflection Δz is equal to z_I . Near the point where a pull-off event takes place, a second minimum, called “out-of-contact”, appears and quickly becomes the predominant one (Figure 3.8D). In this minimum, the tip is not in contact with the surface, and the HG complex is dissociated. In Figure 3.8B to E the change in tip position z_I is simulated by four sequential energy potential curves, with $z_I = 6, 8, 10,$ and 12 Å respectively, corresponding to consecutive data points in a (simulated) pull-off experiment. They show the corresponding changes in U_{tot} , and describe the transition from the “contact” to the “out-of-contact” state as the most energetically favorable situation.

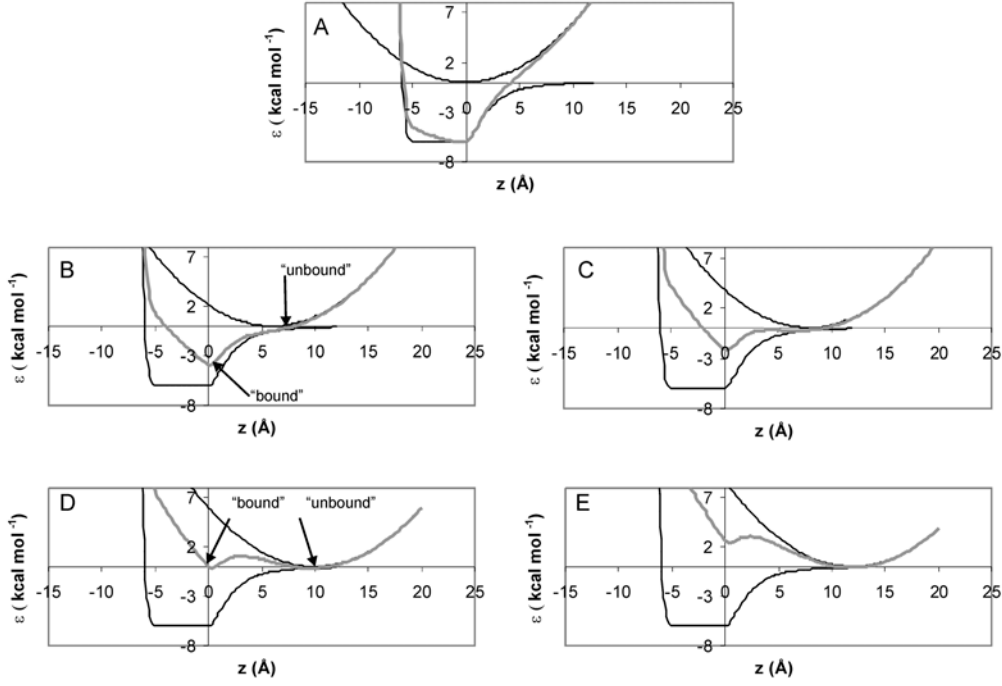


Figure 3.8. Total energy description: U_{tip} (parabola), U_{complex} (black line), and U_{tot} (gray line). The piezo displacement $\neq z$ from A to E is respectively 0, 6, 8, 10 and 12 Å z ($\kappa = 6 \text{ kcal mol}^{-1}$). (Adapted from ref 41.)

According to Boltzmann statistics, the relative probability $p(z)$ for the system to exist in situation $(z, U_{\text{tot}}(z))$ is given by equation 3.6:

$$p_{\text{contact}} \propto e^{-4U_{\text{tot}}(z)/RT} \quad 3.6$$

In the case when two maxima are present, separated by a barrier which has a maximum at $z = z_{\text{bar}}$, the probability for the system to be the “contact” state, p_{contact} is given by equation 3.7, which is a function of z_1 .

$$p_{\text{contact}} \propto \frac{\int_{z_1}^{z_{\text{bar}}} p(z) dz}{\int_{z_1}^{\infty} p(z) dz} \propto \frac{\int_{z_1}^{z_{\text{bar}}} e^{-4U_{\text{tot}}(z)/RT} dz}{\int_{z_1}^{\infty} e^{-4U_{\text{tot}}(z)/RT} dz} \quad 3.7$$

$p_{\text{out-of-contact}}$ can be obtained from integrating $p(z)$ for $z > z_{\text{bar}}$, and $p_{\text{contact}} + p_{\text{out-of-contact}} = 1$.

Figure 3.9 shows p_{contact} as a function of z_1 for $\kappa = 10 \text{ kcal mol}^{-1}$. Here it is seen that p_{contact} drops from 1 to 0 in about 4 Å, *i.e.* within only 2 data points. The specific z_1 value, at which this occurs obviously depends on κ , but the shape of the curve hardly changes. A macroscopic pull-off event thus corresponds to one data point being in the “contact” state while for the next data point the “out-of-contact” state is observed, thus the chance, $p_{\text{pull-off}}$, to observe such a pull-off event can be defined as in equation 3.8.

$$p_{\text{pull-off}}(z_1) = p_{\text{contact}}(z_1) \times p_{\text{out-of-contact}}(z_1+2) = p_{\text{contact}}(z_1) \times (1 - p_{\text{contact}}(z_1)) \quad 3.8$$

The dependence of $p_{\text{pull-off}}$ with z_1 is also shown in Figure 3.9. Again, the step dependence of $p_{\text{pull-off}}$ with z_1 ensures that the pull-off event occurs at a specific data point and that no switching

back and forth between the “contact” and the “out-of-contact” states will be observed in the experimental setup used here, unless one were to detect data points for relatively long periods of time at all z_1 of a pull-off experiment, as was done and observed recently for another system.⁴⁹ The curve also shows that z_1 , for which the pull-off is observed, has a certain distribution (approx. ± 1.5 Å) for an identical HG complex probed under identical conditions, corresponding to a force variability of ± 10 pN.

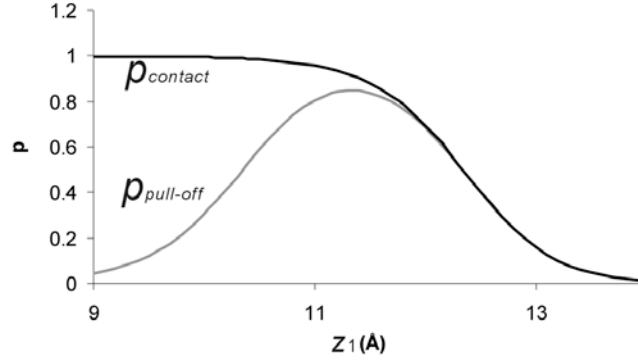


Figure 3.9. Plot of $p_{contact}$ (black line) and $p_{pull-off}$ (gray line) as a function of z_1 ($\kappa = 10$ kcal mol⁻¹) (Adapted from ref 41.).

Once the maximum pull-off probability is determined, the corresponding tip deflection is converted into the force exerted by the cantilever according to equation 3.9, thus determining the pull-off force value.

$$F_{pull-off} = k_{tip} \times \delta z_{max} \quad 3.9$$

3.8.3 Probability Description Using a Harmonic Potential Approximation

Alternative to the numerical integration of $p(z)$, using $U_{tot}(z)$, to give $p_{contact}$, as described above, a semi-analytical expression for $p_{contact}$ can be derived. Here, both the “contact” and “out-of-contact” minima are approximated by a harmonic potential according to equations 3.10 and 3.11:

$$U_{contact} | U_{contact,min} + \frac{1}{2} k_{complex} (z - z_{contact,min})^2 \quad 3.10$$

$$U_{outofcontact} | U_{outofcontact,min} + \frac{1}{2} k_{tip} (z - z_{outofcontact,min})^2 \quad 3.11$$

For well-separated minima, $z_{contact,min} = 0$ and $z_{outofcontact,min} = z_1$, while $U_{contact,min}$ and $U_{outofcontact,min}$ can be approximated by equations 3.12 and 3.13.

$$U_{contact} - U_{tot}(0) | 4\kappa \frac{1}{2} k_{tip} (z_1)^2 \quad 3.12$$

$$U_{outofcontact} - U_{tot}(z_1) | 4\kappa \left[\frac{s}{2z_0} \right]^2 - 4 \left[\frac{s}{2z_0} \right]^6 \quad 3.13$$

To approximate the stiffness of the HG system, a parabola ($U = a \times (z - b)^2 + c$) can be used to fit U_{tot} in proximity of the “contact” minimum, so that $k_{complex} = 2a$. The plot of the stiffness of the complex as a function of z shows a linear correlation leading to $k_{complex} = 23.81$ pN Å⁻¹, with U in kcal mol⁻¹, while $k_{tip} = 8$ pN Å⁻¹, as determined for the gold-coated tips experimentally. Since for our systems U ranges roughly from 5 to 12 kcal mol⁻¹, $k_{complex}$ may range from 125-300 pN Å⁻¹, which in all cases is much higher than the stiffness of the cantilever. It is also seen in the sequence of potential energy graphs (Figure 3.8) and the parabola fittings to the “contact” minima in these graphs that a 5 Å linker is already long enough to avoid any linker chain length dependence of the stiffness of the complex. Now, the probability of being in either minimum, describing the “contact” and the “out-of-contact” states, is governed by the Boltzmann distribution, where each is represented in approximation by its respective harmonic potential. The probability ratio is then given by equation 3.14.

$$\frac{P_{contact}}{P_{out\ of\ 4\ contact}} = \frac{\int_{z_{con}} e^{-4U_{con}(z)/RT} dz}{\int_{z_{coc}} e^{-4U_{coc}(z)/RT} dz} = e^{4+U/RT} \frac{\int_{z_{con}} e^{-4^{1/2}k_{complex}z^2/RT} dz}{\int_{z_{coc}} e^{-4^{1/2}k_{tip}z^2/RT} dz} = \sqrt{\frac{k_{tip}}{k_{complex}}} e^{4+U/RT} \quad 3.14$$

Here, $U = U_{contact,min} - U_{out-of-contact,min}$. The subsequent transformation into $p_{pull-off}$ and $F_{pull-off}$ follows as given in the above text. From this formula, it can be seen that the influence of $k_{complex}$, which is determined by the potential well width parameter s and the guest-dependent well depth parameter U , has only a small influence on $p_{contact}$, and thus on $p_{pull-off}$ and $F_{pull-off}$.

References:

- (1) Crane, H. R. *The Scientific Monthly* **1950**, 70, 376-389.
- (2) Lehn, J. M. *Angewandte Chemie-International Edition* **1990**, 29, 1304-1319.
- (3) Lehn, J. M. *Supramolecular Chemistry: Concepts and Perspectives*; VCH, Weinheim, 1995.
- (4) Bender, M. L.; Komiyama, M. *Cyclodextrin Chemistry*; Berlin: Springer, 1978.
- (5) Szejtli, J. *Cyclodextrin Technology*; Kluwer, Dordrecht, 1988.
- (6) Saenger, W. *Structural Aspects of Inclusion Compounds Formed by Organic Host Lattices* (Atwood, J. L.; Davies, J. E. D.; MacNicol, D. D. Ed.); Academic Press: London, 1984.
- (7) Wenz, G. *Angewandte Chemie-International Edition* **1994**, 33, 803-822.
- (8) Rekharsky, M. V.; Inoue, Y. *Chemical Reviews* **1998**, 98, 1875-1917.
- (9) Ueno, A.; Kuwabara, T.; Nakamura, A.; Toda, F. *Nature* **1992**, 356, 136-137.
- (10) Kuwabara, T.; Nakamura, A.; Ueno, A.; Toda, F. *Journal of the Chemical Society-Chemical Communications* **1994**, 689-690.
- (11) Bügler, J.; Engbersen, J. F. J.; Reinhoudt, D. N. *Journal of Organic Chemistry* **1998**, 63, 5339-5344.
- (12) Corradini, R.; Dossena, A.; Galaverna, G.; Marchelli, R.; Panagia, A.; Sartor, G. *Journal of Organic Chemistry* **1997**, 62, 6283-6289.
- (13) Kuwabara, T.; Takamura, M.; Matsushita, A.; Ueno, A.; Toda, F. *Supramolecular Chemistry* **1996**, 8, 13-15.
- (14) Henke, C.; Steinem, C.; Janshoff, A.; Steffan, G.; Luftmann, H.; Sieber, M.; Galla, H. J. *Analytical Chemistry* **1996**, 68, 3158-3165.
- (15) Mortellaro, M. A.; Nocera, D. G. *Journal of the American Chemical Society* **1996**, 118, 7414-7415.
- (16) van Dienst, E.; Snellink, B. H. M.; von Piekartz, I.; Engbersen, J. F. J.; Reinhoudt, D. N. *Journal of the Chemical Society-Chemical Communications* **1995**, 1151-1152.
- (17) Rojas, M. T.; Koniger, R.; Stoddart, J. F.; Kaifer, A. E. *Journal of the American Chemical Society* **1995**, 117, 336-343.

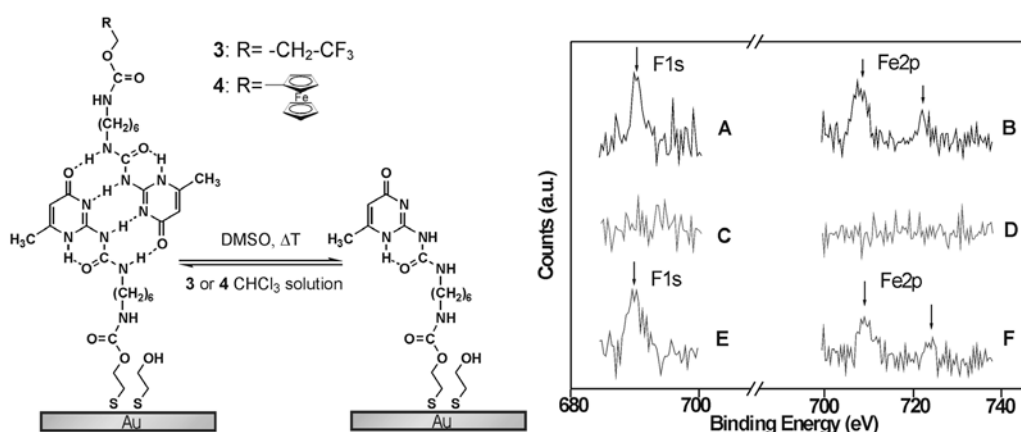
- (18) Binning, G.; Quate, C. F.; Gerber, C. *Physical Review Letters* **1986**, *56*, 930-933.
- (19) Smith, S. B.; Finzi, L.; Bustamante, C. *Science* **1992**, *258*, 1122-1126.
- (20) Ashkin, A.; Schutze, K.; Dziedzic, J. M.; Euteneuer, U.; Schliwa, M. *Nature* **1990**, *348*, 346-348.
- (21) Kishino, A.; Yanagida, T. *Nature* **1988**, *334*, 74-76.
- (22) Evans, E.; Ritchie, K.; Merkel, R. *Biophysical Journal* **1995**, *68*, 2580-2587.
- (23) Evans, E.; Ritchie, K. *Biophysical Journal* **1997**, *72*, 1541-1555.
- (24) Merkel, R.; Nassoy, P.; Leung, A.; Ritchie, K.; Evans, E. *Nature* **1999**, *397*, 50-53.
- (25) Strigl, M.; Simson, D. A.; Kacher, C. M.; Merkel, R. *Langmuir* **1999**, *15*, 7316-7324.
- (26) Simson, D. A.; Strigl, M.; Kacher, C. M.; Merkel, R. *Biophysical Journal* **1999**, *76*, A115-A115.
- (27) Simson, D. A.; Strigl, M.; Hohenadl, M.; Merkel, R. *Physical Review Letters* **1999**, *83*, 652-655.
- (28) Evans, E.; Ludwig, F. *Journal of Physics-Condensed Matter* **2000**, *12*, A315-A320.
- (29) Heymann, B.; Grubmuller, H. *Chemical Physics Letters* **1999**, *303*, 1-9.
- (30) Seifert, U. *Physical Review Letters* **2000**, *84*, 2750-2753.
- (31) Hintendorfer, P.; Raab, A.; Badt, D.; Smith-Gill, S. J.; Schindler, H. *Biophysical Journal* **1998**, *74*, A186-A186.
- (32) Strunz, T.; Oroszlan, K.; Schafer, R.; Guntherodt, H. J. *Proceedings of the National Academy of Sciences of the United States of America* **1999**, *96*, 11277-11282.
- (33) Grandbois, M.; Beyer, M.; Rief, M.; Clausen-Schaumann, H.; Gaub, H. E. *Science* **1999**, *283*, 1727-1730.
- (34) Zlatanova, J.; Lindsay, S. M.; Leuba, S. H. *Progress in Biophysics & Molecular Biology* **2000**, *74*, 37-61.
- (35) Clausen-Schaumann, H.; Seitz, M.; Krautbauer, R.; Gaub, H. E. *Current Opinion in Chemical Biology* **2000**, *4*, 524-530.
- (36) Rief, M.; Grubmuller, H. *ChemPhysChem* **2002**, *3*, 255-261.
- (37) Schönherr, H.; Beulen, M. W. J.; Bügler, J.; Huskens, J.; van Veggel, F. C. J. M.; Reinhoudt, D. N.; Vancso, G. J. *Journal of the American Chemical Society* **2000**, *122*, 4963-4967.
- (38) Zapotoczny, S.; Auletta, T.; de Jong, M. R.; Schönherr, H.; Huskens, J.; van Veggel, F. C. J. M.; Reinhoudt, D. N.; Vancso, G. J. *Langmuir* **2002**, *18*, 6988-6994.
- (39) General reviews on SAMs see Chapter 2; references 90 and 92.
- (40) Schönherr, H.; Paraschiv, V.; Zapotoczny, S.; Crego-Calama, M.; Timmerman, P.; Frank, C. W.; Vancso, G. J.; Reinhoudt, D. N. *Proceedings of the National Academy of Sciences of the United States of America* **2002**, *99*, 5024-5027.
- (41) Auletta, T.; de Jong, M. R.; Mulder, A.; van Veggel, F. C. J. M.; Huskens, J.; Reinhoudt, D. N.; Zou, S.; Zapotoczny, S.; Schönherr, H.; Vancso, G. J.; Kuipers, L. *Journal of the American Chemical Society* **2004**, *126*, 1577-1584.
- (42) de Jong, M. R.; Huskens, J.; Reinhoudt, D. N. *Chemistry-A European Journal* **2001**, *7*, 4164-4170.
- (43) Beulen, M. W. J.; Bügler, J.; de Jong, M. R.; Lammerink, B.; Huskens, J.; Schönherr, H.; Vancso, G. J.; Boukamp, B. A.; Wieder, H.; Offenhauser, A.; Knoll, W.; van Veggel, F. C. J. M.; Reinhoudt, D. N. *Chemistry-A European Journal* **2000**, *6*, 1176-1183.
- (44) de Jong, M. R. *Cyclodextrins for Sensing*, Ph. D. Thesis, page 109; University of Twente: Enschede, 2001.
- (45) Frisbie, C. D.; Rozsnyai, L. F.; Noy, A.; Wrighton, M. S.; Lieber, C. M. *Science* **1994**, *265*, 2071-2074.
- (46) Noy, A.; Vezenov, D. V.; Lieber, C. M. *Annual Review of Materials Science* **1997**, *27*, 381-421.
- (47) Zou, S.; Zapotoczny, S.; de Jong, M. R.; Auletta, T.; Schönherr, H.; Huskens, J.; van Veggel, F. C. J. M.; Reinhoudt, D. N.; Vancso, G. J. *Polymeric Materials: Science & Engineering* **2003**, *88*, 453-454.
- (48) Cleveland, J. P.; Schaffer, T. E.; Hansma, P. K. *Physical Review B* **1995**, *52*, R8692-R8695.
- (49) Williams, P. M.; Moore, A.; Stevens, M. M.; Allen, S.; Davies, M. C.; Roberts, C. J.; Tandler, S. J. B. *Journal of the Chemical Society-Perkin Transactions 2* **2000**, 5-8.
- (50) Roy, R. *Current Opinion in Structural Biology* **1996**, *6*, 692-702.
- (51) Roy, R. *Glycoscience Synthesis of Substrate Analogs and Mimetics*, 1997; Vol. 187.
- (52) Davis, B. G. *Journal of the Chemical Society-Perkin Transactions 1* **1999**, 3215-3237.
- (53) Kiessling, L. L.; Strong, L. E.; Gestwicki, J. E. *Annual Reports in Medicinal Chemistry*, 2000; Vol. 35.
- (54) Lindhorst, T. K. *Host-Guest Chemistry*, 2002; Vol. 218.
- (55) Rojo, J.; Morales, J. C.; Penades, S. *Host-Guest Chemistry*, 2002; Vol. 218.
- (56) Houseman, B. T.; Huh, J. H.; Kron, S. J.; Mrksich, M. *Nature Biotechnology* **2002**, *20*, 270-274.
- (57) Mammen, M.; Choi, S. K.; Whitesides, G. M. *Angewandte Chemie-International Edition* **1998**, *37*, 2755-2794.
- (58) Mulder, A.; Auletta, T.; Sartori, A.; Del Ciotto, S.; Casnati, A.; Ungaro, R.; Huskens, J.; Reinhoudt, D. N. *Journal of the American Chemical Society* **2004**, *126*, 6627-6636.
- (59) Huskens, J.; Mulder, A.; Auletta, T.; Nijhuis, C. A.; Ludden, M. J. W.; Reinhoudt, D. N. *Journal of the American Chemical Society* **2004**, *126*, 6784-6797.
- (60) Mulder, A., Ph. D. Thesis, University of Twente, 2004.
- (61) Evans, E. *Annual Review of Biophysics and Biomolecular Structure* **2001**, *30*, 105-128.
- (62) Williams, P.; Evans, E. *Dynamic Force Spectroscopy: II Multipole Bonds*, 2003.
- (63) Schönherr, H.; Vancso, G. J.; Huisman, B. -H.; van Veggel, F. C. J. M.; Reinhoudt, D. N. *Langmuir* **1999**, *15*, 5541-5546.

Chapter 3

- (64) Hutter, J. L.; Bechhoefer, J. *Review of Scientific Instruments* **1993**, *64*, 3342-3342.
- (65) Sader, J. E. *Journal of Applied Physics* **1998**, *84*, 64-76.
- (66) Lenferink, A. T. M.; Kooyman, R. P. H.; Greve, J. *Sensors and Actuators B-Chemical* **1991**, *3*, 261-265.
- (67) Pangali, C. S.; Rao, M.; Berne, B. J. *Journal of Chemical Physics* **1979**, *71*, 2975-2981.
- (68) Jorgensen, W. L. *Accounts of Chemical Research* **1989**, *22*, 184-189.

Chapter 4

Tunable Surface Molecular Recognition of 2-Ureido-Pyrimidinone Moieties via Quadruple Hydrogen Bonds*



A substrate-immobilized molecular platform for the controlled immobilization and growth of supramolecular architectures was developed based on the self-complementary molecular recognition of the 2-ureido-4[1H]-pyrimidinone (UPy) moieties via quadruple hydrogen bonding. Two novel asymmetric UPy hydroxyalkane disulfides, as well as trifluoromethyl- and ferrocenyl-derivatized external pyrimidinone guests were synthesized. Self-complementary molecular recognition of the pyrimidinone moieties, mediated by a quadruple donor-donor-acceptor-acceptor (DDAA) array of hydrogen bonding sites, was studied in self-assembled monolayers (SAMs) on Au by exploiting the dependence of the dimerization constant on solvent and temperature. Depending on the choice of solvent and temperature, reversible supramolecular recognition between surface-immobilized adsorbates and external guests occurred, as shown by X-ray photoelectron spectroscopy (XPS), differential pulse voltammetry (DPV), atomic force microscopy (AFM) and surface plasmon resonance (SPR) methods. The tunable complex stability on surfaces renders these systems highly suitable for the construction of directionally defined surface-immobilized supramolecular architectures, and forms the basis for further investigations of the force-loading rate dependent crossover from thermodynamic quasi-equilibrium to non-equilibrium states (Chapter 5), as well as for the study of pyrimidinone-based supramolecular polymers at surfaces (Chapter 6).

4.1 Introduction

Self-assembly in biological systems frequently relies on the utilization of multiple non-covalent interactions to define structure *and* achieve functionality.^{1,2} Chief among the guiding principles is molecular recognition.¹⁻¹⁰ Based on the fundamental idea of exploiting weak, yet directional interactions, biology-inspired supramolecular architectures¹¹⁻¹³ at surfaces do not only

* The work described in this Chapter was published in the following articles: Zou, S.; Zhang, Z. H.; Förch, R.; Knoll, W.; Schönherr, H.; Vancso, G. J. *Langmuir* **2003**, *19*, 8618-8621. Schönherr, H.; Zou, S.; Zhang, Z.; Förch, R.; Knoll, W.; Vancso, G. J. *Polym. Prep.* **2003**, *44*, 489-490.

enhance the possibilities for fundamental studies, but can also be utilized in, for instance, (bio)sensor designs.^{14,15}

Owing to their strength, selectivity and directionality, hydrogen bonding interactions are involved in maintaining the integrity of biomolecular structure, information storage and transfer, replication and catalysis in living organisms.¹⁶ Thus H-bonds are among the most useful interactions in supramolecular chemistry. The strength of hydrogen bonding arrays (typically 12-120 kJ mol⁻¹), was exploited to create efficient host molecules for a range of biological guests in aqueous and non-aqueous environments.^{3,16,17} More recently, reversibly stimuli-responsive H-bonded “smart” materials,¹⁸ which change their properties in response to environmental changes, have drawn great attention in supramolecular chemistry, as well as in material science.

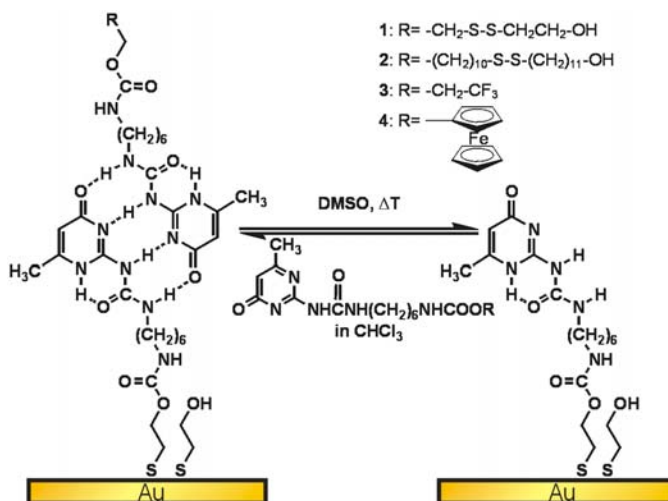
The reversibility and tunability of hydrogen bond formation is of fundamental importance in the dynamic environment within biological systems.^{16,19-21} Current challenges in synthetic systems include the increase of complexity of the assemblies and the enhanced control of stability versus reversibility.²² High dimerization constants of the recognition units are a prerequisite for the formation of defined, robust complexes or supramolecular polymer materials, as shown by many authors.^{18,23,24} For instance, large dimerization constants have been reported for 2-ureido-4[1H]-pyrimidinones (UPy) ($> 10^7$ M⁻¹ in CDCl₃).²⁴⁻²⁷ In recent years, there have been numerous reports on similarly strong dimerization of a variety of hydrogen bonding systems.²⁸⁻³¹ The self-complementary molecular recognition of the previously mentioned pyrimidinone moieties, which is mediated by a quadruple donor-donor-acceptor-acceptor (DDAA) array of hydrogen bonding sites, varies with solvent composition and temperature (for instance: K in 15% dimethyl sulfoxide (DMSO) in CDCl₃ ~ 51 M⁻¹; K decreases more than 10 fold when T increases from 298 K to 333 K in moist CDCl₃).^{26,27}

As shown in this chapter, dithioalkyl-substituted UPys³² can be immobilized on gold surfaces, where they show an enhanced dependence of complex stability on the solvent composition and temperature. These features allow one to change and control the complexation behavior of substrate-immobilized UPys over a broad range (Chapter 5), which renders this system a versatile molecular platform for the controlled immobilization or growth of complex supramolecular architectures, including supramolecular polymers (Chapter 6).

4.2 Molecular Recognition of UPys on Gold Surfaces

For the study of molecular recognition on solid substrates, we have synthesized two novel asymmetrically substituted UPy hydroxyalkane disulfides **1** and **2**, as well as labeled external

pyrimidinone guests comprising trifluoromethyl (**3**) and ferrocenyl (**4**) substitutions (Scheme 4.1). Self-assembled layers on Au were formed by spontaneous adsorption from solution and were characterized by standard techniques³³ (see also section 4.6). Depending on the choice of the solvent (e.g. CHCl₃ or DMSO), and hence complexation constant *K*, molecular recognition is expected at the interface, resulting in mono- and bi-layers of UPy derivatives on gold (Scheme 4.1).



Scheme 4.1. The complex formation of 2-ureido-4[1H]-pyrimidinone moieties at Au surfaces through quadruple hydrogen bonds can be conveniently controlled via solvent or temperature.

Recognition between surface-immobilized adsorbates and external guests (e.g. trifluoromethyl UPy **3** in solution is recognized by UPy disulfide **1** self-assembled on Au, denoted as [Au-**1** + **3**]) occurred efficiently in CHCl₃, as shown by various techniques. For instance, X-ray photoelectron spectroscopy (XPS) and differential pulse voltammetry (DPV)³⁴ show the presence of the labeled guest molecules.

X-ray photoelectron spectroscopy provided information about the composition of the self-assembled layers. XPS spectra exhibited peaks associated with C1s, F1s (or Fe2p), N1s, O1s and S2p. Peak positions were referenced to the binding energy of C1s electrons at 284.8 eV. The binding energies of N1s, O1s and S2p were found at 399.3 eV, 531.9 eV, 161.9 eV (bound sulfur), and 163.1 eV (unbound sulfur), respectively, in agreement with results reported in the literature for organic samples that contain these elements.^{33,35}

The recognition between SAMs of **1** on Au ([Au-**1**]) and external guests **3** and **4** in CHCl₃ leads to the dimeric complexes [Au-**1** + **3**] and [Au-**1** + **4**], respectively. The sequences of XPS spectra shown in Figure 4.1A, B, E, and F confirm the presence of the labels after complexation and recomplexation upon exposure of [Au-**1**] to **3** or **4** in CHCl₃, while their absence is observed after a thorough DMSO rinse (Figure 4.1 C and D).

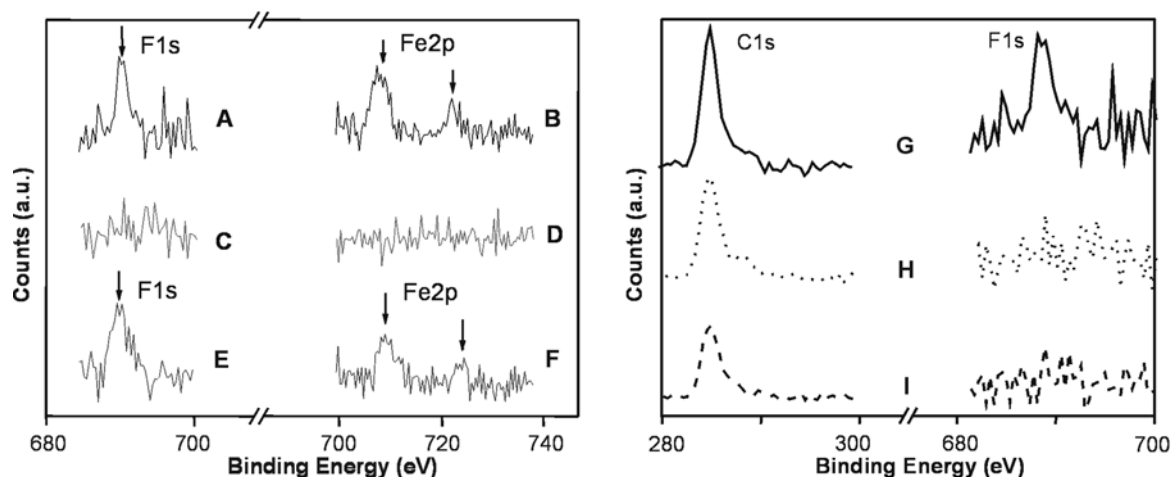


Figure 4.1. Left: High resolution scans of XPS spectra of (A) [Au-1 + **3**] in CHCl_3 and (B) [Au-1 + **4**] in CHCl_3 ; (C) and (D) after rinsing [Au-1 + **3**] and [Au-1 + **4**] with DMSO; (E) and (F) repeated recognition of **3** and **4** by [Au-1] to yield [Au-1 + **3**] and [Au-1 + **4**], respectively. Right: C1s (284.8 eV) and F1s (688.5 eV) signals in XPS spectra of (G) [Au-1+**3**] (solid lines); (H) after rinsing with DMSO, [Au-1] (dotted lines); (I) reference sample of SAM of 11-mercapto-1-undecanol on gold after treatment with **3** in CHCl_3 (dashed lines).

A DMSO rinse of [Au-1 + **3**] removes only the upper leaflet, i.e. the trifluoromethyl derivatized pyrimidinone of the bilayer-type assembly, as shown in Figure 4.1G and H (recorded before and after the rinse). The data confirmed that UPy moieties in CHCl_3 solution recognize surface bound UPys and that decomplexation occurred by rinsing with DMSO. The blanko experiments, performed by exposing **3** to a hydroxyalkanethiol SAM, showed the absence of non-specific adsorption of **3** onto 11-mercapto-1-undecanol layer (Figure 4.1I).

From the ratios of the atomic percentages of F and Fe with respect to the other characteristic elements, determined from the corresponding F1s (binding energy BE = 688.5 eV), and Fe2p peaks (BE = 708.5 eV and 723.2 eV), coverages of >45% and >50% (with respect to all thiolates), respectively, can be estimated.³⁵

The oxidation peak of the ferrocenyl-labeled guest **4** was also detected in differential pulse voltammetry (DPV) measurements,³⁶ thus confirming the molecular recognition of **4** to SAMs [Au-1] (Figure 4.2A). The peak consistently disappeared after a DMSO rinse (Figure 4.2B) and re-appeared after repeated recognition of **4** in CHCl_3 on layer [Au-1] (Figure 4.2C). The data presented in Figure 4.2D show that a blanko experiment of exposing **4** to a 11-mercapto-1-undecanol SAM. The absence of non-specific adsorption of **4** onto a hydroxyalkanethiol SAM was observed.

Hence, molecular recognition between [Au-1] and **3**, as well as **4**, in CHCl_3 proceeds efficiently. The upper limit of residual coverage of **4** after the DMSO rinse can be estimated as less than 4% from the XPS and DPV experiments (Figure 4.1 and 4.2).

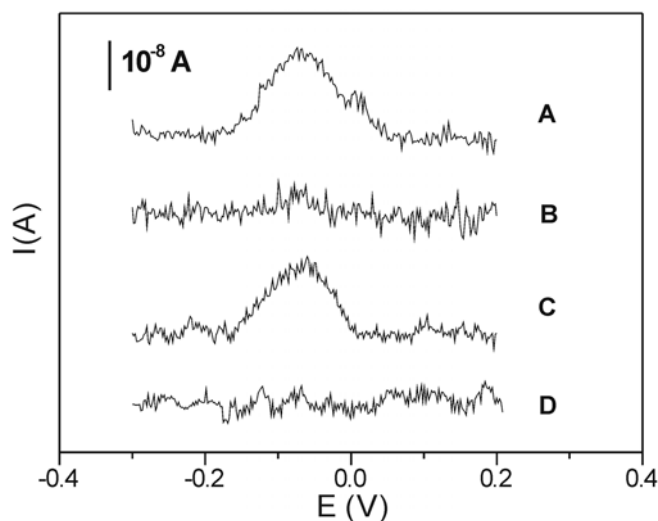


Figure 4.2. Differential pulse voltammograms (0.1 M NaClO₄, Hg/HgSO₄ reference electrode, pulse time 50 ms, interval time 200 ms, pulse height 10 mV) of (A) [Au-1 + 4] in CHCl₃, (B) [Au-1] (after rinsing with DMSO), and (C) repeated recognition of 4 by [Au-1] to yield [Au-1 + 4]. (D) Reference sample of SAM of 11-mercapto-1-undecanol on gold after treating with 4 in CHCl₃.

4.3 Complex Stability

In addition to directly determining the (optical) thickness of the layers and assemblies obtained, surface plasmon resonance (SPR)^{14,37} measurements were applied to confirm the reversibility of the complexation. The measured reflectivity curves (Figure 4.3) were modeled with a matrix-formalism based on the Fresnel equation^{38,39} and the layer thicknesses were thus obtained.

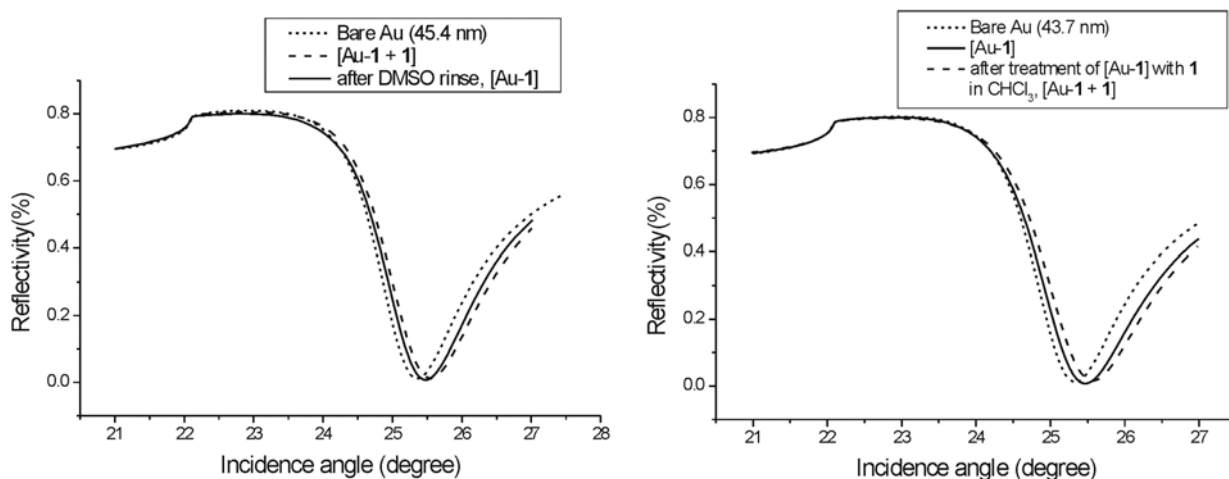


Figure 4.3. Reflectivity scans measured in SPR experiments. The minimum corresponds to the coupling angle. Left: Gold layer (dotted line); complex formed in CHCl₃ on Au, [Au-1+1] (dashed line); after rinsing with DMSO, [Au-1] (solid line). Right: Gold layer (dotted line); monolayer of 1 on Au assembled from DMSO, [Au-1] (solid line); complex formed on monolayer of [Au-1] by assembly from CHCl₃, [Au-1+1] (dashed line).

The thicknesses measured in air for the monolayers and bilayers treated with different guest moieties, assuming a refractive index of the organic layer of 1.50,^{33,37} are summarized in Table 4.1.

Table 4.1. Layer thicknesses measured by SPR against air.

Thickness (nm) of 1 assembled on Au (solvent)	Thickness (nm) of layers after DMSO rinse	Thickness (nm) of [Au- 1] treated with 3 ^a and 4 ^b in CHCl ₃
0.8 ± 0.2 (DMSO)	0.7 ± 0.2	1.5 ± 0.2 ^a 1.6 ± 0.2 ^b
1.4 ± 0.2 (CHCl ₃)	0.8 ± 0.2	1.6 ± 0.2 ^a 1.6 ± 0.2 ^b

The data show that UPy hydroxyalkane disulfide **1** assembled onto Au from DMSO forms a layer ([Au-**1**]) with a thickness of 0.8 ± 0.2 nm. By contrast, the assembly from CHCl₃ leads to a layer with twice the thickness. This observation is interpreted as follows: in CHCl₃ the pre-formed layer of [**1** + **1**] may self-assemble onto the gold surface and forms bilayer [Au-**1** + **1**], while in DMSO, only a monolayer [Au-**1**] is obtained. Consistently with this interpretation, the upper leaflet of the bilayer ([Au-**1** + **1**]) can be removed by a treatment of the layer in boiling CHCl₃ (Table 4.2); it can also be washed off by DMSO, but not by CHCl₃ at 25°C, which indicates that interfacial hydrogen bonding is indeed responsible for the molecular recognition. Consequently, external pyrimidinone guests with a spectroscopic label can be assembled onto the monolayer (see section 4.2).

Table 4.2. Layer thicknesses measured by SPR against air.

Thickness (nm) of 1 assembled on Au in CHCl ₃	Thickness (nm) of layers after deposition of sample in pure CHCl ₃ for 20 hours (25°C)	Thickness (nm) of [Au- 1 + 1] after treatment in boiling CHCl ₃	Thickness (nm) of [Au- 1 + 1] after DMSO rinse (25°C)
1.4 ± 0.2	1.6 ± 0.2	0.9 ± 0.2	0.8 ± 0.2

Interestingly, these dimeric complexes in layers of [Au-**1** + **n**] are stable in contact with pure CHCl₃ for longer than 20 hours without detectable loss of complexed guest (Table 4.2), compared to the half-lifetime of 170 ms of solution pyrimidinone dimers in CDCl₃.²⁷ We can conclude that surface-immobilization leads to a dramatic increase in the apparent lifetime of the dimeric UPy complexes and thus significantly enhances the control of the supramolecular architecture by variations of solvent and temperature. This increase in the apparent lifetime is partially related to an altered environment (dispersion forces and solvation) of the complexes near the SAM surface and, hence, a different activated complex of the dissociation reaction involved.

The SPR data shown in Table 4.2 support the observation that UPy hydroxyalkane disulfide **1** assembled onto Au from CHCl₃ leads to a bilayer structure ([Au-**1** + **1**]); the upper leaflet of the bilayer is not affected by a treatment in CHCl₃ overnight, but can be removed by a treatment of the layer in hot CHCl₃; it can also be washed off by DMSO.

Independently, we determined the thickness differences of the various architectures using contact mode atomic force microscopy (AFM).⁴⁰ Onto a microcontact-printed matrix of octadecanethiol (ODT),⁴¹ **1** was assembled from CHCl₃ in circular areas exposing bare Au. As seen in Figure 4.4, the height differences between the ODT matrix and the bilayer structure, as well as the different architecture obtained by rinsing with DMSO and re-assembly of **1**, are in good agreement with the layer thickness determined by SPR (Table 4.3) and are consistent with the proposed model (Scheme 4.1).

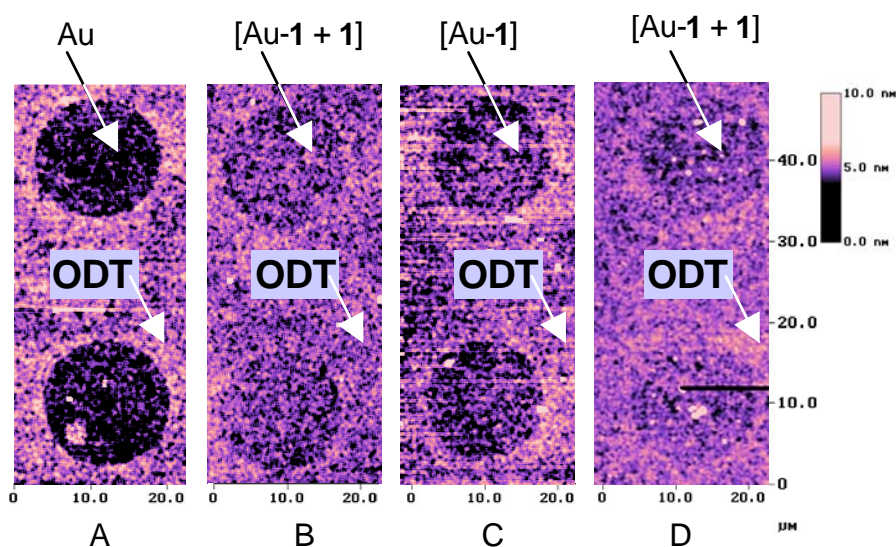


Figure 4.4. Contact mode AFM height images of microcontact printed layers; outside the circles: ODT; inside the circles: (A) bare Au (thickness 1.5 ± 0.3 nm), (B) [Au-**1** + **1**] (thickness 1.1 ± 0.2 nm), (C) after rinsing with DMSO, [Au-**1**] (thickness 0.7 ± 0.2 nm), (D) layer after exposure to **1** in CHCl₃, [Au-**1** + **1**] (thickness 1.1 ± 0.3 nm). The thicknesses of the assemblies were calculated from the differences of the mean heights with respect to ODT.

Table 4.3. Layer thicknesses measured by SPR and AFM.

	Thickness (nm) measured by AFM	Thickness (nm) measured by SPR
ODT	1.5 ± 0.3	-
[Au- 1 + 1]	1.1 ± 0.2	1.4 ± 0.2
[Au- 1]	0.7 ± 0.2	0.8 ± 0.2
[Au- 1 + n]	1.1 ± 0.3^a	1.6 ± 0.2^b

^a **n** = **1**; ^b **n** = **3**.

Thus, the combined labeling and thickness measurements confirm the scenario proposed in Scheme 4.1. Assembly of **1** on Au from DMSO yields monolayers, while layers formed from CHCl₃ resemble bilayers, i.e. hydrogen-bonded dimeric complexes of surface-immobilized **1**. In case of solutions containing a disulfide adsorbate and another substituted pyrimidinone in 1:15 stoichiometry, we also observe "bilayers" of the corresponding complexes.

4.4 Conclusions

SAMs of asymmetric 2-ureido-4[1H]-pyrimidinone-hydroxyalkane disulfide adsorbates on gold show efficient and controllable self-complementary molecular recognition of the pyrimidinone moieties mediated by quadruple hydrogen bonding sites. The observed surface-enhanced apparent dimerization constant can be tuned by solvent composition and temperature, which allows us to control the complex stability. This feature opens the possibility for the construction of more complex, directionally defined surface-immobilized supramolecular architectures, as well as for the study of pyrimidinone-based supramolecular polymers at surfaces and interfaces, which will be discussed in detail in Chapter 5 and 6.

4.5 Experimental

General Methods. The ¹H-NMR spectra were recorded on a Bruker AC 250 spectrometer (250 MHz). ¹H-NMR chemical shifts are given relative to residual CHCl₃ (7.25 ppm). Fast-Atom-Bombardment Mass-Spectrometry (FAB-MS) was carried out on a Finnigan MAT 90 Spectrometer using NBA/NPOE as a matrix.

Synthesis. (6-isocyanatohexylaminocarbonylamino)-6-methyl-4[1H]pyrimidinone and bis-11,11' undecanol disulfide were synthesized according to published procedures.^{42,43}

2-(6-(2-ethyl-2'-hydroxyethyl dithio)hexylaminocarbonylamino)-6-methyl-4[1H]pyrimidinone **1**.

(6-isocyanatohexylaminocarbonylamino)-6-methyl-4[1H]pyrimidinone (293 mg, 1 mmol) was dissolved in 10 mL dry chloroform and added to bis-hydroxyethyl disulfide (0.7 mL, 3 mmol) in 3 mL dry chloroform. After addition of one drop of dibutyltindilaurate, the resulting solution was refluxed and stirred for 16 hours. The crude product was purified by column chromatography on silica using dichloromethane / methanol (95 / 5) as an eluent: isolated yield 10%; ¹H-NMR (250 MHz, CDCl₃): 13.1 (s, 1H, CH₃-C-NH), 11.9 (s, 1H, CH₂-NH-(C=O)-NH), 10.1 (s, 1H, CH₂-NH-(C=O)-NH), 5.8 (s, 1H, CH=C-CH₃), 5.1 (s, 1H, NH-(C=O)-O), 4.3 (t, 2H, CH₂-O-(C=O)), 3.9 (t, 2H, CH₂-CH₂-OH), 3.3 (m, 2H, CH₂-NH-(C=O)-NH), 3.2 (m, 2H, CH₂-

NH(C=O)-O), 2.9 (m, 4H, (CH₂-S)₂), 2.2 (s, 3H, CH₃-C=CH), 1.6-1.4 (m, 8H, CH₂-CH₂-CH₂); mass (FAB-MS), $m/z = 448.6(\text{M}+\text{H})$. Calculated for C₁₇H₂₉N₅O₅S₂: 447.6 g/mol.

2-(6-(11-undecanyl-11'-hydroxyundecanyldithio)hexylaminocarbonyl-amino)-6-methyl-4[1H]pyrimidinone **2**.

(6-isocyanatohexylaminocarbonylamino)-6-methyl-4[1H]pyrimidinone (137 mg, 0.46 mmol) was dissolved in 5 mL dry chloroform and added to bis-11,11' undecanol disulfide (495 mg, 1.3 mmol) in 5 mL dry chloroform. After addition of one drop of dibutyltindilaurate, the resulting solution was refluxed and stirred for 20 hours. The crude product was purified by column chromatography on silica using dichloromethane / methanol (92 / 8) as an eluent: isolated yield 5%; ¹H-NMR (250 MHz, CDCl₃): 13.1 (s, 1H, CH₃-C-NH), 11.9 (s, 1H, CH₂-NH-(C=O)-NH), 10.1 (s, 1H, CH₂-NH-(C=O)-NH), 5.8 (s, 1H, CH=C-CH₃), 4.9 (s, 1H, NH-(C=O)-O), 4.1 (t, 2H, CH₂-O-(C=O)), 3.6 (t, 2H, CH₂-CH₂-OH), 3.3 (m, 2H, CH₂-NH-(C=O)-NH), 3.2 (m, 2H, CH₂-NH(C=O)-O), 2.7 (m, 4H, (CH₂-S)₂), 2.2 (s, 3H, CH₃-C=CH), 1.6-1.4 (m, 44H, CH₂-CH₂-CH₂); mass (FAB-MS), $m/z = 700.4(\text{M}+\text{H})$ and 698.3(M-H). Calculated for C₃₅H₆₅N₅O₅S₂: 699.4 g/mol.

2-(6-trifluoroethylhexylaminocarbonylamino)-6-methyl-4[1H]pyrimidinone **3**.

(6-isocyanatohexylaminocarbonylamino)-6-methyl-4[1H]pyrimidinone (845 mg, 2.88 mmol) was dissolved in 15 mL dry chloroform. Trifluoroethanol (0.5 mL, 6.86 mmol) was added and after addition of one drop of dibutyltindilaurate the resulting solution was refluxed and stirred for 15 hours. The crude product was purified by column chromatography on silica using dichloromethane as an eluent: isolated yield 65%; ¹H-NMR (250 MHz, CDCl₃): 13.1 (s, 1H, CH₃-C-NH), 11.9 (s, 1H, CH₂-NH-(C=O)-NH), 10.1 (s, 1H, CH₂-NH-(C=O)-NH), 5.8 (s, 1H, CH=C-CH₃), 5.5 (s, 1H, NH-(C=O)-O), 4.5 (t, 2H, CF₃-CH₂-O-(C=O)), 3.3 (m, 2H, CH₂-NH-(C=O)-NH), 3.2 (m, 2H, CH₂-NH(C=O)-O), 2.2 (s, 3H, CH₃-C=CH), 1.6-1.4 (m, 8H, CH₂-CH₂-CH₂); mass (FAB-MS), $m/z = 394.3(\text{M}+\text{H})$ and 392.4(M-H). Calculated for C₁₅H₂₂N₅O₄F₃: 393.2 g/mol.

2-(6-ferrocenemethylhexylaminocarbonylamino)-6-methyl-4[1H]pyrimidinone **4**.

(6-isocyanatohexylaminocarbonylamino)-6-methyl-4[1H]pyrimidinone (420 mg, 1.43 mmol) was dissolved in 15 mL dry chloroform and ferrocenemethanol (500 mg, 2.3 mmol) dissolved in 2 mL dry chloroform was added. After addition of one drop of dibutyltindilaurate, the resulting solution was refluxed and stirred for 20 hours. The crude product was purified by column chromatography on silica using dichloromethane as an eluent: isolated yield 35%. ¹H-NMR (250 MHz, CDCl₃): 13.1 (s, 1H, CH₃-C-NH), 11.9 (s, 1H, CH₂-NH-(C=O)-NH), 10.1 (s,

1H, CH₂-NH-(C=O)-NH), 5.8 (s, 1H, CH=C-CH₃), 5.1-4.9 (m, 1H, NH-(C=O)-O and 2H, ferrocene-CH₂-O-(C=O)), 4.3-4.1 (m, 9H, CH=CH), 3.3 (m, 2H, CH₂-NH-(C=O)-NH), 3.2 (m, 2H, CH₂-NH(C=O)-O), 2.2 (s, 3H, CH₃-C=CH), 1.6-1.4 (m, 8H, CH₂-CH₂-CH₂); mass (FAB-MS), m/z = 508.2 (M+H) and 1017.1(2M-H). Calculated for C₂₄H₃₁N₅O₄Fe: 509.2 g/mol.

Preparation of Substrates. Sample substrates (200 nm gold on 2 nm Ti primer deposited onto glass substrates) were purchased from SSENS bv (Hengelo, The Netherlands). Prior to use, these substrates were cleaned in piranha solution (3:1 H₂SO₄: H₂O₂ (30%) by volume), then rinsed with Milli-Q water and ethanol and dried in a nitrogen stream. **Caution: Piranha solution should be handled with extreme caution: it has been reported to detonate unexpectedly.**

Preparation and Characterization of Monolayers. Monolayers were formed by immersing the gold substrates into dilute solution of the corresponding compound and solvent for 10 hours (typical concentration: 1 mM). After rinsing in pure solvent and drying in an N₂ stream, the measurements were performed with minimal delay. The layers formed were characterized by AFM, grazing incidence reflection FT-IR (GIR-FTIR) spectroscopy (see section 4.6), contact angle measurements (see section 4.6), electrochemistry, XPS, and SPR, as described previously.³² All data confirmed the highly reproducible formation of layers with the expected chemical composition, thickness, and order.

X-ray Photoelectron Spectroscopy (XPS). XPS spectra were recorded using a PHI Quantum 2000 Scanning ESCA Microprobe. Spectra were acquired using a monochromated X-ray beam (Al-anode); 100 micrometer diameter / 25 Watt X-ray beam scanned over 1000 μm × 500 μm area at a take-off angle of 30°. Atomic concentrations were determined by numerical integration of the relative peak areas in the detailed element scans using the following sensitivity factors: C1s [0.314], N1s [0.499], O1s [0.733], S2p [0.717], F1s [1.0] and Fe2p [2.946].^{33,35}

Surface Plasmon Resonance Measurements (SPR). Experiments were carried out on a home-built SPR setup,⁴⁴ which is based on the configuration introduced by Kretschmann and Raether.³⁸ A refractive index of $n = 1.50$ was assumed for all organic adlayers.

Differential Pulse Voltammetry Experiments (DPV). Measurements were performed using an Autolab PGSTAT10 potentiostat (ECOCHEMIE, Utrecht, The Netherlands) in a three electrode configuration. The gold sample covered with the corresponding layer was used as the working electrode, Hg/HgSO₄ (MSE) was used as reference (+0.61 V_{NHE}) and Pt wire as the auxiliary electrode. The electrolyte was 0.1 M NaClO₄. The working electrode exposed a surface area of 0.44 cm² to the electrolyte. Prior to the measurements, the cell was degassed by passing

nitrogen through the electrolyte for 5 minutes. Differential pulse voltammograms were recorded at a pulse amplitude of 10 mV, a pulse time of 50 ms, and a time interval of 200 ms.

Atomic Force Microscopy (AFM) Measurements. The measurements were carried out with a NanoScope III AFM (Digital Instruments, Santa Barbara, CA) in contact mode. Constant force AFM scans were performed in air with a load of 3 nN using V-shaped Si₃N₄ cantilevers (Nanoprobes (DI), spring constant of 0.1 N/m). The calibration of the AFM scanner in the z-direction was carried out using a set of three vertical calibration standards (TGZ 01 - 03) with step heights of 25.5 nm, 104 nm, and 512 nm, respectively (Silicon-MDT, Moscow, Russia). All the images shown here were subjected to a first order plane-fitting procedure to compensate for sample tilt and to a zeroth-order flattening. The calculations of the thicknesses were carried out on images without any flattening treatment.

4.6 Appendix (Characterization of SAMs of 1 and 2)

FT-IR Measurements

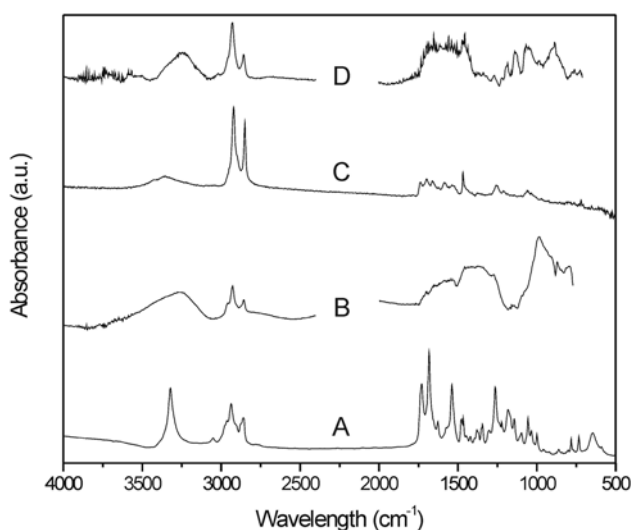


Figure 4.5. FTIR spectra of compound (KBr) (A) **1** and (C) **2**; GIR-FTIR spectra of SAMs of (B) **1** and (D) **2** on gold surface. Prominent bands are the O-H bond at around 3350; the N-H bond (with H-bonding) in the region 3300 ~ 3200 cm⁻¹; the asymmetric C-H stretching vibration, _{as} (CH₂) at ca. 2920 cm⁻¹, the symmetric C-H stretching vibration, _s (CH₂), at ca. 2850 cm⁻¹.

Contact Angle Measurements

Table 4.4. Advancing (θ_a) and receding (θ_r) contact angles measured with ultrapure water on SAMs of **1** and **2**.

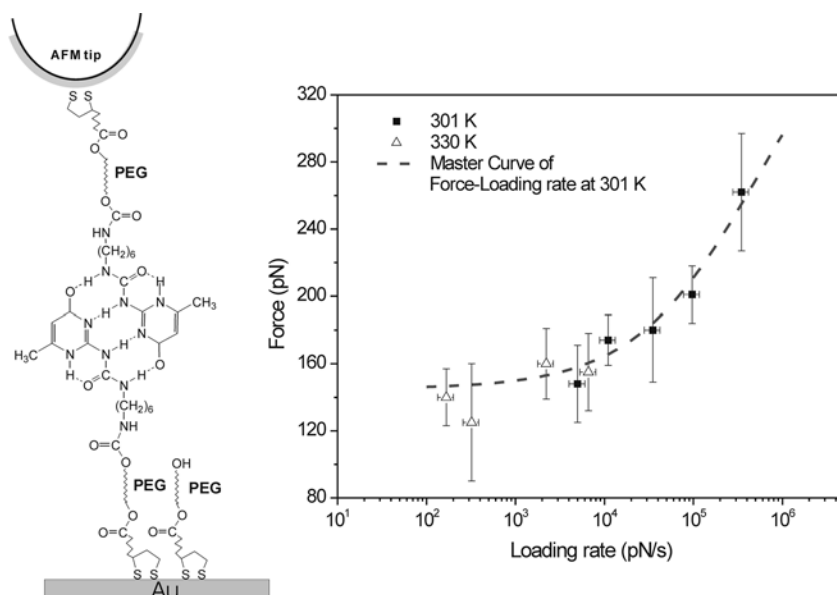
SAM	θ_a (degree)	θ_r (degree)
1	65 ± 3	35 ± 3
2	71 ± 3	42 ± 3

References:

- (1) Buckingham, A. D.; Legon, A. C.; Roberts, S. M. *Principles of Molecular Recognition*; Blackie: London, 1993.
- (2) Behr, J.-P. *The Lock and Key Principle: The State of the Art*; Wiley: Chichester, 1994.
- (3) Cooke, G.; Rotello, V. M. *Chemical Society Reviews* **2002**, *31*, 275-286.
- (4) Lehn, J. M. *Science* **2002**, *295*, 2400-2403.
- (5) Reinhoudt, D. N.; Crego-Calama, M. *Science* **2002**, *295*, 2403-2407.
- (6) Ikkala, O.; ten Brinke, G. *Science* **2002**, *295*, 2407-2409.
- (7) Whitesides, G. M.; Grzybowski, B. *Science* **2002**, *295*, 2418-2421.
- (8) Credo, G. M.; Boal, A. K.; Das, K.; Galow, T. H.; Rotello, V. M.; Feldheim, D. L.; Gorman, C. B. *Journal of the American Chemical Society* **2002**, *124*, 9036-9037.
- (9) Motesharei, K.; Myles, D. C. *Journal of the American Chemical Society* **1994**, *116*, 7413-7414.
- (10) Dawson, S. L.; Elman, J.; Margevich, D. E.; McKenna, W.; Tirrell, D. A.; Ulman, A. *Hydrogels and Biodegradable Polymers For Bioapplications*, 1996; Vol. 627.
- (11) Lehn, J. M. *Angewandte Chemie-International Edition* **1988**, *27*, 89-112.
- (12) Cram, D. J. *Angewandte Chemie-International Edition* **1988**, *27*, 1009-1020.
- (13) Pedersen, C. J. *Angewandte Chemie-International Edition* **1988**, *27*, 1021-1027.
- (14) Haussling, L.; Ringsdorf, H.; Schmitt, F. J.; Knoll, W. *Langmuir* **1991**, *7*, 1837-1840.
- (15) Motesharei, K.; Myles, D. C. *Journal of the American Chemical Society* **1998**, *120*, 7328-7336.
- (16) Jeffery, G. A.; Saenger, W. *Hydrogen Bonding in Biological Structures*; Springer-Verlag: Berlin, 1991.
- (17) Steed, J. W.; Atwood, J. L. *Supramolecular Chemistry*; Wiley, Chichester, 2000.
- (18) Brunsveld, L.; Folmer, B. J. B.; Meijer, E. W.; Sijbesma, R. P. *Chemical Reviews* **2001**, *101*, 4071-4097.
- (19) Buckingham, A. D. *Principles of Molecular Recognition: Intermolecular Forces*; Chapman & Hall: London, 1993.
- (20) Boland, T.; Ratner, B. D. *Proceedings of the National Academy of Sciences of the United States of America* **1995**, *92*, 5297-5301.
- (21) Zhu, C. *Journal of Biomechanics* **2000**, *33*, 23-33.
- (22) Halpern, J. *Proceedings of the National Academy of Sciences of the United States of America* **2002**, *99*, 4762-4762.
- (23) Lehn, J. M. *Macromolecular Symposia* **1993**, *69*, 1-17.
- (24) Sijbesma, R. P.; Beijer, F. H.; Brunsveld, L.; Folmer, B. J. B.; Hirschberg, J. H. K. K.; Lange, R. F. M.; Lowe, J. K. L.; Meijer, E. W. *Science* **1997**, *278*, 1601-1604.
- (25) Beijer, F. H.; Sijbesma, R. P.; Kooijman, H.; Spek, A. L.; Meijer, E. W. *Journal of the American Chemical Society* **1998**, *120*, 6761-6769.
- (26) Beijer, F. H.; Kooijman, H.; Spek, A. L.; Sijbesma, R. P.; Meijer, E. W. *Angewandte Chemie-International Edition* **1998**, *37*, 75-78.
- (27) Sontjens, S. H. M.; Sijbesma, R. P.; van Genderen, M. H. P.; Meijer, E. W. *Journal of the American Chemical Society* **2000**, *122*, 7487-7493.
- (28) Corbin, P. S.; Zimmerman, S. C. *Journal of the American Chemical Society* **1998**, *120*, 9710-9711.
- (29) Gong, B.; Yan, Y. F.; Zeng, H. Q.; Skrzypczak-Jankunn, E.; Kim, Y. W.; Zhu, J.; Ickes, H. *Journal of the American Chemical Society* **1999**, *121*, 5607-5608.
- (30) Boileau, S.; Bouteiller, L.; Laupretre, F.; Lortie, F. *New Journal of Chemistry* **2000**, *24*, 845-848.
- (31) Sherrington, D. C.; Taskinen, K. A. *Chemical Society Reviews* **2001**, *30*, 83-93.
- (32) Zou, S.; Zhang, Z. H.; Förch, R.; Knoll, W.; Schönherr, H.; Vancso, G. J. *Langmuir* **2003**, *19*, 8618-8621.
- (33) Ulman, A. *An Introduction to Ultrathin Organic Films: From Langmuir-Blodgett to Self-Assembly*; Academic Press: New York, 1991.
- (34) Kaifer, A. E.; Gomez-Kaifer, M. *Supramolecular Electrochemistry*; Wiley-VCH: Weinheim, 1999.
- (35) Wagner, C. D.; Riggs, W. M.; Davis, L. E.; Moulder, J. F. *Handbook of X-Ray Photoelectron Spectroscopy*; Perkin-Elmer Corporation: Eden Prairie, MN, 1979.
- (36) Peter, M.; Hempenius, M. A.; Lammertink, R. G. H.; Vancso, G. J. *Macromolecular Symposia* **2001**, *167*, 285-296.
- (37) Knoll, W. *Annual Review of Physical Chemistry* **1998**, *49*, 569-638.
- (38) Kretschmann, E.; Raether, H. *Zeitschrift für Naturforschung A - A Journal of Physical Sciences* **1968**, *23A*, 2135-2136.
- (39) Azzam, R. M. A.; Rashara, N. M. *Ellipsometry and Polarized Light*; Elsevier: Amsterdam, 1987.
- (40) Magonov, S. N.; Whangbo, M.-H. *Surface Analysis with STM and AFM*; VCH: Weinheim, 1996.
- (41) Xia, Y. N.; Whitesides, G. M. *Annual Review of Materials Science* **1998**, *28*, 153-184.
- (42) Folmer, B. J. B.; Sijbesma, R. P.; Versteegen, R. M.; van der Rijt, J. A. J.; Meijer, E. W. *Advanced Materials* **2000**, *12*, 874-878.
- (43) Haussling, L., Ph.D. Thesis, University of Mainz, 1991.
- (44) Rothenhausler, B.; Knoll, W. *Nature* **1988**, *332*, 615-617.

Chapter 5

Rupture Forces of Single Quadruple Hydrogen Bonding Dimers: From Thermodynamic Equilibrium to Non-Equilibrium



For the first time transitions from thermodynamic non-equilibrium to quasi-equilibrium in synthetic supramolecular H-bonding systems were successfully studied by atomic force microscopy (AFM)-based single molecule force spectroscopy (SMFS). The stretching of polyethylene glycol (PEG) spacers and the unbinding behavior of individual 2-ureido-4[1H]-pyrimidinones (UPy) supramolecular complexes formed via self-complementary quadruple hydrogen bonds were investigated by SMFS. The unbinding forces of single quadruple H-bonding arrays were found to be 180 ± 21 pN at a loading rate of 35 ± 0.7 nN/s in hexadecane. At 301 K, these rupture forces were dependent on loading rate in the range of 5 nN/s to 500 nN/s. By contrast, the rupture forces were found to be independent of loading rate from 5 nN/s to 200 nN/s at 330 K in hexadecane. These results indicate that the unbinding behavior of individual supramolecular complexes can be directly probed under both thermodynamic non-equilibrium and quasi-equilibrium conditions. Based on the experimental data, a lifetime of 7 s can be estimated for self-complementary hydrogen-bonded UPy complexes in hexadecane.

5.1 Introduction

Molecular interactions form the basis of highly specific recognition, reaction, transport, regulation and other processes that occur in biology, such as protein-ligand binding, enzyme catalysis, the immune response, signal transduction, genetic code translation and so on.^{1,2} Hydrogen bonding arrays also play a crucial role in determining the secondary, and higher order structures and energetics of biomacromolecules.^{3,4} For example, in the α -helix structure of proteins the combined effects of many hydrogen bonds provide the major driving force for the formation of the tertiary structure.^{3,5}

In the literature, most reports describing molecular interactions dealt mainly with interaction *energies* rather than the *forces* experienced by molecules.⁶ In nanotechnology, several molecular platforms are available that allow one to measure molecular forces.⁷⁻⁹ Molecular objects that interact via weak supramolecular interactions can be ruptured on the single molecule level. The corresponding rupture forces, however, have been shown to depend on the *linker* between these molecular objects and the force probes, as well as on the rate by which the supramolecular bonds are being loaded.¹⁰ Thus the interpretation of rupture force values is of great theoretical and experimental interest, both in the range where rupture forces do not exhibit loading rate dependence (thermodynamic quasi-equilibrium), as well as in the range with loading rate dependence (non-equilibrium).¹¹ Moreover, directly probing the forces of individual hydrogen bonds (or hydrogen bonding arrays) over a range of loading rates can reveal the energy of a single interaction between individual molecules that is difficult (or impossible) to be directly detected.¹⁰⁻¹²

AFM-based force spectroscopy¹³⁻¹⁷ appears to be suitable to address *individual* supramolecular complexes and to directly determine unbinding forces of single, weak supramolecular bonds. As mentioned in Chapter 2.3 (Figure 2.12), a characteristic flexible linker (e.g. polyethylene glycol, PEG) modified with cognitive molecules (moieties) is used to ensure probing of the individual recognition sites.^{18,19} The quantitative rupture force of a single complex (e.g. ligand-receptor pair) is determined by analyzing the pull-off forces of the recorded force curves.

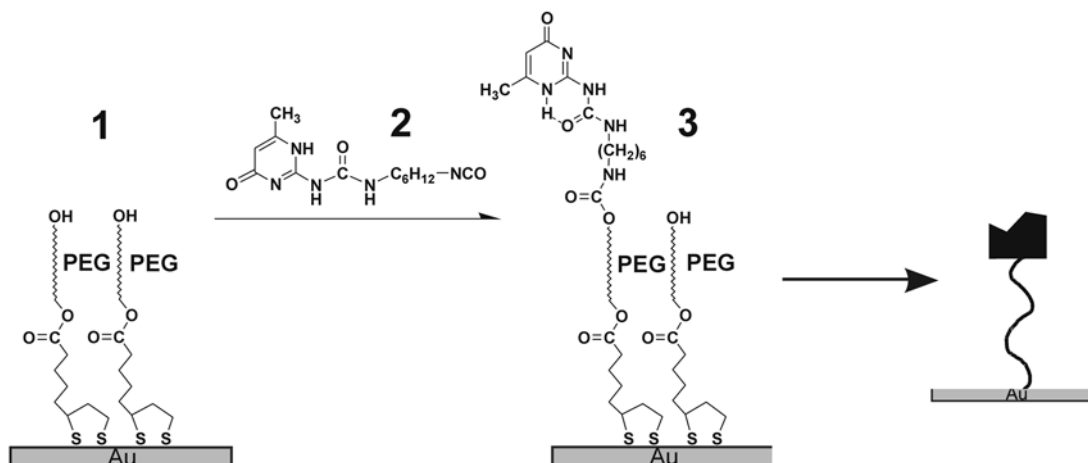
In this Chapter, the unbinding behavior of individual H-bonding arrays in surface-immobilized PEG linked 2-ureido-4[1H]-pyrimidinones (UPy-PEG) moieties²⁰ and the relation between unbinding forces and dissociation time (loading rates) are investigated on the single molecule level using AFM-based force spectroscopy. The unbinding forces of individual UPy complexes formed via quadruple hydrogen bonds were measured under different loading rates at different temperature and solvent conditions. At 330 K, the unbinding behavior of UPy complexes is near equilibrium in hexadecane, while at 301 K, UPy complexes stay in the far-from-equilibrium situation.

5.2 Rupture Forces of Individual Quadruple Hydrogen Bonding Arrays

5.2.1 UPy Complexes on Surfaces

Systematic investigations of the unbinding behavior of quadruple hydrogen bonding arrays were based on the measurements of *individual* molecular interactions present in single UPy complexes. For this purpose, we first prepared monolayer architecture **3** on Au(111), comprising

surface-immobilized ω -hydroxyl PEG chains by coupling UPy isocyanate **2** to the hydroxyl functionalities of a layer of **1** (Scheme 5.1; for characterization also see section 5.6).



Scheme 5.1. The formation of PEG linked 2-ureido-4[1H]-pyrimidinone moieties at Au(111) surfaces.

Similarly to self-assembled layers of **4** on gold surfaces (see Figure 5.1), which were studied in detail as reported in Chapter 4,²⁰ chemically accessible UPy units of layer **3** ensure the complexation between UPy-PEG (**3**) and external guest **5** in CHCl_3 , i.e. to form $[\text{Au-3} + \mathbf{5}]$ complexes on gold surface. The oxidation peak of the ferrocenyl group was detected in differential pulse voltammetry (DPV) measurements, which was consistent with the DPV results measured on $[\text{Au-4} + \mathbf{5}]$ (Figure 5.1). These DPV data indicate that the self-complementary recognition indeed occurred between UPy groups of **3** and **5** and that $[\text{Au-3} + \mathbf{5}]$ complexes were formed on gold surfaces. After rinsing with DMSO, the oxidation peak of the ferrocenyl groups disappeared from voltammograms (Figure 5.1, inset), confirming the unbinding of $[\text{Au-3} + \mathbf{5}]$ complexes caused by the rupture of H-bonds in DMSO.

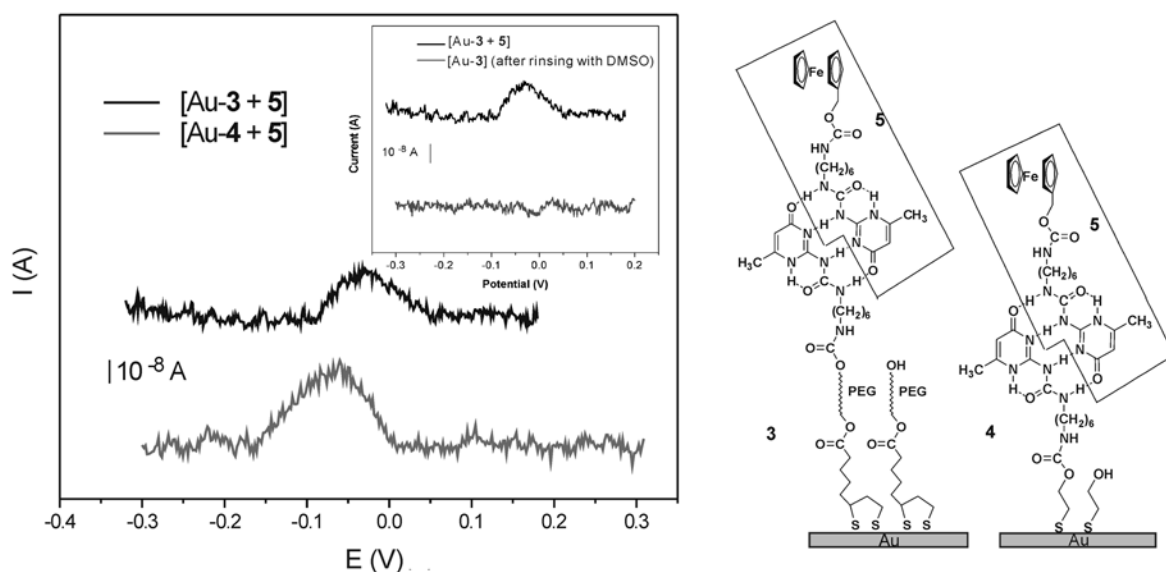


Figure 5.1. Differential pulse voltammograms of ferrocenyl substituted pyrimidinone **5** binding with UPy-PEG-disulfide **3** and UPy-disulfide **4** on gold surfaces recorded in aqueous electrolyte (0.1 M NaClO_4). Inset figure: DPV data of complex $[\text{Au-3} + \mathbf{5}]$ before and after DMSO rinse.

Since the single chain mechanical properties of the PEG spacers are known,^{19,21} we can identify and verify the stretching of *single* macromolecules in subsequent SMFS measurements.

5.2.2 Rupture Forces of Quadruple Hydrogen Bonds

Quadruple H-bonding interactions in individual UPy complexes were probed by SMFS between PEG linked UPy (**3**) immobilized on Au(111) and gold-coated AFM tips functionalized with **4** (Figure 5.2A). Figure 5.2B presents a typical force-extension curve acquired in hexadecane between **3** and **4**. The data were fitted with the m-FJC model,

$$x(F) = \left[\coth\left(\frac{FI_K}{k_B T}\right) - \frac{k_B T}{FI_K} \right] \left[L_{contour} - 2 \frac{n}{K_{segment}} F \right] \quad 5.1$$

where x is the extension of the polymer chain; F is the applied force; I_K (Kuhn length) is the length of the statistically independent segment; n is the number of segments, which equals $L_{contour} / I_K$; $K_{segment}$ is the segment elasticity, which characterizes the deformability of the segment; k_B is the Boltzmann constant; and T is the temperature.

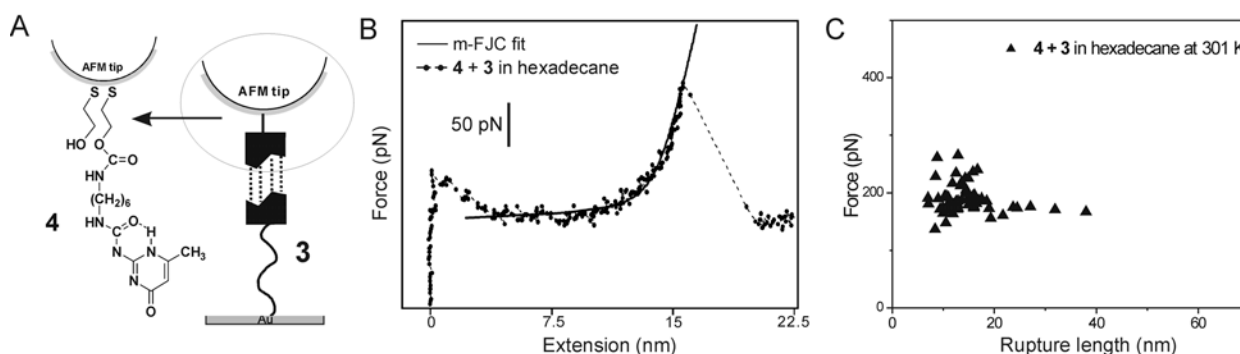


Figure 5.2. (A) Scheme of gold-coated AFM tip functionalized with a SAM of UPy disulfide **4** and Au(111) substrate modified with layer of **3**. (B) Force-extension curve measured between **3** and **4** in hexadecane (at a loading rate of 35 ± 0.7 nN/s and 301 K). The fit of the data to the m-FJC model is shown as a solid line. (C) Plot of rupture forces of the H-bonded UPy complexes vs. the corresponding stretching lengths of the PEG-UPy **3** measured in hexadecane (at a loading rate of 35 ± 0.7 nN/s and 301 K).

The observed stretching event is attributed to the stretching of single PEG spacers of **3**. The Kuhn length of PEG chains was found to be 0.65 ± 0.08 nm and the segment elasticity was 6.2 ± 0.6 nN/nm. These fit parameters agree well with single chain literature data^{19,21} and thus confirm the successful stretching of *single* PEG chains. The observed extension lengths agree favorably with the contour length of the linker (ca. 12 ± 3 nm; PEG chain is 9.5 ± 1.0 nm). Since *single* PEG chains are stretched, the rupture forces of *a single* UPy-UPy complex can be directly determined (by analyzing the pull-off forces) as 180 ± 21 pN (Figure 5.2C) in hexadecane ($T = 301$ K, loading rate 35 nN/s).

Due to the high complexation constant of UPy complexes in hexadecane ($K > 10^9 \text{ M}^{-1}$),²² the value of the rupture forces of single quadruple H-bonding arrays obtained may be expected to be loading rate dependent in the SMFS measurements.

5.3 Correlation between Rupture Forces and Loading Rates

The dissociation rate constant k_{off} of the self-complementary UPys at 300 K in CDCl_3 is approximately 8.5 s^{-1} .^{23,24} A variation of temperature from 280 K to 320 K results in an increase of k_{off} in CDCl_3 by a factor of 50.^{23,24}

Systematic studies of the unbinding behavior of individual quadruple H-bonded PEG-UPy complexes were carried out at 301 K and 330 K in hexadecane, respectively.

5.3.1 Loading Rate Dependence of Rupture Forces at 301 K

In order to determine the relation between the unbinding force of the quadruple H-bonding in UPy complexes and the loading rate, PEG linked ureido-4[1H]-pyrimidinone disulfides **3** were immobilized both on gold-coated AFM tips and gold substrates. Figure 5.3A shows the investigated system schematically.

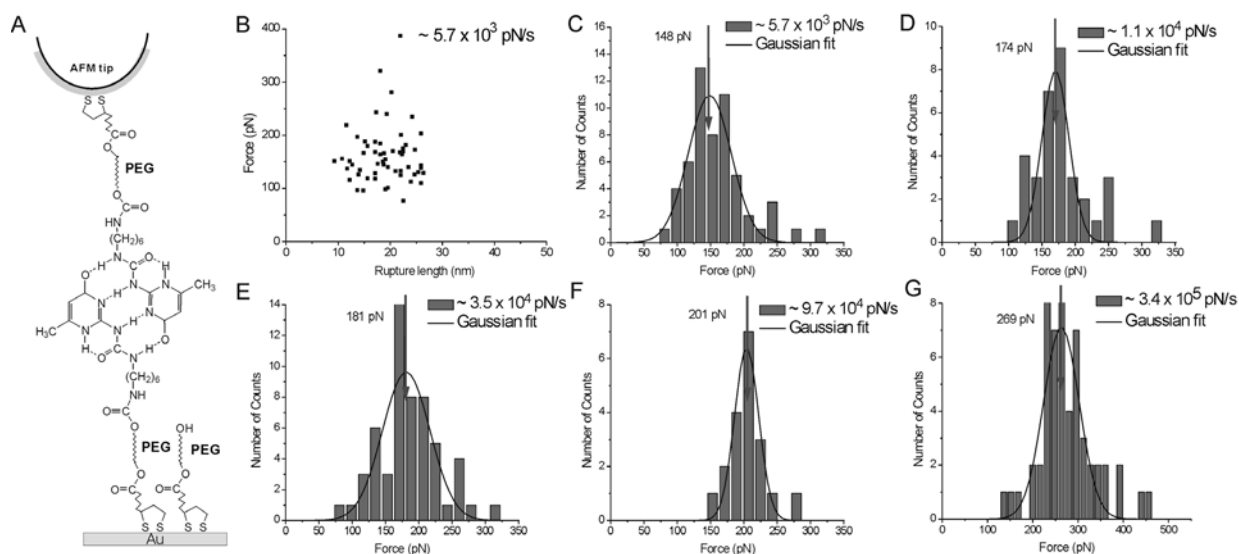


Figure 5.3. (A) Scheme of PEG-UPy disulfide **3** self-assembled both on gold-coated AFM tips and gold substrates. (B) The rupture forces vs. the corresponding rupture lengths of UPy complexes measured under a loading rate of $5.7 (\pm 1.1) \times 10^3 \text{ pN/s}$ at 301 K in hexadecane. Histograms of pull-off forces of individual UPy complexes at loading rates of (C) $5.7 (\pm 1.1) \times 10^3 \text{ pN/s}$, (D) $1.1 (\pm 0.2) \times 10^4 \text{ pN/s}$, (E) $3.5 (\pm 0.7) \times 10^4 \text{ pN/s}$, (F) $9.7 (\pm 1.9) \times 10^4 \text{ pN/s}$, and (G) $3.4 (\pm 0.7) \times 10^5 \text{ pN/s}$ at 301 K in hexadecane. Solid lines in (C) – (G) are Gaussian fits to the corresponding histograms.

SMFS experiments were carried out to determine the values of the unbinding forces of self-complementary PEG-UPy moieties mediated by quadruple hydrogen bonds. The pull-off forces of the force curves acquired at 301 K in hexadecane under different loading rates were analyzed (Figure 5.3 B-G). For the analysis, only those rupture forces were taken into account that

corresponded to rupture lengths between 11 and 25 nm* (Figure 5.2B). Since the contour length of each PEG-UPy linker should be around 12 nm, the criterion ensured that only unbinding force data of single complexes were taken into account. Histograms of rupture forces measured at loading rates between ~ 5 nN/s and ~ 500 nN/s were obtained, as shown in Figure 5.3C to G. The influence of solvent and drag forces under high loading velocities (>50 nN/s) were not considered.

Figure 5.4 presents the plot of rupture forces versus loading rates at 301 K. The rupture forces increase with increasing loading rates (slope of ~ 19 pN). The same modified AFM tip with PEG-UPy **3** was utilized in these measurements with different loading velocities, thus the slope (force-loading rate dependence) is not influenced by the spring constant of the tip. The observed dependence indicates that the SMFS measurements (at 301 K in hexadecane) are carried out under thermodynamic *non-equilibrium* conditions.

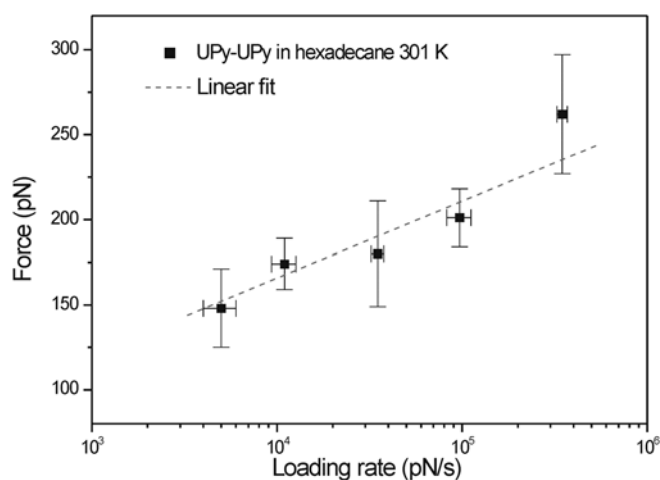


Figure 5.4. Plot of rupture force versus loading rate at 301 K in hexadecane.

5.3.2 Loading Rate Independence of Rupture Forces at 330 K

With increasing temperature the complexation (dimerization) constant of UPys decreases due to the faster dissociation rate, as mentioned above. At higher temperatures the relation between rupture forces of UPy complexes and loading rates may show a different characteristic compared to the presented dependence-trend at 301 K.

Thus temperature dependent SMFS experiments in hexadecane were carried out at different loading rates in the UPy system, (with PEG spacers on both the gold surface and the AFM tip) as shown in section 5.3.1 (Figure 5.3). Again, the criterion of stretching lengths between 11 and 25

* One fully stretched PEG spacer should show ~ 12 nm contour length on the force-extension curve. If two PEG spacers (Figure 5.3A) were both stretched completely, the stretching length of the corresponding force-extension curve should be around 24 nm. Taking the polydispersity into account, the criterion of the extension length of the PEG spacers for single UPy complexes was chosen as 11 to 25 nm.

nm was chosen for analyzing the force-extension curves obtained in SMFS measurements. Figure 5.5A to D show the histograms of rupture forces at different loading rates measured on individual quadruple hydrogen bonded UPy complexes in hexadecane at 330 K.

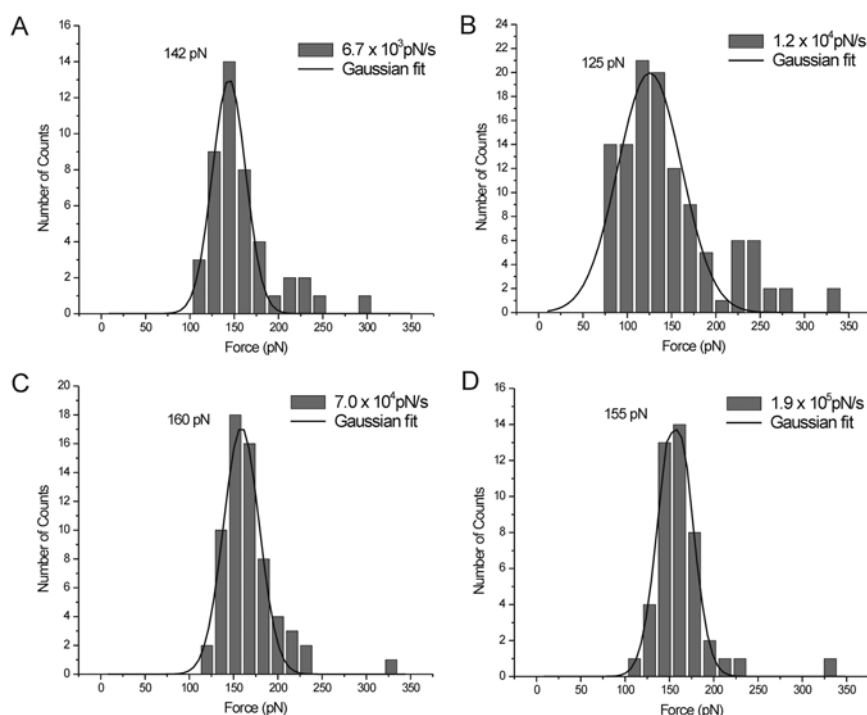


Figure 5.5. Histograms of rupture forces of individual UPy complexes determined at 330 K in hexadecane at loading rates of (A) $6.7 (\pm 1.3) \times 10^3$ pN/s, (B) $1.2 (\pm 0.2) \times 10^4$ pN/s, (C) $6.9 (\pm 1.4) \times 10^4$ pN/s, and (D) $1.9 (\pm 0.4) \times 10^5$ pN/s. Solid lines are Gaussian fits to the corresponding histograms.

Figure 5.6 demonstrates the relation of rupture force versus loading rate measured at 330 K in hexadecane. In the range between 5 nN/s and 200 nN/s, the rupture forces are *independent* of the loading rates. Assuming that the complexation constant of quadruple H-bonds decreases 10 times in hexadecane at 330 K (i.e. $K \sim 10^8 \text{ M}^{-1}$), and that the dissociation rate constant increases 50 times relative to 301 K,^{23,24} Evans' model predicts that the rupture force will depend on the loading rate for loading rates exceeding 300 nN/s (see section 5.4 for details).¹¹

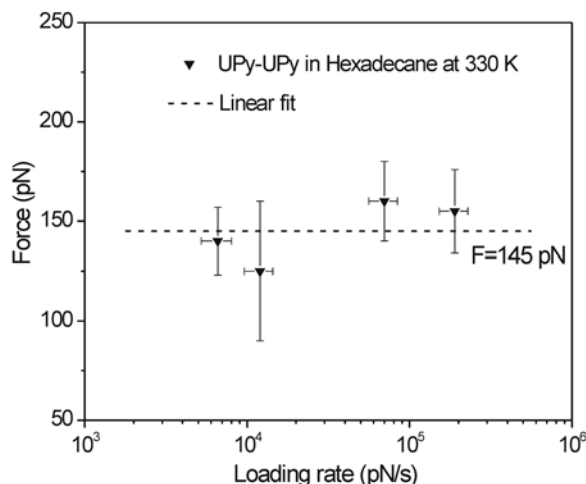


Figure 5.6. Plot of rupture force versus loading rate at 330 K in hexadecane.

5.4 Crossover from Thermodynamic Quasi-Equilibrium to Non-Equilibrium

As already mentioned in Chapter 2.2.2, the complexation via weak interactions, e.g. ligand-receptor binding, is a reversible reaction. The average lifetime of a weak bond, $t_{\text{off}}(0)$, is given by $t_{\text{off}}(0)=1/k_{\text{off}}$. The energy landscape of the bond is tilted when an external force is applied, which increases the probability of the bond re-formation after a rupture event i.e. unbinding took place. The crossover from near-equilibrium to far-from-equilibrium situation is thus expected to be located around loading rates, for which the forward rate of the barrier overcomes the backward rate (for details, see Chapter 2.2.2 and refs. 8 to 10). In far-from-equilibrium situations, the two binding partners are further separated after dissociation has occurred. Therefore, rebinding and back-reactions are negligible.

For the unbinding in non-equilibrium situations, the effective force (or most probable rupture force) f^* is a function of loading rate r_f :

$$f^* \approx f \ln(r_f / r_f^0) \quad 5.2$$

where the thermal activation introduces the characteristic scale force f , and a thermal scale for loading rate $r_f^0 \approx f / t_{\text{off}}(0)$.

In supramolecular H-bonded UPy systems, the dissociation rate and the complexation constant in toluene at 300 K have been reported as $\sim 0.6 \text{ s}^{-1}$ and $6 \times 10^8 \text{ M}^{-1}$, respectively.²⁴ The lifetime of the quadruple H-bonds is estimated as 5 seconds in hexadecane ($K \sim 10^9 \text{ M}^{-1}$).^{24,25} This life time suggests that the unbinding of single UPy complexes can happen in non-equilibrium situations during the SMFS measurement (time scale of \sim millisecond, Chapter 3.1). As shown in Figure 5.4, the linear force-logarithm loading rate (in the range from 5 nN/s to 500 nN/s) dependence at 301 K agrees well with this indication.

From the force – loading rate data obtained in SMFS measurements and equation 5.2, the rupture force–loading rate dependence at 301 K can be predicted to occur at pulling rates faster than 7 nN/s ($f = 19 \text{ pN}$, $t_{\text{off}}(0) = 5 \text{ s}$, and $f^* = 145 \text{ pN}$, see below).

When increasing the temperature to 330 K, the life time of the quadruple H-bonds may decrease 50 times in solution.²⁵ The average rupture force showed an *independence* of the loading rate between 3 nN/s and 200 nN/s at 330K (Figure 5.6), indicating that the rupture events of the self-complementary UPy complexes occur in quasi-equilibrium. Similar to the calculation for the case at 301 K, the rupture force – loading rate dependence at 330 K should occur at loading rates faster than 300 nN/s ($f = 19 \text{ pN}$, $t_{\text{off}}(0) = 0.1 \text{ s}$, and $f^* = 145 \text{ pN}$), which is consistent with our experimental results.

Plotting the two dynamic rupture force spectra in one graph, as shown in Figure 5.7,[†] the crossover force (from loading rate independent to dependent) is observed at ~ 145 pN, which was used in the calculations above, at a loading rate of ~ 5.6 nN/s. A lifetime of ~ 7 seconds of a single quadruple H-bonding array in hexadecane can be calculated using equation 5.2.

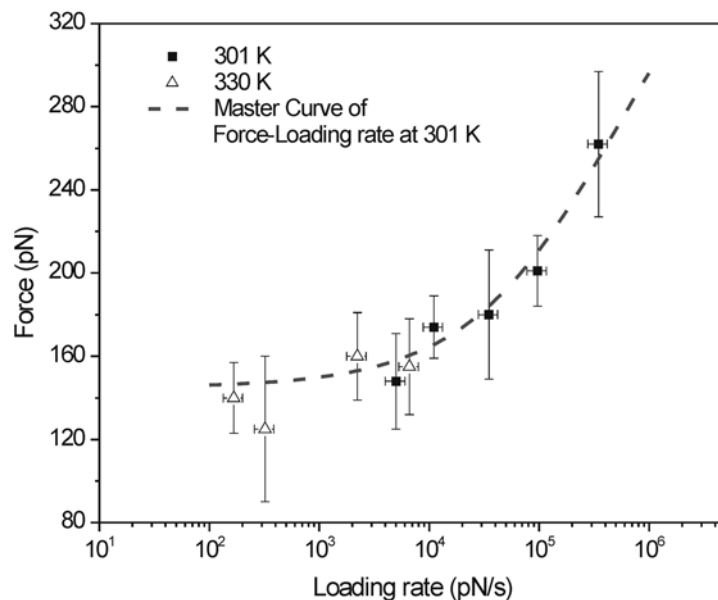


Figure 5.7. Crossover from loading rate independence to loading rate dependence of unbinding forces of individual UPy complexes in hexadecane.

5.5 Conclusions

The unbinding forces of individual supramolecular complexes of ureido-pyrimidinone derivatives formed via self-complementary quadruple hydrogen bonds were studied by single molecule force spectroscopy. The rupture forces of individual quadruple H-bonded complexes are 180 ± 21 pN at loading rate of a 35 ± 0.7 nN/s. These force values are loading rate dependent in the range of 5 nN/s to 500 nN/s at 301 K. The rupture forces change with temperature and show a loading rate independence in the range of 5 nN/s to 200 nN/s at 330 K. Using SMFS, the unbinding of supramolecular quadruple hydrogen bonded UPy complexes can be directly probed in quasi-equilibrium and non-equilibrium states by controlling the temperature and/or solvent composition. The crossover force is determined as ~ 145 pN. The dynamic spectrum of rupture forces as a function of loading rate provides a lifetime of 7 seconds for quadruple H-bonded UPy complexes at gold surface.

[†] The force – logarithmic loading rate data can be shifted and superimposed using the following equations: $f_{\text{U}} \sim \Psi \rho_s k_B T \ln / K_{\text{eq}} (\beta)^2$ and $f^* \sim f \ln / r_f / r_f^0 C$, and the known K_{eq} for the different temperatures. The resulting superimposed curve is called the *master curve* at the chosen reference temperature (301K). Details about master curves can be found in (a) Sperling, L. H. *Introduction to Physical Polymer Science*; John Wiley & Sons: New York, 2001; and (b) Rubinstein, M.; Colby, R. H. *Polymer Physics*; Oxford University Press: New York, 2003.

5.6 Experimental

General Methods. The $^1\text{H-NMR}$ spectra were recorded on a Bruker AC 250 spectrometer (250 MHz). $^1\text{H-NMR}$ chemical shifts are given relative to residual CHCl_3 (7.25 ppm). FT-IR spectroscopy data were collected on a BIO-RAD model FTS575C FT-IR spectrometer.

Synthesis. All experiments were performed under an argon atmosphere. Chloroform was dried with molsieves. Commercial products were used without further purification unless mentioned.

1,2-dithiolane-3-pentyl-derivatized PEG **1**.

1,2-dithiolane-3-pentanoic acid (1.16 mmol) was added to a solution of PEG (3.1 mmol, $M_n = 1600$ g/mol, $M_w = 1690$ g/mol, PDI = 1.06, as confirmed by independent GPC measurements, Fluka), N,N' -dicyclohexylcarbodiimide (1.2 mmol, Aldrich), and 4-dimethylaminopyridine (0.11 mmol, Fluka) in 50 mL CH_2Cl_2 at 0°C . After 1 hour the solution was allowed to warm to RT and stirring was continued for 3 hours. After removal of the precipitated dicyclohexylurea by filtration, the product was dried under reduced pressure (yield 85%). $^1\text{H-NMR}$ (250 MHz, CDCl_3): 4.2 (t, 2H, $\text{CH}_2\text{-O-(C=O)}$), 3.7-3.5 (m, 144H, $\text{CH}_2\text{-CH}_2\text{-O}$), 1H, lipoic ring CH-S-S), 3.2-3.1 (m, 2H, lipoic ring $\text{CH}_2\text{-CH}_2\text{-S}$), 2.8 (br.s. 1H, $\text{CH}_2\text{-CH}_2\text{-OH}$), 2.5-2.4 (m, 2H, $\text{CH}_2\text{-(C=O)}$), 2.4, 1.9 (2H, lipoic ring $\text{CH}_2\text{-CH-S}$), 1.7-1.4 (m, 6H, $\text{CH}_2\text{-CH}_2\text{-CH}_2$). IR (KBr): 3350, 2930, 2870, 1735, 1467, 1345, 1280, 1245, 1150, 1115, 1061, 960, 946, 842 cm^{-1} .

PEG-UPy disulfide **3** on Au Surface.

On gold substrates, SAMs of **1** were prepared from 1 mM CH_2Cl_2 solution²⁰ and reacted with 2.5 mmol **2** ((6-isocyanatohexylaminocarbonylamino)-6-methyl-4[1H]pyrimidinone, see Chapter 4) in 10 ml CHCl_3 solution for 24 hours using one drop of dibutyltindilaurate (Aldrich) as catalyst.²⁶ FT-IR measurements were carried out before reacting with the pyrimidinone isocyanate **2**, as well as after the reaction. The C=O stretching peaks at 1670 and 1595 cm^{-1} were observed after the reaction, which indicates the successful attachment of pyrimidinone groups to the PEG-disulfide **1** on gold. After rinsing with DMSO, the intensities of the two peaks decreased, which is consistent with the interpretation that the H-bonds are broken and thus decomplexation occurred.^{20,27} Dynamic contact angle measurements (using ultrapure water on SAMs **1** and **3**) show that after the surface reaction, the hydrophobicity and the contact angle hysteresis of the layer increased (for **3**, advancing angle (degree) of 52 ± 3 , receding angle of 22 ± 3 , for **1**, advancing angle of 28 ± 3 , and receding angle of 20 ± 3 were obtained). This strongly indicates that the pyrimidinone groups were successfully linked to the surface.

Pyrimidinone disulfide 4.

See Chapter 4: 2-(6-(2-ethyl-2'-hydroxyethyl dithio)hexylaminocarbonylamino) -6-methyl-4[1H]pyrimidinone.

Preparation of Substrates and Self-assembled Layers. Gold substrates (11 Δ 11 mm², 250 nm Au on 2 nm Cr on borosilicate glass) for SMFS measurements were purchased from Metallhandel Schröer GmbH (Lienen, Germany). Au(111) samples were obtained by annealing these substrates in a high purity H₂ flame for 5 minutes. Sample substrates for DPV experiments (200 nm gold on 2 nm Ti primer deposited onto glass substrates in a vacuum of 5 Δ 10⁻⁶ mbar) were purchased from SSENS bv (Hengelo, The Netherlands). Prior to use, these substrates were cleaned in piranha solution (3:1 H₂SO₄: H₂O₂ (30%) by volume), then rinsed with MilliQ water and ethanol and dried in a nitrogen stream. *Caution: Piranha solution should be handled with extreme caution: it has been reported to detonate unexpectedly.* Self-assembled layers were formed by immersing the gold substrates into dilute solutions of the corresponding compound solution for 10 hours (typical concentration: 1 mM). After rinsing with pure solvent and drying in an N₂ stream,²⁰ measurements were performed with minimal delay.

Differential Pulse Voltammetry Experiments (DPV).^{20,28} Measurements were performed using an Autolab PGSTAT10 potentiostat (ECOCHEMIE, Utrecht, The Netherlands) in a three electrode configuration. A gold substrate covered with the corresponding layer was used as the working electrode, Hg/HgSO₄ (MSE) was used as reference (+0.61 V_{NHE}). A Pt wire was employed as the auxiliary electrode. The electrolyte was 0.1 M NaClO₄. The working electrode exposed a surface area of 0.44 cm² to the electrolyte. Prior to the measurements, the cell was degassed by passing nitrogen through the electrolyte for 5 minutes. Differential pulse voltammograms were recorded at a pulse amplitude of 10 mV, a pulse time of 50 ms, and a time interval of 200 ms.

AFM and Tip Modification. The AFM measurements were carried out with a NanoScope IIIa multimode AFM (Digital Instruments (DI), Santa Barbara, CA) utilizing a liquid cell (DI). Triangular shaped silicon nitride cantilevers and silicon nitride tips (DI) coated with ca. 2 nm Ti and ca. 50 nm Au in high vacuum (SSENS b.v. Hengelo NL) were functionalized with a self-assembled monolayer of pyrimidinone disulfide **4** (no PEG linker). The loading rate was determined from the true force/time rate near the rupture events on force-extension curves.

The temperature of the liquid inside the liquid cell was controlled by a custom-made heating device. This heating device was based on a Peltier element assembled with epoxy glue (thermal conductivity 0.0002 W/cm K) onto an AFM sample disk. Samples of gold substrates

were attached directly over the Peltier element. The electrical and temperature measurements were performed using a DMM 3020 Digital Multimeter (Kontron Electronic). The Peltier was connected to a DC power supply (Delta Elecktronika) and a Fluke 52 II Thermometer using a K type thermocouple probe (Fluke). The temperature calibration of the heating device in air was performed using n-alkanoic acids (decanoic, dodecanoic, tetradecanoic and hexadecanoic, Aldrich) with known melting points. The temperature calibrations in water and hexadecane with liquid cell in AFM set-up were also performed by measuring the transient curves of the response time at different steps of increasing the applied current.²⁹

Force Data Analysis. Before fit the experimental curves to the m-FJC model, the deflection-piezo displacement data are transformed into actual force-extension (distance) curves. The slope (voltage/length) of the recorded trace (obtained from the AFM measurements, “force calibration” mode, reflecting the bending of the cantilever upon contacting and indenting the substrate surface) is determined. Following this, the real distance z between the AFM tip and the surface is obtained using $z = z_0 - 1/\text{slope} \Delta \text{Defl}$ (z_0 and Defl are the series of numbers representing the x and y axis of the raw DI data, respectively). Then, the spring constant, k_c , of the cantilever is determined from the thermal oscillation spectrum (“power spectrum density” in the DI software) of the cantilever (Chapter 2.3). The true force-extension (distance) curve, which is simply obtained by $F = k_c \Delta (z - z_0)$, can be finally plotted against distance z . After recording a set of force profiles in the way described above, the stretching lengths of the respective curves were determined by the extension length corresponding to ~ 250 pN (at this force, $> 80\%$ of the polymer chain is deemed to be fully stretched).

The fitting procedure using the m-FJC model was then carried out as follows: first, the extended Langevin function (equation 5.1) and the force-extension data are entered in Microsoft Excel. Followed by setting the “contour length” L (in equation 5.1) to the corresponding stretching length (x_L , Figure 5.8), the two fitting parameters Kuhn length and segment elasticity were determined. The statistical error of the fit can be calculated from the standard deviation between the fitted values and the experimental data. For force curves without any deviation at or close to zero extension on the retracting trace, the relative error can be as small as $\sim 10^{-5}$. However, if the recorded force curves shown an adhesion signal larger than 50 pN, the error of the fit could drastically increase. Thus an offset of the curve in either extension or force or both axes may be performed to decrease the error of fit. As an example, in the force trace shown below, the absolute force and extension values of the start fitting point A, must be set around zero by applying a simple linear shift of the original force-extension data, calculated using the commercial software e.g. IGOR Pro 4.0 (WaveMetrics, Inc.). The absolute values of the force

and the corresponding extension length are provided. Here, the “contour length” value for the fitting should be changed to the value of $x_L - x_0$. This change will not influence the fitting results as the Kuhn length and segment elasticity do not depend on the extension dependent. The fits can be superimposed to the original force curve.

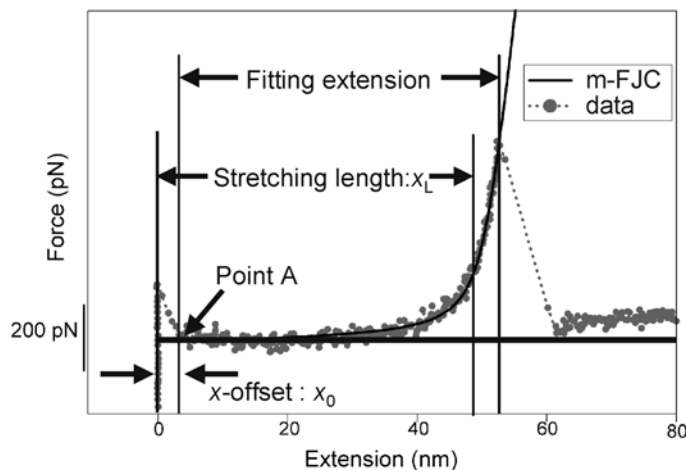


Figure 5.8. Force-extension curve (dotted line) with a superimposed fit to the m-FJC model (solid line).

5.7 Appendix

The value of the complexation constant of UPy complexes in 15% DMSO / chloroform has been reported to be as low as $\sim 50 \text{ M}^{-1}$. At 301 K, the rupture forces of individual quadruple hydrogen bonded UPy complexes were measured in the loading rate range between $\sim 15 \text{ nN/s}$ and $\sim 100 \text{ nN/s}$ in 15% DMSO / isopropanol. The rupture force versus loading rate data are plotted in Figure 5.9. The force data are *independent* of loading rates at 301 K in the range of $15 \text{ nN/s} \sim 100 \text{ nN/s}$ measured in 15% DMSO / isopropanol, indicating that the recorded rupture events occur at near-equilibrium situation, which is consistent with the expectation.

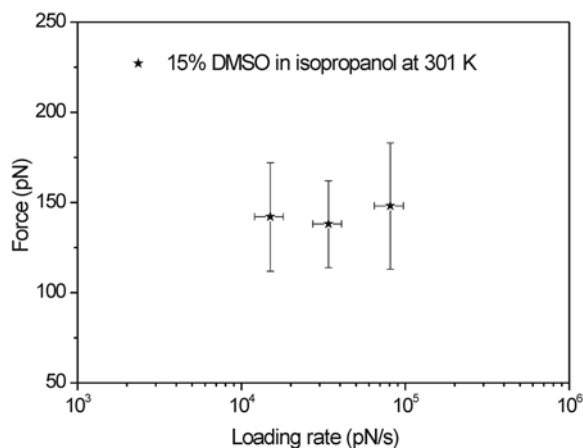


Figure 5.9. Plot of rupture force versus loading rate at 301 K in 15% DMSO in isopropanol.

Unexpectedly, the rupture force values measured in DMSO-isopropanol are ~ 135 pN, which is twice as high as the expected 65 pN.[‡] This may be due to the underestimated complexation constant of the surface immobilized UPy complexes in DMSO-isopropanol. Moreover, DMSO is a high viscosity solvent and the influence of the solvent was not taken into account during the determination of the rupture force values, which may also result in a deviation.

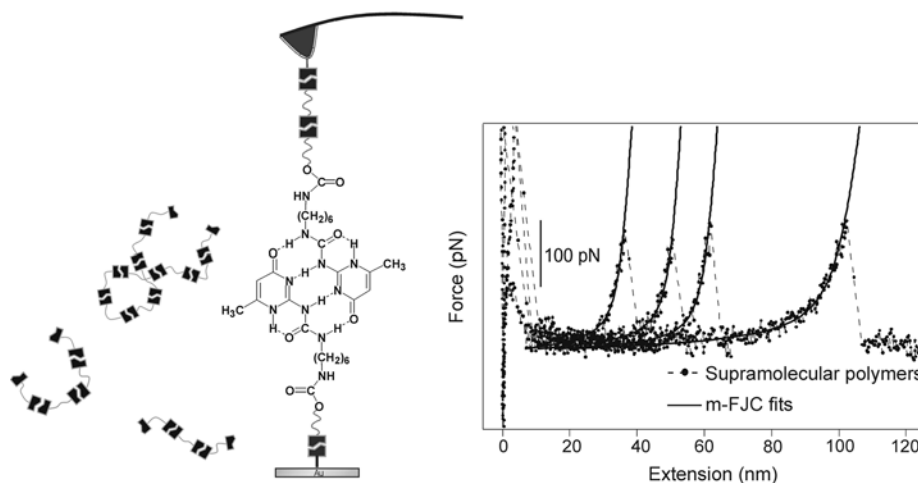
Reference:

- (1) Buckingham, A. D. *Principles of Molecular Recognition: Intermolecular Forces*; Chapman & Hall: London, 1993.
- (2) Cramer, F. *The Lock-and-Key Principle: Emil Fischer's Lock-and-Key Hypothesis after 100 Years*; John Wiley & Sons: Chichester, 1994.
- (3) Jeffrey, G. A.; Saenger, W. *Hydrogen Bonding in Biological Structures*; Springer-Verlag: Berlin, 1991.
- (4) Stryer, L. *Biochemistry*; 4th Ed.; W. H. Freeman and Company: New York, 1995.
- (5) Lehninger, A. L. *Biochemistry*; 2nd Ed.; Worth Publishers, Inc.: New York, 1979.
- (6) Israelachvili, J. N. *Intermolecular and Surface Forces*; 2nd Ed.; Academic Press, London, 1991.
- (7) Clausen-Schaumann, H.; Seitz, M.; Krautbauer, R.; Gaub, H. E. *Current Opinion in Chemical Biology* **2000**, *4*, 524-530.
- (8) Evans, E.; Heinrich, V.; Ludwig, F.; Rawicz, W. *Biophysical Journal* **2003**, *85*, 2342-2350.
- (9) Williams, P. M.; Moore, A.; Stevens, M. M.; Allen, S.; Davies, M. C.; Roberts, C. J.; Tendler, S. J. B. *Journal of the Chemical Society-Perkin Transactions 2* **2000**, 5-8.
- (10) Evans, E.; Ritchie, K. *Biophysical Journal* **1997**, *72*, 1541-1555.
- (11) Evans, E. *Annual Review of Biophysics and Biomolecular Structure* **2001**, *30*, 105-128.
- (12) Merkel, R.; Nassoy, P.; Leung, A.; Ritchie, K.; Evans, E. *Nature* **1999**, *397*, 50-53.
- (13) Lee, G. U.; Chrisley, L. A.; Colton, R. J. *Science* **1994**, *266*, 771-773.
- (14) Florin, E. L.; Moy, V. T.; Gaub, H. E. *Science* **1994**, *264*, 415-417.
- (15) Janshoff, A.; Neitzert, M.; Oberdorfer, Y.; Fuchs, H. *Angewandte Chemie-International Edition* **2000**, *39*, 3213-3237.
- (16) Hugel, T.; Seitz, M. *Macromolecular Rapid Communications* **2001**, *22*, 989-1016.
- (17) Zhang, W.; Zhang, X. *Progress in Polymer Science* **2003**, *28*, 1271-1295.
- (18) Hinterdorfer, P.; Kienberger, F.; Raab, A.; Gruber, H. J.; Baumgartner, W.; Kada, G.; Riener, C.; Wielert-Badt, S.; Borcken, C.; Schindler, H. *Single Molecules* **2000**, *1*, 99-103.
- (19) Kienberger, F.; Pastushenko, V. P.; Kada, G.; Gruber, H. J.; Riener, C.; Schindler, H.; Hinterdorfer, P. *Single Molecules* **2000**, *1*, 123-128.
- (20) Zou, S.; Zhang, Z. H.; Förch, R.; Knoll, W.; Schönherr, H.; Vancso, G. J. *Langmuir* **2003**, *19*, 8618-8621.
- (21) Oesterhelt, F.; Rief, M.; Gaub, H. E. *New Journal of Physics* **1999**, *1*, 6.1.
- (22) ten Cate, A. T.; Sijbesma, R. P. *Macromolecular Rapid Communications* **2002**, *23*, 1094-1112.
- (23) Beijer, F. H.; Sijbesma, R. P.; Kooijman, H.; Spek, A. L.; Meijer, E. W. *Journal of the American Chemical Society* **1998**, *120*, 6761-6769.
- (24) Sontjens, S. H. M.; Sijbesma, R. P.; van Genderen, M. H. P.; Meijer, E. W. *Journal of the American Chemical Society* **2000**, *122*, 7487-7493.
- (25) Beijer, F. H.; Kooijman, H.; Spek, A. L.; Sijbesma, R. P.; Meijer, E. W. *Angewandte Chemie-International Edition* **1998**, *37*, 75-78.
- (26) Folmer, B. J. B.; Sijbesma, R. P.; Versteegen, R. M.; van der Rijt, J. A. J.; Meijer, E. W. *Advanced Materials* **2000**, *12*, 874-878.
- (27) Peter, M.; Hempenius, M. A.; Lammertink, R. G. H.; Vancso, G. J. *Macromolecular Symposia* **2001**, *167*, 285-296.
- (28) Kaifer, A. E. G.-K. *Supramolecular Electrochemistry*; Wiley-VCH; Weinheim, 1999.
- (29) Vera, I. J. *Research Project Report*; University of Twente: Enschede, 2004.

[‡] The most probable rupture force at near-equilibrium can be estimated as: $f_{\cup} \sim \Psi \rho_s k_B T \ln / K_{eq} \Phi^2$, for details see Chapter 2.2.2. Here, $\rho_s = 125$ pN/nm, $K_{eq} = 55$.

Chapter 6

Stretching and Rupturing Individual Supramolecular Macromolecules by Force Spectroscopy*



The unbinding behavior of single supramolecular polymer chains based on quadruple hydrogen-bonds between 2-ureido-4[1H]-pyrimidinone (UPy) moieties was studied by atomic force microscopy (AFM)-based force spectroscopy. The stretching of poly(ethylene glycol) (PEG) spacers in reversible supramolecular polymer chains and rupture forces of individual UPy complexes were probed in AFM force-displacement (*f-d*) measurements in hexadecane. In the presence of a bis-UPy PEG derivative, *f-d* curves recorded with AFM tips and Au substrates both functionalized with a short chain UPy disulfide revealed stretching lengths of macromolecules up to 180 nm. The elasticity parameters of the stretched chains (Kuhn length of 0.68 ± 0.08 nm and segment elasticity of 7.6 ± 2.5 nN/nm) were equal to the values obtained in dimer experiments (Chapter 5). The mean value of the rupture forces of single UPy complexes observed for the supramolecular polymers in hexadecane of 173 ± 26 nN (at a loading rate of 35 nN/s, 301 K) was to within the error the same as the rupture force of the dimeric complex (180 pN ± 23 , Chapter 5). The rupture forces decreased with increasing rupture length in agreement with the theory by Evans *et al.* The observation of stretching events, which were attributed to the probing of individual supramolecular polymers, opens the pathway to elucidate properties of these dynamic, reversibly aggregated polymers as a function of various external parameters at the single molecule level.

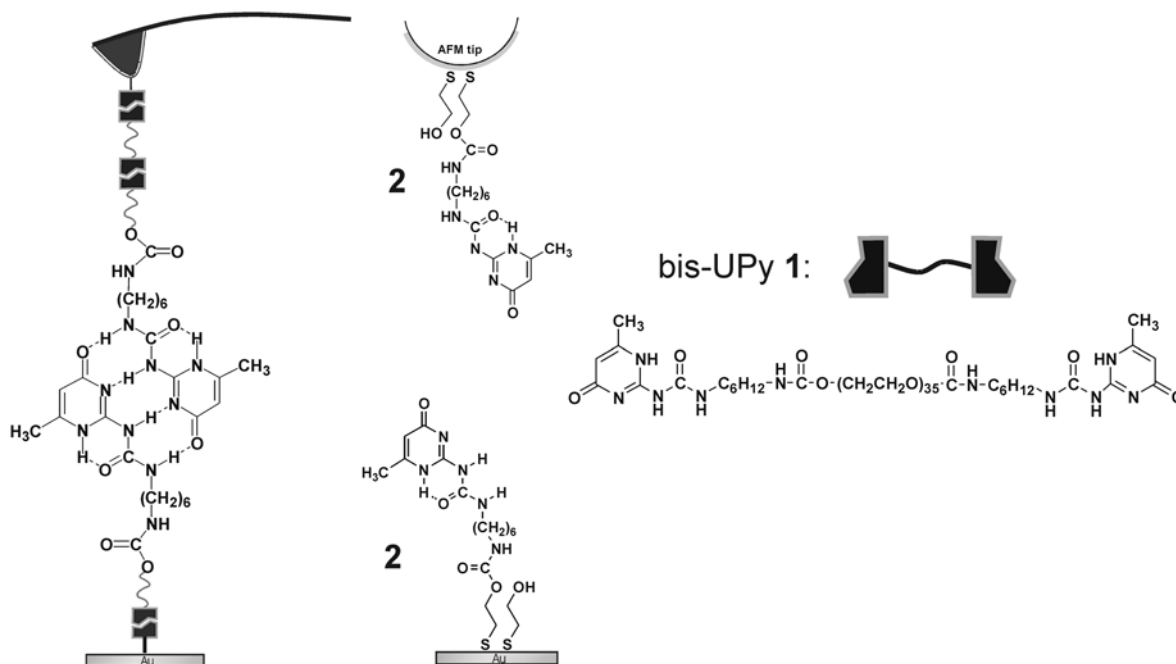
6.1 Introduction

Inspired by nature, supramolecular chemistry utilizes multiple, reversible cooperative intermolecular interactions, such as hydrogen bonding, to fabricate self-organized structures with a very rich structural hierarchy.^{1,2} The corresponding intermolecular interactions (forces)³ govern the interplay of order and mobility,⁴ as well as the properties *and* functionality (recognition, reaction, transport, regulation etc.) in such systems.⁵⁻⁹

* Part of the results in this Chapter has been published: Zou, S.; Schönherr, H.; Vancso, G. J. *Angew. Chem. Int. Ed.*, **2005**, in press (DOI:10.1002/anie.200460963).

In recent years, supramolecular polymers¹⁰⁻¹² (also called reversible polymers), comprised of bi-functional monomeric units that are reversibly aggregated via relatively strong non-covalent interactions,¹³⁻¹⁸ were described. A prime example are the supramolecular polymers formed via self-complementary recognition of the quadruple hydrogen-bonded 2-ureido-4[1H]-pyrimidinone (UPy) motif, introduced by Meijer, Sijbesma, and co-workers.^{11,12,19-21} Owing to the highly dynamic character of the aggregation, these materials possess a truly unique combination of tunable properties, such as viscosity, composition and effective chain length on one hand, and short equilibration times on the other hand.¹¹ Even though these properties are a direct consequence of the presence of multiple weak interactions, typically the equilibrium complexation constants and complex life-times serve as measures for the strength of the interactions.²² Recently, theoretical work by van der Gucht et al.²³ shed some light on forces between surfaces in the presence of reversible polymers. From an experimental point of view, however, little is known about the actual underlying inter- and intra-molecular forces, in particular those that are present in supramolecular polymers.²⁴

AFM-based single molecule force spectroscopy (SMFS)²⁵⁻³⁶ appears to be suitable to address interaction forces and to directly probe *individual* supramolecular polymer chains. As illustrated in Scheme 6.1, such experiments would involve the probing of a dynamic "macromolecule" that is comprised of reversibly aggregated self-complementary building blocks (e.g. bis-UPy **1**).



Scheme 6.1. Scheme of the investigated system. Supramolecular polymers, which are formed by self-complementary association of the bifunctional PEG derivative **1**, can be probed by AFM utilizing gold coated AFM tips and Au(111) substrates both functionalized with SAMs of the asymmetrically substituted UPy disulfide **2** in hexadecane.

In this Chapter, the interactions between individual surface-immobilized pyrimidinone moieties³⁷ and the stretching of reversible supramolecular polymer chains were probed in AFM force-displacement measurements in hexadecane and DMSO / isopropanol mixtures. Our results open the pathway to elucidate the properties of these dynamic, reversibly aggregated polymers as a function of various external parameters on the molecular scale.

6.2 Stretching and Rupturing of Individual Supramolecular Polymers

The systematic investigation of the single chain mechanical properties of supramolecular polymers formed via self-complementary quadruple hydrogen-bonds of 2-ureido-4[1H]-pyrimidinones is an extension of the measurements of the *individual* molecular interactions present in these supramolecular polymers, as discussed in Chapter 5. The rupture force of a pair of self-complementary UPy moieties mediated by quadruple hydrogen bonds is 180 ± 21 pN in hexadecane at 301 K, measured with a loading rate of 35 pN/s (see Chapter 5.3). The typical extension length, corresponding to one PEG spacer, is about 12 nm. The mechanical properties of PEG spacers in **1** are known from the literature^{38,39} and were confirmed in Chapter 5 with a Kuhn length of 0.65 ± 0.08 nm and a segment elasticity of 6.2 ± 0.6 nN/nm.

In order to probe the single chain mechanical properties of UPy-based *supramolecular polymers*, SMFS measurements were carried out with tips and substrates both modified with the short chain UPy disulfide **2**³⁷ in the presence of bis-UPy **1** ($\sim 10^{-3}$ mM) in hexadecane (Scheme 6.1). Owing to the high complexation constant of $\sim 10^9$ M⁻¹ and a life time in excess of seconds (Chapter 5),^{21,22} bis-UPy will form supramolecular polymers with an effective degree of polymerization of ~ 40 in solution (see also section 6.4).

Figure 6.1A shows typical force-extension curves measured under these experimental conditions. Significant restoring forces were observed for extensions > 30 nm. From fits to the modified freely jointed chain model (m-FJC, equation 6.1)[†], a Kuhn length of 0.68 ± 0.08 nm and a segment elasticity of 7.6 ± 2.5 nN/nm were obtained, respectively. The elasticity parameters are to within the experimental error equal to the data measured for a single PEG chain, indicating that a *single* PEG "chain" is being stretched. The force-extension curves were normalized by the extension that refers to a force value of 150 pN, as shown in Figure 6.1B. The

[†] The m-FJC model describes extension x as function of force F :

$$x(F) = \left[\coth\left(\frac{FI_K}{k_B T}\right) - \frac{k_B T}{FI_K} \right] \left[L_{\text{contour}} - 2 \frac{n}{K_{\text{segment}}} F \right] \quad 6.1$$

where x is the extension of the polymer chain, F is the applied force; I_K (Kuhn length) is the length of the statistically independent segment, n is the number of segments, which equals to L_{contour}/I_K ; K_{segment} is segment elasticity, which characterizes the deformability of the segment; k_B is the Boltzmann constant; and T is the temperature.

set of normalized curves superimposes well, confirming that individual PEG chains were stretched.

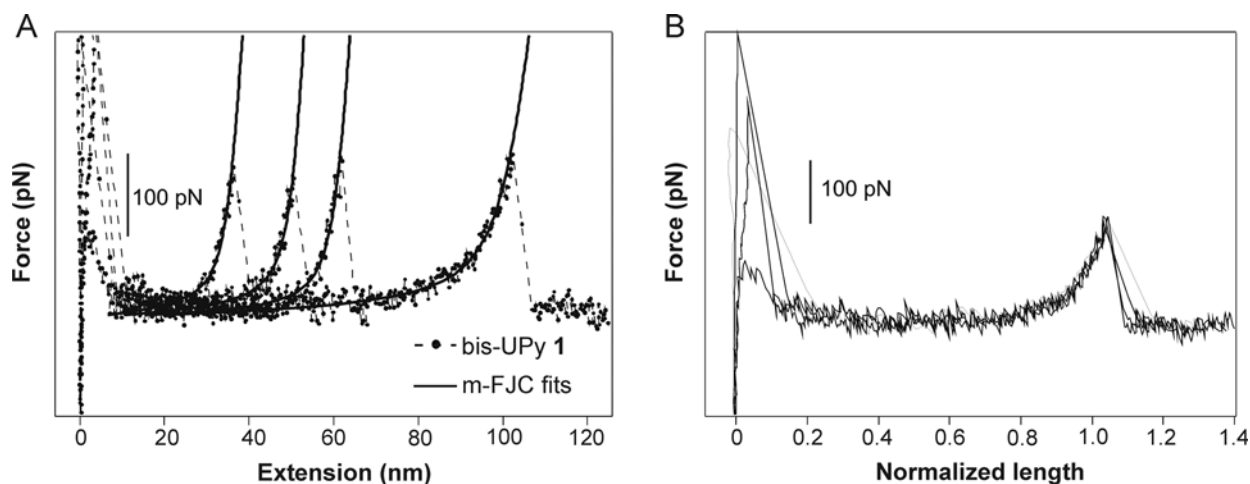


Figure 6.1. (A) Force-extension curves measured between gold-coated AFM tip and Au(111) sample functionalized both with layers of the short chain UPy-disulfide **2** in the presence of the bifunctional bis-UPy PEG derivative **1** in hexadecane at 301 K, loading rate ~ 35 nN/s. The fits of the data to the m-FJC model are shown as solid lines. (B) Superposition of normalized force curves shown in (A).

Figure 6.2 shows the histogram of observed pull-off forces at loading rate of ~ 35 nN/s (301 K, in hexadecane). The mean value of the rupture forces observed in these experiments of 173 ± 26 pN is to within the error equal to the rupture force of the dimeric complex (~ 180 pN, Chapter 5.3).

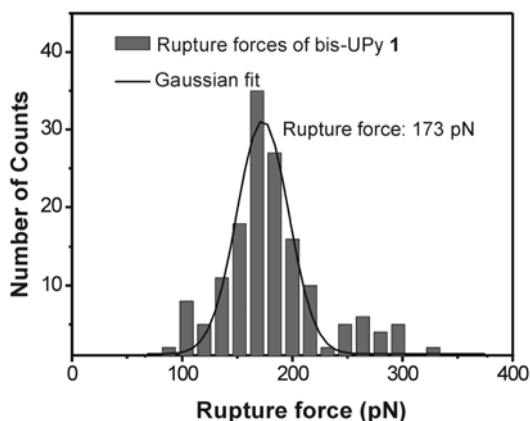


Figure 6.2. Histogram of rupture forces observed in single macromolecule stretching experiments between gold-coated AFM tip and Au(111) sample functionalized both with layers of short chain UPy-disulfide **2** in the presence of bis-UPy PEG derivative **1** in hexadecane (loading rate: ~ 35 nN/s, 301 K).

From the histogram of measured rupture lengths, shown in Figure 6.3A, it can be seen that stretching events of more than 150 nm were detected in hexadecane. These lengths correspond to a "degree of polymerization" of up to 15, assuming a "monomer length" of 12 nm. The significantly longer stretching lengths (\gg contour length of a single PEG segment: ~ 12 nm, Figure 6.3A) indicate that supramolecular polymers were directly probed, which appears to be

reasonable considering the lifetimes (~ 7 seconds) of UPy complexes in hexadecane (Chapter 5.4). By contrast, f-d curves recorded in 15% DMSO in isopropanol (Figure 6.3B) showed a markedly different stretching length distribution.^{11,19} In this case, only very short chains (~ 15 nm) were stretched, similar to the data observed for the dimer experiment in hexadecane (Figure 6.3A, dimer results).

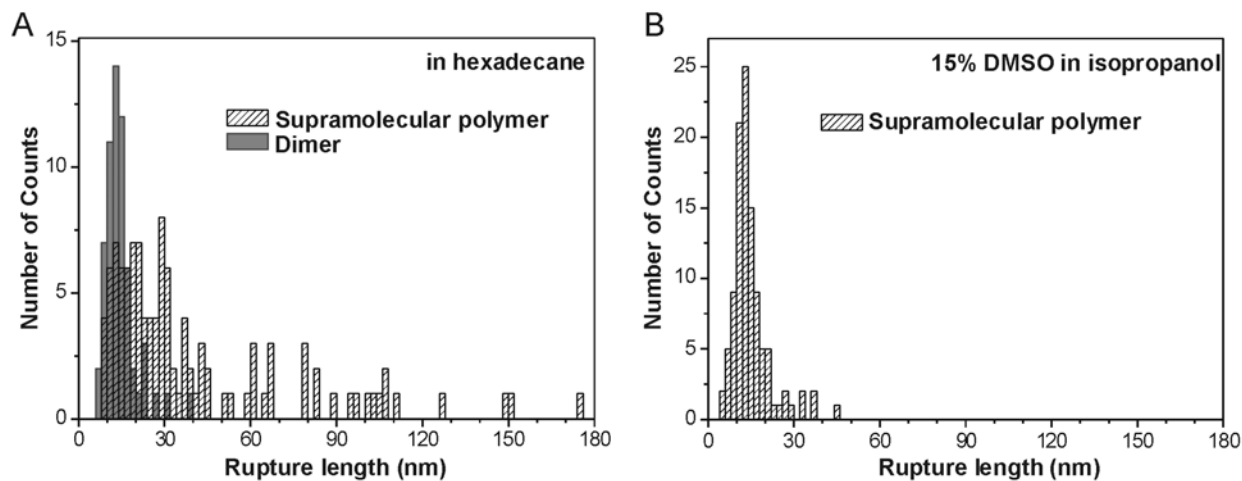


Figure 6.3. Histogram of rupture lengths observed for the experiment (A) probing the interaction of supramolecular polymers and dimers in hexadecane at 301 K; (B) probing the supramolecular polymer in 15% DMSO / isopropanol at 301 K.

A very similar reduction in rupture lengths was observed in blocking experiments with a trifluoromethyl functionalized UPy derivative **3**. The rupture forces of UPy complexes vs the corresponding stretching lengths in the supramolecular polymers in the presence and absence of **3** are plotted in Figure 6.4A.

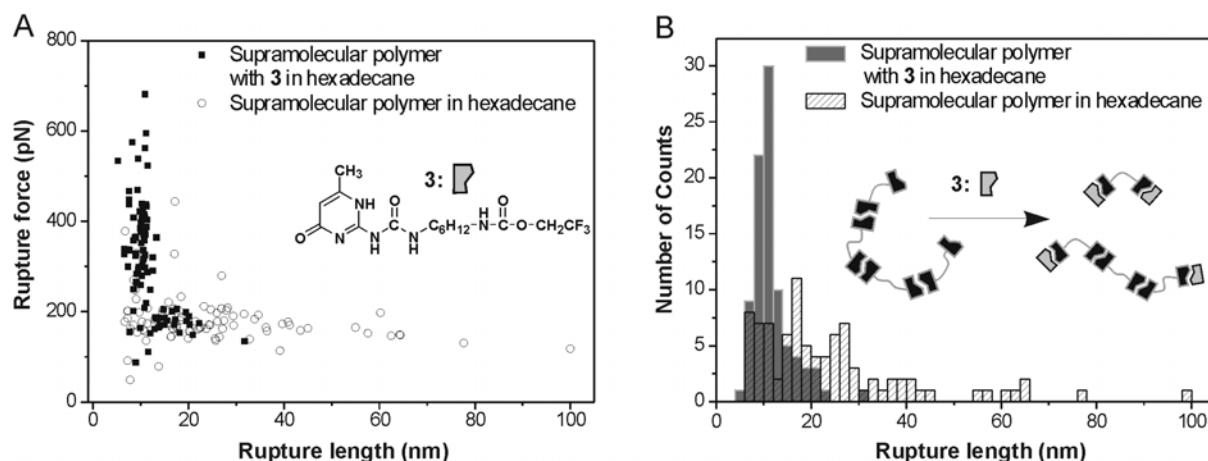


Figure 6.4. (A) Rupture forces vs rupture lengths and (B) histograms of rupture lengths observed for UPy supramolecular polymers in hexadecane with and without end capper **3** (0.5 mM).

The addition of the chain stopper **3** (0.5 mM in hexadecane) significantly reduces the mean stretching length observed for the supramolecular polymers (21 ± 14 nm in the absence of **3** in

hexadecane) to lengths consistent with a single PEG chain (11 ± 4 nm in the presence of **3**), as shown in Figure 6.4B. The rupture forces observed in the presence of **3** are partially increased likely due to the effect of the trifluoromethyl end group of **3**. A small population of forces located around ~ 180 pN (Figure 6.3A), however, may suggest some residual dimerization (mean rupture forces: 184 ± 45 pN in the absence of **3**[‡] vs 317 ± 125 pN in the presence of **3**). This residual dimerization is consistent with the long complex lifetimes in hexadecane and the limited concentration of **3** in the solution owing to limited solubility.

6.3 Discussion

The significantly longer stretching lengths (Figure 6.3A) compared to the dimer experiments and the markedly different stretching length distributions in the blocking experiments in hexadecane (Figure 6.4B), as well as the short chains stretched in 15% DMSO isopropanol (Figure 6.3B), indicate that individual supramolecular polymers were addressed by SMFS. The rupture forces observed for the complexes in supramolecular polymers of ~ 173 pN and for dimers of ~ 180 pN in hexadecane were found to decrease slightly with increasing length of the stretched supramolecular polymer chain. Figure 6.5 shows a plot of the observed rupture forces (at a loading rate of 35 nN/s) vs. the number of PEG-linkers N . The rupture force values decrease with increasing number of stretched PEG linkers.

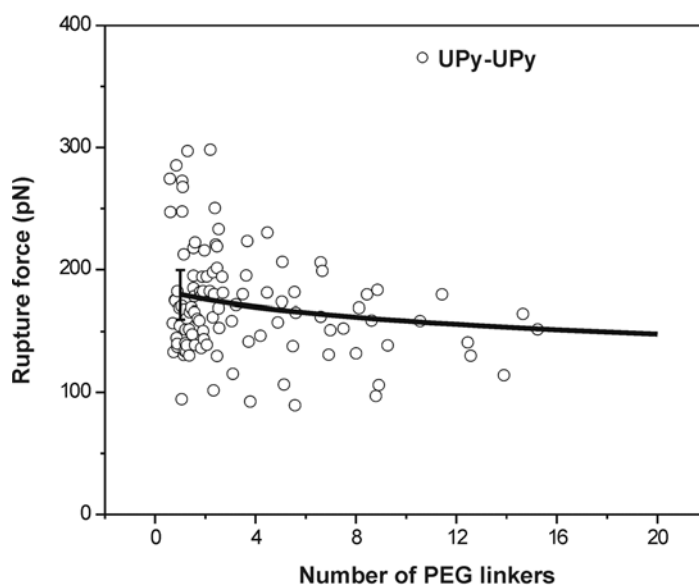


Figure 6.5. Plot of rupture forces observed for UPy supramolecular polymers in hexadecane vs. the number of PEG linkers (N) at loading rate of 35 nN/s, 301 K. The solid line is the predicted relation for rupture forces of N independent bonds in series.

[‡] In this particular data set, the mean rupture forces of individual bis-UPy complexes of 173 ± 20 pN were determined from the maximum of the rupture force distribution after excluding rupture forces attributed to non-specific adhesion (forces > 300 pN).

This observation is in full agreement with theoretical considerations based on the model developed by Evans and coworkers.⁴⁰⁻⁴³ The predicted dependence of the so-called most probable rupture force f^* of N independent bonds in series (equation 6.2) is overlaid on the plot of rupture forces vs. the number of PEG linkers N , as shown in Figure 6.5.

$$f^* = f \Psi(r_f / 4 \ln(N) \beta) / f_{\text{single}} \quad (6.2)$$

where r_f denotes the loading rate and f the thermal scale force (the slope of ~ 19 pN was determined from the rupture force vs. loading rate plot, see also Figure 5.4), and f_{single}^* equals to 180 pN as obtained in the dimer studies (Chapter 5.3).

Stretching lengths of supramolecular polymers of up to 180 nm were detected in hexadecane. The plot of frequency of extension events vs number of repeat units in the stretched supramolecular polymers, calculated based on the length of one repeat unit, assuming a “monomer length” of 12 nm (Figure 6.6), suggests that the probability to stretch a supramolecular polymer chain that bridges the gap between substrate and tip is an exponential function of the chain length.

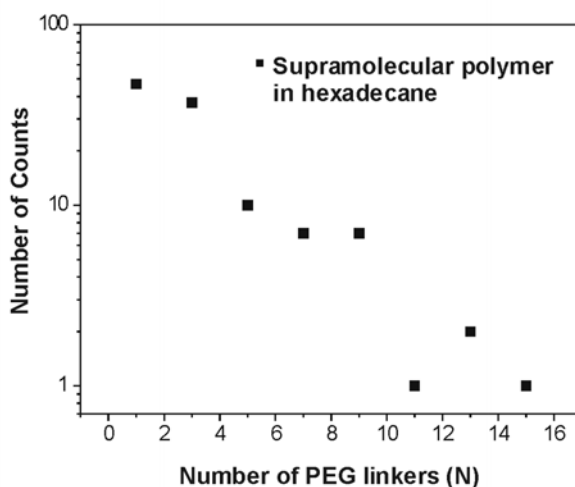


Figure 6.6. Frequency of rupture events vs number of repeat units in stretched supramolecular polymers (Figure 6.3A, supramolecular polymers) calculated based on the length of one repeat unit observed in hexadecane.

We observed in our AFM experiments that supramolecular polymers with a chain length as long as 15 monomer units were stretched. Based on the model described in Chapter 6.6 (appendix), we would expect a value of ~ 40 in solution (Figure 6.7). However, independent of the length an exponential decay of the distribution of effective length vs. degree of polymerization is expected based on the model (Figure 6.7 inset). The sampling of the rupture length in the AFM experiment may lead to an underestimation since the attachment sites for the telechelic UPy derivatives on the AFM tip are not restricted to the very end of the tip, while the

supramolecular polymer "chain" may also be attached to the substrate at a location outside the tip - sample contact area.

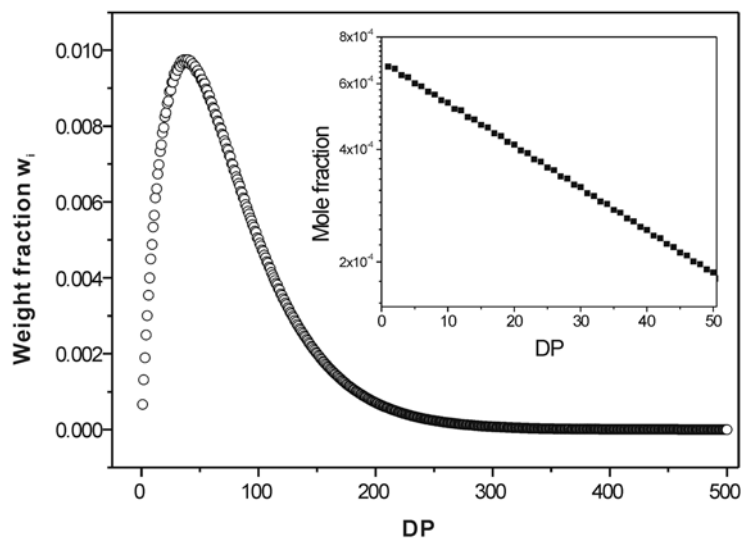


Figure 6.7. Calculated weight fraction (inset: mole fraction) vs degree of polymerization (DP) for bis-UPy **1** in 10^{-3} mM hexadecane solution (details: see section 6.6).

6.4 Conclusions

The AFM data discussed in this Chapter show that supramolecular polymers can indeed be investigated at the single molecule level. In PEG-based UPy supramolecular polymer materials, the individual reversible linking sites along a supramolecular polymer chain, i.e. the complexes based on self-complementary recognition of 2-ureido-4[1H]-pyrimidinone, act as independent bonds in series. The rupture force of an individual self-complementary UPy complex in supramolecular polymers was measured to be ~ 173 pN at a loading rate of 35 pN/s. Since the material properties, including viscosity, composition, and chain length, are functions of various external parameters and stimuli, which can be investigated in situ, highly useful information for the design and construction of nanometer scale devices and stimuli-responsive systems will now become directly accessible from SMFS experiments.

6.5 Experimental

General Methods. The ^1H -NMR spectra were recorded on a Bruker AC 250 spectrometer (250 MHz). ^1H -NMR chemical shifts are given relative to residual CHCl_3 (7.25 ppm). FT-IR spectroscopy data were collected on a BIO-RAD model FTS575C FT-IR spectrometer.

Synthesis. All experiments were performed under an argon atmosphere. Chloroform was dried with molsieves. Commercial products were used without further purification unless mentioned.

PEG linked bis-pyrimidinone **1** was synthesized according to published procedures.⁴⁴ To a solution of 5 mmol PEG (Fluka, $M_n = 1600$ g/mol, $M_w = 1690$ g/mol, PDI = 1.06, as confirmed by independent GPC measurements) in 200 mL chloroform, 22 mmol (6-isocyanatohexylaminocarbonylamino)-6-methyl-pyrimidinone **4** (see Chapter 4.6) was added. After addition of one drop of dibutyltindilaurate (Aldrich), the resulting solution was refluxed and stirred for 24 hours. 250 mL chloroform was added and the solution was filtered. After concentrating the solution back to 150 mL, 1 gram of silica (Merck kieselgel 60) and 1 drop of dibutyltindilaurate were added, and the mixture was heated at 60°C for one hour. The silica was removed by filtration and the chloroform was removed under reduced pressure. The resulting material was dried under reduced pressure. The absence of **4** in the material was checked by FT-IR spectroscopy. Precipitation of polymers from chloroform into methanol yields the pure telechelic polymer **1** (yield: 55%). ¹H-NMR (250 MHz, CDCl₃): 13.1 (s, 2H, CH₃-C-NH), 11.9 (s, 2H, CH₂-NH-(C=O)-NH), 10.1 (s, 2H, CH₂-NH-(C=O)-NH), 5.8 (s, 2H, CH=C-CH₃), 4.9 (br.s., 2H, NH-(C=O)-O), 4.2 (t, 4H, CH₂-O-(C=O)), 3.7 - 3.3 (m, ~144H, CH₂-CH₂-O; 4H, CH₂-NH-(C=O)-NH), 3.2 (m, 4H, CH₂-NH(C=O)-O), 2.2 (s, 6H, CH₃-C=CH), 1.6-1.4 (m, 16H, CH₂-CH₂-CH₂). IR (KBr): 3322, 3226, 3046, 2956, 2930, 2869, 1705, 1670, 1595, 1534, 1455, 1350, 1251, 1146, 1108, 951, 845 cm⁻¹.

Trifluoromethyl functionalized UPy derivative **3**: see Chapter 4, 2-(6-trifluoroethylhexylaminocarbonylamino)-6-methyl-4[1H]pyrimidinone **3**.

Preparation of Substrates for SAM Characterization. Gold substrates (11 Δ 11 mm², 250 nm Au on 2 nm Cr on borosilicate glass) for SMFS measurements were purchased from Metallhandel Schröer GmbH (Lienen, Germany). Au(111) samples were obtained by annealing these substrates in a high purity H₂ flame for 5 minutes. Prior to use, these substrates were cleaned in piranha solution (3:1 H₂SO₄: H₂O₂ (30%) by volume), then rinsed with MilliQ water and ethanol and dried in a nitrogen stream. *Caution: Piranha solution should be handled with extreme caution: it has been reported to detonate unexpectedly.*

Preparation of Monolayers. Monolayers were formed by immersing the gold substrates into dilute solution of the corresponding compound and solvent for 10 hours (typical concentration: 1 mM). After rinsing with pure solvent and drying in an N₂ stream, the measurements were performed with minimal delay.³⁷

AFM and Tip Modification. The AFM measurements were carried out with a NanoScope IIIa multimode AFM Digital Instruments (DI), Santa Barbara, CA utilizing a liquid cell (DI). Triangular shaped silicon nitride cantilevers and silicon nitride tips (DI) coated with ca. 2 nm Ti and ca. 50 nm Au in high vacuum (SSENS b.v. Hengelo NL) were functionalized with a self-assembled monolayer of pyrimidinone disulfide **2** (no PEG linker).³⁷ The loading rate was determined from the f-d curves based on linear fitting to the last 10 experimental points prior to rupture.

6.6 Appendix: Model for Degree of Polymerization

Assume that the association constants k_i for all n -mers are identical, which are denoted as k . The same assumption is made for all the dissociation constants $k_{\mathcal{N}}$, denoted as $k_{\mathcal{N}}$. The maximum repeat unit N in the n -mer is infinite; the time derivatives of the concentrations of different n -mers can be described as,

$$\begin{aligned} \frac{d[A_1]}{dt} &= 4k[A_1]^2 - 4k[A_1][A_2] - 4k[A_1][A_3] - 4k[A_1][A_4] - \dots \\ \frac{d[A_2]}{dt} &= k[A_1]^2 - 4k[A_2][A_1] - 4k[A_2][A_3] - 4k[A_2][A_4] - \dots \\ \frac{d[A_3]}{dt} &= k[A_1][A_2] - 4k[A_3][A_1] - 4k[A_3][A_2] - 4k[A_3][A_4] - \dots \\ \frac{d[A_4]}{dt} &= k[A_1][A_3] - 4k[A_4][A_1] - 4k[A_4][A_2] - 4k[A_4][A_3] - \dots \\ &\dots \\ \frac{d[A_n]}{dt} &= k \prod_{i=1}^{n/2} [A_i] - 4k[A_n] \prod_{i=1}^N (1 - \tau_{i,n}) [A_i] - (n-4)k_{\mathcal{N}} [A_n] + 2k_{\mathcal{N}} \prod_{i=1}^{n-2} [A_i] \end{aligned}$$

where the brackets represent concentrations. The initial concentration of monomer is equal to $[A_0]$, and mass concentration therefore yields $[A_0] = \sum_{i=1}^N [A_i]$. In the equilibrium situation, the left-hand side of above equations is equal to zero.

Defining the n variables $D_n = \prod_{i=1}^N [A_i]$, the above equations can be rewritten as:

$$\frac{d[A_1]}{dt} = 4k[A_1]^2 - 4k[A_1]D_2 - 2k_{\mathcal{N}}D_2 = 0 \quad \heartsuit \quad D_2 = \frac{2k[A_1]^2}{2k_{\mathcal{N}} - k[A_1]}$$

(note that D_n is finite and positive, hence $[A_1] \in (0, 2k_{\mathcal{N}}/k)$)

$$\frac{d[A_2]}{dt} = k[A_1]^2 - 4k[A_2]D_1 - 4k[A_2]^2 - 4k[A_2]k[A_2] - 2k[A_2]D_3 = 0 \quad \heartsuit \quad D_1 = D_2 + 2[A_1], \quad D_3 = D_2 + 4[A_2]$$

$$\frac{d[A_n]}{dt} = k \frac{n/2}{i+1} [A_i][A_{n-4i}] - 4k[A_n]D_1 - 4k[A_n]^2 - 4(n-4)k[A_n]k[A_n] - 2k[A_n]D_n = 0$$

$$\text{So, } k[A_n]^2 + 2\{kD_1 + 2(n-4)k\}[A_n] + 4k \frac{n/2}{i+1} [A_i][A_{n-4i}] - 4kD_n = 0$$

Once the ratio of k/k_{off} and the initial monomer concentration $[A_0]$ are known, the equilibrium concentration of n -mer in the solution can be worked out *numerically* with an initial guess of $[A_1]$.

Figure 6.7 shows the calculated weight fraction (inset: mole fraction) vs degree of polymerization based on the numerical solution of $[A_n]$ with an initial concentration of 10^{-3} mM for bis-UPy and $\frac{k}{k_{\text{off}}} = 10^9 \text{ M}^{-1}$. The average degree of polymerization is around 40.

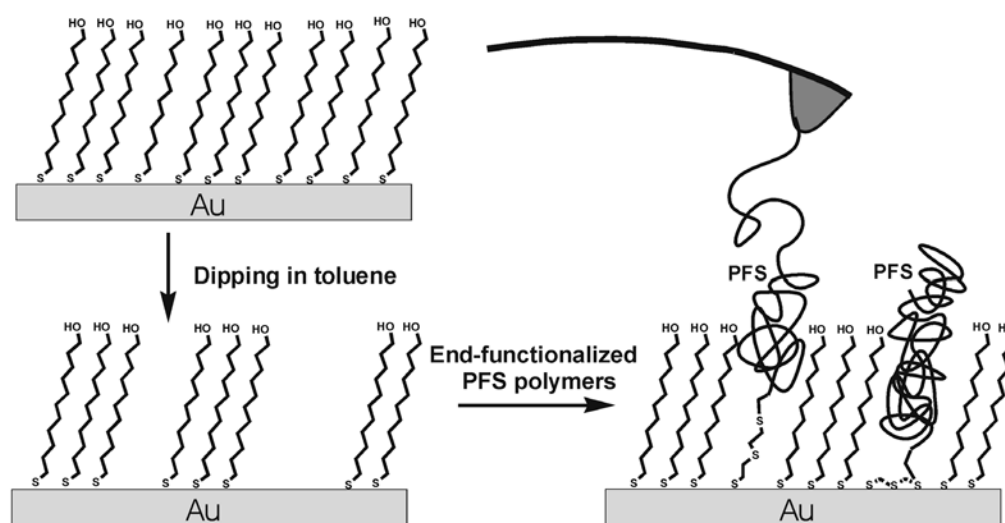
References:

- (1) Lehn, J. M. *Supramolecular Chemistry: Concepts and Perspectives*; John Wiley & Sons: New York, 1995.
- (2) Reinhoudt, D. N. (Ed.) *Supramolecular Materials and Technologies*; John Wiley & Sons: New York, 1999.
- (3) Israelachvili, J. N. *Intermolecular and Surface: With Applications to Colloidal and Biological Systems*; Academic Press: New York, 1991.
- (4) Ringsdorf, H.; Schlarb, B.; Venzmer, J. *Angewandte Chemie-International Edition* **1988**, *27*, 113-158.
- (5) Buckingham, A. D. *Principles of Molecular Recognition: Intermolecular Forces*; Chapman & Hall: London, 1993.
- (6) Cramer, F. *The Lock-and-Key Principle: Emil Fischer's Lock-and-Key Hypothesis After 100 Years*; John Wiley & Sons: Chichester, 1994.
- (7) Cooke, G.; Rotello, V. M. *Chemical Society Reviews* **2002**, *31*, 275-286.
- (8) Lehn, J. M. *Science* **2002**, *295*, 2400-2403.
- (9) Reinhoudt, D. N.; Crego-Calama, M. *Science* **2002**, *295*, 2403-2407.
- (10) Lehn, J. M. *Makromolekulare Chemie-Macromolecular Symposia* **1993**, *69*, 1-17.
- (11) Sijbesma, R. P.; Beijer, F. H.; Brunsveld, L.; Folmer, B. J. B.; Hirschberg, J.; Lange, R. F. M.; Lowe, J. K. L.; Meijer, E. W. *Science* **1997**, *278*, 1601-1604.
- (12) Brunsveld, L.; Folmer, B. J. B.; Meijer, E. W.; Sijbesma, R. P. *Chemical Reviews* **2001**, *101*, 4071-4097.
- (13) Drain, C. M.; Russell, K. C.; Lehn, J. M. *Chemical Communications* **1996**, 337-338.
- (14) Mathias, J. P.; Simanek, E. E.; Whitesides, G. M. *Journal of the American Chemical Society* **1994**, *116*, 4326-4340.
- (15) Vreekamp, R. H.; vanDuynhoven, J. P. M.; Hubert, M.; Verboom, W.; Reinhoudt, D. N. *Angewandte Chemie-International Edition* **1996**, *35*, 1215-1218.
- (16) Corbin, P. S.; Zimmerman, S. C. *Journal of the American Chemical Society* **1998**, *120*, 9710-9711.
- (17) Gong, B.; Yan, Y. F.; Zeng, H. Q.; Skrzypczak-Jankun, E.; Kim, Y. W.; Zhu, J.; Ickes, H. *Journal of the American Chemical Society* **1999**, *121*, 5607-5608.
- (18) Boileau, S.; Bouteiller, L.; Laupretre, F.; Lortie, F. *New Journal of Chemistry* **2000**, *24*, 845-848.
- (19) Beijer, F. H.; Kooijman, H.; Spek, A. L.; Sijbesma, R. P.; Meijer, E. W. *Angewandte Chemie-International Edition* **1998**, *37*, 75-78.
- (20) Beijer, F. H.; Sijbesma, R. P.; Kooijman, H.; Spek, A. L.; Meijer, E. W. *Journal of the American Chemical Society* **1998**, *120*, 6761-6769.
- (21) ten Cate, A. T.; Sijbesma, R. P. *Macromolecular Rapid Communications* **2002**, *23*, 1094-1112.
- (22) Sontjens, S. H. M.; Sijbesma, R. P.; van Genderen, M. H. P.; Meijer, E. W. *Journal of the American Chemical Society* **2000**, *122*, 7487-7493.
- (23) van der Gucht, J.; Besseling, N. A. M.; Fleer, G. J. *Journal of Chemical Physics* **2003**, *119*, 8175-8188.

- (24) Kersey, F. R.; Lee, G.; Marszalek, P.; Craig, S. L. *Journal of the American Chemical Society* **2004**, *126*, 3038-3039.
- (25) Hugel, T.; Seitz, M. *Macromolecular Rapid Communications* **2001**, *22*, 989-1016.
- (26) Janshoff, A.; Neitzert, M.; Oberdorfer, Y.; Fuchs, H. *Angewandte Chemie-International Edition* **2000**, *39*, 3213-3237.
- (27) Zhang, W.; Zhang, X. *Progress in Polymer Science* **2003**, *28*, 1271-1295.
- (28) Rief, M.; Oesterhelt, F.; Heymann, B.; Gaub, H. E. *Science* **1997**, *275*, 1295-1297.
- (29) Bemis, J. E.; Akhremitchev, B. B.; Walker, G. C. *Langmuir* **1999**, *15*, 2799-2805.
- (30) Butt, H. J.; Kappl, M.; Mueller, H.; Raiteri, R.; Meyer, W.; Ruhe, J. *Langmuir* **1999**, *15*, 2559-2565.
- (31) Li, H. B.; Linke, W. A.; Oberhauser, A. F.; Carrion-Vazquez, M.; Kerkvliet, J. G.; Lu, H.; Marszalek, P. E.; Fernandez, J. M. *Nature* **2002**, *418*, 998-1002.
- (32) Gutsman, T.; Fantner, G. E.; Kindt, J. H.; Venturoni, M.; Danielsen, S.; Hansma, P. K. *Biophysical Journal* **2004**, *86*, 3186-3193.
- (33) Merkel, R.; Nassoy, P.; Leung, A.; Ritchie, K.; Evans, E. *Nature* **1999**, *397*, 50-53.
- (34) Schönherr, H.; Beulen, M. W. J.; Bügler, J.; Huskens, J.; van Veggel, F. C. J. M.; Reinhoudt, D. N.; Vancso, G. J. *Journal of the American Chemical Society* **2000**, *122*, 4963-4967.
- (35) Zapotoczny, S.; Auletta, T.; de Jong, M. R.; Schönherr, H.; Huskens, J.; van Veggel, F. C. J. M.; Reinhoudt, D. N.; Vancso, G. J. *Langmuir* **2002**, *18*, 6988-6994.
- (36) Auletta, T.; de Jong, M. R.; Mulder, A.; van Veggel, F. C. J. M.; Huskens, J.; Reinhoudt, D. N.; Zou, S.; Zapotoczny, S.; Schönherr, H.; Vancso, G. J.; Kuipers, L. *Journal of the American Chemical Society* **2004**, *126*, 1577-1584.
- (37) Zou, S.; Zhang, Z. H.; Förch, R.; Knoll, W.; Schönherr, H.; Vancso, G. J. *Langmuir* **2003**, *19*, 8618-8621.
- (38) Oesterhelt, F.; Rief, M.; Gaub, H. E. *New Journal of Physics* **1999**, *1*, 6.1.
- (39) Hinterdorfer, P.; Kienberger, F.; Raab, A.; Gruber, H. J.; Baumgartner, W.; Kada, G.; Riener, C.; Wielert-Badt, S.; Borken, C.; Schindler, H. *Single Molecules* **2000**, *1*, 99-103.
- (40) Evans, E.; Ritchie, K.; Merkel, R. *Biophysical Journal* **1995**, *68*, 2580-2587.
- (41) Evans, E.; Ritchie, K. *Biophysical Journal* **1997**, *72*, 1541-1555.
- (42) Evans, E. *Annual Review of Biophysics and Biomolecular Structure* **2001**, *30*, 105-128.
- (43) Evans, E.; Williams, P. *Physics of Bio-Molecules and Cells*; EDP Science Spinger-Verlag, 2002.
- (44) Folmer, B. J. B.; Sijbesma, R. P.; Versteegen, R. M.; van der Rijt, J. A. J.; Meijer, E. W. *Advanced Materials* **2000**, *12*, 874-878.

Chapter 7

Grafting of Single, Stimuli-Responsive Poly(ferrocenylsilane) Polymer Chains to Gold Surfaces*



A systematic investigation of the insertion behavior of ethylene sulfide end-functionalized poly(ferrocenylsilanes) (PFS) derivatives into pre-formed SAMs was carried out in order to develop a robust and reproducible procedure that allows us to obtain individually isolated PFS macromolecules covalently attached to solid substrates for AFM-based single molecule force spectroscopy experiments. Redox-responsive PFS molecules were attached individually to gold surfaces by grafting ethylenesulfide-functionalized PFS into the defects of pre-formed self-assembled monolayers (SAMs) of different γ -mercapto-alkanols on Au(111). AFM, contact angle, as well as cyclic and differential pulse voltammetry measurements were carried out to characterize the morphology, wettability, and surface coverage of the grafted layers, in order to optimize conditions for obtaining molecularly isolated PFS molecules. The surface coverage could be controlled via the chain length of the thiol molecule and the concentration of the PFS toluene solution, but not via the insertion time or the chain length of the PFS macromolecules. The isolated PFS macromolecules were subjected to *in situ* AFM-based single molecule force spectroscopy measurements. The single chain elasticity of PFS in isopropanol could be successfully fitted with the modified freely-jointed chain (m-FJC) model yielding a Kuhn segment length of 0.33 ± 0.05 nm and a segment elasticity of 32 ± 5 nN/nm.

7.1 Introduction

The bottom-up construction of molecular level machines (motors) is one of the most challenging aspects in the pursuit of nanotechnology and thus has recently attracted a great deal of attention.¹⁻⁴ Complementary to artificial molecular machines, there exists a plethora of natural

* The work described in this Chapter has been published: Zou, S.; Ma, Y.; Hempenius, M. A; Schönherr, H.; Vancso, G. J. *Langmuir* **2004**, *20*, 6278-6287.

ones, such as the F_0F_1 -ATP synthase,⁵⁻⁷ kinesine and myosine⁸ and flagellar motors in bacteria.⁹ The most obvious way to supply energy and make a machine work is through an exergonic chemical reaction, which needs chemical, photochemical and/or electrochemical energy input. The potential of artificial light-powered molecular machines has been explored by, among others, the groups of Gaub,¹⁰ Brouwer^{11,12} and Feringa.²⁻⁴

Macroscopic electromechanical actuators have been proposed a decade ago¹³ and have been pioneered in many different laboratories,¹⁴⁻¹⁶ yet true molecular machines powered by a redox process are still unknown. One of the key challenges is to interface such nanometer-sized or molecular devices with the macroscopic world.¹⁰ The detection, spectroscopy and identification of single molecules are therefore essential elements for a successful construction of molecular machines.

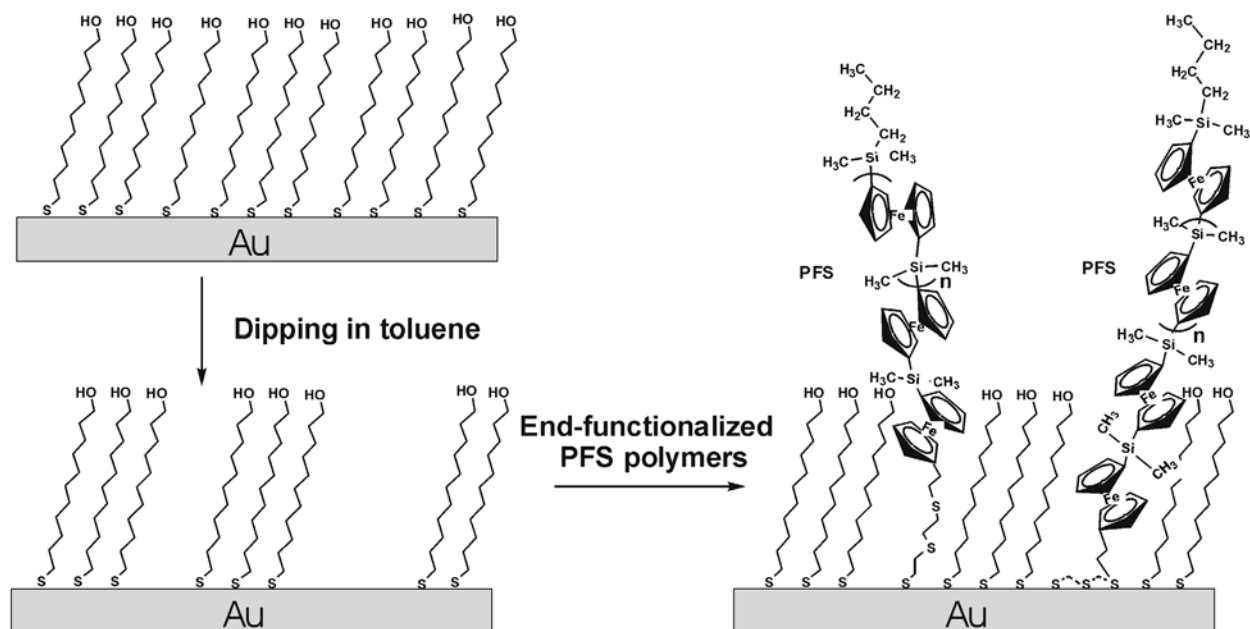
The functionality of traditional organic polymers can be significantly enriched or complemented, and the corresponding scope can be enhanced, through the development of the corresponding macromolecular chemistry of *inorganic and organometallic* materials. These polymers are of growing importance in light of the promising electrical, magnetic, optical, and catalytic properties that these materials possess.^{17,18} In many cases these polymers possess important properties, which are distinctively different compared to those of their organic counterparts, owing to the presence of the incorporated "new" elements. For example, poly(ferrocenylsilane) (PFS),¹⁹ composed of alternating ferrocene and alkylsilane units in the main chain, belong to this class of materials. In contrast to multistep procedures,^{20,21} PFS can be employed, for instance, in single step reactive ion etching processes, due to the remarkable etching barrier properties of this organometallic polymer. As an example for the rich range of possible applications, thin films of block copolymers containing PFS blocks and various laterally structured surfaces comprising PFS have been used in "maskless" lithography applications as versatile templates.²²⁻²⁴

PFS can also be reversibly oxidized and reduced by means of electrochemistry.²⁵ In previous studies, the introduction of a thiol end-functionality was exploited for the immobilization of poly(ferrocenylsilane) on gold surfaces by self-assembly.²⁶⁻²⁸ Reversible redox-induced morphology and volume/thickness changes of neat self-assembled poly(ferrocenylsilane) layers on gold were studied in situ by using electrochemical atomic force microscopy (ECAFM), surface plasmon resonance (SPR) spectroscopy and X-ray reflectometry combined with cyclic voltammetry (CV) and differential pulse voltammetry (DPV). These effects are intimately related to the changes in solubility and conformations of the macromolecules upon oxidation or reduction, respectively. Thus, surface-immobilized PFS

constitutes an interesting electrochemically addressable stimuli-responsive system. The results obtained by DPV²⁹ also showed that the polymer chains in the neat PFS layers were packed such that substantial interchain (through space) segment-segment interactions were observed.²⁸

Using AFM-based single molecule force spectroscopy (see also Chapter 2.3), typical force fingerprints, elastic properties and deformation of organic polymer chains, as well as of bio-macromolecules, can be revealed.³⁰⁻³⁷ Recently, the contour length changes by a light induced cis-trans isomerization of an azobenzene-containing polymer have been reported.¹⁰

In this chapter, the unique combination of both the visualization and force sensing capabilities of AFM will be utilized to address, i.e. to locate, physically contact and finally stretch, individual stimuli-responsive macromolecules in an attempt to realize a single molecule machine. For the purpose of studying the response of PFS macromolecules to external redox or chemical stimuli on the single molecule level using AFM, a generic strategy³⁸ for preparing surfaces that expose individual macromolecules with large intermolecular spacings was further developed. The strategy relies on the insertion of thiol end-functionalized molecules into the defects formed in pre-formed self-assembled monolayers (SAMs),³⁹⁻⁴⁷ when these are immersed in solvents (Scheme 7.1).⁴⁸⁻⁵³ The mechanism for this process consists of rapid dissociation of surface-bound thiols, possibly as disulfides, followed by slow macromolecule adsorption.⁴⁶



Scheme 7.1. Schematic of insertion strategy employed to immobilize isolated PFS macromolecules on gold surfaces.

Systematic investigations of the insertion behavior of ethylenesulfide-functionalized PFS into the defects of pre-formed SAMs of different γ -mercapto-alkanols on Au(111) will be discussed (Scheme 7.1). By a variation of insertion time, concentration of the PFS solution,

molecular mass of PFS and chain length of the ω -mercapto-alkanols, the optimal conditions to obtain molecularly isolated PFS molecules were determined. These isolated PFS macromolecules were then subjected to in situ stretching in AFM-based force spectroscopy experiments. These data form the basis for the investigation of the response of PFS macromolecules to external redox or chemical stimuli on the single molecule level, as will be discussed in Chapter 8.

7.2 Control of PFS Surface Coverage

The insertion process of ethylene sulfide end-capped PFS into SAMs of ω -mercapto-alkanols on Au(111) was studied in detail in order to identify the parameters that control PFS surface coverage.

7.2.1 Effect of Insertion Time

The effect of adsorption time on surface coverage was estimated in CV measurements of pre-formed 6-mercapto-1-hexanol (C6OH) SAMs that were exposed to a $8 \Delta 10^{-5}$ M PFS₅₀ (the notation of PFS corresponds to the monomer/initiator ratios, see section 7.7) solution in toluene for insertion times between 1 and 10 minutes. Complementary wettability data were obtained by contact angle measurements with water as a probe liquid. The cyclic voltammograms of PFS layers show two reversible redox peaks, which are associated with the different oxidation potentials of Fe atoms as a result of intermetallic coupling with oxidized or neutral neighboring Fe atoms in the main chain.^{25,54,55} Since the PFS molecules in our system are electroactive and undergo reversible oxidation and reduction,²⁶ the surface coverage of ferrocenyl sites (Γ_{Fc}) for all layers can be determined according to:^{23,56}

$$\Gamma_{Fc} = \frac{Q_{Fc}}{n_e F A} \quad (7.1)$$

where Q_{Fc} is the charge passed for the oxidation/reduction of ferrocenyl sites, n_e is the number of electrons involved in the electron transfer process (here $n_e = 1$), F is the Faraday constant ($F = 96485 \text{ C}\cdot\text{mol}^{-1}$), and A is the geometric surface area of the electrode ($A = 0.44 \text{ cm}^2$).

Q_{Fc} is calculated by integrating the areas under the redox peaks of the cyclic voltammograms (see e.g. Figure 7.1). Then the number of grafted chains per unit area (Γ) was calculated by dividing Γ_{Fc} by the degree of polymerization. The corresponding surface coverages, obtained by analyzing the cyclic voltammograms according to equation 7.1, and the corresponding advancing contact angles measured with water are shown in Table 7.1.

Table 7.1. Advancing water contact angles, values of charge and surface coverages for insertion of PFS₅₀ from toluene (concentration: $8 \Delta 10^{-5}$ M) into C6OH for different time intervals.

t (min)	1	2	4	10
a (°)	51 ± 2	51 ± 2	51 ± 2	51 ± 2
Q_{Fc} (C)	$(2.0 \pm 0.5) \Delta 10^{-6}$	$(2.6 \pm 0.5) \Delta 10^{-6}$	$(1.8 \pm 0.5) \Delta 10^{-6}$	$(2.7 \pm 0.5) \Delta 10^{-6}$
(chain/nm ²)	$(5.7 \pm 0.1) \Delta 10^{-3}$	$(7.4 \pm 0.1) \Delta 10^{-3}$	$(5.1 \pm 0.1) \Delta 10^{-3}$	$(7.7 \pm 0.1) \Delta 10^{-3}$

The advancing water contact angles for each insertion time are identical to within the experimental error, thus all these samples exhibit equal surface hydrophobicity averaged over the contact area with the water drop used in the contact angle experiments. The PFS₅₀ surface coverages for different insertion times also showed no significant difference. These data indicate that the insertion process has reached its dynamic equilibrium within even the shortest accessible experimental time interval. Based on this conclusion, we fixed a standard time of 2 minutes for all other experiments.

7.2.2 Effect of Chain Length of SAMs

SAMs of 2-mercapto-ethanol (C2OH), C6OH, and 11-mercapto-1-undecanol (C11OH) on gold were exposed to PFS₅₀ solutions in toluene for 2 minutes. Drastically different coverages were observed by CV (Figure 7.1).

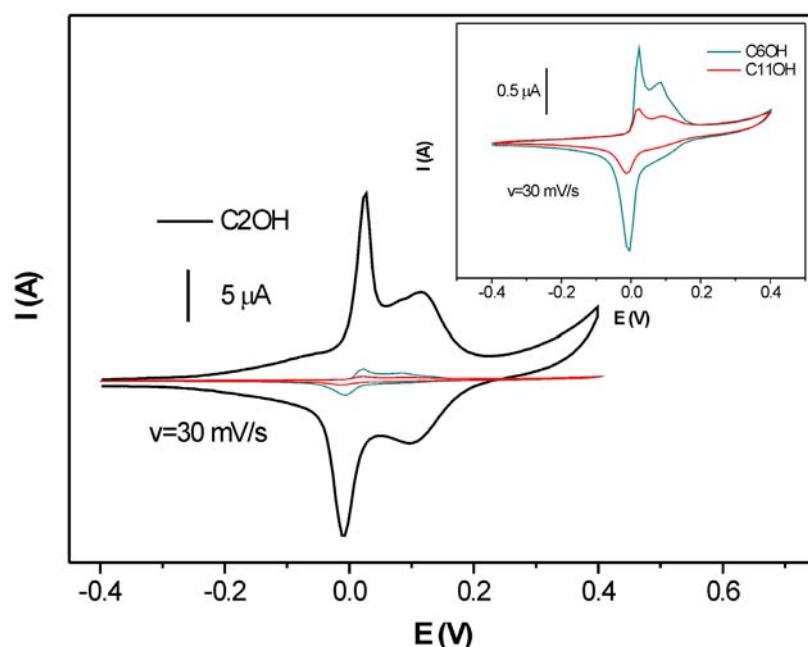


Figure 7.1. Cyclic voltammograms for PFS₅₀ end-grafted from toluene (concentration: $8 \Delta 10^{-5}$ M) into different SAMs for 2 minutes: C2OH, C6OH and C11OH (scan rate $v = 30$ mV/s, 0.1 M NaClO₄ aqueous electrolyte solution, reference electrode Hg/HgSO₄, counter electrode Pt). The inset shows the data for PFS inserted into C6OH and C11OH with enlarged ordinate.

The PFS surface coverage decreased markedly with increasing the alkane segment of the mercapto-alkanols comprising the SAMs; at the same time, the values of the contact angles were lower. Values of quantitative surface coverages estimated from the CV data using equation 7.1 and the corresponding advancing water contact angles are summarized in Table 7.2.

Table 7.2. Advancing water contact angles, values of charge and surface coverage for insertion of PFS₅₀ from toluene (concentration: $8 \Delta 10^{-6}$ M) into C2OH, C6OH and C11OH, respectively, for 2 minutes compared with values of a complete PFS₅₀ layer and a neat C11OH layer.

	α (°)	Q_{Fc} (C)	(chain/nm ²)
Neat PFS ₅₀	96 ± 2	$(1.00 \pm 0.05) \Delta 10^{-4}$	$(2.80 \pm 0.06) \Delta 10^{-1}$
C2OH	86 ± 2	$(1.10 \pm 0.07) \Delta 10^{-5}$	$(3.10 \pm 0.19) \Delta 10^{-2}$
C6OH	27 ± 2	$(4.30 \pm 0.21) \Delta 10^{-7}$	$(1.20 \pm 0.06) \Delta 10^{-3}$
C11OH	21 ± 2	$(2.20 \pm 0.11) \Delta 10^{-7}$	$(6.20 \pm 0.31) \Delta 10^{-4}$
Neat C11OH	16 ± 2	-	-

7.2.3 Effect of Concentration of PFS Solutions

An increase in concentration of the PFS₅₀ solution used for insertion led to similar changes as obtained for a decrease in chain length of the thiol molecules. Advancing contact angles measured with water on samples prepared by insertion of PFS₅₀ into C2OH, C6OH and C11OH increased with increasing PFS concentration (see Figure 7.2A). A similar trend was observed in detailed CV experiments. Figure 7.2B shows the comparison of cyclic voltammograms of samples obtained by insertion of PFS₅₀ from $8 \Delta 10^{-4}$, $8 \Delta 10^{-5}$, and $8 \Delta 10^{-6}$ M toluene solution into C11OH for 2 minutes. The peak currents (i_{pc} and i_{pa}), as well as the charge transfer in the redox process, increased with increasing concentration.

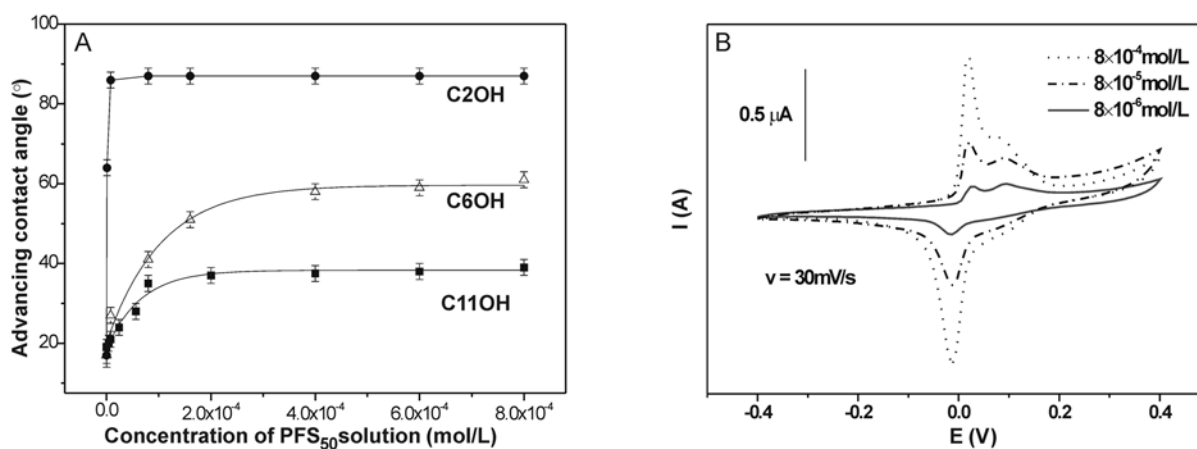


Figure 7.2. (A) Advancing water contact angles measured on samples obtained by insertion of PFS₅₀ from toluene with different concentrations into C2OH, C6OH and C11OH for 2 minutes (the lines serve as a guide to the eye). (B) Cyclic voltammograms of PFS₅₀ inserted from $8 \Delta 10^{-4}$ M, $8 \Delta 10^{-5}$ M, and $8 \Delta 10^{-6}$ M toluene solution into C11OH (scan rate $v = 30$ mV/s, 0.1 M NaClO₄ aqueous electrolyte solution, reference electrode Hg/HgSO₄, counter electrode Pt).

The coverage data obtained for all SAMs from the CV data can be fitted with a Langmuir isotherm.⁵⁷

$$\chi = \frac{kc}{1 + kc} \quad (7.2)$$

assuming that the maximum surface coverage (θ) is 1.0 in each set. Here χ is the relative PFS surface coverage; c is the concentration of the PFS solution and k is the equilibrium constant.

The fitted data are shown in Figure 7.3. It is observed that the k values obtained, which denote the ratio between corresponding adsorption and desorption rate constants, decrease from 5.0×10^{-4} L/mol to 2.6×10^{-4} L/mol and 1.7×10^{-4} L/mol for C2OH, C6OH, and C11OH, respectively, showing that the driving force for the adsorption process decreases with increasing chain length of the SAMs. These results agree well with the mentioned contact angle data, as well as with AFM images (see belows). Since the detection limit of CV ($\sim 10^{-7}$ A) limits the quantification of surface coverage to $\sim 10^{-5}$ chain/nm², further investigations on the very low coverage PFS layers were based on DPV and the Langmuir isotherms (Figure 7.3) to predict the value of the surface coverage.

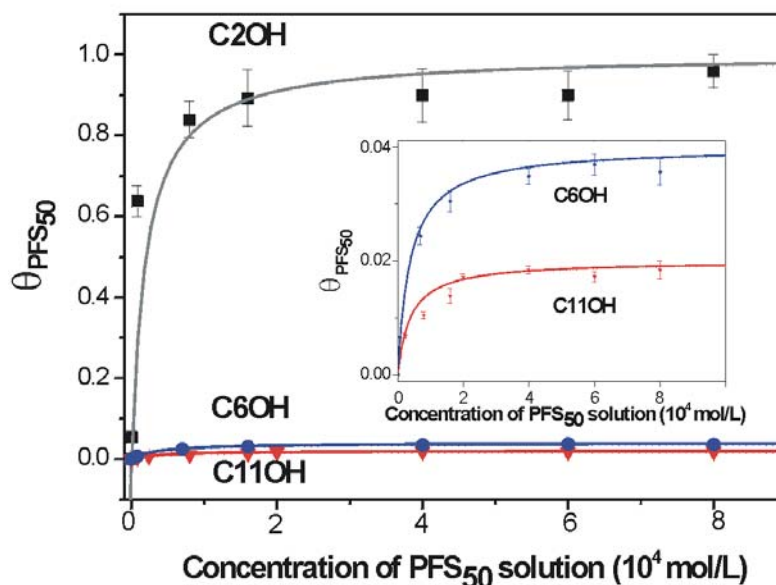


Figure 7.3. The dependence of PFS₅₀ surface coverage, determined by CV, on concentration of PFS₅₀ for insertion into (A) C2OH; (B) C6OH and (C) C11OH. The inset shows the data for C6OH and C11OH in more detail. The lines correspond to fitted Langmuir isotherms.

Figure 7.4 shows the differential pulse voltammograms measured on samples prepared by insertion of PFS from different concentrations of PFS₅₀ into C11OH. The two oxidation peaks can still be clearly resolved in the differential pulse voltammogram, although the CV (no data shown) did not show any oxidation waves on the samples shown as B and C in Figure 7.4. The surface coverages calculated according to the Langmuir isotherm were $\sim 5 \times 10^{-5}$ chain/nm²

and $\sim 1 \Delta 10^{-5}$ chain/nm² for PFS insertion from $8 \Delta 10^{-7}$ M (B) and $2 \Delta 10^{-7}$ M solution (C), respectively. The detection limit for DPV was estimated as $\sim 10^{-6}$ chain/nm², which is obtained by insertion of PFS from $1 \Delta 10^{-7}$ M solution into C11OH.

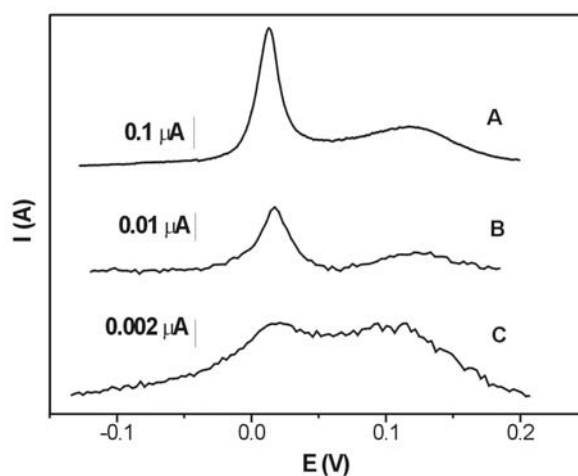


Figure 7.4. Differential pulse voltammograms recorded on PFS₅₀ end-grafted from (A) $8 \Delta 10^{-6}$ M; (B) $8 \Delta 10^{-7}$ M; (C) $2 \Delta 10^{-7}$ M toluene solution into C11OH (pulse time 50 ms, interval time 200 ms, pulse height 10 mV, 0.1 M NaClO₄ aqueous solution).

7.2.4 Effect of Molar Mass of PFS

The effect of molar mass of the polymer on the adsorption process was investigated using PFS₁₀₀. CV measurements of samples prepared by PFS₁₀₀ insertion from $4 \Delta 10^{-6}$ M toluene solution into C11OH were carried out with an identical monomer concentration as for PFS₅₀. The CV data for both samples showed two reversible redox peaks and the integrated charge transfer ($\sim 2.2 \Delta 10^{-7}$ C) in these two voltammograms are the same (see Figure 7.5). Thus, the molar mass (in the range of 12 to 25 kg/mol) of the polymer molecules has no pronounced effect on the obtained surface coverages.

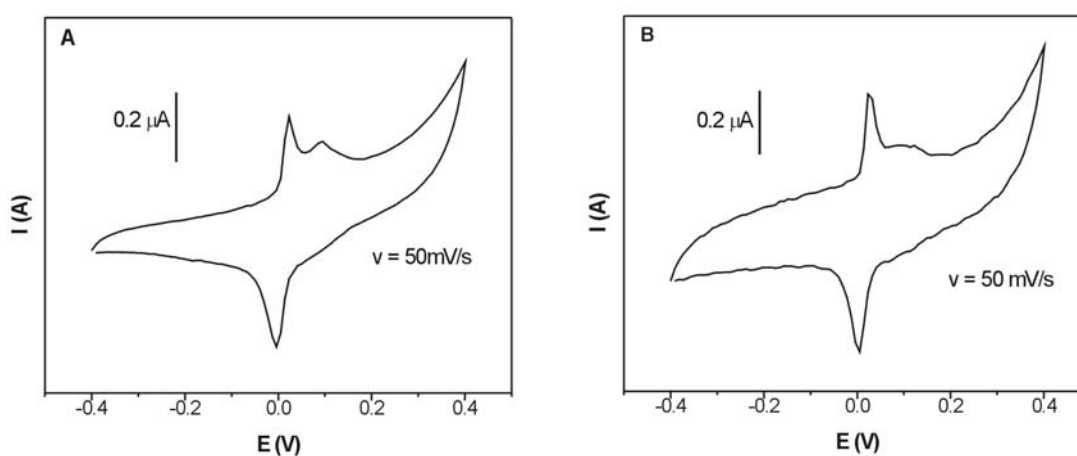


Figure 7.5. Cyclic voltammograms of (A) PFS₁₀₀ and (B) PFS₅₀ inserted from $8 \Delta 10^{-6}$ M and $4 \Delta 10^{-6}$ M toluene solution, respectively, into C11OH (scan rate $v = 50$ mV/s, 0.1 M NaClO₄ aqueous electrolyte solution, reference electrode Hg/HgSO₄, counter electrode Pt).

7.3 Isolation of PFS Macromolecules

For the ultimately targeted single molecule force spectroscopy experiments of surface-immobilized PFS, isolation of the chains is required. As seen in DPV and AFM experiments, the properties of PFS chains inserted into SAMs on gold showed an apparent difference compared to those in neat PFS layers.

7.3.1 Isolation Effects Detected by DPV

Figure 7.6 compares the DPV results for a full layer of PFS₅₀ with PFS₅₀ inserted in a C2OH SAM with high and low coverages. In the voltammograms, the integrated area under the first peak (seen as a shoulder at -0.1 V), which is attributed to the oxidation of the small fraction of Fe atoms that are in the close proximity to the gold surface,^{27,55,58} is decreasing relative to the second peak with decreasing PFS coverage. Furthermore, the ratio of the integrated areas under the second and third oxidation peak changed gradually from 1:2 to 1:1.

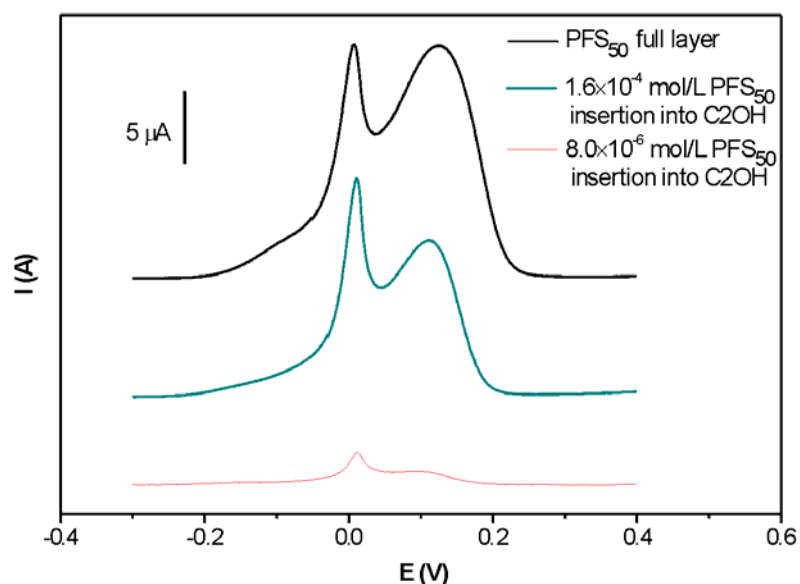


Figure 7.6. Differential pulse voltammograms recorded on full layer of PFS₅₀, PFS₅₀ inserted from $1.6 \Delta 10^{-4}$ M toluene solution into C2OH, and PFS₅₀ inserted from $8 \Delta 10^{-6}$ M toluene solution into C2OH (pulse time 50 ms, interval time 200 ms, pulse height 10 mV, 0.1 M NaClO₄ aqueous electrolyte solution).

Figure 7.7 presents the comparison of DPV results for a full layer of PFS₁₀₀ (Figure 7.7A, surface coverage determined from CV is ~ 0.15 chains/nm²) and the insertion of PFS₁₀₀ into C11OH SAMs (Figure 7.7B, surface coverage determined from CV is $\sim 6.2 \Delta 10^{-4}$ chains/nm²). After insertion of PFS into SAMs, the first oxidation peak virtually disappeared and the ratio of the integrated areas under the two remaining peaks changed to 1:1.

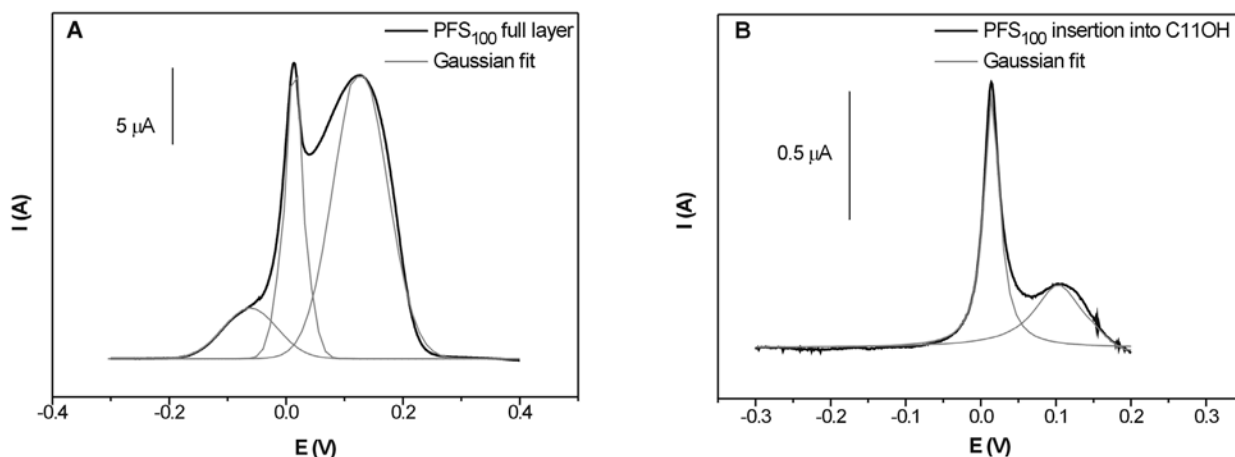


Figure 7.7. Differential pulse voltammograms recorded on: (A) PFS₁₀₀ full layer; (B) PFS₁₀₀ inserted from $4 \Delta 10^{-6}$ M toluene solution into C11OH (pulse time 50 ms, interval time 200 ms, pulse height 10 mV, 0.1 M NaClO₄ aqueous electrolyte solution). The data has been deconvoluted using a Gaussian (multiple peaks) fitting procedure (commercially available software Origin 7.0).

7.3.2 Isolation of PFS Detected in AFM Images

The DPV results discussed in section 7.3.1 were complemented by tapping mode (TM) AFM data acquired in air (Figure 7.8). All images show triangular terraces with 60° angles, which are typical for Au(111).^{59,60} Figure 7.8A shows a bare C11OH SAM, which appears to be homogeneous, except for the well-known depressions in the gold.⁴² For PFS inserted into a C2OH SAM, densely packed, barely protruding features were revealed (Figure 7.8B), while for PFS inserted into C6OH and C11OH SAMs showed isolated elevated, round features (Figure 7.8C, D). These round features have an average height of 4 ± 2 nm and an average diameter of 10 - 12 nm, as estimated in cross-sectional analyses. As the thiol chain length changes from C2 to C11, less features are observed (see below).

Assuming the specific gravity (ρ) of the PFS₅₀ polymer to be the same as the bulk value of PFS (1.26 g/cm^3),²⁴ and the molecular mass (M_n) of PFS₅₀ as 12500 g/mol, the average volume that one PFS₅₀ molecule occupies is calculated to be 17 nm^3 by using the following equation:

$$\bar{V}_i \mid \frac{M_n}{N_A \rho} \quad (7.3)$$

where N_A is the Avogadro constant ($N_A = 6.022 \Delta 10^{23} \text{ mol}^{-1}$). The diameter of a sphere that corresponds to this volume value is 3.2 nm, which is calculated by:

$$D \mid 2\left(\frac{3\bar{V}_i}{4\phi}\right)^{\frac{1}{3}} \quad (7.4)$$

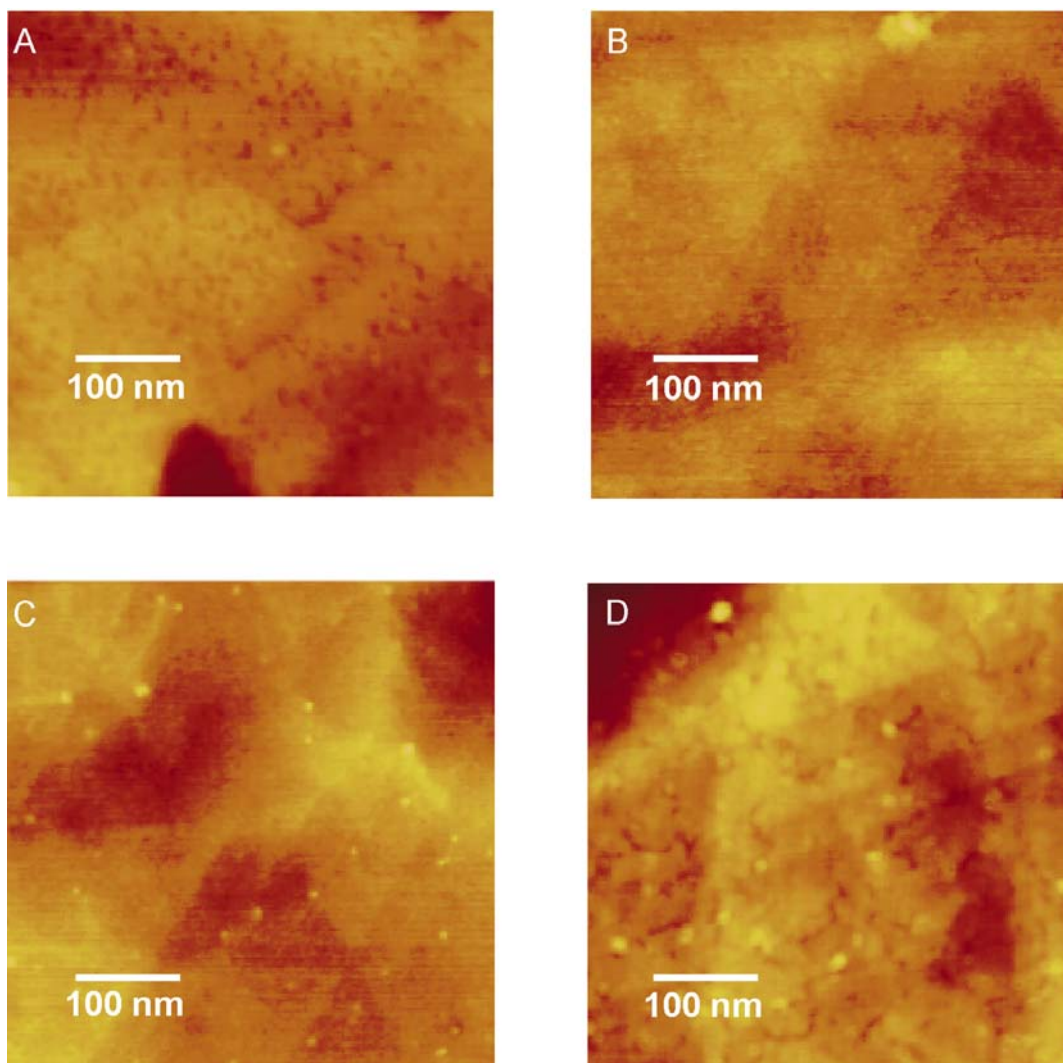


Figure 7.8. Tapping mode (TM)-AFM height images (acquired in air) for (A) bare SAM of C11OH on Au(111); and after insertion of PFS₅₀ from toluene (concentration: $8 \Delta 10^{-6}$ M) into (b) C2OH, (c) C6OH and (D) C11OH on Au (111) for 2 min (scan size 500 nm Δ 500 nm, z range is 10 nm for all images). The rms roughness for the neat SAM shown in A of 0.2 nm increases to 0.5 nm after insertion of PFS₅₀ inserted into C2OH (B).

Considering that the polydispersity of the PFS₅₀ polymer chains in our experiment is 1.14,^{24,27,28} the theoretical diameter of a spherical polymer chain will have an approximate value of $\sim 2 - 4$ nm. The height of the observed features (4 ± 2 nm) is in excellent agreement with this value, thus indicating the dot-like features observed in the TM-AFM images above are single PFS₅₀ polymer chains. For PFS₅₀ insertion into C6OH and C11OH, the surface coverages of PFS₅₀ on gold (Figures 7.8C and 7.8D) were determined by counting the number of features in areas of $300 \Delta 300$ nm². The corresponding results were compared to the surface coverages obtained from the CV measurements, as shown in Table 7.3. Especially for the long chain SAM (smaller relative error), the agreement of the surface coverage values obtained by the different techniques is very good.

Table 7.3. Values of charge and surface coverage data calculated from CV and TM-AFM, respectively, for PFS₅₀ inserted into C6OH and C11OH from toluene for 2 minutes.

SAM	Q _{Fc} (C)	(chain/nm ²) by CV	(chain/nm ²) by AFM
C6OH	^a (4.3 ± 0.2) Δ 10 ⁻⁷	(1.2 ± 0.1) Δ 10 ⁻³	(3.0 ± 0.9) Δ 10 ⁻⁴
C11OH	^b (2.2 ± 0.1) Δ 10 ⁻⁷	(6.2 ± 0.3) Δ 10 ⁻⁴	(4.2 ± 0.2) Δ 10 ⁻⁴
	^c (1.6 ± 0.1) Δ 10 ⁻⁶	(4.5 ± 0.4) Δ 10 ⁻³	(5.5 ± 0.4) Δ 10 ⁻³

^{a,b} concentration: 8 Δ 10⁻⁶ M, ^c concentration: 8 Δ 10⁻⁴ M.

The same trend was detected for decreasing concentrations. Figure 7.9 shows TM-AFM images obtained on samples prepared by PFS insertion into C11OH SAMs from 8 Δ 10⁻⁴ M and 8 Δ 10⁻⁶ M PFS₅₀ solution, respectively. Cross-sectional analyses showed the same radii and heights of the features as in Figure 7.8.

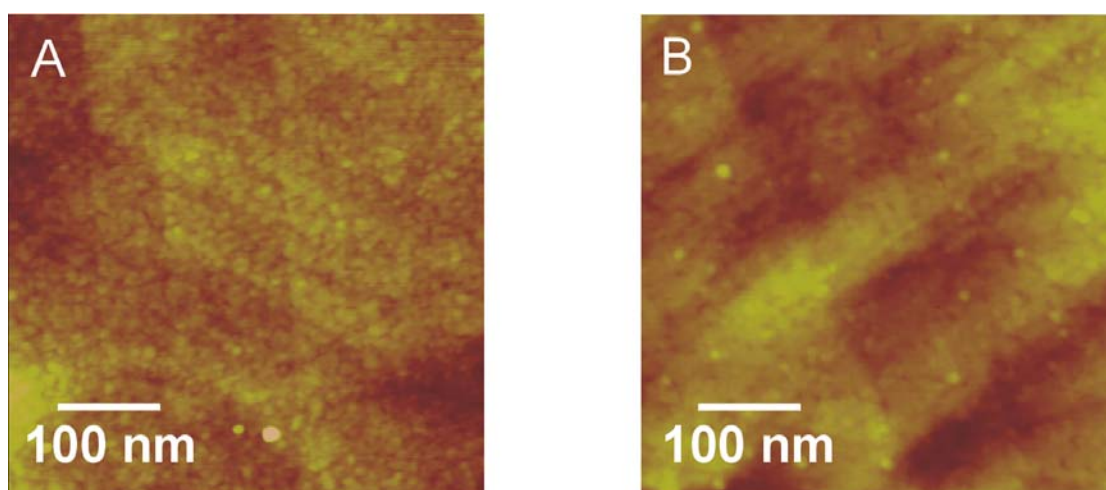


Figure 7.9. TM-AFM height images (acquired in air) of PFS₅₀ inserted from toluene solutions of different concentrations into C11OH for 2 minutes, A: 8 Δ 10⁻⁴ M; B: 8 Δ 10⁻⁶ M (scan size 500 nm Δ 500 nm, z range is 10 nm for both images).

7.4 AFM Based Single Molecule Force Spectroscopy

The elasticity of PFS₁₀₀ polymer chains in neat layers and as *isolated* chains was probed by single molecule force spectroscopy (SMFS). These experiments were carried out by in situ AFM using isopropanol as the solvent and normal Si₃N₄ cantilevers. Figure 7.10A shows a force - displacement curve acquired in SMFS experiments on neat layers of PFS₁₀₀ on Au. Multiple force signals are present in the plot. By contrast, the force-displacement curves of stretched PFS

chains that are immobilized as isolated chains on the sample show single stretching and pull-off events, as illustrated in Figure 7.10B.[†]

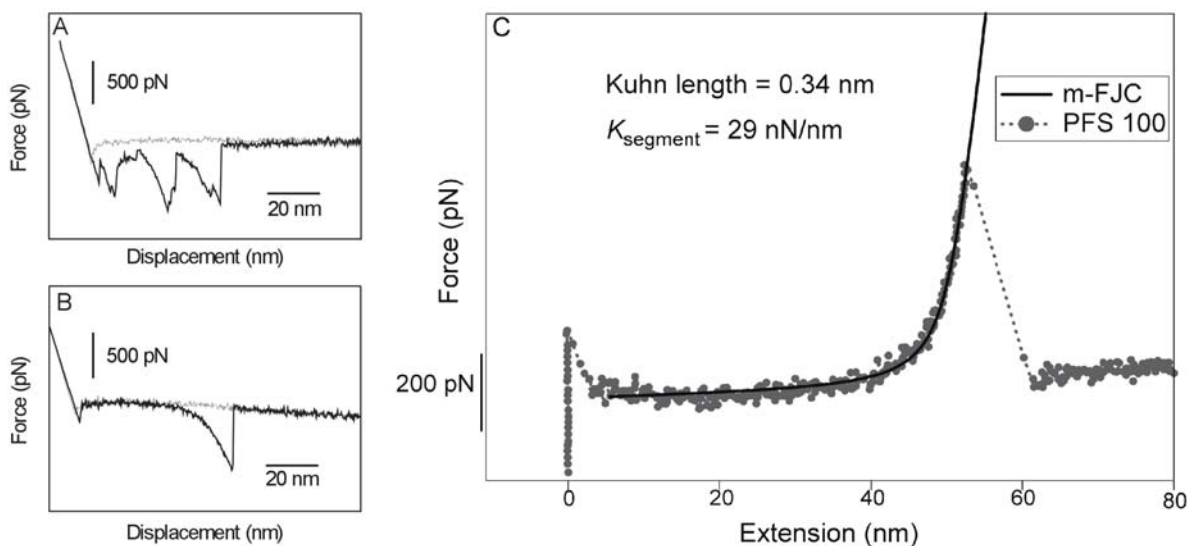


Figure 7.10. Representative force-displacement curves obtained by in situ AFM using isopropanol as the solvent on (A) PFS₁₀₀ full layer; (B) isolated PFS₁₀₀ macromolecules inserted from $8 \Delta 10^{-6}$ M toluene solution into C11OH; (AFM cantilever spring constant: $0.08 \Delta 0.015$ N/m) (C) force curve of a PFS₁₀₀ polymer chain and superimposed fit using the m-FJC model. The fit parameters for this particular force extension curve are shown.

The force-extension curves were fitted by the modified freely-jointed chain (m-FJC) model (Figure 7.10C) and yielded a Kuhn length of $0.33 \Delta 0.05$ nm^{61,62} and a segment elasticity K_{segment} of $32 \Delta 5$ nN/nm.[‡] The extension distance, representing the elastic response of the polymer, was about 55 nm (see Figure 7.10B).

7.5 Discussion

The systematic investigation of the insertion behavior of ethylene sulfide end-functionalized PFS derivatives into pre-formed SAMs was carried out in order to develop a

[†] The frequency of observed stretching events was estimated as 1 - 2 % for samples in which isolated PFS₁₀₀ macromolecules were inserted from $8 \Delta 10^{-6}$ M toluene solution into C11OH. While multiple force signals were frequently observed in neat layers, the frequency of single stretching events was < 5% based on all successful stretching events, which is about 30% of the tip-sample contact cycles. Since multiple events are not only due to the multiple chain stretching, but can also be caused by stretching of multiple loops of a single chain, the data are most consistent with the notion that isolated chains are exposed on the corresponding samples.

[‡] The m-FJC model (eq 7.5), which is typically used as a statistical model to describe the elongation of single polymer chains to large deformations, is an extension of the freely-jointed chain (FJC) model.^{28,34,35}

$$x(F) = \left[\coth\left(\frac{FI_K}{k_B T}\right) - \frac{k_B T}{FI_K} \right] \left(L_{\text{contour}} - 2 \frac{nF}{K_{\text{segment}}} \right), \quad (7.5)$$

where x is the extension of the polymer chain, F is the applied force; I_K (Kuhn length) is the length of the statistically independent segment, n is the number of segments, which equals L_{contour} / I_K ; K_{segment} is segment elasticity, which characterizes the deformability of the segment; k_B is the Boltzmann constant; and T is the temperature.

robust and reproducible procedure that allows us to obtain individually isolated PFS macromolecules covalently attached to solid substrates for AFM-based single molecule force spectroscopy experiments. Upon exposure of SAMs of different ω -mercapto-alkanols on Au(111) to ethylene sulfide end-functionalized PFS, as shown above, layers with altered surface properties were obtained. Based on atomic force microscopy, contact angle, and electrochemistry measurements, the polymer surface coverage was shown to be sensitive to the chain length of the ω -mercapto-alkanols molecules and to the concentration of the PFS solution, but not to the insertion time, nor to the molar mass of PFS.

The insensitivity to adsorption time on the time scales probed is likely related to the rapid defect formation and insertion of PFS into these defects. A corresponding replacement reaction would yield the same result. In a previous study it has been shown that the rate of defect formation is not the rate-limiting step.⁴⁶ Since the molar mass of the ethylene sulfide end-functionalized PFS was not found to play a significant role on the attained coverages, the insertion process is unlikely diffusion controlled.

The surface hydrophilicity assessed by contact angle measurements decreased notably with decreasing chain length of the alkanethiols, as well as with increasing PFS concentration (Figures 7.1 and 7.2, Table 7.2). The electrochemistry (Figures 7.1 to 7.4, Table 7.2) and AFM data (Figures 7.8 and 7.9) showed the same trend. While the properties probed are very different for each of the three methods, the data are very consistent.

All investigated pre-formed SAMs present high surface energy surfaces due to the exposed hydroxyl groups.⁶³ The advancing water contact angles of $\sim 15 - 18^\circ$ which are in excellent agreement with the literature,⁶³ were found to increase after insertion of the more hydrophobic PFS chains ($\theta_a(\text{PFS}) = 96^\circ$). Since the contact angles of two component ultrathin films correspond to a weighted mean of the contact angles of the pure components,⁶⁴ the increase in hydrophobicity with both decreasing chain length and increasing concentration qualitatively indicates an increasing fraction of adsorbed PFS. However, the cross sectional area of a thiol molecule and a PFS polymer coil are not identical, hence the Cassie equation⁶⁴ is not applicable to estimate the surface coverage quantitatively.

Cyclic voltammetry, on the other hand, can be employed in a quantitative manner to estimate the polymer surface coverage. The CV data fully confirmed the trends observed already in the wettability data. With increasing chain length of the pre-formed SAMs (from C2 to C11), the surface coverage values of PFS are dramatically reduced (Figure 7.1, Table 7.2). Compared to neat layers of PFS, a coverage of one, two, or three orders of magnitude less was observed for PFS inserted into C2OH, C6OH and C11OH, respectively. Similarly, the reduction in

concentration of the PFS solutions leads to a decrease in surface coverage (Figures 7.2 to 7.4). Since the surface coverage can be successfully described by a Langmuir isotherm, the surface coverage at very low concentrations can be predicted. Direct proof for the presence of PFS in such layers, and a qualitative dependence of coverage on concentration was obtained by DPV (Figure 7.4).

Furthermore, an excellent agreement of the PFS₅₀ surface coverages obtained by CV and those estimated from AFM images of samples prepared under exactly the same conditions were obtained (Figures 7.8 and 7.9, Table 7.3). From the analysis of the AFM data and a comparison with the surface coverages obtained by CV, we conclude a good agreement on the number of elevated dot-like features observed by AFM and the number of PFS macromolecules deduced from the charge passed for oxidation and reduction (Table 7.3). This good agreement is a reliable confirmation of the interpretation that the isolated round features observed by AFM are indeed individual PFS macromolecules.

The exact dimensions of the surface-immobilized PFS macromolecules cannot be directly extracted from the AFM data. The corresponding feature heights (4 ± 2 nm) and diameters (10 - 12 nm) obtained from cross-sectional analyses may possess significant systematic errors. In particular the width is certainly an overestimate due to tip convolution effects. Close inspection of Figure 7.8C and 7.8D reveals different feature sizes. These are caused by different tips utilized in the experiments. While a quantitative deconvolution is in principle possible, we have not deconvoluted the data, in order to avoid artifacts caused by such procedures. The feature height may appear too low due to compression of the polymer chain by the repulsive forces exerted by the AFM tip,⁶⁵ or alteration the resonance curve due to adhesive interactions.⁶⁶⁻⁶⁸ In addition to the nanometer scale dimensions of the features observed in AFM images, the good agreement of surface coverages according to AFM and CV (Table 7.3) and the reduced interchain segment-segment interaction observed in DPV (Figure 7.7) support the interpretation that the observed features are individual PFS macromolecules. The typical spacing of neighboring individual PFS chains of $\varnothing 40$ nm (e.g. Figure 7.8) compared to the tip - sample contact area of approximately 1.7 nm^2 § shows that multiple chain stretching in the SMFS experiments is very unlikely.

The control over the PFS surface coverage can be linked to the determinant role of PFS concentration as the driving force for adsorption on the one hand and to the mechanism of

§ Using Hertz theory (see Timoshenko, S. P.; Goodier, J. N. *Theory of Elasticity*; McGraw-Hill, New York, 1970) and assuming a typical tip radius R of 25 nm, a reduced elastic modulus K of the contact of 64 GPa (see e.g. Noy, A.; Frisbie, C. D.; Rozsnyai, L. F.; Wrighton, M. S.; Lieber, C. M. *J. Am. Chem. Soc.* **1995**, *117*, 7943), and a load of 1 nN, we obtain the radius of the contact area a as: $a = ((R/K) L)^{1/3}$ (7.6).

insertion, as well as to the order and arrangement of the pre-formed SAMs, on the other hand. The concentration dependence, which can be described by a Langmuir isotherm (Figure 7.3), is qualitatively similar for the three SAMs systems described. The difference among the rate constants for adsorption and desorption for SAMs with different chain lengths is related to the structures and orders of the corresponding SAMs.

As shown previously, the rapid desorption of surface bound thiols as disulfides, leads to the formation of defects in SAMs. Into these defects thiol or sulfide adsorbates can insert and subsequently covalently bind to the surface.^{45,46} It is well established that the number of inherent defects, as well as the conformational irregularity of the monolayers, decrease with increasing chain length of the thiol adsorbates.⁴⁸⁻⁵³ Owing also to the importance of interchain van der Waals interactions for SAM stability, an increase in chain length can be expected to result in a decrease in the number of new defects formed in the SAMs, when it is exposed to toluene (Scheme 7.1). Thus, longer chain SAMs can be expected to possess fewer defects for insertion of end-functionalized PFS. In addition, it may also be argued that, depending on the size of the defect, there is an increasing difficulty of the thiol end group of the PFS to reach the gold surface for SAMs with increasing chain length. Consequently, the resulting PFS surface coverages should decrease with increasing chain length of the thiols comprising the SAMs.

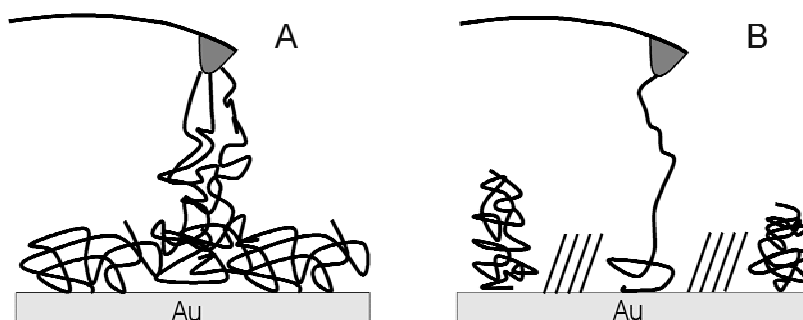
In the absence of clustering, this low coverage implies the presence of isolated PFS chains. In particular, the DPV data show evidence in support of this assertion. The contribution of the small fraction of Fe atoms that are in the close proximity to the gold surface to the oxidation trace of the differential pulse voltammograms (shoulder at -0.1 V), decreased with decreasing surface coverage (Figures 7.6 and 7.7). The reason might be that the number of Fe atoms that are closest to the gold surface becomes smaller with decreasing surface coverage of PFS on gold. In addition, the regularity of SAMs increases according to the increase of chain length of the thiol molecules.⁴⁸⁻⁵³ Thus, the inert effect of long chain SAMs on charge transfer results in a progressive difficulty for the Fe atoms to reach the gold surface. As shown in the voltammograms in Figures 7.6 and 7.7, the first peak becomes gradually undetectable.

More importantly, the ratio of the integrated areas under the second and third oxidation peak changed from 1:2 to 1:1 (Figures 7.6 and 7.7). This observation is in good accordance with previous results obtained on neat PFS layers.²⁷ It has been argued that under poor solvent conditions the 1:2 ratio results from the consideration of the interchain segment-segment interactions between the polymer chains in the thin film. The 1:1 ratio indicates that interchain segment-segment interactions among the PFS polymer chains are virtually absent. As we already know from the CV measurements that in our approach the PFS surface coverages were

continuously decreasing, we conclude that the interchain PFS segment-segment interactions become negligible with decreasing PFS surface coverage.

These data, together with the mentioned wettability, CV, and AFM data indicate that the surface-immobilized PFS macromolecules are indeed isolated as individual molecules. The force - displacement data recorded in AFM-based single molecule force spectroscopy measurements in different solvents on PFS₁₀₀ are also fully consistent with this interpretation. While we observed multiple force signals (stretching and pull-off events) during the same retraction of the AFM tip from a neat PFS layer (Figure 7.10A), the same experiment carried out on isolated PFS chains led to the almost exclusive observation of single force signals (Figure 7.10B).

The multiple force signals observed for neat PFS layers are ascribed to multichain adsorption to the tip and subsequent simultaneous stretching (Scheme 7.2A).^{30,31,35,38,69,70} In this case, the AFM tip adsorbs more than one chain and the chain that bears the highest load would detach from the tip first, followed by the other chains at a later stage. This scenario results in the multiple pull-off events observed. By contrast, the single events observed for experiments carried out on isolated PFS chains are an indication for the stretching of individual molecules (see Scheme 7.2B).



Scheme 7.2. Schematic of PFS (A) multiple-chain adsorption and (B) individual-chain adsorption on the AFM tips.

Despite the different contour lengths of the polymers chains, all the force-displacement curves acquired on isolated PFS chains show similar characteristics: the deflection rises monotonically with the extension of the polymer chain until a rupture point is reached; then the force suddenly drops to the original state. The extension distance, representing the elastic response of the polymer (see Figure 7.10B), was found to be < 70 nm (< 60 nm with a probability of > 95 %) with a mean value of 34.7 ± 12.5 nm, see Figure 7.11. This compared favorably with the contour length of the PFS₁₀₀ polymer chain that can be estimated by using the assumed mean length of the repeating unit as 6.3 \AA^{58} multiplied by the degree of polymerization (92) as ~ 58 nm.

From the fit of the force-extension curves by the m-FJC model (Figure 7.10C) we can see that the extended Langevin function describes the elastic properties of PFS well in both the low- and high-force regimes.^{30,34} This indicates that the elasticity of PFS at low forces is dominated by the entropic contribution; in the high-force regime, the elasticity of PFS is governed by both entropy and enthalpy. By fitting more than 60 experimental force-extension curves of different contour lengths, we found that all of the PFS filaments possess an identical Kuhn length of 0.33 ± 0.05 nm and a segment elasticity K_{segment} of 32 ± 5 nN/nm, although the lengths of these filaments vary from ~ 10 nm to ~ 70 nm (Figure 7.11).

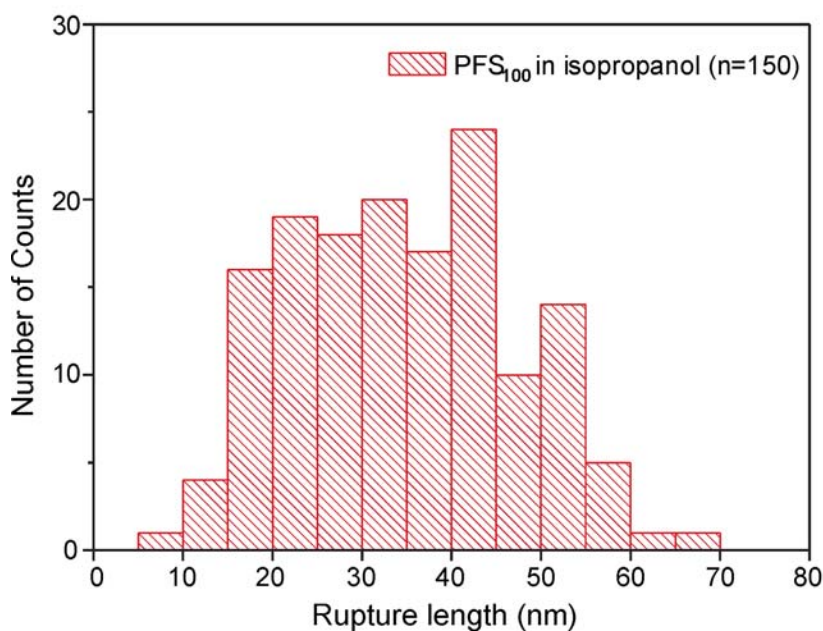


Figure 7.11. Histogram for PFS₁₀₀ polymer chain stretching lengths obtained from SMFS force-extension curves.

These two findings, the linear scaling of the elastic properties with the contour length and the identical segment elasticities and Kuhn lengths for all polymer chains, corroborate that individual PFS chains are stretched and that the deformation of a *single* chain under tension is measured. Since PFS is end-grafted covalently onto gold surfaces and was stretched in isopropanol, the resultant PFS layer consists mainly of PFS loops and tails of various lengths. Thus, the deformation of single PFS filaments in this study represents the deformation of single PFS loops or tails.

As mentioned in the Introduction, surface-immobilized PFS has been shown previously to undergo reversible redox-induced morphology and volume/thickness changes in neat self-assembled layers on gold.^{24,27,28} These effects, which are related to the changes in solubility and conformation of the macromolecules upon oxidation or reduction, respectively, can be expected to alter their elasticity as well.⁶² Thus, in conjunction with the immobilization strategy, it is in

principle possible to fabricate a true molecular machine based on this surface-immobilized stimuli-responsive PFS system. The possibility of achieving a molecular motor will be discussed in Chapter 8.

7.6 Conclusions

PFS macromolecules were successfully immobilized on gold surfaces through the insertion of ethylene sulfide end-functionalized PFS from toluene solution into pre-formed self-assembled monolayers of hydroxyl-terminated alkanethiols on gold. AFM, contact angle and electrochemical measurements were carried out to characterize the morphology, wettability and surface coverages of the mixed layers. The data obtained complement and agree well with each other. PFS surface coverages depended on the chain lengths of the thiol molecule and the concentration of the PFS toluene solution, but not on the insertion time or the chain length of the end-functionalized PFS molecules. Very low surface coverages were achieved by insertion from very dilute PFS solution into long-chain SAMs. Differential pulse voltammetry provided a very useful tool in elucidating the isolation effects that exist in mixed layers of lower PFS surface coverage. In samples with very low PFS surface coverages most of the interchain interactions were avoided, which is a requirement for the investigation of single PFS chain elongation by single molecule force spectroscopy. The immobilized isolated PFS₁₀₀ macromolecules were for the first time subjected to in situ AFM for SMFS measurements in isopropanol. The elasticity of single PFS₁₀₀ polymer chains was determined by fitting the experimental results with the m-FJC model, which showed, depending on the applied force, entropic and partly enthalpic elastic behavior of this polymer.

7.7 Experimental

Materials. Ethylene sulfide end-functionalized poly(ferrocenyldimethylsilanes), prepared by treating living poly(ferrocenyldimethylsilanes) with ethylene sulfide, were available from previous studies.²⁶⁻²⁸ The notation of the polymers corresponds to the monomer/initiator ratios. The following molar mass data were determined by GPC in THF, relative to polystyrene standards: PFS₅₀ ($M_n = 12.5$ kg/mol, $DP_n = 50$, $M_w/M_n = 1.14$), PFS₁₀₀ ($M_n = 22.6$ kg/mol, $DP_n = 92$, $M_w/M_n = 1.13$).²⁶⁻²⁸ 2-hydroxy-ethanethiol and 11-mercapto-1-undecanol, were purchased from Aldrich Chemical Co., 6-mercapto-1-hexanol was purchased from Fluka Chemical Co. and used as received.

Substrates and Samples. (a) Gold substrates ($11 \Delta 11 \text{ mm}^2$, 250 nm Au on 2 nm Cr on borosilicate glass) for AFM measurements were purchased from Metallhandel Schröer GmbH (Lienen, Germany). Au(111) samples were obtained by annealing these substrates in a high purity H_2 flame for 5 minutes.^{71,72} (b) Round gold substrates for electrochemistry measurements (2.5 cm diameter, 200 nm gold on 5 nm Ti primer deposited onto glass substrates in a vacuum of 5×10^{-6} mbar) were purchased from SSENS b.v. (Hengelo, The Netherlands). Prior to use, these substrates were cleaned in piranha solution (7:3 H_2SO_4 : H_2O_2 (30%) by volume), then rinsed with Milli-Q water and ethanol and dried in a nitrogen stream. **Caution: Piranha solution should be handled with extreme caution: it has been reported to detonate unexpectedly.**

Self-assembled monolayers (SAMs) of 2-mercapto ethanol, 6-mercapto-1-hexanol, and 11-mercapto-1-undecanol were prepared by immersing cleaned gold substrates into $0.5 \Delta 10^{-3}$ M solutions in ethanol overnight to ensure maximum coverage and order. For the investigation of mixed surface layers, insertions were carried out by dipping rinsed (dichloromethane, ethanol, MilliQ water, ethanol, dichloromethane in sequence) substrates with pre-formed SAMs into solutions of PFS of the corresponding DP and concentration for different times (see text for details). For the single PFS₁₀₀ chain stretching experiments, samples were prepared by immersion in $0.5 \Delta 10^{-3}$ M 11-mercapto-1-undecanol overnight, followed by rinsing and dipping into $8 \Delta 10^{-6}$ M, PFS toluene solution (standard solution) for 2 minutes. After dipping into the PFS solutions, the samples were cleaned by placing them in toluene (20 mL) and dichloromethane (20 ml) for 10 min, respectively, followed by drying in a stream of nitrogen. The PFS solutions were deaerated with Argon gas and covered with aluminum foil to prevent oxidation. All the glassware used were cleaned with Piranha solution and subsequently rinsed with large amounts of MilliQ water.

CV and DPV Experiments. Measurements were performed using an Autolab PGSTAT10 potentiostat (ECOCHEMIE, Utrecht, The Netherlands) in a three-electrode configuration. The gold substrate covered with the corresponding layer was used as the working electrode, Hg/HgSO₄ (MSE) was used as reference (+0.61 V_{NHE}) and Pt wire as the auxiliary electrode. The electrolyte was 0.1 M NaClO₄ aqueous solution. The working electrode exposed a surface area of 0.44 cm^2 to the electrolyte. Prior to the measurements, the cell was degassed by passing nitrogen through the electrolyte for 5 minutes. Cyclic voltammograms were recorded between $-0.4 \text{ V}_{\text{MSE}}$ and $+0.4 \text{ V}_{\text{MSE}}$ with different scan rates. Differential pulse voltammograms were recorded between $-0.4 \text{ V}_{\text{MSE}}$ and $+0.4 \text{ V}_{\text{MSE}}$ with a pulse amplitude of 10 mV, a pulse time of 50 ms, and a time interval of 200 ms.

Contact Angle Measurements. Contact angles were measured immediately after preparing the samples, with an OCA 15 plus (dataphysics instruments GmbH, Germany) contact angle microscope equipped with a CCD camera. Advancing contact angles were determined automatically by drop shape analysis during the growth of the droplet at a constant flow rate (1 $\mu\text{L/s}$). Contact angles were measured using ultrasonically degassed MilliQ water.

Atomic Force Microscopy Measurements (AFM). Surface morphology measurements were carried out with a NanoScope IIIa AFM (Digital Instruments (DI), Santa Barbara, CA) equipped with a phase box. Tapping mode AFM scans were performed in air using silicon cantilevers/tips with a spring constant of 28 - 58 N/m (Nanosensors, Wetzlar, Germany). Force spectroscopy experiments were performed by in situ AFM in liquid environment with a NanoScope IIIa multimode AFM fitted with a DI liquid cell (volume $\sim 50 \mu\text{L}$). Commercially available V-shaped Si_3N_4 cantilevers (DI) were used. Each cantilever was calibrated after a given experiment according to the equipartition method, by measuring the thermal excitation of the tip to compute its spring constant.^{59,60,73,74} The measured spring constants of the cantilevers varied between 0.065 to 0.090 N/m. The number of nanometer-scaled features was determined by counting the features on at least three areas (each with a dimension of $300 \Delta 300 \text{ nm}^2$) of the same sample and calculating the average.

Force Data Analysis. The SMFS data were analyzed as described in Chapter 5.

References:

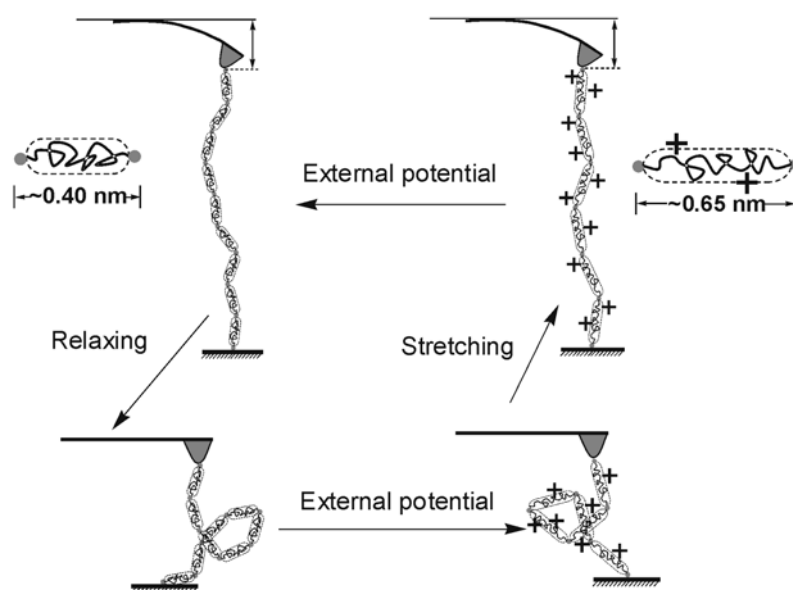
- (1) Stoddart, J. F. *Accounts of Chemical Research* **2001**, *34*, 410-411.
- (2) Hania, P. R.; Telesca, R.; Lucas, L. N.; Pugzlys, A.; van Esch, J.; Feringa, B. L.; Snijders, J. G.; Duppen, K. *Journal of Physical Chemistry a* **2002**, *106*, 8498-8507.
- (3) Geertsema, E. M.; Koumura, N.; ter Wiel, M. K. J.; Meetsma, A.; Feringa, B. L. *Chemical Communications* **2002**, 2962-2963.
- (4) van Delden, R. A.; Hurenkamp, J. H.; Feringa, B. L. *Chemistry-A European Journal* **2003**, *9*, 2845-2853.
- (5) Yin, H.; Wang, M. D.; Svoboda, K.; Landick, R.; Block, S. M.; Gelles, J. *Science* **1995**, *270*, 1653-1657.
- (6) Walker, J. E. *Angewandte Chemie-International Edition* **1998**, *37*, 2309-2319.
- (7) Boyer, P. D. *Angewandte Chemie-International Edition* **1998**, *37*, 2297-2307.
- (8) Vale, R. D.; Milligan, R. A. *Science* **2000**, *288*, 88-95.
- (9) Noji, H.; Yasuda, R.; Yoshida, M.; Kinosita, K. *Nature* **1997**, *386*, 299-302.
- (10) Hugel, T.; Holland, N. B.; Cattani, A.; Moroder, L.; Seitz, M.; Gaub, H. E. *Science* **2002**, *296*, 1103-1106.
- (11) Brouwer, A. M.; Frochot, C.; Gatti, F. G.; Leigh, D. A.; Mottier, L.; Paolucci, F.; Roffia, S.; Wurpel, G. W. H. *Science* **2001**, *291*, 2124-2128.
- (12) Gatti, F. G.; Lent, S.; Wong, J. K. Y.; Bottari, G.; Altieri, A.; Morales, M. A. F.; Teat, S. J.; Frochot, C.; Leigh, D. A.; Brouwer, A. M.; Zerbetto, F. *Proceedings of the National Academy of Sciences of the United States of America* **2003**, *100*, 10-14.
- (13) Baughman, R. H. *Synthetic Metals* **1996**, *78*, 339-353.
- (14) Smela, E.; Ingnas, O.; Lundstrom, I. *Science* **1995**, *268*, 1735-1738.
- (15) Kaneto, K.; Kaneko, M.; Min, Y.; Macdiarmid, A. G. *Synthetic Metals* **1995**, *71*, 2211-2212.
- (16) Baughman, R. H.; Cui, C. X.; Zakhidov, A. A.; Iqbal, Z.; Barisci, J. N.; Spinks, G. M.; Wallace, G. G.; Mazzoldi, A.; De Rossi, D.; Rinzler, A. G.; Jaschinski, O.; Roth, S.; Kertesz, M. *Science* **1999**, *284*, 1340-1344.
- (17) Abd-El-Aziz, A. S. *Macromolecular Rapid Communications* **2002**, *23*, 995-1031.
- (18) Manners, I. *Journal of Polymer Science Part A-Polymer Chemistry* **2002**, *40*, 179-191.

- (19) Kulbaba, K.; Manners, I. *Macromolecular Rapid Communications* **2001**, *22*, 711-724.
- (20) Spatz, J. P.; Sheiko, S.; Moller, M. *Advanced Materials* **1996**, *8*, 513-&.
- (21) Park, M.; Harrison, C.; Chaikin, P. M.; Register, R. A.; Adamson, D. H. *Science* **1997**, *276*, 1401-1404.
- (22) Lammertink, R. G. H.; Hempenius, M. A.; van den Enk, J. E.; Chan, V. Z. H.; Thomas, E. L.; Vancso, G. J. *Advanced Materials* **2000**, *12*, 98-103.
- (23) Lammertink, R. G. H.; Hempenius, M. A.; Chan, V. Z. H.; Thomas, E. L.; Vancso, G. J. *Chemistry of Materials* **2001**, *13*, 429-434.
- (24) Lammertink, R. G. H., Ph. D. thesis, University of Twente, 2000.
- (25) Foucher, D. A.; Ziembinski, R.; Tang, B. Z.; Macdonald, P. M.; Massey, J.; Jaeger, C. R.; Vancso, G. J.; Manners, I. *Macromolecules* **1993**, *26*, 2878-2884.
- (26) Peter, M.; Lammertink, R. G. H.; Hempenius, M. A.; van Os, M.; Beulen, M. W. J.; Reinhoudt, D. N.; Knoll, W.; Vancso, G. J. *Chemical Communications* **1999**, 359-360.
- (27) Peter, M.; Hempenius, M. A.; Lammertink, R. G. H.; Vancso, G. J. *Macromolecular Symposia* **2001**, *Volume 167*, 285-296.
- (28) Peter, M.; Hempenius, M. A.; Kooij, E. S.; Jenkins, A. T. A.; Roser, S. J.; Knoll, W.; Vancso, G. J. *Langmuir* **2004**, *20*, 891-897.
- (29) Kaifer, A. E. G.-K. *Supramolecular Electrochemistry*; Wiley-VCH; Weinheim, 1999.
- (30) Lee, G. U.; Chrisey, L. A.; Colton, R. J. *Science* **1994**, *266*, 771-773.
- (31) Rief, M.; Oesterhelt, F.; Heymann, B.; Gaub, H. E. *Science* **1997**, *275*, 1295-1297.
- (32) Marszalek, P. E.; Oberhauser, A. F.; Pang, Y. P.; Fernandez, J. M. *Nature* **1998**, *396*, 661-664.
- (33) Bemis, J. E.; Akhremitchev, B. B.; Walker, G. C. *Langmuir* **1999**, *15*, 2799-2805.
- (34) Li, H. B.; Linke, W. A.; Oberhauser, A. F.; Carrion-Vazquez, M.; Kerkviliet, J. G.; Lu, H.; Marszalek, P. E.; Fernandez, J. M. *Nature* **2002**, *418*, 998-1002.
- (35) Zhang, W.; Zhang, X. *Progress in Polymer Science* **2003**, *28*, 1271-1295.
- (36) Janshoff, A.; Neitzert, M.; Oberdorfer, Y.; Fuchs, H. *Angewandte Chemie-International Edition* **2000**, *39*, 3213-3237.
- (37) Hugel, T.; Seitz, M. *Macromolecular Rapid Communications* **2001**, *22*, 989-1016.
- (38) Furukawa, K.; Ebata, K.; Matsumoto, N. *Applied Physics Letters* **1999**, *75*, 781-783.
- (39) Ulman, A. *An Introduction to Ultrathin Organic Films: From Langmuir-Blodgett to Self-Assembly*; Academic Press: New York, 1991.
- (40) Schreiber, F. *Progress in Surface Science* **2000**, *65*, 151-256.
- (41) Dubois, L. H.; Nuzzo, R. G. *Annual Review of Physical Chemistry* **1992**, *43*, 437-463.
- (42) Poirier, G. E. *Chemical Reviews* **1997**, *97*, 1117-1127.
- (43) Tour, J. M.; Jones, L.; Pearson, D. L.; Lamba, J. J. S.; Burgin, T. P.; Whitesides, G. M.; Allara, D. L.; Parikh, A. N.; Atre, S. V. *Journal of the American Chemical Society* **1995**, *117*, 9529-9534.
- (44) Bumm, L. A.; Arnold, J. J.; Cygan, M. T.; Dunbar, T. D.; Burgin, T. P.; Jones, L.; Allara, D. L.; Tour, J. M.; Weiss, P. S. *Science* **1996**, *271*, 1705-1707.
- (45) Huisman, B. H.; Schönherr, H.; Huck, W. T. S.; Friggeri, A.; van Manen, H. J.; Menozzi, E.; Vancso, G. J.; van Veggel, F. C. J. M.; Reinhoudt, D. N. *Angewandte Chemie-International Edition* **1999**, *38*, 2248-2251.
- (46) Friggeri, A.; Schönherr, H.; van Manen, H. J.; Huisman, B. H.; Vancso, G. J.; Huskens, J.; van Veggel, F. C. J. M.; Reinhoudt, D. N. *Langmuir* **2000**, *16*, 7757-7763.
- (47) Koutsos, V.; van der Vegte, E. W.; Hadziioannou, G. *Macromolecules* **1999**, *32*, 1233-1236.
- (48) Schonenberger, C.; Sondaghuethorst, J. A. M.; Jorritsma, J.; Fokkink, L. G. J. *Langmuir* **1994**, *10*, 611-614.
- (49) Sondaghuethorst, J. A. M.; Schonenberger, C.; Fokkink, L. G. J. *Journal of Physical Chemistry* **1994**, *98*, 6826-6834.
- (50) Nuzzo, R. G. A., D. L. *J. Am. Chem. Soc.* **1983**, *105*, 4481-4483.
- (51) Porter, M. D.; Bright, T. B.; Allara, D. L.; Chidsey, C. E. D. *J. Am. Chem. Soc.* **1987**, *109*, 3559-3568.
- (52) Laibinis, P. E.; Fox, M. A.; Folkers, J. P.; Whitesides, G. M. *Langmuir* **1991**, *7*, 3167-3173.
- (53) Vaidya, B.; Chen, J. H.; Porter, M. D.; Angelici, R. J. *Langmuir* **2001**, *17*, 6569-6576.
- (54) Nguyen, M. T.; Diaz, A. F.; Dementev, V. V.; Pannell, K. H. *Chemistry of Materials* **1993**, *5*, 1389-1394.
- (55) Pudelski, J. K.; Foucher, D. A.; Honeyman, C. H.; Macdonald, P. M.; Manners, I.; Barlow, S.; Ohare, D. *Macromolecules* **1996**, *29*, 1894-1903.
- (56) Forster, R. J.; Keyes, T. E.; Vos, J. G. *Interfacial Supramolecular Assemblies*; John Wiley & Sons Ltd, England, 2003.
- (57) Atkins, P. W. *Physical Chemistry*; 6th ed.; Oxford University Press: Oxford Melbourne Tokyo, 1998.
- (58) Rulkens, R.; Lough, A. J.; Manners, I.; Lovelace, S. R.; Grant, C.; Geiger, W. E. *Journal of the American Chemical Society* **1996**, *118*, 12683-12695.
- (59) Florin, E. L.; Rief, M.; Lehmann, H.; Ludwig, M.; Dornmair, C.; Moy, V. T.; Gaub, H. E. *Biosensors & Bioelectronics* **1995**, *10*, 895-901.
- (60) Butt, H. J.; Jaschke, M. *Nanotechnology* **1995**, *6*, 1-7.
- (61) Zou, S.; Ma, Y.; Hempenius, M. A.; Schönherr, H.; Vancso, G. J. *Langmuir* **2004**, *20*, 6278-6287.
- (62) Shi, W. Q.; Cui, S.; Wang, C.; Wang, L.; Zhang, X.; Wang, X. J. *Macromolecules* **2004**, *37*, 1839-1842.
- (63) Bain, C. D.; Evall, J.; Whitesides, G. M. *Journal of the American Chemical Society* **1989**, *111*, 7155-7164.

- (64) Cassie, A. B. D. *Discuss. Faraday Soc.* **1948**, 3, 11.
- (65) Marsh, T. C.; Vesenka, J.; Henderson, E. *Nucleic Acids Research* **1995**, 23, 696-700.
- (66) van Noort, S. J. T.; van der Werf, K. O.; de Grooth, B. G.; van Hulst, N. F.; Greve, J. *Ultramicroscopy* **1997**, 69, 117-127.
- (67) Ebenstein, Y.; Nahum, E.; Banin, U. *Nano Letters* **2002**, 2, 945-950.
- (68) Schönherr, H.; Frank, C. W. *Macromolecules* **2003**, 36, 1188-1198.
- (69) Yamamoto, S.; Tsujii, Y.; Fukuda, T. *Macromolecules* **2000**, 33, 5995-5998.
- (70) Ortiz, C.; Hadziioannou, G. *Macromolecules* **1999**, 32, 780-787.
- (71) Manne, S.; Butt, H. J.; Gould, S. A. C.; Hansma, P. K. *Applied Physics Letters* **1990**, 56, 1758-1759.
- (72) Schönherr, H.; Vancso, G. J.; Huisman, B. -H.; van Veggel, F. C. J. M.; Reinhoudt, D. N. *Langmuir* **1999**, 15, 5541-5546.
- (73) Hutter, J. L.; Bechhoefer, J. *Review of Scientific Instruments* **1993**, 64, 3342-3342.
- (74) Sader, J. E. *Journal of Applied Physics* **1998**, 84, 64-76.

Chapter 8

Force Spectroscopy of Individual Stimuli-Responsive Poly(ferrocenylsilane) Macromolecules: Towards a Redox-Driven Molecular Motor



We investigated external stimuli-responsive poly(ferrocenylsilanes) (PFS) polymers, as a model system, in order to realize an electrochemically powered molecular motor. Surface immobilized PFS macromolecules were reversibly oxidized and reduced in situ by applying an electrochemical potential or chemically oxidized by addition of tetracyanoethylene. The single chain elasticities of individual neutral and oxidized PFS macromolecules were determined by single molecule force spectroscopy (SMFS) and subsequent fitting of the force-extension data using the modified freely-jointed chain model. The entropic elasticity of the neutral PFS chains (Kuhn length of ~ 0.40 nm) was found to be larger than that of the oxidized PFS chain (Kuhn length of ~ 0.65 nm) in the lower force regime, whereas the segment elasticities suggest an increasing elasticity for the oxidized PFS in the high force regime. The elasticities can be reversibly controlled in situ by adjusting the applied potential in electrochemical SMFS experiments. For the operating cycle of a defined single PFS molecule (degree of polymerization, $DP=80$), a work of $\sim 3.4 \Delta 10^{-19}$ J was estimated based on the single chain experimental data. The efficiency was estimated as 5%. In principle, PFS-based single molecule motors can be optimized by reducing the input energy to reach an efficiency of 10%.

8.1 Introduction

In response to the corresponding signals, biological molecular motors, such as the ATP synthase,¹⁻³ kinesine⁴ and myosin,⁵ and flagellar motors⁶ in bacteria, are capable of performing specific duties powered by external energy sources in a highly controlled fashion. These biological motors, which function as molecular rotors (gears), transporters, or propulsion pumps,

have been optimized for these specific tasks in the process of evolution. By contrast, the design and realization of synthetic molecular motors are in its infancy. Compared to their natural counterparts, synthetic molecular motors,* including molecular switches, shuttles, scissors, rotating modules and muscles,⁷⁻¹² do not possess highly sophisticated functions yet in the organized manner to perform a certain task.

The investigation and use of nanoscopic mechanical energy transducers require interfacing with the macroscopic world. In this respect, the application of surfaces proves to be invaluable for the arrangement and ordering of the corresponding molecular components. As introduced in Chapter 2.3 and Chapter 7.1, mechanical experiments with single macromolecules have been carried out to demonstrate subtle differences in polymer chain conformational changes. Conformational transitions, such as for instance force-induced chair-to-boat transitions in polysaccharides, have been widely investigated,¹³⁻¹⁶ and the mechanical manipulation of single pyranose rings has been achieved. Single molecule force spectroscopy (SMFS) by AFM techniques has proven to be a successful strategy to address and probe nanometer-sized devices with macroscopic instrumentation.

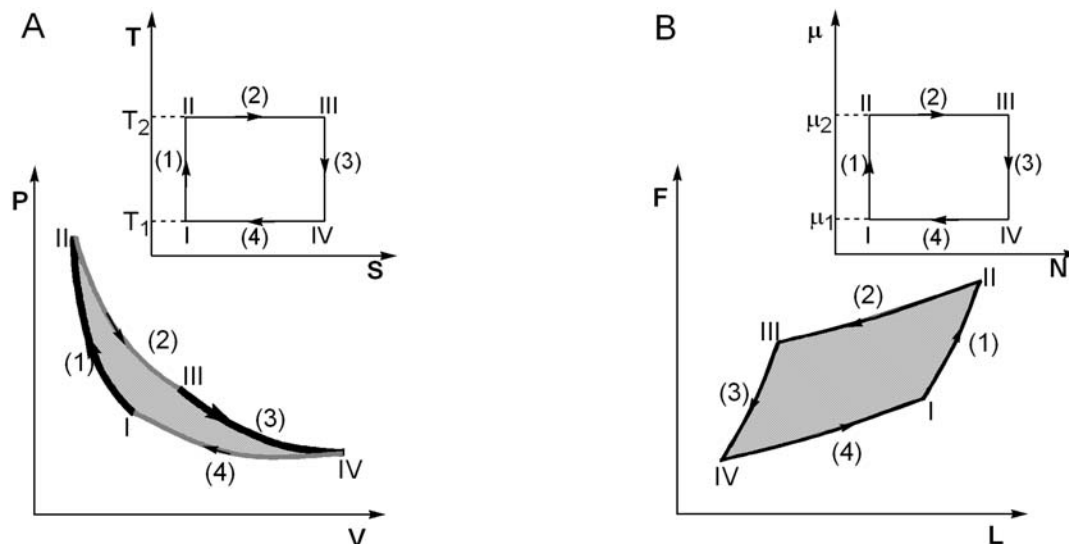
Stimuli-responsive polymers are of growing interest due to their importance both as models for fundamental concepts in polymer physics (solution dynamics) and their relevance to many biological systems. Zhang *et al.* have reported single chain elasticity studies on thermally sensitive poly(N-isopropylacrylamide) (PNIPAM) molecules by SMFS.¹⁷ Thermally induced coil-to-globule transitions of individual PNIPAM chains were detected and could be used as a model system for protein unfolding studies. Recently, an elegant example of a polymer comprising azobenzene units along the main chain, which was stretched and contracted by an externally applied stimulus, i.e. light, was reported by the group of Gaub.¹⁸ Switching between the *trans*- and *cis*-azo isomers could selectively change the contour length of the polymer chain. In principle this chain could perform work and may serve as a model for a single macromolecule-based motor.

In this Chapter, we report on the investigation of previously unexplored stimuli, namely electrochemical and chemical stimuli, for tuning the elasticity of individual responsive polymer

* Molecular motors may be defined as follows: a molecule is operated in a controlled cyclic fashion to perform mechanical movement (output) as a consequence of appropriate external stimulation (input). During the operating process, a number of steps are executed, which correspond to changes in conformation and/or in chemical state of the molecules. Eventually the molecules are reset to the initial conformation. The steps of the mechanical cycle are coupled to the states of a chemical cycle (stimulated by light, electric or other possible fuels) that generates the energy necessary to fuel the movement.

chains in an attempt to realize a single (macro)molecular motor. The system is based on the PFS system introduced in Chapter 7.

To understand how a motor can perform work and convert energy, examples of model cycles are described in Scheme 8.1.



Scheme 8.1. Schematics of (A) Carnot cycle with ideal gas; (B) isothermal chemical cycle with collagen as working substance. The amount of work produced from each cycle is shown as the shaded area. (B) was adopted from ref [20].

The most efficient thermal engine with an ideal gas is the Carnot cycle[†] (Scheme 8.1 A). The amount of the work (W_{out}) produced by the system, shown as the shaded area in Scheme 8.1A, is equal to the net heat transferred during the processes. The efficiency of the cycle, ξ , is defined as the amount of the work produced by the system divided by the supplied heat (heat-in), which leads to:

$$\xi = \left| \frac{W_{\text{out}}}{Q_{\text{H}}} \right| = \frac{T_{\text{high}} - T_{\text{low}}}{T_{\text{high}}}$$

In electrochemistry, isothermal chemical cycles are known to yield more (electrical) work from the oxidation of chemicals than the work that is accessible from thermal cycles (where the same chemicals are burned in order to create the high temperature reservoir).¹⁹ A direct coupling between the change of chemical free energy and the production of mechanical work can be

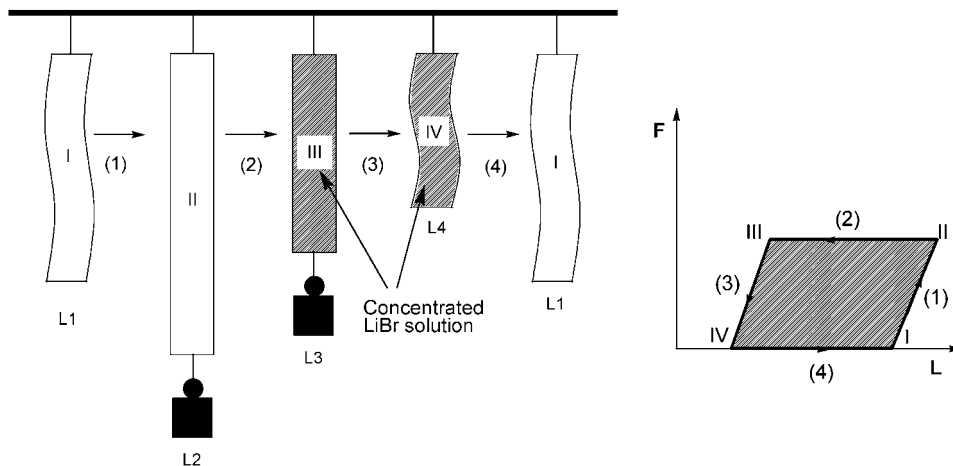
[†] The steps in the cycle are: (1) Compression at constant entropy; (2) Isothermal expansion at temperature T_{high} . Heat flows into the system from a reservoir: Q_{H} (positive), with entropy change $\int_{\text{I}}^{\text{II}} dS = Q_{\text{H}}/T_{\text{high}}$; (3) Expansion at constant entropy; (4) Isothermal compression at temperature T_{low} back to the original state (I). Heat flows from the system into a reservoir: Q_{C} (negative). The entropy change of the system is $\int_{\text{III}}^{\text{IV}} dS = Q_{\text{C}}/T_{\text{low}}$. This completes one Carnot cycle.

obtained by employing a macromolecular working substance.[‡] Scheme 8.1(B) shows a cyclic operation of a cross-linked collagen tape between a reservoir of high chemical potential and one of low chemical potential.²⁰ This isothermal, chemical cycle of collagen also consists of four work strokes: (1) isochoric stretching; (2) isopotential contraction; (3) isochoric contraction, and (4) isopotential stretching. Here, we are dealing with an open system. The cycle derives its power from the isothermal transport of salt and water from high to low chemical potential, just as the thermal cycle derives its power from the transport of entropy from high to low temperature. The efficiency of this isothermal chemical cycle is defined as:

$$\xi = \frac{\oint F dL}{\div \sigma_s \div N_s + \div \sigma_w \div N_w}$$

where, the subscripts s and w denote salt and water, respectively; $\div \sigma$ is the difference of chemical potential between the two reservoirs, and $\div N$ is the amount of substances entering the collagen tape.

Scheme 8.2 shows schematically how one measures the work performed by a crosslinked collagen tape.[§]



Scheme 8.2. The four-stroke laboratory experiment on collagen contraction, and work performance. Adopted from ref [20].

The cyclic integral $\oint F dL$ is to a very good approximation equal to $F/L_2 - L_3$ because the slopes of the isochoric strokes (1) and (3) are both steep. From the experimental results, it is

[‡] Steinberg *et al.* have pointed out that collagen tape can be used for this purpose.¹⁹ Such tape contains a triple helix conformation, oriented in the direction of the fiber and tape axis. Upon exposure to a concentrated salt solution (e.g., 5 M LiBr), the triple helix is not stable and denatures into a random-coil state, where the molecular dimensions are much smaller. As a result the whole tape contracts. Upon removal of the salt or lowering its concentration (e.g. 2.5 M LiBr), the collagen renatures to the oriented triple helix form. Consequently, the tape lengthens again.

[§] First the collagen tape is soaked in a lower concentration LiBr solution bath. A weight is tied at the end of the tape, which lengthens the tape. After the collagen is treated in a concentrated LiBr solution bath, the conformational change of the triple helix structure shortens its length and the weight is raised. When the weight is taken off, the length of the tape decreases. When the tape is soaked in the dilute LiBr solution, it elongates again due to the conformational change of the collagen.

known that $\div N_s$ and $\div N_w$ are of the same order of magnitude. However, $\div \sigma_w$ is much smaller than $\div \sigma_s$. Consequently it is sufficient to calculate the efficiency from:

$$\xi \approx \frac{F/L_2 \cdot 4 L_3 \theta}{\div \sigma_s \div N_s}.$$

The principle described above can be transferred to the single molecule level by using a stimuli-responsive system. Here, an essential component of designing a molecular motor is to change the conformational or chemical state of the molecule, i.e. by reversibly control of the elasticity of the polymer chain (before and after stimulation). PFS macromolecules were investigated as a possible model system in this respect owing to the possibility of reversible oxidation and reduction of ferrocenyl groups along the polymer chains.²¹⁻²³

In a very recent independent force spectroscopy study Shi *et al.* have reported on a PFS single chain elasticity investigation.²⁴ In this paper, the authors attempted to measure the stretching behavior of single PFS homopolymer chains before and after chemical oxidation with FeCl₃. The results showed similar entropic elasticities (Kuhn lengths) for both the neutral *and* the chemically oxidized PFS homopolymer chains. The similar elasticities of PFS in different states may be due to an incomplete chemical oxidation of the whole polymer chain, as well as the unfavorable solubility of the oxidized PFS molecules. This may have resulted in stretching measurements that were taken on partially oxidized or neutral PFS homopolymer chains, even though PFS was believed to be fully oxidized.

After chemical oxidation PFS containing copolymers, for instance poly(styrene-*block*-ferrocenyldimethylsilanes) (PS-*b*-PFS), showed an increased solubility compared to the PFS homopolymer in organic solvents such as THF and toluene.²⁵ This feature could be useful to realize sufficiently high degrees of chemical oxidation of PFS. Therefore the elasticity of chemically oxidized single PS-*b*-PFS polymer chains was investigated by AFM-based SMFS in addition to the isolated PFS₁₀₀ (Chapter 7) molecules and PFS homopolymer, which can be electrochemically addressed. By the combination of electrochemistry with SMFS, i.e. by applying an external potential to individual PFS₁₀₀ and/or PFS homopolymer chains in situ during the SMFS experiments, the changes of elasticity between neutral and oxidized PFS homopolymers can be determined. The advantage of using an electrochemical stimulus is that it achieves the reversible oxidation and reduction of PFS chains, while the chemical oxidation is a quasi-static process.

In this Chapter, the principle of a single (macro)molecular motor based on PFS molecules is demonstrated by investigating the stretching behavior of individual neutral and oxidized poly(ferrocenyldimethylsilane) (PFS_{homo}) chains, PS-*b*-PFS chains, as well as PFS₁₀₀, by SMFS.

The elasticity of neutral and oxidized PFS chains could be controlled by applying chemical and/or electrochemical stimuli resulting in a redox-mechanical cycle of a molecular motor.

8.2 Single Chain Elasticity Measurements on Neutral PFS Macromolecules

In order to compare differences of elasticity between neutral and oxidized PFS chains, individual neutral PFS₁₀₀, PFS_{homo} and PS-*b*-PFS chains were probed by single molecule force spectroscopy. Since the targeted electrochemistry experiments are often carried out in aqueous solutions, the single chain stretching was studied first in isopropanol and then in aqueous solutions of NaClO₄.

8.2.1 Neutral PFS Chains Measured in Isopropanol

Typical force vs extension curves of neutral PFS₁₀₀, PFS_{homo} and PS-*b*-PFS chains probed in isopropanol are shown in Figure 8.1A. Force-extension curves obtained from all three polymers show similar characteristics: the force value rises with the extension of the polymer chain, and drops to zero when the rupture point is reached. Until reaching its fully extended configuration, the polymer chain exhibits no measurable conformational transitions, indicating that no detectable thermal activation barriers are overcome along the trajectory of mechanical stretching. The observation of different extension (stretching) lengths is attributed to the fact that the chains adhere via physisorption to the tip, resulting in varying position of attachment points along a given chain in different stretching experiments.

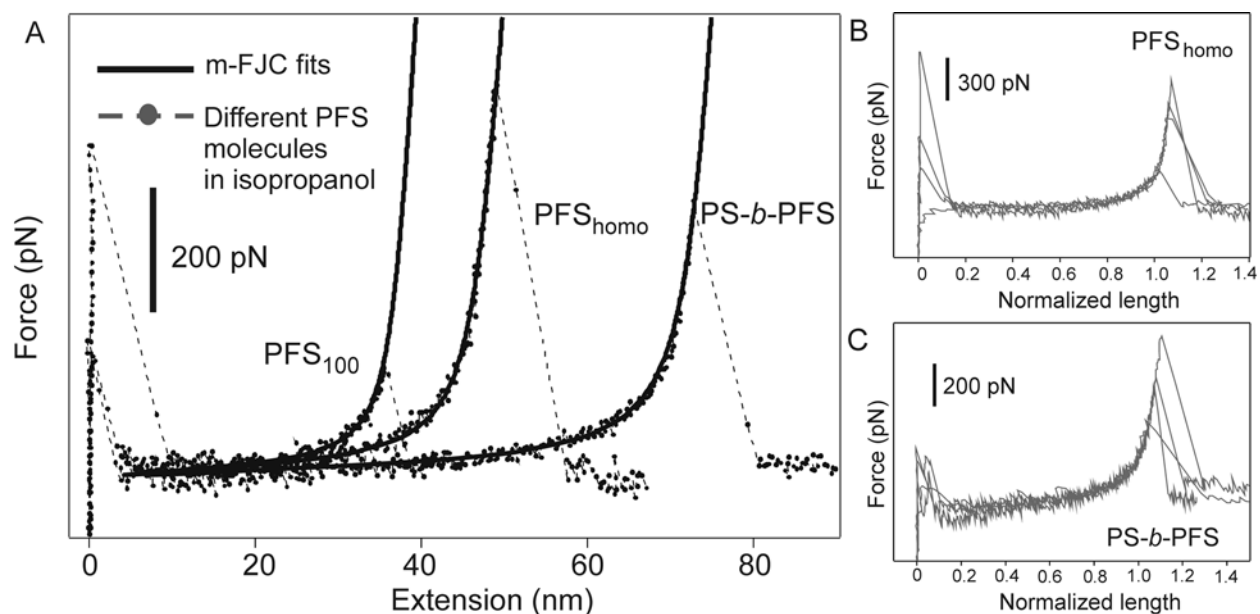


Figure 8.1. (A) Force vs extension traces of individual neutral PFS_{homo}, PFS_{homo} and PS-*b*-PFS polymer chains stretched in isopropanol with superimposed m-FJC fits shown as solid lines. (B) and (C): Superposition of normalized force curves for PFS_{homo} and PS-*b*-PFS, respectively.

The force-extension curves were fitted to the modified freely-jointed chain (m-FJC) model (see Chapter 2.3.3 and Chapter 7.5), plotted as a solid line in Figure 8.1A. The obtained values of Kuhn lengths I_K and segment elasticities K_{segment} are summarized in Table 8.1. The force – extension curves were also normalized by the extension that correspond to the same force value (250 pN), as shown in Figure 8.1B and 8.1C for PFS_{homo} and PS-*b*-PFS, respectively. Both sets of normalized curves superimpose well.

Table 8.1 Single chain elasticities of individual neutral PFS polymer chains probed in isopropanol (fitted by the m-FJC model).

solvent	PFS ₁₀₀		PFS _{homo}		PS- <i>b</i> -PFS		PS	
	Kuhn length (nm)	K_{segment} (nN/nm)	Kuhn length (nm)	K_{segment} (nN/nm)	Kuhn length (nm)	K_{segment} (nN/nm)	Kuhn length (nm)	K_{segment} (nN/nm)
isopropanol	0.35 ± 0.03	32 ± 3	0.37 ± 0.04	31 ± 4	0.39 ± 0.05	23 ± 5	0.40 ± 0.03	18 ± 3

From the fits of the force-extension curves (Figure 8.1A), we can see that the extended Langevin function describes both entropic (both low and high force regime) and enthalpic (high force regime) elasticities of all three PFS polymer chains very well. The normalized force profiles^{**} of neutral PFS₁₀₀, PFS_{homo}, and PS-*b*-PFS in isopropanol, and the identical segment elasticities and Kuhn lengths for all polymer chains, respectively, confirm that individual PFS chains were stretched and the deformation of single chains of a given type under tension was measured. All PFS homopolymer chains (PFS₁₀₀ and PFS_{homo}) possess an identical Kuhn length and segment elasticity. The parameters determined for PFS₁₀₀ are, to within the experimental errors, identical to the ones obtained in Chapter 7 ($I_K=0.33 \pm 0.05$ nm, $K_{\text{segment}}=32 \pm 5$ nN/nm) as well as to those of PFS_{homo} (Table 8.1). However, the segment elasticity differs from the values obtained for PS-*b*-PFS ($I_K=0.39 \pm 0.05$ nm, $K_{\text{segment}}=23 \pm 5$ nN/nm).

In order to understand the difference between elasticities obtained for homo PFS polymer and the block copolymer chains, single chain stretching experiments were carried out on polystyrene (PS) homopolymer chains in isopropanol. The fitted force-extension curves yielded a Kuhn length of 0.40 ± 0.03 , and K_{segment} of 18 ± 3 nN/nm. This result indicates that the lower segment elasticity of PS-*b*-PFS can be attributed to the contribution of the elasticity of the PS block.

^{**} The frequency of observed stretching events was around 1% for all of the three polymers. The m-FJC fitting was carried out (in these particular analyses) on 35, 73 and 67 force profiles from 2, 6 and 4 different experiments for neutral PFS₁₀₀, PFS_{homo} and PS-*b*-PFS in isopropanol, respectively.

8.2.2 Neutral PFS Chains Measured in 0.1 M NaClO₄

The targeted redox chemistry of PFS is typically performed in aqueous solution. In order to determine the effect of the solvent (isopropanol vs aqueous electrolyte solution) on the single polymer chain elasticity, similar elasticity studies on PFS₁₀₀ and PFS_{homo} were carried out in an aqueous solution of 0.1 M NaClO₄ by SMFS using normal Si₃N₄ AFM tips.

Figure 8.2 presents the force-extension curves and corresponding fits to the m-FJC model obtained in single chain stretching measurements on PFS₁₀₀ and PFS_{homo} in 0.1 M aqueous solution of NaClO₄, respectively. The fit parameters (Kuhn lengths and segment elasticities) are listed in Table 8.2. Similar to the results obtained for all three types of PFS chains stretched in isopropanol, all force curves acquired from the single chain stretching measurements in NaClO₄ for PFS₁₀₀ and PFS_{homo} show no detectable conformational transition.

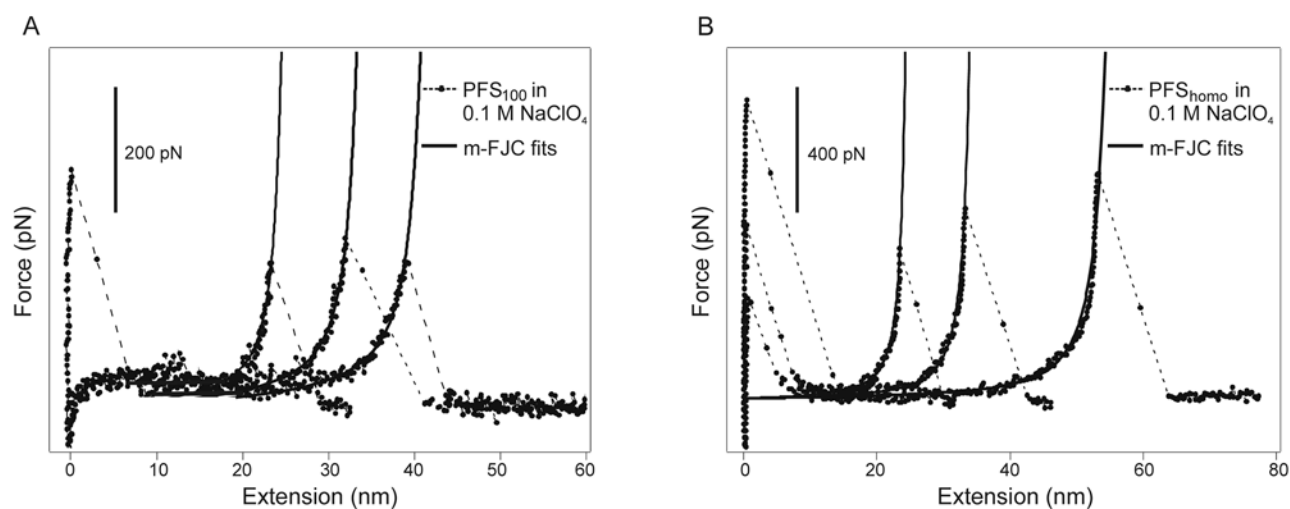


Figure 8.2. Force–extension curves of individual neutral (A) PFS₁₀₀ and (B) PFS_{homo} polymer chains measured in 0.1 M NaClO₄. Solid lines represent the superimposed m-FJC fits, respectively.

Table 8.2 Single chain elasticities of individual neutral PFS polymer chains probed in 0.1 M NaClO₄ (fitted by the m-FJC model).

solvent	PFS ₁₀₀		PFS _{homo}	
	Kuhn length (nm)	K_{segment} (nN/nm)	Kuhn length (nm)	K_{segment} (nN/nm)
0.1 M NaClO ₄	0.38 ± 0.03	30 ± 4	0.39 ± 0.05	35 ± 6

Despite different molar masses and end-functional groups, the Kuhn lengths of PFS₁₀₀ and PFS_{homo} obtained from m-FJC fits show identical values of ~ 0.40 nm (Table 8.2). As for K_{segment} , values of 30 ± 4 and 35 ± 6 nN/nm were observed for PFS₁₀₀ and PFS_{homo} chains, respectively. The slight deviation for the mean value of the enthalpy dominated elasticity (seen in the high force regime) may be due to the fact that most of the force curves obtained on PFS₁₀₀ showed

lower force values than the force curves obtained for PFS_{homo}.^{††} The data also show that the elasticity of PFS is very similar in the different solvents, i.e. ethanol (Chapter 7), isopropanol and aqueous solution of NaClO₄.

8.3 Single Chain Elasticity Measurements on Oxidized PFS Macromolecules

The ability to reversibly control the elasticity of PFS chains (neutral and oxidized) by external stimuli may be used to realize a molecular motor. After obtaining the elastic properties of neutral PFS chains, we now focus on the determination of the elastic properties of oxidized PFS chains. Following the discussion of the chemical oxidation, the reversible electrochemical oxidation of PFS is discussed in detail.

8.3.1 Chemically Oxidized PFS Macromolecules

Figure 8.3 shows representative force curves obtained in SMFS experiments on chemically oxidized PFS₁₀₀, PFS_{homo} and PS-*b*-PFS chains, respectively. To compare the force-extension relationship and the elasticity of different polymer chains with different extension lengths, the force traces were fitted with the m-FJC model and normalized by their lengths at the same given force (250 pN). The corresponding Kuhn lengths and segment elasticities are summarized in Table 8.3. Force curves of PFS_{homo} with different stretching lengths superimpose after normalization, as do the normalized force curves of PS-*b*-PFS. The superposition of normalized force curves, as well as the m-FJC fits, for PFS_{homo} and PS-*b*-PFS respectively, indicate the elongation of single polymer chains for both sets of data.

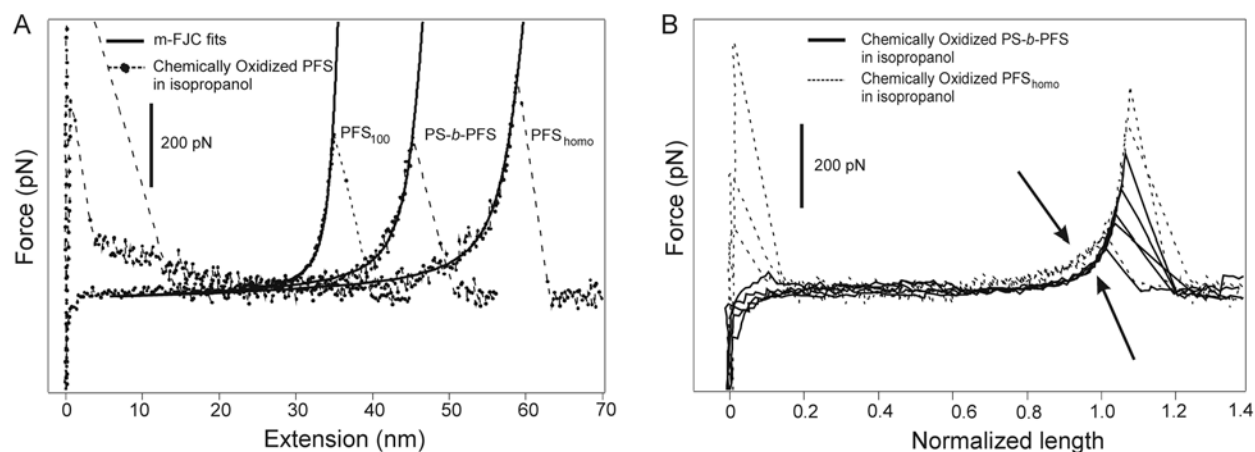


Figure 8.3. (A) Force–extension curves of individual chemically oxidized PFS₁₀₀, PFS_{homo} and PS-*b*-PFS chains stretched in isopropanol with superimposed m-FJC fits (shown as solid lines). (B) Superposition of normalized force curves for PFS_{homo} (dot lines) and PS-*b*-PFS (solid lines). The arrows denote different elasticities between PFS_{homo} and PS-*b*-PFS.

^{††} For the three particular force curves in Figure 8.2B, the segment elasticities obtained by fits to the m-FJC model that fitted the force curves up to 400 pN show a 23% (average) decrease compared to the mean value of $K_{\text{segment}} \sim 35 \pm 6$ nN/nm (Table 8.2).

Table 8.3 Single chain elasticities of neutral and chemically oxidized PFS and PS polymer chains fitted by m-FJC model.

	PFS ₁₀₀		PFS _{homo}		PS- <i>b</i> -PFS		PS	
	Kuhn length (nm)	K_{segment} (nN/nm)	Kuhn length (nm)	K_{segment} (nN/nm)	Kuhn length (nm)	K_{segment} (nN/nm)	Kuhn length (nm)	K_{segment} (nN/nm)
Neutral polymer chains in isopropanol	0.35 ± 0.03	32 ± 3	0.37 ± 0.04	31 ± 4	0.39 ± 0.05	23 ± 5	0.40 ± 0.03	18 ± 3
Chemically oxidized polymer chains in isopropanol	0.36 ± 0.04	34 ± 3	0.41 ± 0.05	35 ± 6	0.63 ± 0.05	27 ± 5	0.40 ± 0.02	19 ± 4

By contrast, the data for PFS_{homo} and PFS₁₀₀ on one hand, and the data for PS-*b*-PFS on the other hand, clearly differ (Figure 8.3B). Oxidized PS-*b*-PFS chains show a lower *entropic* elasticity compared to chemically oxidized PFS_{homo} chains, while latter ones yield identical elasticity parameters compared to the neutral PFS to within the experimental error.

From the m-FJC fit results, shown in Table 8.3 for PFS with different molar mass and end-functional groups, almost identical Kuhn lengths (~ 0.40 nm) and K_{segment} values (~ 35 nN/nm) were determined for PFS₁₀₀ and PFS_{homo}. These data are also identical to those of the neutral PFS, to within the experimental error. For PS-*b*-PFS chains, m-FJC fits yield an increased Kuhn length of 0.63 ± 0.05 nm and K_{segment} values of 27 ± 5 nN/nm, which are clearly different from PFS homopolymers.

The observations of unaltered elasticity parameters for PFS₁₀₀ and PFS_{homo} upon the chemical oxidation process can be explained by the incomplete oxidation of the PFS homopolymer chains. This may be caused by the unfavorable solubility of the (partially) oxidized PFS. Following this interpretation, the obtained elasticities represent the properties of partially oxidized (very low degree of oxidation) or even neutral PFS homopolymer chains. By contrast, in the copolymer case, the ferrocenyl units along the chains can be oxidized to a much higher extent by the charge transfer oxidation reagent TCNE due to the better solubility of the block copolymer chains that allows the formation of $[\text{Fe}(\text{C}_5\text{H}_5)_2]^+[\text{TCNE}]^-$.²⁵ The interpretation would be consistent with the observation of altered elasticities following electrochemical oxidation (see section 8.3.2), as well as the report by Shi *et al.* who used FeCl₃ as chemical oxidation agent for PFS homopolymers.²⁴ The elasticity of the PS block is not altered after the oxidation of PS-*b*-PFS by TCNE, as shown by the Kuhn length of 0.40 ± 0.02 nm, and K_{segment} of 19 ± 4 nN/nm for PS homopolymer. These values are to within the error identical to the data obtained without TCNE treatment (Table 8.3).

8.3.2 Electrochemically Oxidized PFS Macromolecules

A central requirement for a molecular motor is the possibility to run a cycle in a reversible manner (or periodically) to produce work. This requirement is difficult to achieve chemically. Reversible electrochemical oxidation and reduction are much more promising, as shown in Chapter 7.2-7.5. Therefore, the elasticity of electrochemically oxidized PFS₁₀₀ and PFS_{homo} were studied by SMFS using the AFM set-up equipped with an external potentiostat.

The electrochemical responses of PFS₁₀₀ and PFS_{homo} were determined using cyclic voltammetry (CV) in the electrochemical SMFS measurement configuration. Figure 8.4 shows the CV data recorded in 0.1 M NaClO₄ aqueous solution (in situ in the AFM liquid cell), in which the reversible redox behavior for the PFS polymers is clearly recognized. The oxidation and reduction potentials were obtained using a Pt reference electrode (instead of Hg/HgSO₄ used in Chapter 7); hence the values have shifted to more positive potentials compared to the CV data shown in Chapter 7.^{22,23,26}

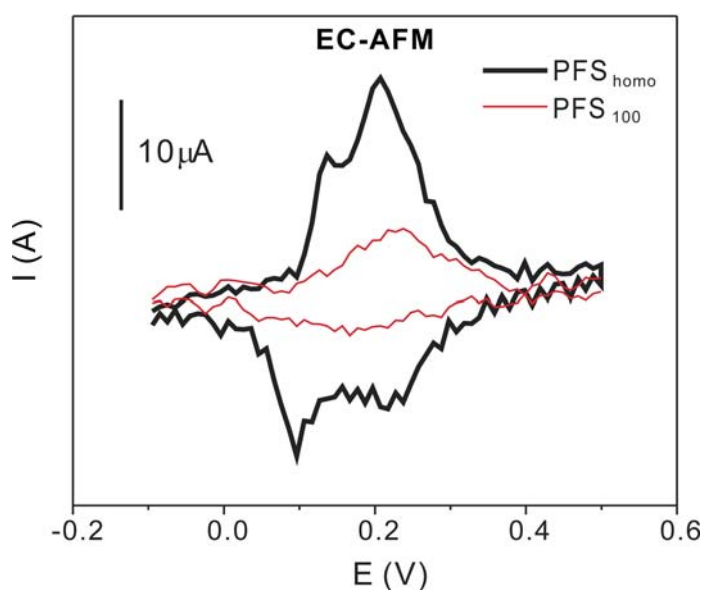


Figure 8.4. Cyclic voltammograms of PFS_{homo} layer (thick line), obtained by spin-coating from $\sim 1.5 \Delta 10^{-10}$ M toluene solution on gold substrates (layer thickness: 7 ± 2 nm), and PFS₁₀₀ layer self-assembled from $4 \Delta 10^{-7}$ M toluene solution on gold substrates recorded in SMFS experimental configuration equipped with an external potentiostat using an electrochemical liquid cell (scan rate $v = 50$ mV/s, 0.1 M NaClO₄ as electrolyte, working electrode: Au substrate; reference and counter electrode: Pt).

The cyclic voltammograms indicate that PFS homopolymer chains can be reversibly oxidized and reduced by applying an external potential. Instead of using isolated polymer chains as described in Chapter 7, the voltammogram of PFS₁₀₀ (shown in Figure 8.4, thin line) was recorded on neat PFS₁₀₀ layers prepared from toluene solution to increase the electrochemical redox signal. The surface coverages of different PFS polymer chains can be estimated using the same method illustrated in Chapter 7.2. The integrated charge transfer is $\sim 1.8 \Delta 10^{-5}$ C for

PFS₁₀₀, calculated from the CV plot. The surface coverage of ferrocenyl sites (Γ_{Fc}) can be determined based on the transferred charge over the electrode area.^{‡‡} The number of PFS₁₀₀ chains per unit area (ρ) is calculated by dividing Γ_{Fc} to the degree of polymerization (DP, 92 for PFS₁₀₀), which gives a value of $\rho = 3.2 \Delta 10^{-2}$ chains/nm² (in our experiments, $A = 0.35$ cm²). Following the same procedure, the integrated charge transfer for PFS_{homo} can be obtained as $\sim 4.9 \Delta 10^{-5}$ C. The calculated surface coverage of PFS_{homo} chains gives the value of $\rho = 3.0 \Delta 10^{-2}$ chains/nm².

Samples with PFS₁₀₀ and PFS_{homo} chains were subjected to the SMFS measurements under a constant external potential of +0.5 V. The force-extension curves of electrochemically oxidized PFS molecules are presented in Figure 8.5 together with fits to the m-FJC model.

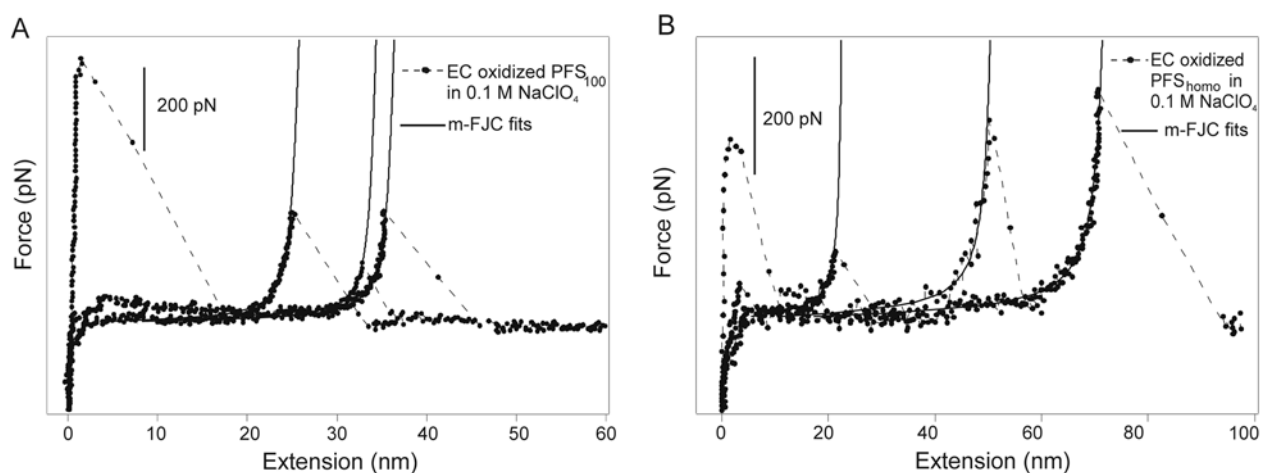


Figure 8.5. Force-extension curves of electrochemically oxidized (A) PFS₁₀₀ and (B) PFS_{homo} superimposed with m-FJC fits (solid lines).

The fit parameters of electrochemically oxidized PFS homopolymer chains are listed and compared to the elasticity data of neutral chains in Table 8.4.

Table 8.4 Single chain elasticities of individual neutral and electrochemically oxidized PFS polymer chains probed in 0.1 M NaClO₄ (fitted by the m-FJC model).

neutral polymer in	PFS ₁₀₀		PFS _{homo}	
	Kuhn length (nm)	K_{segment} (nN/nm)	Kuhn length (nm)	K_{segment} (nN/nm)
0.1 M NaClO ₄	0.38 ± 0.03	30 ± 4	0.39 ± 0.05	35 ± 6
Electrochemically oxidized polymers in 0.1 M NaClO ₄	0.65 ± 0.05	45 ± 8	0.63 ± 0.04	39 ± 6

^{‡‡} $\Gamma_{Fc} = \frac{Q_{Fc}}{nFA}$, n is the number of electrons involved in the electron transfer process ($n=1$), F is the Faraday constant and A is the geometric surface area of the electrode ($A = 0.35$ cm²).

We observed for both systems a significant increase in Kuhn length compared to the neutral state. The trend of the elasticity parameters upon oxidation is qualitatively similar to the trend observed for the chemically oxidized block copolymer, i.e. the segment elasticities and in particular the Kuhn lengths increase.

The clearly different elastic properties of oxidized PFS molecules compared to the neutral PFS homopolymers, as determined by means of SMFS after electrochemical oxidation, show that control of the elasticity by changing from oxidized PFS to neutral PFS reversibly, and thereby a single molecule motor based on PFS, can in principle be realized.

8.4 Changing the Elasticity of PFS between the Neutral and Oxidized States

After chemical and/or electrochemical oxidation of the ferrocenyl groups, the polymers bear positive charges that are distributed along the polymer chains. From the classical Odijk-Skolnick-Fixman (OSF) theory,^{27,28} it is expected that the electrostatic interactions between the charges along the polymer chain increase the distances between like-charged segments, i.e. it favors the stretched conformation of the chains. This effect is expected to increase the Kuhn length (or persistence length) of the molecules by an additional electrostatic contribution. Our experimental results, i.e. an increase of the Kuhn length from of ~0.40 nm in the neutral state to ~0.65 nm in the oxidized state agree well with this expectation. The increase in Kuhn length corresponds to a lower restoring force or elasticity of the oxidized PFS.

As pointed out in section 8.3.1, the elasticity of PS-*b*-PFS filaments may include a contribution from PS blocks (which itself is identical for the neutral and the oxidized states). This contribution can be estimated as 27%.^{§§} The changes of elasticity induced either by chemical or electrochemical stimuli offer the possibility for realizing the ultimate target: a simple mechanical molecular motor based on controlling the elasticity.

8.5 Chemically and Electrochemically Induced Mechanical Work

As explained in section 8.1, the output or the work of a thermal cycle is the mechanical energy converted from the transferred heat. For the molecular motor using a single polymer

^{§§} (1) The calculation was performed by calculating a weighted average of $L(\text{PS-}b\text{-PFS})$:

$$L(\text{PS-}b\text{-PFS}) = x L(\text{PS}) + (1-x) L(\text{PFS}),$$

where L is the modified Langevin function (equation 7.5), and x is the fraction of PS block in the copolymer chain. This function was fitted to the force-extension curve of oxidized PS-*b*-PFS with a Kuhn length of 0.63 nm and a K_{segment} of 27 nN/nm. This procedure yielded the result of $x = 27\%$.

chain as working substance (Figure 8.6A), the mechanical work (output) of the cycle corresponds to the effectively converted electrochemical potential.

One possible experimental cycle to realize the molecular motor is illustrated in Figure 8.6B, which is defined by keeping the deflection of the cantilever constant in SMFS measurements, i.e. constant force, during the transition from the oxidized state to the neutral state (vice versa).*** The mechanical branches are determined by the elasticities of the polymer, which are well described by the m-FJC model in the low force range.

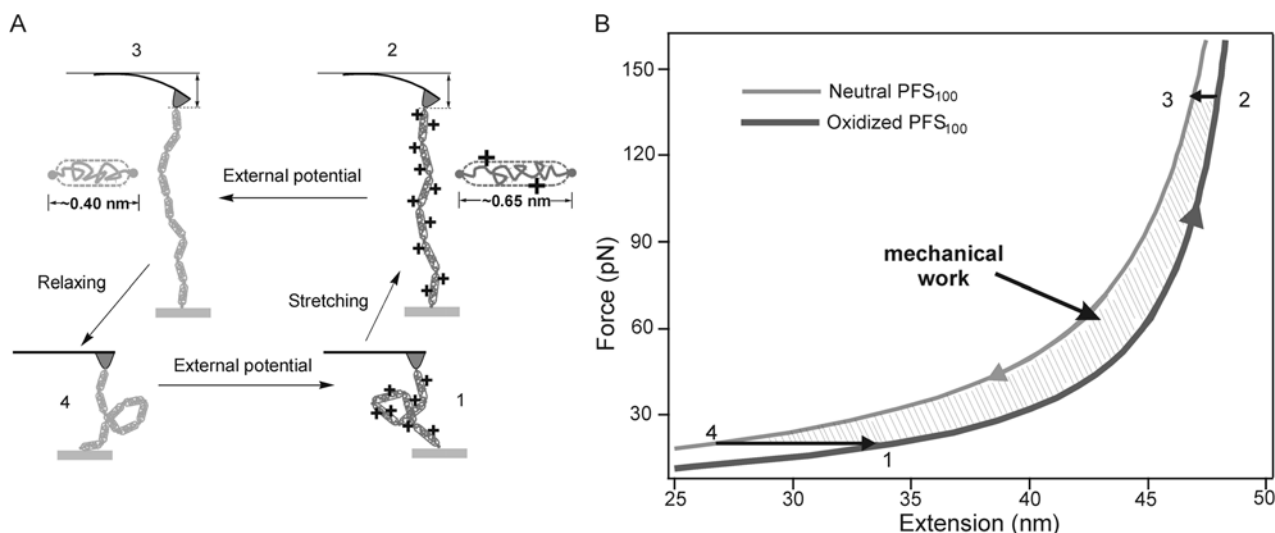


Figure 8.6. (A) Schematic illustration of a single molecule operating cycle with electroactive macromolecules. (B) Experimental realization of the single molecule operating cycle with PFS macromolecules (DP=80) powered by an electrochemical potential. Force curves are plotted based on the m-FJC function with Kuhn lengths of 0.40 nm (neutral PFS) and 0.65 nm (oxidized PFS), and segment elasticities of 30 nN/nm (neutral PFS), and 45 nN/nm (oxidized PFS).

As shown in Figure 8.6B, starting from a force of 20 pN (point 1) under an applied constant external potential of +0.5 V, an individual, oxidized PFS polymer chain of 50 nm contour length is pulled to a force of 140 pN (point 2). At a constant force of 140 pN, the PFS chain is reduced to its neutral state by controlling the external potential back to 0 V (point 3), resulting in a change of the elasticity of the polymer chain. Then the force on the polymer is reduced back to 20 pN (point 4). Finally the cycle is completed by applying the external potential of +0.5 V in order to completely oxidize the whole PFS chain. By periodically controlling the

*** One can also define the cycle with constant piezo extension during the oxidation or reduction processes, if the contraction ratio (before and after oxidation) of the polymer chain against the external force is known. In our experiments, it was not possible to measure the change of the contour length of a particular chain before and after oxidation. These data are also not reported in the literature. It is important to note that the elasticity (in terms of Kuhn length and segment elasticity) of the single polymer chain does not depend on the extension or contour lengths of the polymer, but only reflects the intrinsic properties of the polymer itself. In our experiments, it was not possible to hold the neutral polymer chain between the AFM tip and the substrate and reversibly oxidize/reduce it during force-extension measurements. However, by recording force-extension data at the very same x, y position both in neutral and oxidized states, it may be possible to stretch the “same” PFS chain before and after electrochemical oxidation.

external potential, the corresponding oxidized and/or neutral PFS chains can be created to realize the operating cycle. From the cycle, the mechanical work performed by the PFS polymer chain may be calculated as the integral of the area of the cycle. A work of $3.4 \Delta 10^{-19}$ J is obtained from the cycle in Figure 8.6.

8.6 Efficiency of Converting Electrochemical Energy to Mechanical Work

It is instructive to analyze the efficiency of the cycle shown in Figure 8.6. Assuming that all electrons (80 electrons/chain in Figure 8.6)^{†††} reach the PFS chain, a maximum efficiency of the PFS electrochemical–mechanical energy conversion at the molecular level can be estimated as:

$$\xi = \frac{W_{out}}{\div \sigma \div N}$$

where, W_{out} is the mechanical work, $\div \sigma$ is the change of the electrochemical potential and $\div N$ is the number of transferred charges during the oxidation/reduction processes.

For the electrochemically oxidized PFS_{homo}, assuming that each ferrocenyl group has been oxidized to ferrocenium and each unit bears one charge, the change of electrochemical potential is estimated as:

$$\div \sigma = \bar{\sigma}_i - \sigma_i = z_i F \div \lambda \quad \mathbf{8.1}$$

here, $\bar{\sigma}_i$ is the chemical potential of the electrochemically oxidized PFS chain (also called electrochemical potential), σ_i is the chemical potential of the neutral PFS chain, z_i is number of charges per redox center ($z_i = 1$), F is the Faraday constant (96486 C mol^{-1}) and $\div \lambda$ is the electric potential to complete the oxidation of the entire PFS chain.

Hence, an energy of $\sim 6.4 \Delta 10^{-18}$ J is needed under the externally applied potential (0.5 V) to complete one cycle, as calculated using equation 8.1. With the total mechanical work of $3.4 \Delta 10^{-19}$ J (estimated from the area of the cycle), an efficiency of $\sim 5\%$ is obtained for this simple electrochemical mechanical motor.

The maximum efficiency ξ of the single molecule optomechanical cycle reported by Hugel *et al.* was estimated as $\sim 10\%$.¹⁸ In our studies, a potential difference of 0.5 V was used to ensure the complete oxidation of the entire polymer chain on the Au electrode surface. However, if an individual polymer chain close to the electrode surface can be addressed, the external potential

^{†††} A monomer repeat unit is ~ 0.63 nm for PFS homopolymer chains and the entire PFS₁₀₀ chain of ~ 58 nm can be calculated by 0.63×92 (DP). So for a PFS chain with 50 nm contour length, the DP can be calculated as $50 / 0.63 = 80$.

difference could be reduced to 0.25 V, which obviously would increase the efficiency to ~10% (approaching the same value reported by Hugel *et al.*).

Considering the effect of chain length might influence on the efficiency of the cycle, the mechanical work performed by different polymer chain lengths of 10, 30, 50, 100 and 180 nm (for PFS_{homo}, M_w=77500, the maximum chain length is 180 nm) was calculated (Table 8.5). Longer PFS chains perform more work, but because of the concomitant increase in the electrochemical energy, the efficiency remains virtually unchanged.

Table 8.5 Calculated W_{out} from the cycles with different contour lengths.

Contour length (nm)	Single chain Work _{out} Δ 10 ⁻¹⁹ J	External input Δ 10 ⁻¹⁹ J	Efficiency %
10	0.7	13	5.4
30	2.2	40	5.4
50	3.4	64	5.3
100	7.1	133	5.3
180	12.8	228	5.6

The simplified estimate of the efficiency shown above does not explicitly take into account the contribution of the counter ions, nor possible energy dissipation. Since the efficiency (for one molecule with a constant number of redox active centers) is directly related to the work (W_{out}), which in turn is related to the elasticity difference between the two states, the efficiency can potentially be increased by enhancing the relative change of elasticity upon oxidation/reduction.

8.7 Conclusions

It has been demonstrated that external chemical or electrochemical stimuli can be used to induce reversible elasticity changes of individual PFS chains on surfaces by changing the redox state between neutral and oxidized. The changes were assessed at the single molecule level by SMFS. Using the m-FJC model to fit the force-extension data measured on single PFS chains, an increased Kuhn length of ~ 0.65 nm and segment elasticity of ~ 45 nN/nm are obtained compared to the Kuhn length of ~0.40 nm and segment elasticity of ~ 30 nN/nm for neutral PFS. The detected changes of the elasticity of individual chemical/electrochemical-stimuli-responsive PFS chains are the basis for the demonstration of the principle of a single (macro)molecular motor. For PFS homopolymers with DP ~80 a work of ~ 3.4 Δ 10⁻¹⁹ J and an efficiency of 5% were estimated based on the experimental data.

8.8 Experimental

Materials. Poly(ferrocenyldimethylsilane) (PFS_{homo}), and poly(styrene-*block*-ferrocenyldimethylsilane) (PS-*b*-PFS) were available from other studies (using anionic polymerization, synthesized by Igor Korczagin).²⁹ The following molar mass data were determined by GPC in THF, relative to polystyrene standards: PFS₁₀₀ ($M_n = 22600$ g/mol, $DP_n = 92$, $M_w/M_n = 1.13$).^{22,26,30} PFS_{homo} ($M_n = 71670$, $M_w = 75420$, $M_w/M_n = 1.05$), PS-*b*-PFS ($M_n = 77680$, $M_w = 78440$, $M_w/M_n = 1.01$, 22.8% (by mass), 19.8% (by volume) ferrocenyl groups). Polystyrene standards ($M_w = 20650$, $M_w/M_n = 1.03$; $M_w = 79000$, $M_w/M_n = 1.16$) for GPC were used for the blanko experiments.

Polymers were chemically oxidized using tetracyanoethylene (TCNE) in CH₂Cl₂ at RT with equal mole fraction to ferrocenyl groups until the color of the solution became dark green.

Substrates and Samples. (a) Gold substrates (11 Δ 11 mm², 250 nm Au on 2 nm Cr on borosilicate glass) for electrochemical oxidation SMFS measurements were purchased from Metallhandel Schröer GmbH (Lienen, Germany). Au(111) samples were obtained by annealing these substrates in a high purity H₂ flame for 5 minutes.^{31,32} PFS₁₀₀ SAMs were prepared from dilute toluene solutions (~ 0.005 mg/L) following the standard procedures discussed in Chapter 7.7. PFS_{homo} thin layers were prepared by spin-coating a very dilute toluene solution (~ 0.005 mg/L) on Au(111) substrates. (b) Spin-coating films from a toluene solution (~ 0.005 mg/mL) of PFS on silicon wafers, film thicknesses (< 10 nm) were determined with a Plasmos SD 2002 ellipsometer, using a wavelength of 632.8 nm (refractive index=1.687). Prior to use, all these substrates were cleaned in piranha solution (7:3 H₂SO₄: H₂O₂ (30%) by volume), then rinsed with Milli-Q water and ethanol and dried in a nitrogen stream. ***Caution: Piranha solution should be handled with extreme caution: it has been reported to detonate unexpectedly.***

Force Measurements. Force spectroscopy experiments were performed by in situ AFM in liquid environment with a NanoScope IIIa multimode AFM (Digital Instruments (DI), Santa Barbara, CA) fitted with either a normal DI liquid cell or DI electrochemical liquid cell (volume in each case ~ 50 μ L). Commercially available V-shaped Si₃N₄ cantilevers (DI) were used. Each cantilever was calibrated after a given experiment according to the equipartition method, by measuring the thermal excitation of the tip to compute its spring constant.^{33,34} The measured spring constants of the cantilevers varied between 0.075 and 0.105 (± 0.017) N/m.

For electrochemical SMFS experiments, a DI electrochemical liquid cell equipped with an external Autolab PGSTAT10 potentiostat (ECOCHEMIE, Utrecht, The Netherlands) was used. The polymer covered gold substrate served as the working electrode; Pt wires were used as

reference and counter electrodes. The electrolyte used was 0.1 M NaClO₄ in water. Prior to the experiments, the electrolyte was deaerated by passing nitrogen through the solution for 5 minutes. Cyclic voltammograms were recorded between $-0.1 V_{Pt}$ and $+0.5 V_{Pt}$ at a scan rate of 50 mV/s. An external potential of +0.5 V was maintained during the force measurements to ensure the complete oxidation of PFS molecules.

References:

- (1) Wang, H. Y.; Oster, G. *Nature* **1998**, *396*, 279-282.
- (2) Keller, D.; Bustamante, C. *Biophysical Journal* **2000**, *78*, 541-556.
- (3) Bustamante, C.; Keller, D.; Oster, G. *Accounts of Chemical Research* **2001**, *34*, 412-420.
- (4) Vale, R. D.; Milligan, R. A. *Science* **2000**, *288*, 88-95.
- (5) Rayment, I.; Holden, H. M.; Whittaker, M.; Yohn, C. B.; Lorenz, M.; Holmes, K. C.; Milligan, R. A. *Science* **1993**, *261*, 58-65.
- (6) Atsumi, T.; McCarter, L.; Imae, Y. *Nature* **1992**, *355*, 182-184.
- (7) Balzani, V.; Credi, A.; Raymo, F. M.; Stoddart, J. F. *Angewandte Chemie-International Edition* **2000**, *39*, 3349-3391.
- (8) Feringa, B. L. *Accounts of Chemical Research* **2000**, *33*, 346-353.
- (9) Collin, J. P.; Dietrich-Buchecker, C.; Gavina, P.; Jimenez-Molero, M. C.; Sauvage, J. P. *Accounts of Chemical Research* **2001**, *34*, 477-487.
- (10) Pease, A. R.; Jeppesen, J. O.; Stoddart, J. F.; Luo, Y.; Collier, C. P.; Heath, J. R. *Accounts of Chemical Research* **2001**, *34*, 433-444.
- (11) Schalley, C. A.; Beizai, K.; Vogtle, F. *Accounts of Chemical Research* **2001**, *34*, 465-476.
- (12) Balzani, V.; Credi, A.; Venturi, M. *Proceedings of the National Academy of Sciences of the United States of America* **2002**, *99*, 4814-4817.
- (13) Ludwig, M.; Rief, M.; Schmidt, L.; Li, H.; Oesterhelt, F.; Gautel, M.; Gaub, H. E. *Applied Physics A-Materials Science & Processing* **1999**, *68*, 173-176.
- (14) Rief, M.; Oesterhelt, F.; Heymann, B.; Gaub, H. E. *Science* **1997**, *275*, 1295-1297.
- (15) Li, H. B.; Rief, M.; Oesterhelt, F.; Gaub, H. E.; Zhang, X.; Shen, J. C. *Chemical Physics Letters* **1999**, *305*, 197-201.
- (16) Marszalek, P. E.; Oberhauser, A. F.; Pang, Y. P.; Fernandez, J. M. *Nature* **1998**, *396*, 661-664.
- (17) Zhang, W. K.; Zou, S.; Wang, C.; Zhang, X. *Journal of Physical Chemistry B* **2000**, *104*, 10258-10264.
- (18) Hugel, T.; Holland, N. B.; Cattani, A.; Moroder, L.; Seitz, M.; Gaub, H. E. *Science* **2002**, *296*, 1103-1106.
- (19) Steinberg, I. Z. O., A.; Katchalsky, A. *Nature* **1966**, *210*, 568.
- (20) Pines, E.; Wun, K. L.; Prins, W. *Journal of Chemical Education* **1973**, *50*, 753-756.
- (21) Foucher, D.; Ziembinski, R.; Petersen, R.; Pudelski, J.; Edwards, M.; Ni, Y. Z.; Massey, J.; Jaeger, C. R.; Vancso, G. J.; Manners, I. *Macromolecules* **1994**, *27*, 3992-3999.
- (22) Peter, M.; Hempenius, M. A.; Lammertink, R. G. H.; Vancso, G. J. *Macromolecular Symposia* **2001**, *167*, 285-296.
- (23) Zou, S.; Ma, Y.; Hempenius, M. A.; Schönherr, H.; Vancso, G. J. *Langmuir* **2004**, *20*, 6278-6287.
- (24) Shi, W. Q.; Cui, S.; Wang, C.; Wang, L.; Zhang, X.; Wang, X. J. *Macromolecules* **2004**, *37*, 1839-1842.
- (25) Hempenius, M. A. Private discussions.
- (26) Peter, M.; Hempenius, M. A.; Kooij, E. S.; Jenkins, A. T. A.; Roser, S. J.; Knoll, W.; Vancso, G. J. *Langmuir* **2004**, *20*, 891-897.
- (27) Odijk, T. *Macromolecules* **1979**, *12*, 688-693.
- (28) Skolnick, J.; Fixman, M. *Macromolecules* **1977**, *10*, 944-948.
- (29) Lammertink, R. G. H.; Hempenius, M. A.; Thomas, E. L.; Vancso, G. J. *Journal of Polymer Science Part B-Polymer Physics* **1999**, *37*, 1009-1021.
- (30) Peter, M.; Lammertink, R. G. H.; Hempenius, M. A.; van Os, M.; Beulen, M. W. J.; Reinhoudt, D. N.; Knoll, W.; Vancso, G. J. *Chemical Communications* **1999**, 359-360.
- (31) Manne, S.; Butt, H. J.; Gould, S. A. C.; Hansma, P. K. *Applied Physics Letters* **1990**, *56*, 1758-1759.
- (32) Schönherr, H.; Vancso, G. J.; Huisman, B. -H.; van Veggel, F. C. J. M.; Reinhoudt, D. N. *Langmuir* **1999**, *15*, 5541-5546.
- (33) Florin, E. L.; Rief, M.; Lehmann, H.; Ludwig, M.; Dornmair, C.; Moy, V. T.; Gaub, H. E. *Biosensors & Bioelectronics* **1995**, *10*, 895-901.
- (34) Butt, H. J.; Jaschke, M. *Nanotechnology* **1995**, *6*, 1-7.

Summary

Molecular level visualization, sensing (by force), manipulation, and control of supramolecular assemblies and polymeric materials have been explored in this Thesis on the nanoscale using self-assembled monolayers (SAMs) and atomic force microscopy (AFM)-based platforms. Molecular forces in synthetic supramolecular host-guest and H-bonding complexes, direct detection of supramolecular H-bonded polymers, as well as mechanical properties of stimuli-responsive organometallic polymer chains have been studied by AFM-based single molecule force spectroscopy (SMFS). Under thermodynamic quasi-equilibrium conditions, rupture forces of individual host-guest complexes between β -cyclodextrin (β -CD) and various apolar guest molecules have been found to correlate with the corresponding complexation constants. Transitions from non-equilibrium to quasi-equilibrium states controlled by temperature in synthetic H-bonding (ureidopyrimidinone) systems have been observed on a single molecule level for the first time. The probing of reversible supramolecular H-bonding polymers, and the investigation of mechanical properties of stimuli-responsive poly(ferrocenylsilane) (PFS) macromolecules as a model system to realize an electrochemically powered molecular motor by SMFS have also been presented in the Thesis.

With the emergence of nanoscience and nanotechnology, many established fields have been integrated to tackle new scientific and technological challenges. In Chapter 2, a brief account has been given regarding structure, property, fabrication and function of bottom-up controlled molecular objects, including biological systems and synthetic supramolecular complexes. The combination of emerging SMFS experiments with new theories describing single molecular forces is anticipated to provide a solid foundation for the *nanoscience* of molecular forces and their dependence on approach and withdrawal rates. Molecular forces, that allow one to observe and manipulate nanostructures, have been playing an increasingly important role also in *nanotechnology* due to the widespread use of AFM-based platforms (e.g. in nanofabrication). These platforms enable controlled probing and placement of isolated nanoscale objects in a one-to-one fashion between the given nano-objects and the macroscale tool (AFM set-up). As a step towards achieving full control over objects with molecular scale dimensions, SMFS has been applied in this Thesis to previously unexplored supramolecular and polymer systems.

Expanding on previous work that addressed the unbinding force of ferrocenyl-derivatized guest molecules and -CD SAMs, Chapter 3 describes the rupture forces of individual host-guest complexes between -CD in SAMs and various apolar guest molecules in aqueous medium determined by force spectroscopy measurements. The analysis of the rupture force histograms revealed periodic distributions of forces, which were characteristic for each guest moiety. The observed force quanta of 39 ± 15 , 45 ± 15 , 89 ± 15 , and 102 ± 15 pN determined for anilyl, tolyldyl, tert-butylphenyl, and adamantly guests, respectively, were attributed to the unbinding forces of single host-guest complexes. The host-guest complex rupture forces were probed under thermodynamic quasi-equilibrium as indicated by the lack of loading rate dependences. The force quanta and the thermodynamic parameters of the inclusion complexes, determined by isothermal titration calorimetry and surface plasmon resonance measurements, followed the same trend. The experimental data agreed well with an equilibrium model based on the evaluation of the potential energy landscape of AFM tip-surface interactions. Finally, the unbinding forces measured for multivalent interactions using a bis-adamantly-derivatized guest were consistent with theoretical considerations.

A substrate-immobilized molecular platform for the controlled immobilization and growth of supramolecular architectures was developed based on the self-complementary molecular recognition of 2-ureido-4[1H]-pyrimidinone (UPy) moieties via quadruple hydrogen bonding, as presented in Chapter 4. Two novel asymmetric UPy disulfides, as well as trifluoromethyl and ferrocenyl-derivatized UPy guests were synthesized. The observed surface-enhanced apparent dimerization constant could be tuned by solvent composition and temperature, which allowed us to control the complex stability. This feature opens the possibility for the construction of more complex, directionally defined surface-immobilized supramolecular architectures, as well as for the study of pyrimidinone-based supramolecular polymers at surfaces and interfaces.

Unbinding behavior of individual supramolecular complexes of UPy derivatives formed via self-complementary quadruple hydrogen bonds studied by SMFS was described in Chapter 5. The rupture forces of individual quadruple H-bonding arrays were 180 ± 21 pN at a loading rate of 35 ± 0.7 nN/s in hexadecane and were found to be loading rate dependent in the range of 5 nN/s to 500 nN/s at 301 K. The rupture forces changed with temperature and were independent of loading rate in the range of 5 nN/s to 200 nN/s at 330 K. Thus the rupture forces of supramolecular H-bonded UPy complexes showed a crossover from quasi-equilibrium to non-equilibrium following changes in temperature. The crossover force was found to be 145 ± 20 pN. These results constitute the first report of force measurements in synthetic H-bonding systems that revealed transitions from non-equilibrium to quasi-equilibrium states controlled by

temperature. A similar crossover was also observed following changes of the solvent composition.

The AFM data discussed in Chapter 6 showed that reversible supramolecular polymers could be investigated at the single molecule level. In poly(ethylene glycol) – based UPy supramolecular polymer materials, the individual reversible linking sites along a supramolecular polymer chain, i.e. the complexes based on self-complementary recognition of UPy groups, acted as independent bonds in series. The rupture force of an individual self-complementary UPy complex in supramolecular polymers was measured to be 173 ± 23 pN at a loading rate of 35 ± 0.7 pN/s. Since material properties, including viscosity, composition, or chain length, are functions of various external parameters and stimuli, which can be investigated in situ, highly useful information for the design and construction of nanometer scale devices and stimuli-responsive systems has now become directly accessible from SMFS experiments.

Systematic investigations of the insertion behavior of ethylene sulfide end-functionalized poly(ferrocenylsilane) (PFS) derivatives into pre-formed SAMs were carried out, as described in Chapter 7. A robust and reproducible procedure allowed us to obtain individually isolated PFS macromolecules covalently attached to solid substrates. AFM, contact angle and electrochemical measurements were carried out to characterize the morphology, wettability and surface coverages of the mixed layers. PFS surface coverages depended on the chain lengths of the thiol molecule and the concentration of the PFS solution in toluene, but not on the insertion time and the chain length of the end-functionalized PFS molecules. Very low surface coverages were achieved by insertion from very dilute PFS solutions into long-chain SAMs. Differential pulse voltammetry provided a very useful tool to elucidate the isolation effects that existed in mixed layers of lower PFS surface coverage. In samples with very low PFS surface coverages most of the interchain interactions were avoided, which was a requirement for the investigation of single PFS chain elongation by SMFS. The immobilized isolated PFS macromolecules were subjected to in situ AFM for SMFS measurements for the first time in isopropanol. The elasticity of PFS single polymer chains was determined by fitting the experimental results with the modified freely-jointed chain (m-FJC) model, which showed, depending on the applied force, entropic and partly enthalpic elastic behavior of this polymer.

Chapter 8 demonstrates that external chemical or electrochemical stimuli could be used to induce reversible elasticity changes of individual PFS chains on surfaces by changing the redox state between neutral and oxidized. The changes were assessed at the single molecule level by SMFS. Using the m-FJC model to fit the force-extension data measured on single oxidized PFS chains, an increased Kuhn length of ~ 0.65 nm and segment elasticity of ~ 45 nN/nm were

Summary

obtained compared to neutral PFS with a Kuhn length of ~ 0.40 nm and a segment elasticity of ~ 30 nN/nm. The detected changes of the elasticity of individual stimuli-responsive PFS macromolecules were the basis for the demonstration of the principle of a electrochemically or chemically driven single (macro)molecular motor. For PFS homopolymer with a degree of polymerization of 80, a work of $3.4 \Delta 10^{-19}$ J and an efficiency of 5% were estimated based on the experimental data.

Samenvatting

Visualisatie op moleculair niveau, krachtmetingen, manipulatie op het niveau van een enkel molecuul en controle over supramoleculaire structuren en polymere materialen zijn in dit proefschrift op nanometerschaal onderzocht door gebruik te maken van zelforganiserende monolagen (SAMs) en atomic force microscopy (AFM). Moleculaire krachten in synthetische supramoleculaire host-guest en waterstofbrug-vormende complexen, directe detectie van supramoleculaire H-brug gebonden polymeren, als ook de mechanische eigenschappen van stimulus-responsive organmetaal polymeerketens zijn bestudeerd met behulp van AFM-gebaseerde krachtspectroscopie op het niveau van een enkel molecuul (SMFS). In experimenten onder omstandigheden van thermodynamisch quasi-evenwicht waarin de kracht gemeten wordt die noodzakelijk is om complexen van η -cyclodextrine (η -CD) en verschillende apolaire moleculen (guests) te verbreken, blijkt er een duidelijke correlatie tussen deze kracht en de corresponderende complexeringsconstanten te bestaan. Overgangen van niet-evenwichts- naar quasi-evenwichtstoestanden in synthetische H-brug vormende (ureidopyrimidinone) systemen, aangestuurd door het variëren van de temperatuur, zijn voor het eerst waargenomen op een enkel-molecuul niveau. Tot slot worden de bestudering van reversibele supramoleculaire H-brug gebonden polymeren, en de mechanische eigenschappen van stimulus-responsive poly(ferrocenylsilaan) (PFS) macromoleculen, die gelden als een modelsysteem voor een electrochemisch aangedreven moleculaire motor door SMFS, gepresenteerd in dit proefschrift.

Met de opkomst van nanowetenschap en nanotechnologie zijn veel reeds bestaande (maar traditioneel gescheiden) gebieden geïntegreerd om op deze wijze nieuwe wetenschappelijke en technologische uitdagingen het hoofd te bieden. In Hoofdstuk 2 wordt een beknopt overzicht gegeven van de structuur, eigenschappen, fabricage en de functie van bottom-up gerealiseerde moleculaire objecten, waaronder zowel biologische systemen als synthetische supramoleculaire complexen. De combinatie van SMFS experimenten met nieuwe theorieën die krachten behorend bij enkelvoudige moleculen beschrijven legt naar verwachting een solide basis voor de *nanoscience* van moleculaire krachten en hun afhankelijkheid van toenaderings- en terugtrekkingssnelheden. Moleculaire krachten, die het mogelijk maken om nanostructuren te observeren en te manipuleren, spelen een nog steeds groeiende rol in *nanotechnology* door het wijdverspreide gebruik van AFM-gebaseerde technieken (bijvoorbeeld in nanofabrication).

Met deze technieken is het mogelijk om op een gecontroleerde wijze geïsoleerde nano-objecten te bestuderen en te positioneren. Als een volgende stap in de richting van volledige controle over objecten van moleculaire afmetingen wordt in dit proefschrift SMFS toegepast op nieuwe supramoleculaire en polymeer systemen.

Voortbouwend op eerder werk waarin de kracht werd bepaald die nodig is om ferrocenyl-afgeleide gastmoleculen los te trekken van η -CD SAMs, worden in Hoofdstuk 3 de krachten beschreven die benodigd zijn om individuele host-guest complexen van η -CD in SAMs met verschillende apolaire gastmoleculen te verbreken in een wateromgeving. Deze krachten werden gemeten in krachtspectroscopie experimenten. De analyse van deze krachten aan de hand van histogrammen liet duidelijk periodieke verdelingen van krachten zien die karakteristiek zijn voor ieder specifiek gastmolecuul. De geobserveerde krachtquanta van 39 ± 15 , 45 ± 15 , 89 ± 15 en 102 ± 15 pN voor de anilyl, toluidyl, *tert*-butylphenyl and adamantyl groepen, respectievelijk, vertegenwoordigen de benodigde kracht om enkelvoudige complexen van guest en η -CD te verbreken. De krachten zijn gemeten onder condities van thermodynamisch quasi-evenwicht, wat bevestigd wordt door het feit dat de krachten onafhankelijk bleken te zijn van de loading rate. De krachtquanta en de thermodynamische parameters van deze complexen, die bepaald zijn met behulp van isothermische titratie calorimetrie en surface plasmon resonantie metingen, volgen dezelfde trend. De experimentele data correleren zeer goed met een evenwichtsmodel dat gebaseerd is op het potentiële energielandschap dat volgt uit de interacties tussen de AFM tip en het oppervlak. Tenslotte bleken de gemeten host-guest-verbrekende krachten voor multivalente interacties in het geval van een bis-adamantyl-afgeleid molecuul overeen te komen met theoretische overwegingen.

Een substraat-geïmmobiliseerd moleculair platform voor de gecontroleerde immobilisatie en groei van supramoleculaire architecturen werd ontwikkeld, gebaseerd op 2-ureido-4[1H]-pyrimidinone (UPy) eenheden, die via een 4-voudige waterstofbrug zelf-complementair zijn, zoals is gepresenteerd in Hoofdstuk 4. Twee nieuwe asymmetrische UPy disulfides, als ook trifluormethyl- en ferrocenyl-afgeleide UPy moleculen werden gesynthetiseerd. De waargenomen oppervlakte-verhoogde schijnbare waarde van de dimerisatieconstante kon aangepast worden door oplosmiddelsamenstelling en temperatuur, waardoor een volledige controle over de stabiliteit van het complex werd verkregen. Dit opent nieuwe perspectieven voor de constructie van meer complexe, georiënteerde supramoleculaire architecturen, maar kan ook gebruikt worden voor de studie van pyrimidinone gebaseerde supramoleculaire polymeren aan oppervlakken en grensvlakken.

In Hoofdstuk 5 worden experimenten beschreven waarin SMFS wordt gebruikt om de breekkracht te meten van individuele supramoleculaire complexen van UPy afgeleiden, die bijeengehouden worden met een 4-voudige waterstofbrug. De kracht benodigd om individuele arrays van 4 waterstofbruggen te verbreken bedroeg 180 ± 21 pN, gemeten met een loading rate van 35 ± 0.7 nN/s in hexadecaan. Deze krachten bleken loading rate afhankelijk te zijn in een bereik van 5 tot 500 nN/s bij een temperatuur van 301 K. De breekkrachten veranderden met de temperatuur en waren onafhankelijk van de loading rate in het gebied van 5 tot 200 nN/s bij 330 K. Dit betekent dat de breekkrachten van supramoleculaire H-gebonden UPy complexen een overgang vertoonden van quasi-evenwicht naar niet-evenwicht als gevolg van veranderingen in temperatuur. De kracht bij het cross-over point was 145 ± 20 pN. Deze resultaten vormen een allereerste demonstratie van krachtmetingen aan synthetische waterstofbrug-gebonden systemen die overgangen van niet-evenwichts naar quasi-evenwichtstoestanden laten zien als gevolg van een temperatuursverandering. Een soortgelijke overgang werd gevonden als gevolg van een verandering in de samenstelling van het oplosmiddel.

De AFM resultaten beschreven in Hoofdstuk 6 laten zien dat reversibele supramoleculaire polymeren bestudeerd kunnen worden op het niveau van een enkel molecuul. In poly(ethyleen glycol) gebaseerde UPy supramoleculaire polymeren gedragen de individuele reversibele verbindingen van een supramoleculaire polymeerketen (complexen gebaseerd op de zelfcomplementariteit van de UPy groepen) zich als onafhankelijke bindingen in serie. De gemeten breekkracht van een individueel zelf-complementair UPy complex in supramoleculaire polymeren was 173 ± 23 pN bij een loading rate van 35 ± 0.7 pN/s. Omdat materiaaleigenschappen zoals viscositeit, samenstelling en ketenlengte functies zijn van verscheidene externe parameters en stimuli die in situ onderzocht kunnen worden, wordt zeer waardevolle informatie verkregen uit de SMFS experimenten voor het ontwerp en de constructie van nanometerschaal devices en stimuli-responsive systemen.

In Hoofdstuk 7 is systematisch gekeken naar de insertie van ethyleen sulfide eind-gefunctionaliseerde poly(ferrocenylsilane) (PFS) afgeleiden in reeds gevormde zelf-georganiseerde monolagen (SAMs). Een robuuste en reproduceerbare methode stelde ons in staat om geïsoleerde PFS macromoleculen covalent gebonden aan een vast oppervlak te realiseren. Verschillende technieken, zoals AFM, contacthoek en electrochemische metingen werden uitgevoerd om de morfologie, wettability en oppervlakte-bedekkingsgraad van de gemengde lagen te bepalen. De PFS bedekkingsgraad hing af van de ketenlengte van het thiol molecuul gebruikt voor de reeds gevormde SAMs en de concentratie van PFS in de oplossing, maar niet van de insertietijd of de ketenlengte van de eind-gefunctionaliseerde PFS moleculen. Zeer lage

bedekkingsgraden werden bereikt door insertie vanuit zeer verdunde PFS oplossingen in long-chain SAMs. Differential pulse voltammetry bleek een zeer nuttige methode te zijn om de isolatie effecten te ontrafelen die optreden in de gemengde lagen met lage PFS bedekkingsgraad. In samples met een zeer lage bedekkingsgraad van PFS moleculen worden interketen interacties vermeden, wat een vereiste was voor het onderzoek naar enkelvoudige keten elongatiemetingen door middel van SMFS. Voor het eerst werden de geïmmobiliseerde geïsoleerde PFS moleculen onderworpen aan in situ AFM voor SMFS metingen in isopropanol. De elasticiteit van individuele PFS polymeerketens werd bepaald door een fit van de experimentele resultaten met een modified freely-jointed chain (m-FJC) model. Hieruit bleek dat, afhankelijk van de uitgeoefende kracht, het polymeer entropisch en ook deels enthalpisch elastisch gedrag vertoont.

In Hoofdstuk 8 wordt aangetoond dat een externe chemische of electrochemische stimulus gebruikt kan worden om reversibele elasticiteitsveranderingen teweeg te brengen in individuele PFS ketens op oppervlakken, als gevolg van een verandering in de redox toestand van het molecuul van neutraal naar geoxideerd. De veranderingen zijn gemeten op het niveau van enkelvoudige moleculen met behulp van SMFS. Door het fitten van de force-extension data met het modified FJC model werd gevonden dat een enkele geoxideerde PFS keten een Kuhn lengte van ~ 0.65 nm heeft en een segment elasticiteit van ~ 45 nN/nm, in vergelijking met ~ 0.40 nm en ~ 30 nN/nm voor de keten in de neutrale toestand. Deze gedetecteerde veranderingen in de elasticiteit van individuele stimuli-responsive PFS macromoleculen vormen de basis voor de demonstratie van het principe van een electrochemisch of chemisch gedreven single-molecule motor. Voor het PFS homopolymer (polymerisatiegraad is 80) werd een arbeid van 3.4×10^{-19} J en een efficiëntie van 5% geschat, gebaseerd op de experimentele data.

Acknowledgements

I always considered it trite and exaggerated of thesis authors to list a full set of people who were 'invaluable'; always, that is, until I wrote my own thesis and realized just how deeply I am in debt to the people who have contributed to the work presented here.

First and foremost, I want to extend deep sense of gratitude to my promotor, Prof. Dr. G. Julius Vancso, for offering me the opportunity pursuing my Ph.D study in the MTP group. Dear Julius, thank you so much for your guidance and endless encouragement throughout all these years. I cannot thank you enough for giving me the freedom and lively atmosphere where I have benefited from the collaboration with many people. I truly appreciate the personal advice and concern on my future.

I wish to express my humble regards to my assistant promoter, Dr. Holger Schönherr for all his active suggestions and constant support. Dear Holger, thank you very much for your thoughtful consideration, unlimited patience, and always being available for discussions. Thanks a lot for teaching me so much, for spending an awful amount of time on my presentations, posters, and papers.

There are numerous people who contributed to the research described in this thesis. Firstly, I am very grateful to Prof. David Reinhoudt, Dr. Jurriaan Huskens, Dr. Menno de Jong, Dr. Alart Mulder and Dr. Tommaso Auletta from the SMCT group, for their collaborative work described in Chapter 3. My gratitude is also extended to Dr. Zhihong Zhang, Dr. Renate Förch and Prof. Wolfgang Knoll (MPIP, Mainz, Germany) for their help in carrying out the SPR measurements presented in Chapter 4. Dr. Rob Lammertink, Dr. Maria Peter and Igor Korczagin are highly acknowledged for sharing their valuable chemicals with me. I wish to thank Yujie Ma and Ivan Mera, for their excellent Master-project work that has been incorporated in Chapter 7 and Chapter 5.

I owe many thanks to the committee members, especially to Prof. Jan Greve and my former supervisor Prof. Xi Zhang. With their advice and support, I came to Twente and had the four-year study going well. I would like to express my appreciation to the project leader, Dr. Martin Bennink for his continuous support and for his translating the English summary into Dutch. Dr. Wouter den Otter is acknowledged for reading and correcting the thesis.

Acknowledgements

I am very grateful to Dr. Mark Hempenius for his admirable suggestions with the synthesis and translation issues. Appreciative words cannot be enough to thank Ing. Clemens Padberg for his constant help with instruments and computers. I would like to mention all the ladies: Genevieve, Lena, Karin, Cindy, Gerda and Thelma for their kind help. I also thank Zlata and Netty de Groot for their assistance.

I have been extremely lucky to meet many wonderful colleagues during these years. It would be impossible to mention all the names of people that have helped me in one way or another. Nevertheless, I would like to express my special thanks to Dr. Szczepan Zapotoczny, for his valuable assistance and warm-hearted help during my very first half year. I also want to thank Dr. Xuemei Li and Dr. Barbara Dordi for sharing their experience and giving suggestions on many measurements. I am awfully thankful to all past and present MTP members for their help and kindness. I have enjoyed enormously working with you. I also appreciate the kind help from members of other groups (PBM, RBT, STEP, SMCT).

Many of these fantastic people became more than just colleagues. Dear Attila, Bon-Hua, Chuanliang, Fenghua, HE Tao, Jing, Lanti, LI Xiang, LI Xiao, Menglin, XU Hong, XU Jiang, Xuemei, Yujie, ZHANG Zheng, and Zhiyuan, thank you very much for your company, your help (whenever needed), and the enjoyable moments you have given to me.

Finally, and most importantly, I want to thank my family for their unconditional support and absolute understanding, especially to my dear Mum and my beloved husband Yuguo!

Shan

Publications

REVIEWED:

1. Stretching and rupturing individual supramolecular polymer chains by AFM
Zou, S.; Schönherr, H.; Vancso, G. J. *Angew. Chem. Int. Ed.* 2005, in press.
2. Grafting of single, stimuli-responsive poly(ferrocenylsilane) polymer chains to gold surfaces
Zou, S.; Ma, Y.; Hempenius, M. A.; Schönherr, H.; Vancso, G. J. *Langmuir* 2004, 20, 6278-6287.
3. Beta-cyclodextrin host-guest complexes probed under thermodynamic equilibrium: thermodynamics and AFM force spectroscopy
Auletta, T.; de Jong, M. R.; Mulder, A.; van Veggel, F. C. J. M.; Huskens, J.; Reinhoudt, D. N.; **Zou, S.**; Zapotoczny, S.; Schönherr, H.; Vancso, G. J.; Kuipers, L. *J. Am. Chem. Soc.* 2004, 126, 1577-1584.
4. Tunable complex stability in surface molecular recognition mediated by self-complementary quadruple hydrogen bonds
Zou, S.; Zhang, Z.; Förch, R.; Knoll, W.; Schönherr, H.; Vancso, G. J. *Langmuir* 2003, 19, 8618-8621.
5. Single-molecule force spectroscopy on carrageenan by means of AFM
Xu, Q.; **Zou, S.**; Zhang, W.; Zhang, X. *Macromol. Rapid. Commun.* 2001, 22, 1163-1167.
6. Study on polymer micelles of hydrophobically modified ethyl hydroxyethyl cellulose using single-molecule force spectroscopy
Zou, S.; Zhang, W.; Zhang, X.; Jiang, B. *Langmuir* 2001, 17, 4799-4808
7. Single polymer chain elongation of poly(N-isopropylacrylamide) and poly(acrylamide) by atomic force microscopy
Zhang, W.; **Zou, S.**; Wang, C.; Zhang, X. *J. Phys. Chem. B* 2000, 104, 10258-10264.
8. Single-molecule force spectroscopy on Bombyx mori silk fibroin by atomic force microscopy
Zhang, W.; Xu, Q.; **Zou, S.**; Li, H.; Xu, W.; Zhang, X.; Shao, Z.; Kudera, M.; Gaub, H. *Langmuir* 2000, 16, 4305-4308.
9. Layer-by-layer self-assembled multilayer films containing the organic pigment, 3,4,9,10-perylenetetracarboxylic acid, and their photo- and electroluminescence properties
Sun, J.; **Zou, S.**; Wang, Z.; Zhang, X.; Shen, J. *Mater. Sci. & Eng. C* 1999, 10, 123-126.
10. Layer-by-layer assemblies of polycation bearing Os complex with electroactive and electroinactive polyanions and their electrocatalytic reduction of nitrite
Sun, J.; Sun, Y.; **Zou, S.**; Zhang, X.; Sun, C.; Wang, Y.; Shen, J. *Macromol. Chem. Phys.* 1999, 200, 840-844.
11. Multilayer assemblies of colloidal ZnS doped with silver and polyelectrolytes based on electrostatic interaction
Sun J.; Hao, E.; Sun, Y.; Zhang, X.; Yang, B.; **Zou, S.**; Shen, J.; Wang, S. *Thin Solid Films* 1998, 327, 528-531.

UNREVIEWED:

12. Molecular Interactions in Supramolecular Dimers and Polymers by Force Spectroscopy
Vancso, G. J.; **Zou, S.**; Schönherr, H. *Polym. Mater.: Sci. & Eng.* 2004, 90, 18-19.
13. Tunable complex stability in surface molecular recognition mediated by self-complementary quadruple hydrogen-bonds.
Schönherr, H.; **Zou, S.**; Zhang, Z.; Förch, R.; Knoll, W.; Vancso, G. J. *Polym. Preprints* 2003, 44, 489-490.
14. Single molecular interactions in supramolecular host-guest systems by AFM
Zou, S.; Zapotoczny, S.; de Jong, M. R.; Auletta, T.; Schönherr, H.; Huskens, J.; van Veggel, F. C. J. M.; Reinhoudt D. N.; Vancso, G. J. *Polym. Mater.: Sci. & Eng.* 2003, 88, 453-454.
15. Single molecule probing of polymers and supramolecular materials
Vancso, G. J.; Schönherr, H.; **Zou, S.**; de Jong, M. R.; Huskens, J.; Tomczak, N.; Vallee, R.; van Hulst, N. F.; Reinhoudt, D. N. *Polym. Mater.: Sci. & Eng.* 2003, 88, 141-142.

Curriculum Vitae

Shan ZOU was born on August 6, 1975 in Changchun, P. R. China. In 1994, she entered the College of Chemistry, Jilin University (Changchun, China) without taking the National exams due to her outstanding performance in Chemistry Olympiad (1994) of high school students all over China. Four years later, she obtained her Bachelor's degree (with distinction). In the same year, she joined the research group of Prof. Dr. Xi ZHANG to pursue her Master Degree in the Key Lab of Supramolecular Structure and Materials, Jilin University. With a thesis entitled "Study on Polymer Micelles of Hydrophobically Modified Ethyl Hydroxyethyl Cellulose Using Single-Molecule Force Spectroscopy", she graduated in 2001. Thereafter, she joined Material Science and Technology of Polymers group in University of Twente, the Netherlands, as a Ph.D. student under the supervision of Prof. Dr. G. Julius Vancso. Her Ph.D. research subjects covered molecular level visualization, sensing (by force), manipulation, and control of supramolecular assemblies and polymeric materials on the nanoscale using self-assembled monolayers (SAMs) and atomic force microscopy (AFM)-based platforms. She is currently working as a research fellow in the same group. Starting from May 1st, 2005, she will work in the research group of Prof. Dr. Gilbert C. Walker (University of Toronto) as a postdoctoral researcher.